The Role of van der Waals Interactions on the Electronic Properties of Molecules and Materials

Technische Universität
Berlin

Fritz-Haber-Institut der
Max-Planck-Gesellschaft

Nicola Ferri

Berlin 2017

The Role of van der Waals Interactions on the Electronic Properties of Molecules and Materials

vorgelegt von
M.Sc. Nicola Ferri
geb. Ponte dell'Olio (Italien)

von der Fakultät II - Mathematik und Naturwissenschaften
der Technischen Universität Berlin
zur Erlangung des akademischen Grades

Doktor der Naturwissenschaften
Dr.rer.nat.

genehmigte Dissertation

Promotionsausschuss:

Vorsitzender: Prof. Dr. Michael Kneissl
Gutachter: Prof. Dr. Andreas Knorr
Gutachter: Prof. Dr. Alexandre Tkatchenko
Tag der wissenschaftlichen Aussprache: 07.04.2017

Berlin 2017

"hunc igitur terrorem animi tenebrasque necessest
non radii solis neque lucida tela diei
discutiant sed naturae species ratioque."

—Lucretius, De Rerum Natura

ABSTRACT

Long-range van der Waals (vdW) interactions play a fundamental role in the structure and stability of many systems, ranging from small dimers to complex hybrid inorganic/organic systems (HIOS). However, how strong is the effect of vdW interactions on the electronic properties of molecules and extended systems? It is often argued that the vdW energy has a small, or even negligible, direct influence on the electron density, $n(\mathbf{r})$, and derived electronic properties, since the vdW energy represents only a tiny fraction (0.001%) of the total electronic energy.

To answer the question posed above, we developed and employed a fully self-consistent (SC) implementation of the density-dependent interatomic vdW functional of Tkatchenko and Scheffler and its extension to surfaces. Not surprisingly, vdW self-consistency leads to tiny modifications of the structure, stability, and electronic properties of molecular dimers and crystals. However, sizable effects are found in the electronic properties of large molecular complexes. Moreover, unexpectedly large changes in the binding energies, distances and electrostatic moments are detected for highly polarizable alkali metal dimers. Most importantly, vdW interactions produced complex and sizable electronic charge redistribution in the vicinity of metallic surfaces and at organic/metal interfaces.

As a result, for several coinage metal (111) surfaces, self-consistency induces modifications in the surface dipole, leading to an increase of up to $0.30\,$eV in the computed workfunctions. Furthermore, in the case of HIOS, SC vdW entails modifications of up to $0.22\,$eV in the shift of the interface workfunction, a property induced by molecular adsorption. The underlying mechanism responsible for the workfunction modifications stems from an interplay between two effects driven by SC vdW interactions: (i) the modification of the interface dipole, and (ii) a reduction in the charge transfer between the molecule and the surface.

In conclusion, the analysis of SC vdW effects performed in this work demonstrates the importance of vdW interactions on the electronic properties of different classes of systems, with self-consistency systematically improving the agreement between the theoretical predictions and the experimental measurements. Overall, our study reveals a nontrivial connection between electrostatics and long-range electron correlation effects.

ZUSAMMENFASSUNG

Langreichweitige van der Waals (vdW) Wechselwirkungen spielen eine fundamentale Rolle in der strukturellen Stabilität vieler Systeme – von kleinen Dimeren bis hin zu komplexen hybriden anorganisch/organischen Systemen (HIOS). Wie stark ist allerdings der Effekt der vdW Wechselwirkung auf die elektronischen Eigenschaften von Molekülen und ausgedehnten Systemen? Da die vdW Energie nur einen Bruchteil (0.001%) der elektronischen Gesamtenergie darstellt wird oft argumentiert, dass sie einen kleinen oder gar vernachlässigbaren unmittelbaren Einfluss auf die Elektronendichte $n(\mathbf{r})$ und die davon abgeleiteten elektronischen Eigenschaften hat.

Um die oben gestellte Frage zu beantworten, haben wir eine vollständig selbstkonsistente (SC) Implementierung des dichteabhängigen, interatomaren vdW Funktionals von Tkatchenko und Scheffler und dessen Erweiterung auf Oberflächen entwickelt und verwendet. Wie zu erwarten, führte die vdW-Selbstkonsistenz nur zu kleinen Veränderungen in Struktur, Stabilität und elektronischen Eigenschaften von molekularen Dimeren und Kristallen. Jedoch konnten wir deutlichere Effekte in der elektronischen Struktur von großen molekularen Komplexen feststellen. Unerwartet große Abweichungen traten bei den Bindungsenergien und -längen, sowie den elektrostatischen Momenten stark polarisierbarer Alkalimetall-Dimere auf. Die wichtigsten Unterschiede durch die vdW Wechselwirkungen ließen sich jedoch anhand beträchtlicher Umverteilungen der Elektronendichte an metallischen Oberflächen und organisch/metallischen Grenzflächen beobachten.

Als Resultat finden wir für diverse *Coinage Metal* (111) Oberflächen, dass die Selbstkonsistenz Veränderungen des Oberflächendipols induziert, welche zu einer Erhöhung von bis zu $0.3\,\text{eV}$ in den berechneten Austrittsarbeiten führt. Weiterhin finden wir für den Fall von HIOS, dass SC vdW zu Verschiebungen in der Grenzflächen-Austrittsarbeit von bis zu $0.22\,\text{eV}$ führt – eine Eigenschaft, die durch molekulare Adsorption verursacht wird. Der zugrundeliegende Mechanismus, welcher verantwortlich für die Veränderungen in der Austrittsarbeit ist, stammt vom Zusammenwirken zweier Effekte der SC vdW Wechselwirkungen: (i) die Veränderung der Grenzflächen-Dipole und (ii) eine Reduzierung des Ladungstransfers zwischen Molekül und Oberfläche.

Im Ergebnis zeigt unsere hier dargestellte Analyse der SC vdW Effekte die Wichtigkeit der vdW Wechselwirkungen für die elektronischen Eigenschaften anhand unterschiedlicher Arten von Systemen, welche mit Hilfe der Selbstkonsistenz systematisch die Übereinstimmung zwischen theoretischen Vorhersagen und experimentellen Messungen verbessern konnte. Insgesamt stellt unsere Studie einen nicht-trivialen Zusammenhang zwischen der Elektrostatik und langreichweitigen Elektronenkorrelationen fest.

Contents

List of Notations and Symbols

$\mathscr{H}$ Total Hamiltonian. 8

$\mathbf{r}$ Electron position. 9

$\mathbf{R}$ Nuclear position. 9

Ψ Total electronic wavefunction. 10

H_e Total electronic Hamiltonian. 10

ψ_i One electron spin-orbital. 14

$h(\mathbf{r})$ One-particle operator. 15

$v_{\mathrm{H}}(\mathbf{r})$ Hartree potential. 15

E_0 Ground-state energy. 16

Ψ_0 Hartree-Fock ground-state wavefunction. 16

$\mathcal{F}$ Fock operator. 17

$v_{\mathrm{ex}}(\mathbf{r})$ Exchange operator. 17

ϵ_i Single-particle eigenvalue. 19

E_{corr} Correlation energy. 22

$\mathcal{V}$ Perturbation potential. 26

$n(\mathbf{r})$ Electron density. 31

$g(E)$ Density of states. 33

$n_0(\mathbf{r})$ Ground-state electron density. 35

$v_{\mathrm{ext}}(\mathbf{r})$ External potential. 35

$\chi(\mathbf{r}, \mathbf{r}', \omega)$ Response function. 47

$\chi_0(\mathbf{r}, \mathbf{r}', \omega)$ Non-interacting response function. 47

$G(\mathbf{r}\sigma t, \mathbf{r}'\sigma' t')$ Single-particle Green's function. 50

$\Theta(t - t')$ Step function. 50

$G_0(\mathbf{r}\sigma t, \mathbf{r}'\sigma' t')$ Unperturbed single-particle Green's function. 51

α Polarizability. 60

$\mathrm{vdW}^{\mathrm{TS}}$ Tkatchenko-Scheffler interatomic van der Waals functional. 60

$w(\mathbf{r})$ Hirshfeld partitioning weight. 62

a_0 Lattice constant. 74

$\mathrm{vdW}_{\mathrm{sc}}^{\mathrm{TS}}$ Self-consistent implementation of the $\mathrm{vdW}^{\mathrm{TS}}$ functional. 93

$\mathrm{vdW}_{\mathrm{sc-old}}^{\mathrm{TS}}$ Non-optimized version of the $\mathrm{vdW}_{\mathrm{sc}}^{\mathrm{TS}}$ functional. 105

E_b Binding energy. 109

D Debye, CGS unit of the electric dipole moment. 113

Φ Workfunction of the clean metal surface. 125

E_F Fermi energy. 125

V_{vac} Electrostatic potential in the vacuum region. 126

$\Delta\Phi$ Workfunction shift. 133

Φ' Workfunction of the hybrid system. 134

List of Abbreviations

DFA density functional approximations. 7

BO Born-Oppenheimer. 9

HF Hartree-Fock. 13

CI Configuration interaction. 21

RPA Random phase approximation. 29

DFT Density-functional theory. 31

XC Exchange-correlation. 31

HEG Homogeneous electron gas. 32

KS Kohn-Sham. 37

EXX Exact-exchange. 40

LDA Local density approximation (DFT functional). 41

GGA Generalized gradient approximation. 42

PBE Perdew, Burke and Ernzerhof (DFT functional). 43

ACFD Adiabatic-connection fluctuation-dissipation. 47

TS Tkatchenko-Scheffler. 60

LZK Lifshitz-Zaremba-Kohn. 70

SC Self-consistent. 83

H-F Hellmann-Feynman. 96

HIOS Hybrid inorganic/organic systems. 131

Bz Benzene (molecule). 135

DIP Diindenoperylene (molecule). 139

XSW X-ray standing waves. 139

STM Scanning tunneling microscope. 139

LEED Low-energy electron diffraction. 139

DOS Density of states. 142

MODOS Molecular orbital density of states. 142

UPS Ultraviolet photoelectron spectroscopy. 146

Introduction

Since the earliest observations of natural phenomena, one of the central ambitions in science has been understanding the fundamental laws that describe interactions in matter. In the XVIII and XIX centuries, thanks to the technological progress, numerous scientists dedicated much effort in investigating ensembles of many interacting particles, including gases and liquids. As a result of these investigations it emerged that besides local strong bondings, referred nowadays as covalent interactions, all particles can experience long-ranged forces, the so-called non-covalent interactions. One of the most important contributions in this regard was done by J. D. van der Waals, who proposed in 1873 his well-known equation for gases and liquids, which corrects the ideal gas law by accounting for excluded volume and attraction between the different particles. Thanks to his seminal work, his name is commonly used as a synonym for non-covalent interactions.

Van der Waals (vdW) interactions are ubiquitous and play a prominent role in a broad spectrum of phenomena occurring at very different scales: from polymorphism in molecular crystals [1], heterogeneous catalysis [2] and drug-protein binding [3] and even cohesion in soft asteroids [4]. In the context of surface science, central to the present work, vdW forces can strongly influence adsorption/desorption processes, controlling both static and dynamical properties of substrate-adsorbate complexes [5–10]. Notably, this work has been done at the Fritz Haber institute, which is named after one of the pioneers of surface science. The discoveries of Fritz Haber in catalysis were rewarded with the Nobel prize in 1918 and lead to the Haber-Bosch process, still largely used to date for the industrial production of ammonia (fertilizers and explosives). Later, the study of processes occurring at surfaces has been developed tremendously over about a century. Nowadays, much effort is dedicated to characterize and design the structure and the properties of interfaces. These systems can possess a range of electronic properties that the individual components forming the interface do not exhibit [11]. Some of the most promising applications include multi-layered materials and nanomaterials for electrochemical energy conversion and storage as solar-energy devices, sensors, heterogeneous catalysis, light emitting devices and materials with specific properties as flexible LCD, high-strength fibers or flame retardant coatings. The interface properties are the result of a complex interplay between covalent bonds, charge transfer processes, vdW forces, hydrogen bonds and Pauli repulsion. Therefore,

controlling and manipulating the functionalities at the interface represent formidable challenges, investigated both theoretically and experimentally.

In this context, it becomes clear that a thorough comprehension of the subtle laws that govern vdW interactions is necessary in order to model and predict structures and properties of a wide range of systems. The first microscopic understanding of non-covalent forces dates back to the seminal work of F. London, around 1930, and was made possible by the advent of quantum mechanics. In particular, the vdW attraction between isotropic well-separated fragments was explained as stemming from correlated quantum mechanical fluctuations of the electronic charge, resulting in mutually induced electric multipoles. This approach provided a solid justification to the well known C_6/R^6 power law expression for intermolecular dispersion interactions, earlier postulated by van der Waals. However, we note that despite the large progress made in many-body theories and the simplicity of London's formulation, developing an efficient electronic structure method that is able to capture both covalent and non-covalent interactions still remains one of the main challenges of present-day parameter-free atomistic modeling.

Density-functional theory (DFT) is the method of choice for the theoretical description of ground-state cohesive and electronic properties of atoms, molecules, bulks and adsorption phenomena. DFT offers the advantages of a first-principle quantum mechanical theory (*ab initio*) with a good compromise between accuracy and efficiency. On the whole, DFT represents the most popular electronic structure method and the success of this theory significantly contributed to the development of quantum chemistry and theoretical condensed matter physics. In principle, DFT is an exact theory for the ground-state electron density and energy. In practice, however, approximations need to be employed for quantum-mechanical exchange-correlation effects *via* the so-called density functional approximations (DFAs). Thus, the accuracy and the efficiency of DFT largely depends on the chosen DFA.

The most popular DFAs are constructed from the local electron density (and its gradient). Therefore, they are unable to capture non-local interactions, such as the long-ranged vdW interactions. Many remedies have been proposed to include the vdW interactions within the DFT framework. In this work we employed the scheme of Tkatchenko and Scheffler (TS), in combination with semi-local DFAs. The TS functional includes hybridization and other semi-local effects induced on atoms by the chemical environment. Moreover, many-body effects arising in solids can be effectively included into the TS functional *via* two extensions that model i) ionic solids and semiconductors and ii) metal surfaces and adsorption of atoms/molecules on surfaces (vdW$^{\mathrm{surf}}$).

In the literature the importance of vdW effects in the cohesive forces between atoms and molecules has been extensively addressed. Moreover, electronic structure calculations have unraveled the qualitative and quantitative role of vdW interactions in the structure and stability of solids and interfaces. In this regard, the TS functional contributed in determining that vdW interactions can indeed affect the cohesive properties of solids such as lattice constants, bulk moduli and cohesive energies. However, a thorough analysis of the role of vdW interactions on the electronic properties of molecules

and extended systems has still not been performed to date.

Typically, long-range vdW energies represent a crucial, but tiny fraction ($\sim 0.001\%$) of the electronic energy. Hence, the influence of vdW interactions on the electronic properties is often assumed to be rather small, if not negligible. For this reason, vdW interactions are usually incorporated as a perturbative correction to the total DFT energy. In other words, the vdW energy is added after the convergence of the electron density, obtained *via* the self-consistent (SC) procedure. On the other hand, in a fully SC scheme, the electronic vdW potential would be directly part of the DFT effective potential. In this way, at convergence, the effects of vdW interactions would be automatically included into the total energy, the electron density and electronic properties.

In this work, we present a fully SC implementation of the TS and the vdW$^{\mathrm{surf}}$ functionals. The effects of a SC treatment of vdW interactions on the electronic properties are assessed for a wide range of different systems: from dimers (e.g. diatomic dimers, water dimer) to complex hybrid inorganic/organic systems, passing through large molecular systems and metal surfaces. Not surprisingly, vdW interactions induce only small changes in the cohesive and electronic properties of molecular dimers and crystals. However, self-consistency turns out to be very important for highly polarizable systems, metallic surfaces and hybrid organic/inorganic systems.

This dissertation is structured as follows. The first part summarizes the theoretical background, underlying the electronic structure methods related to this work. Particular attention will be dedicated to DFT and the most popular DFAs. The second chapter contains an overview of the various pairwise approaches for including vdW interactions into DFT. A part of this chapter is dedicated to the modeling of vdW interactions in metals and for adsorption phenomena. This part will focus on the possible treatments of the many-body effects coming from the substrate and between the substrate and an adsorbed atom. Among all the vdW-inclusive methods presented, the TS and the vdW$^{\mathrm{surf}}$ functionals will be discussed in greater detail.

The third chapter is dedicated to the self-consistent implementation of the TS method. First, the electronic structure code used in this work, FHI-aims, is presented and described. In this way the reader is introduced to some technical aspects that will be useful to understand better the SC implementation. As a second step, the SC equations are derived analytically from the TS energy formula. In the last part, the SC implementation is described in detail, along with the procedure performed to reduce the computational cost and possible future optimizations. Finally, the computational efficiency is benchmarked, considering the implementation before and after the optimization procedure. Comparisons with other DFT functionals are also shown.

In the fourth chapter we discuss applications of the self-consistent TS and vdW$^{\mathrm{surf}}$ methods. In the fist section non-periodic systems are analyzed, including small rare-gas dimers, benzene dimers, C_{60} fullerene, large DNA-protein complexes. The chapter starts with the analysis of SC effects on the binding energies and on the different components of the total energy. After that, the effects in the electron density are discussed and compared with high-level quantum-chemical calculations. The special case of the alkali-

metal dimers is considered in the final part. These small systems are largely bound by vdW interactions and turned out to be particularly sensitive to SC effects.

The last two sections are dedicated to metal surfaces and hybrid organic/inorganic systems. The SC effects on the electron density are shown, along with the ensuing modifications in the electronic properties. The hybrid systems present a particularly interesting interplay of different effects. We will discuss each one of these systems through a detailed study of the electron density modifications. The population analysis of the molecular orbitals is also presented.

The dissertation is concluded with a summary of the results obtained so far and an outlook with the ideas for future studies and the remaining challenges.

Part I

The Many-Body Problem

1 Theoretical Background

1.1 Introductory Remarks

This chapter introduces the basic concepts, notations and approximations underlying the *ab initio* (non empirical) electronic structure methods employed throughout this Thesis. The formalism presented here constitutes the backbone to tackle the many-body problem and is a necessary prerequisite before moving to the detailed description of the various methodologies. After a general discussion of the many body problem we will explain and motivate a central approximation in condensed matter physics and quantum chemistry, implying that all the methods presented here treat the electrons as quantum objects and focus on the solution of electronic problem, whereas the nuclei are treated as classical particles and can be considered fixed in a given configuration with respect to the electron motion.

The second part of this chapter describes wavefunction-based methods, starting with the formalism behind the Hartree-Fock (HF) approximation and building the hierarchy of quantum-chemical methods up to the formally exact solution of the electron many-body problem. In passing, several different techniques used to approximate the exact solution of the many-body problem will be discussed as well. Then, we will introduce the theoretical method of central importance in this thesis: the density-functional theory (DFT). Similarly to the HF approximation, DFT will be discussed starting with the original ideas and concepts and ending with the most popular approximations and extensions. In principle DFT is an exact theory, however we will see that for practical calculations it is necessary to employ many different approximations. In the last section of this chapter, the concept of Green's function will be introduced, along with Green's function based electronic structure methods.

The exact solution of the many-body problem, within the approximation of a finite basis set [1], is computationally prohibitive and can be applied only to a restricted set of very simple and small systems. Therefore, all the electronic structure methods that will be presented in this work lead to approximate results. For example, the missing contribution to the total energy in the Hartree-Fock approximation is called the correlation energy. Formally, correlation is present in DFT, but its exact form is unknown, hence it is approximated with density functional approximations (DFA). A variety of

[1] The exact analytic solution of the Scrödinger equation is available only for a one-electron system.

procedures are available for computing approximations of the correlation energy and improving upon the HF and the DFT methods. For instance, the post-HF method of configuration interaction takes into account excited electronic configurations, built upon the HF ground-state. Another widely used technique is the many-body perturbation theory, which can be employed in both the Hartree-Fock and DFT frameworks. Very briefly, the perturbation theory treats the missing correlation part as a perturbative term in the total Hamiltonian and allows to analytically expand the correlation energy as an infinite series, which is truncated for practical calculations. Naturally, the computational cost of the approximation rapidly increases with respect to the number of terms retained in the series. On the other hand, the accuracy in perturbation theory is not improved systematically with additional terms, but converges with an oscillatory behavior.

In this work we will focus on a specific part of the correlation: the long-range correlation interactions, also referred to as van der Waals energy. Within the DFT framework, the long-range correlation interactions are absent in most of the popular DFA. To remedy this situation two different paths can be followed: i) an *ad hoc* correction of the total energy or ii) the introduction of a new term in the Hamiltonian, *i.e.* a modification of the DFA. The former solution, called *a posteriori*, is applied at the end of a calculation and guarantees a modest computational cost. However, such corrections are limited only to the total energy. The argument commonly used to justify this approach is that the long-range correlation contributions are quantitatively small, hence they are typically considered not important for the electronic properties. On the other hand, the long-range correlation interactions can be added as a part of the DFA, consistently throughout the electronic structure calculation. In this way the long-range correlation is directly included into all quantities and properties in a self-consistent way. The comparison between the *a posteriori* and the self-consistent approaches, is one of the main goals of this work.

1.2 The Many-Body Hamiltonian

The Hamiltonian ($\mathscr{H}$) of a piece of matter composed by electrons and nuclei, in the absence of an external electromagnetic field, can be written as

$$\mathscr{H} = T_e + T_n + V_{e-e} + V_{n-n} + V_{e-n}\,, \tag{1.1}$$

where T_e and T_n are the electronic and nuclear kinetic energy operators. V_{e-e} and V_{n-n} are the electron–electron and nuclear–nuclear Coulomb repulsion, and the last term, V_{e-n}, is the electron–nuclear Coulomb attraction. Neglecting relativistic effects [2], the

[2] The equation in the fully relativistic case is the Dirac equation.

Hamiltonian (1.1) can be explicitly written as:

$$\begin{aligned}\mathscr{H} = \; & - \sum_{i}^{N_e} \frac{\hbar^2}{2m_e}\nabla_i^2 - \sum_{I}^{N_n} \frac{\hbar^2}{2M_I}\nabla_I^2 + \\ & + \frac{1}{2}\sum_{i\neq j}^{N_e} \frac{e^2}{|\mathbf{r}_i - \mathbf{r}_j|} + \frac{1}{2}\sum_{I\neq J}^{N_n} \frac{Z_I Z_J e^2}{|\mathbf{R}_I - \mathbf{R}_J|} - \sum_{i}^{N_e}\sum_{I}^{N_n} \frac{Z_I e^2}{|\mathbf{r}_i - \mathbf{R}_I|}\,,\end{aligned} \tag{1.2}$$

where the indices i, j refer to electrons and I, J to nuclei. M_I is the nuclear mass, Z_I the nuclear charge. N_e and N_n are the total number of electrons and nuclei respectively, the two expressions containing the electron–electron and nuclear–nuclear interactions do not to consider the self-interaction terms $i = j$ and $I = J$. Here and in the rest of this chapter we adopt Gaussian units for notational simplicity. The eigenfunctions of the Hamiltonian with time-independent potential are obtained *via* the solution of the time-independent Schrödinger equation:

$$\mathscr{H}|\Theta\rangle = \mathscr{E}|\Theta\rangle\,, \tag{1.3}$$

where $\mathscr{E}$ is the total energy of the system and Θ is the many-body wavefunction, which depends on both electronic and nuclear coordinates, $\Theta = \Theta(\{\mathbf{r}_i\}, \{\mathbf{R}_I\})$. In this general formulation of the many-body problem each nucleus and each electron is free to move in all three spatial directions and the solution of Equation 1.3 implies a problem of $3N_e + 3N_n$ ($4N_e$ considering the spin variables) degrees of freedom. If follows that a feasible solution of the many-body Hamiltonian implies the introduction of some approximations, as the Born-Oppenheimer approximation, discussed in the next section.

1.3 The Born-Oppenheimer Approximation

A key approximation is the Born-Oppenheimer (BO) or adiabatic approximation, developed by Max Born and J. Robert Oppenheimer in 1927 [12]. The BO provides a great simplification of the Schrödinger equation (see Equation 1.3) by separating the dynamics of electrons and nuclei. This approximation is based on the fact that the nuclei are much heavier than the electrons and the ratio m_e/M_n is very small. It follows that, in the so-called "adiabatic" procedure, the electrons are considered to move much faster than the nuclei and their dynamics can be decoupled and studied for fixed nuclear positions. In other words, the nuclear positions $\mathbf{R}_I$ become parameters, and the electronic Hamiltonian can be separated from the general one (see Equation 1.2). A second advantage is that the nuclear–nuclear Coulomb repulsion V_{n-n} is a constant for any given configuration. The solutions of the electronic problem are eigenvalues that depends on the positions $\mathbf{R}$ of the nuclei. Subsequently, each solution is used inside an eigenvalue equation for the nuclei, which contains also the nuclear kinetic term and the

nucleus–nucleus repulsion [3].

In practice, the total wavefunction can be factorized into a nuclear κ and an electronic part Ψ:

$$|\Theta\rangle = |\kappa\rangle \otimes |\Psi\rangle \,, \tag{1.4}$$

where the nuclear part depends on the set of nuclear positions $\{\mathbf{R}_I\}$, while the electronic wavefuncion depends on both $(\{\mathbf{R}_I\}, \{\mathbf{r_i}\})$. In the same spirit, the total Hamiltonian 1.1 can be partitioned in two parts

$$H = H_e + T_n + V_{n-n} \,, \tag{1.5}$$

where H_e refers to the electronic part

$$H_e = T_e + V_{e-e} + V_{e-n} \,. \tag{1.6}$$

Here the assumption is that the nuclear kinetic term is removed from the electronic Hamiltonian and the nuclear coordinates enter H_e as parameters, *i.e.* the electronic eigenvalue equations are solved for a set of clamped nuclear positions. Considering ν electronic eigenfunctions for H_e, the Schrödinger equation for the electronic part reads

$$H_e|\Psi_\nu(\mathbf{r},\mathbf{R})\rangle = E_\nu(\mathbf{R})|\Psi_\nu(\mathbf{r},\mathbf{R})\rangle \,, \quad \text{with } \nu = 1,\ldots,N \,. \tag{1.7}$$

The assumption of "clamped-nuclei" is justified by considering that the mass ratio between nuclei and electrons is on the order of 10^4, therefore the nuclear kinetic energy—given by $p^2/2m$—is usually much smaller than the electronic one. As a second step, the solution of Equation 1.7 yields to the Schrödinger equation for the nuclear motion

$$[T_n + V_{n-n} + E_\nu(\mathbf{R})]|\kappa_\nu(\mathbf{R})\rangle = E_\nu^{\mathrm{Tot}}|\kappa_\nu(\mathbf{R})\rangle \,, \tag{1.8}$$

where the sum over the eigenvalues E_ν^{Tot} is the total energy of the system and includes the contributions from electrons and nuclei.

We can now investigate the validity of the BO approximation. Considering the total Hamiltonian in Equation 1.5, and a multiplication from the left side by $\langle\Psi_{\nu'}(\mathbf{r},\mathbf{R})|$, the expression becomes:

$$\Big[\langle\Psi_{\nu'}(\mathbf{r},\mathbf{R})|T_n|\Psi_\nu(\mathbf{r},\mathbf{R})\rangle + V_{n-n} + E_\nu(\mathbf{R})\Big]|\kappa_\nu(\mathbf{R})\rangle = E_\nu^{\mathrm{Tot}}|\kappa_\nu(\mathbf{R})\rangle \,, \tag{1.9}$$

where we have used the property

$$\langle\Psi_{\nu'}(\mathbf{r},\mathbf{R})|\Psi_\nu(\mathbf{r},\mathbf{R})\rangle = \delta_{\nu'\nu} \tag{1.10}$$

[3] The nucleus–nucleus repulsion can be formally included into the electronic Hamiltonian. In this way the nuclear eigenvalue equation is written with the electronic eigenvalue and the nuclear kinetic term. For this reason the nuclear eigenvalue equation is historically referred as *nuclear motion* or *nuclear dynamics*, even though it is a time-independent equation.

and the result of Equation 1.7. It is clear that the coupling involves the nuclear kinetic term, often referred as vibronic coupling term. Now, the product rule can be used to expand the coupling term:

$$\begin{aligned}\langle\Psi_{\nu'}(\mathbf{r},\mathbf{R})|T_n|\Psi_\nu(\mathbf{r},\mathbf{R})\rangle &= \delta_{\nu'\nu}T_n + \\ + \quad \sum_I^{N_n}\frac{\hbar^2}{2M_I}\Big[2\langle\Psi_{\nu'}(\mathbf{r},\mathbf{R})|\nabla_I|\Psi_\nu(\mathbf{r},\mathbf{R})\rangle\nabla_I &+ \langle\Psi_{\nu'}(\mathbf{r},\mathbf{R})|\nabla_I^2|\Psi_\nu(\mathbf{r},\mathbf{R})\rangle\Big]\,.\end{aligned} \tag{1.11}$$

It follows that, within the BO approximation, the second and third term are assumed to be zero. In this way, the uncoupled set of eigenvalue equations of the form of Equation 1.8 is recovered. The off-diagonal elements of the second and third terms involve interactions between different electronic states and are called non-adiabatic, while the diagonal elements are adiabatic. In general, the typical contribution of the kinetic term $\nabla_I^2\Psi_\nu(\mathbf{r},\mathbf{R})$ is of the same order as $\nabla_i^2\Psi_\nu(\mathbf{r},\mathbf{R})$. Consequently $\hbar^2/(2M_I)\nabla_I^2\Psi_\nu(\mathbf{r},\mathbf{R}) \approx p_e^2/(2M_I) = (m_e/M_I)T_e$. The same procedure can be applied to ∇_I and the small ratio m_e/M_I justifies the BO assumption. We consider now, for simplicity, only the adiabatic term that contains the gradient, the second term in Equation 1.11. The following passages can be easily applied also to the third term, with the same qualitative conclusions. First, the expression can be written in terms of the electronic Hamiltonian and eigenvalues

$$\langle\Psi_{\nu'}(\mathbf{r},\mathbf{R})|\nabla_I|\Psi_\nu(\mathbf{r},\mathbf{R})\rangle = \frac{\langle\Psi_{\nu'}(\mathbf{r},\mathbf{R})|\big[\nabla_I, H_e\big]|\Psi_\nu(\mathbf{r},\mathbf{R})\rangle}{E_\nu(\mathbf{R}) - E_{\nu'}(\mathbf{R})}\,. \tag{1.12}$$

Second, the matrix element at the numerator can be evaluated by expanding the commutator and performing the derivation:

$$\langle\Psi_{\nu'}(\mathbf{r},\mathbf{R})|\nabla_I H_e\big|\Psi_\nu(\mathbf{r},\mathbf{R})\rangle = iZ_Ie^2\sum_i^{N_e}\frac{(\mathbf{r}_i - \mathbf{R}_I)}{|\mathbf{r}_i - \mathbf{R}_I|^3}\,. \tag{1.13}$$

Since this element is finite, the coupled nuclear kinetic term becomes large only when the denominator in Equation 1.12 tends to zero, *i.e.* when the two electronic eigenvalues assume similar values, $E_\nu(\mathbf{R}) \simeq E_{\nu'}(\mathbf{R})$. Considering now the BO potential energy surface, defined as $E_\nu^{\mathrm{BO}}(\mathbf{R}) = V_{n-n} + E_\nu(\mathbf{R})$, it follows that the BO approximation is valid when the potential surfaces are well separated:

$$E_0^{\mathrm{BO}}(\mathbf{R}) \ll E_1^{\mathrm{BO}}(\mathbf{R}) \ll \cdots \ll E_N^{\mathrm{BO}}(\mathbf{R})\,, \quad \text{for all } \mathbf{R} \tag{1.14}$$

From these observations it is evident that the BO approximation breaks down in case of crossing between electronic states. For example, considering organic molecules and UV photoabsorption, a conical intersection between the ground and the excited state can be present, depending on the shape of the molecule. In this case, the activated molecule produces an ultrafast non-adiabatic internal conversion [13], without the emission of

radiation. Other important physical phenomena, as the Jahn-Teller distortion (degeneracies of the electronic ground-state) or the non-adiabatic electron–phonon coupling can, for example, lead to a modification of the band gap or affect transport and vibrational properties, as in the case of graphene [14]. Nevertheless, the BO approximation holds in many cases, in particular for systems composed by elements with large atomic numbers. Intuitively, this conclusion can be argued by looking the small ratio m_e/M_I. However, considering for example metallic systems, phenomena beyond the BO approximation, as phonon-mediated superconductivity, can occur [14]. All the results presented in this thesis are obtained within the BO approximation, with the nuclei fixed at the equilibrium configuration.

2 The Hartree-Fock Method and Beyond

The quest for the solution of the interacting many-body electronic Hamiltonian dates back to the end of the 1920. At that time many efforts were concentrated towards the description of the energy levels of materials in order to reproduce, for example, X-ray spectra. Potential terms with empirical parameters were commonly used to represent the experimental data. Hartree, on the other hand, proposed to tackle the many-body problem with a trial wave function (ansatz) and to solve the Schrödinger equation from first principles. The aim of this chapter is to give a general overview of the seminal approach of Hartree and Fock (HF), used to describe the ground-state of the many-electron systems, as well as the methods built upon the HF theory in order to improve its performances. The HF method represents a fundamental starting point for many methodologies used nowadays. Some of the concepts and tools introduced here, as the variational approach, the self-consistent procedure and the one-electron approximation, are general ingredients in the framework of many-body theory. They are employed in the formulation of the density-functional theory too, the electronic structure method used in this thesis. We suggest the interested reader that more complete and detailed explanations on the subject can be found in solid-state physics and quantum chemistry books as Grosso and Pastori Parravicini [15] or Szabo and Ostlund [16]. In order to keep the formulas as simple as possible, from now on we will adopt atomic units, $e^2 = m_e = \hbar = 1$, instead of the SI units.

We consider now the (electronic) Hamiltonian defined in Equation 1.6, which results in the N-electron eigenvalue problem

$$H_e \Psi(\mathbf{r}_1\sigma_1, \ldots, \mathbf{r}_N\sigma_N) = E\Psi(\mathbf{r}_1\sigma_1, \ldots, \mathbf{r}_N\sigma_N)\,, \tag{2.1}$$

where domain and codomain of the Hamiltonian is the Hilbert space product of $\mathbb{R}^3$ spaces (times two dimensional Hilbert spaces for the spin). The variables $\mathbf{r}_i\sigma_i$ are the spatial and spin variables of the i-th electron, with $\mathbf{r}_i \in \mathbb{R}^3$.

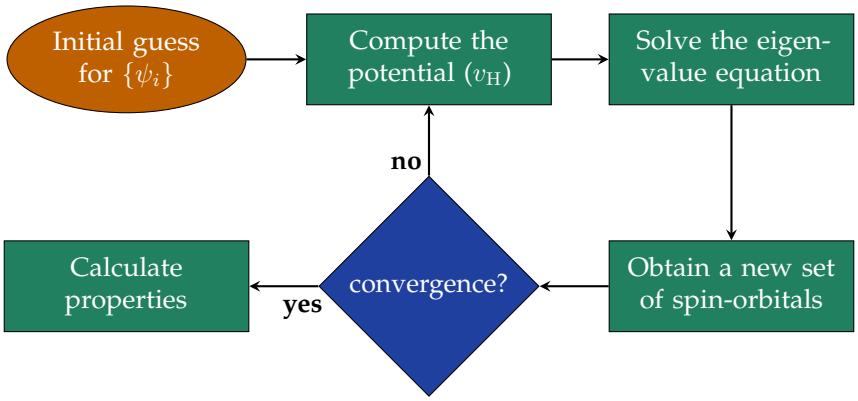

Figure 2.1: Flowchart diagram representing the important steps of the Hartree self-consistent-field procedure.

2.1 The Hartree Approximation

In 1927, one year after the formulation of the Schrödinger equation, Hartree introduced an *ab initio* electronic structure method to solve the many-body problem. The central idea is to approximate the many-body wavefunction with a product of single-electron wavefunctions. Starting with a trial many-body wavefunction it is possible to minimize the energy of the system by varying the orbitals (see Appendix A). This iterative procedure is called Hartree method or self-consistent field (SCF) method.

Consider a set of orthonormal spin-orbitals $\{\psi_i(\mathbf{r}\sigma)\}$, where $\psi_i(\mathbf{r}\sigma) = \phi_i(\mathbf{r})\chi_i(\sigma)$ is the product between the spatial orbital and the spin part. In the Hartree theory, the ground-state wavefunction is expressed as a simple product of N one-electron spin-orbitals [17] in the form

$$\Psi_0^H(\mathbf{r}_1\sigma_1,\ldots,\mathbf{r}_N\sigma_N) = \psi_1(\mathbf{r}_1\sigma_1)\ldots\psi_N(\mathbf{r}_N\sigma_N)\,, \quad \text{with the norm } \|\Psi_0^H\| = 1\,, \tag{2.2}$$

where the wavefunction is an element of the N-particle Hilbert space $\mathcal{H}_N = \mathcal{H}\otimes\cdots\otimes\mathcal{H}$, the tensor product of N Hilbert spaces. Throughout this thesis, we use short-hand notations where space and spin variables can be omitted. To avoid confusion, we will adopt a consistent notation, for instance ψ_i will always refer to spin-orbitals, while the orbital and the spin parts are ϕ and χ, with the corresponding arguments $\mathbf{r}$ and σ. The Hartree product neglects the correlation in the position of the electrons, in fact the probability of the total wavefunction is equal to the product of single particle wavefunctions. The indistinguishability (antisymmetry) of the electrons is another missing ingredient in the Hartree approximation and the Pauli exclusion principle has to be introduced *ad hoc*, avoiding multiple occupancy for any given spin-orbital.

However, the Hartree method is historically important because it introduces the idea to use the variational principle to obtain a set of eigenvalue equations, paving the way

for the *ab initio* methodologies. The Hartree eigenvalue equation has the form

$$[h(\mathbf{r}) + v_{\mathrm{H}}(\mathbf{r})]\psi_i(\mathbf{r}\sigma) = \epsilon_i \psi_i(\mathbf{r}\sigma)\,, \tag{2.3}$$

where $h(\mathbf{r})$ is the one-particle operator and describes the kinetic energy and the potential energy due to the nuclei, for a single electron. The second term, $v_{\mathrm{H}}(\mathbf{r})$, called here the Hartree potential, describes the electron–electron Coulomb interactions

$$v_{\mathrm{H}}(\mathbf{r}) = \sum_{j=1}^{\mathrm{occ}} \int \frac{\phi_j^*(\mathbf{r}')\phi_j(\mathbf{r}')}{|\mathbf{r}-\mathbf{r}'|} d\mathbf{r}'\,, \quad \text{with density } n(\mathbf{r}') = \sum_{j=1}^{\mathrm{occ}} |\phi_j(\mathbf{r}')|^2\,. \tag{2.4}$$

From this last term, it follows that the Hartree approximation consists of an electron moving in the effective field that corresponds to the Coulomb potential, generated by the charge of all the other $N-1$ electrons. To obtain the N-particle eigenfunction, one needs to find a set of single particle states $\psi_i(\mathbf{r}\sigma)$ that solves the eigenvalue problem in Equation 2.3. The non-linearity of the Hartree equation implies an iterative solution, called self-consistent-field (SCF), summarized in Figure 2.1. Convergence is reached when the resulting eigenfunctions correspond to the spin-orbitals used in the previous calculation. In practice, a smooth convergence is guaranteed using various techniques. For example, the new guess is a mixture of old and new eigenfunction, in this way large wavefunction fluctuations are avoided. Solving the Hartree eigenvalue equation is an *ab initio* calculation, where no approximations are introduced in the electronic Hamiltonian or during the self-consistent iterations. In general, the one-particle wavefunctions of a system present complex shapes and can be described with an expansion in terms of well known functions, as the atomic orbitals. Naturally, the choice of the basis functions affects the computational efficiency and the accuracy of the final results. The idea is to use different mathematical functions, for example the Gaussian function (in combination with spherical harmonics), to describe the basis set needed $(s, p, \ldots)$. Of course, an increasing number of functions (larger basis set) would increase the computational cost.

2.2 The Hartree-Fock Equations

Even though the Hartree method used the Pauli exclusion principle to avoid the presence of two electrons in the same quantum state, it neglects the *correct* statistics for Fermionic particles. The correction of the Hartree approximation with the inclusion of the Fermi-Dirac statistics has been provided in 1930 in the works of Fock [18] and Slater [19]. Both scientists, independently, succeed to introduce the spin variable and the Pauli exclusion principle. They used an explicitly antisymmetric wavefunction, a Slater determinant. Given a system of N-electrons and a set $\{\psi_i\}$ of N one-particle wavefunctions, the Slater

determinant can be written as

$$\Psi(\mathbf{r}_1\sigma_1,\ldots,\mathbf{r}_n\sigma_n)=\frac{1}{\sqrt{N!}}\begin{vmatrix}\psi_1(\mathbf{r}_1\sigma_1) & \psi_2(\mathbf{r}_1\sigma_1) & \cdots & \psi_N(\mathbf{r}_1\sigma_1)\\ \psi_1(\mathbf{r}_2\sigma_2) & \psi_2(\mathbf{r}_2\sigma_2) & \cdots & \psi_N(\mathbf{r}_2\sigma_2)\\ \psi_1(\mathbf{r}_3\sigma_3) & \psi_2(\mathbf{r}_3\sigma_3) & \cdots & \psi_N(\mathbf{r}_3\sigma_3)\\ \vdots & & \ddots & \vdots\\ \psi_1(\mathbf{r}_N\sigma_N) & \cdots & & \psi_N(\mathbf{r}_N\sigma_N)\end{vmatrix}. \tag{2.5}$$

It is convenient to introduce the following short-hand notations to write the many-body wavefunction in a compact form

$$\Psi = A\{\psi_1\psi_2\ldots\psi_N\} = \frac{1}{\sqrt{N!}}\det\{\psi_1\psi_2\ldots\psi_N\}\,, \tag{2.6}$$

where A is the antisymmetrization operator. An important property of the determinantal wavefunction is that the motion of electrons with parallel spin is correlated, thus the Slater determinant introduces exchange-correlation effects. Also, the Pauli exclusion principle is satisfied and no more than one electron can occupy a spin-orbital. Having two electrons with the same spin-orbital, would lead to two equal columns in Equation 2.5, making the determinant zero.

In the Hartree-Fock method the ground-state of the many-body system is described with a single Slater determinant. Starting with a determinant state Ψ, the expectation value $E = \langle\Psi|H_e|\Psi\rangle$ can be minimized, according to the variational principle. The minimum value corresponds to the ground-state energy,

$$E_0 = \inf_{\Psi}\langle\Psi|H_e|\Psi\rangle = \langle\Psi_0|H_e|\Psi_0\rangle\,, \quad \|\Psi\| = 1\,, \tag{2.7}$$

with the normalization of single particle orbitals used as a constraint, see Appendix A and Ψ_0 is the HF ground-state wavefunction.

Considering now the electronic Hamiltonian, we can separate the terms into a one-electron and two-electrons operators, the first one includes the kinetic energy and the electron–nucleus Coulomb attraction

$$\mathcal{O}_1 = \sum_i h(i) = \sum_i^{N_e}\left[-\frac{1}{2}\nabla_i^2 - \sum_I^{N_n}\frac{Z_I}{|\mathbf{r}_i-\mathbf{R}_I|}\right]. \tag{2.8}$$

The second operator takes into account the electron–electron interactions

$$\mathcal{O}_2 = \frac{1}{2}\sum_{i\neq j}^{N_e}\frac{1}{|\mathbf{r}_i-\mathbf{r}_j|}\,, \tag{2.9}$$

where the summation goes over both indices. This definition is equivalent to the integral definition of the Coulomb potential, seen for the Hartree term in Equation 2.4. The indices are not to be confused with the wavefunction indices, but are associated with the

two dummy (integration) variables, which span all over the 3D space. The expectation value of the ground-state $E_0 = \langle\Psi_0|H_e|\Psi_0\rangle = \langle\Psi_0|(\mathcal{O}_1 + \mathcal{O}_2)|\Psi_0\rangle$, keeping in mind the form of the wavefunction as defined in Equation 2.5, can be written as

$$E_0^{(\mathrm{HF})} = \sum_i^{(\mathrm{occ})} \langle\psi_i|h|\psi_i\rangle + \frac{1}{2}\sum_{ij}^{(\mathrm{occ})} \left[\langle\psi_i\psi_j|\frac{1}{r_{12}}|\psi_i\psi_j\rangle - \langle\psi_i\psi_j|\frac{1}{r_{12}}|\psi_j\psi_i\rangle\right]. \tag{2.10}$$

For the first operator, the expectation value computed with an antisymmetrized wavefunction corresponds to a sum of one-electron expectation values. The same result is obtained when a simple product of one particle spin-orbitals is used, as in the Hartree method, see Equation 2.2. On the other hand, the two-electron operator, acting on a Slater determinant produces two terms: a "classical" Coulomb repulsion and an exchange contribution. Because of the exchange operator, the ground-state energy obtained with a Slater determinant is always lower (or equal) than the one obtained with a simple Hartree product of the same spin-orbitals. The lower energy is linked to the fact that, with the exchange contribution, the electrons with parallel spin are correlated and kept separated in space.

Following the variational principle, we want to minimize $E = E(\{\psi_i\})$. This task can be achieved using the standard method of Lagrange multipliers, subject to the condition that the spin-orbitals are orthonormal and employing the functional variation technique, see Appendix A.2. In practice, an infinitesimal variation of the N spin-orbitals is performed $\psi_i \to \psi_i + \delta\psi_i$ and, to guarantee the stationary condition, the Lagrange multipliers must be set to be equal to zero. The result of the functional variation is a set of N non-linear integro-differential equations

$$\mathcal{F}(\mathbf{r})\psi_i(\mathbf{r}\sigma) = \left[h(\mathbf{r}) + v_{\mathrm{H}}(\mathbf{r}) - v_{ex}(\mathbf{r})\right]\psi_i(\mathbf{r}\sigma) = \epsilon_i\psi_i(\mathbf{r}\sigma)\,, \quad i = 1, 2, \ldots, N\,, \tag{2.11}$$

where $\mathcal{F}$ is called the Fock operator, $h(\mathbf{r})$ and $v_{\mathrm{H}}(\mathbf{r})$ are defined in Equation 2.8 and Equation 2.4 respectively. The last term, $v_{\mathrm{ex}}(\mathbf{r})$, is an integral operator called the exact-exchange operator, or simply "exchange" in HF context, and defined as

$$v_{ex}(\mathbf{r})\psi_i(\mathbf{r}\sigma_i) = \sum_j^{\mathrm{occ}} \left[\int \frac{\psi_j^*(\mathbf{r}'\sigma_j)\psi_i(\mathbf{r}'\sigma_j)}{|\mathbf{r} - \mathbf{r}'|} d\mathbf{r}'\right]\psi_j(\mathbf{r}\sigma_i)\,. \tag{2.12}$$

It is evident that the exchange operator lacks a simple classical interpretation and involves the substitution of the electrons in $\mathbf{r}$ and $\mathbf{r}'$ between ψ_i and ψ_j. In other words, the value of the operator, acting on ψ_i, depends on the value of ψ_i in every point in space, not only in $\psi_i(\mathbf{r})$, as in the case of the Hartree potential. Since there is no spin dependency in the definition in Equation 2.12, the integral over the spin variables can be carried out easily. The spin function $\chi_i(\sigma)$ can assume the value spin up α or spin

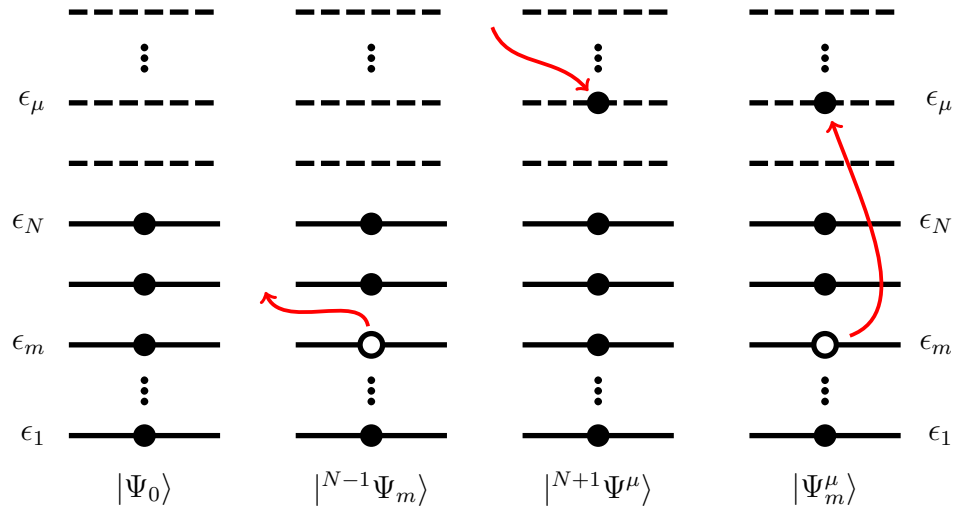

Figure 2.2: From left to right: schematic representation of the N-electron ground-state (on the left), compared with two examples of ionized states and one excited state. Second column from left: one electron is removed from the occupied spin-orbital ψ_m. Third column from left: one extra electron is added to a virtual spin-orbital ψ_μ. The last case, the column on the right, represents an excited state, where the electron in ψ_m is promoted to an empty orbital ψ_μ.

down β, with the orthonormality condition

$$\langle\alpha(\sigma)|\alpha(\sigma)\rangle = 1 \quad \text{and} \quad \langle\alpha(\sigma)|\beta(\sigma)\rangle = 0\,. \tag{2.13}$$

Considering now that the exchange term involves an overlap between two different wavefunctions, the integral is non-zero only if ψ_i and ψ_j have the same spin part.

Usually, the Hartree and the exchange potentials provide sizable contributions to the total energy, for this reason they both enter the self-consistent cycle (see Figure 2.1), unified under the name of HF potential: $v_{\mathrm{HF}}(\mathbf{r})$. On the other hand, in some approximations, it is a common strategy to compute certain terms after convergence (*a posteriori*) and add their contributions to the converged total energy. In this way the energy is corrected with a modest computational cost. An example will be presented in the context of the coupled cluster method, beyond HF, see Section 2.5.1. The coupled cluster provides a series of terms, computed with excited determinants, which are computationally very demanding. In practical application, the couple cluster is truncated to a certain order and the last term is usually computed *a posteriori*. Typically, this approximation is justified when the correction term is quantitatively small. Nevertheless, its validity needs to be tested in practice, case by case. A central part of this thesis will focus exactly on this subject, in relation to vdW interactions within the density-functional theory framework.

2.3 Ground-State and Ionization Energies

The Hartree-Fock eigenvalue equations must be solved self-consistently to obtain the set of eigenvalues ϵ_i and single-particle spin-orbitals ψ_i. In principle, the Fock operator admits an infinite number of solutions and an eigenvalue is assigned to each one. Among all the possible solutions, the N spin-orbitals with the lowest energy form the HF ground-state $|\Psi_0\rangle$, represented in the left column of Figure 2.2. Considering a single spin-orbital that belongs to the ground-state, the corresponding eigenvalue can be found with the product of Equation 2.11 with another spin-orbital

$$\epsilon_i = \langle\psi_j|\mathcal{F}|\psi_i\rangle = \epsilon_i\delta_{ij}\,. \tag{2.14}$$

Therefore, the Fock operator has a diagonal representation on the basis of the eigenfunction and the diagonal elements are the single particle orbital energies.

The expression for the ground-state total energy, obtained directly from the total Hamiltonian, is written in Equation 2.10 and contains the factor $\frac{1}{2}$, which is absent in the HF eigenvalue equations. For this reason, the sum of all the orbital energies ϵ_i is not the ground-state energy. The HF total energy, written in term of the eigenvalues, is given by

$$E_0^{(\mathrm{HF})} = \sum_i^{(\mathrm{occ})} \epsilon_i - \frac{1}{2}\sum_{ij}^{(\mathrm{occ})} \left[\langle\psi_i\psi_j|\frac{1}{r_{12}}|\psi_i\psi_j\rangle - \langle\psi_i\psi_j|\frac{1}{r_{12}}|\psi_j\psi_i\rangle\right]. \tag{2.15}$$

The explanation can be found in the eigenvalue equation, where the single particle ψ_i interacts—through the two-body operator—with all the remaining $N-1$ particles. If we consider a second spin-orbital ψ_j, the interaction is still between the j-th spin-orbital and all the other wavefunctions. But in this way, the two-body interaction between electron i and j is counted twice. For this reason the expression in Equation 2.15 "corrects" the sum over the single-particle eigenvalues with a subtraction of $\frac{1}{2}$ of the Coulomb and exchange contributions.

Koopmans' Theorem

The physical meaning of the single-particle eigenvalues is attained by considering ionization phenomena. First we consider $|^{N-1}\Psi_m\rangle$, represented graphically in Figure 2.2. This is the ground-state determinant where an electron in the occupied state ψ_m is removed and brought to infinity, *i.e.* no residual interactions remain between the lone electron and $|^{N-1}\Psi_m\rangle$. Before proceeding we assumed ideal ionization processes only, where the electronic orbitals are kept in the *frozen-orbital* approximation, *i.e.* the remaining $N-1$ orbitals of the ion are identical with those of the N-electron state. The HF energies are computed using Equation 2.10 and $\langle^{N-1}\Psi_m|H_e|^{N-1}\Psi_m\rangle$ for the ground-state and the $(N-1)$-electron determinant respectively. The energy necessary

to remove the electron from the ground-state, called ionization potential, is defined as

$$\mathrm{IP} = E_0^{(\mathrm{HF})}(N-1) - E_0^{(\mathrm{HF})}(N) = -\epsilon_m \,. \tag{2.16}$$

Thus, the energy needed for the ionization process is simply the HF energy (with opposite sign) associated with the removed electron. Usually, the orbital energies ϵ_m are negative, meaning that the IP is positive and a certain amount of energy is required to remove the electron from the ground-state.

Similarly as above, we consider $|^{N+1}\Psi^{\mu}\rangle$, a $(N+1)$-electron single determinant (Figure 2.2, third column). In this case, the energy required to add an extra electron in ψ_μ is called electron affinity and is given by

$$\mathrm{EA} = E_0^{(\mathrm{HF})}(N) - E_0^{(\mathrm{HF})}(N+1) = -\epsilon_\mu \,, \tag{2.17}$$

where a positive EA (negative ϵ_μ) indicates that the $(N+1)$-electron system is more stable than $|\Psi_0\rangle$.

With the two results discussed above, a physical interpretation can be given to the Lagrange multipliers ϵ_i, summarized in the Koopmans' theorem.

Theorem 1 (Koopmans' Theorem) *The energy required to remove/add an electron from/to the spin-orbital ψ_m is the opposite of the Hartree-Fock eigenvalue ϵ_m.*

In practice, the "frozen-orbital" approximation neglects the optimization of the determinants, that lowers the total electronic energy. Consequently, Koopmans' calculations tend to overestimate the ionization potentials and produce too negative electronic affinities. Another shortcoming is the lack of *correlation effects*, which are absent in the HF approximation of single determinant wavefunction and will be an important matter of the next chapters. The correlation energies increase with the number of electrons, leading to error cancellations for ionization potentials, but add to the error for electron affinity.

In concluding this part, we consider a last case (sketched in Figure 2.2, last column) where an electron is transferred from the spin-orbital ψ_m to the unoccupied orbital ψ_μ. The transition energy ΔE between the ground and the excited state is computed similarly to IP and EA,

$$\begin{aligned} \Delta E &= \langle \psi_m^\mu | H_e | \Psi_m^\mu \rangle - \langle \Psi_0 | H_e | \Psi_0 \rangle = \\ &= \epsilon_\mu - \epsilon_m - \left[\langle \psi_\mu \psi_m | \frac{1}{r_{12}} | \psi_\mu \psi_m \rangle - \langle \psi_\mu \psi_m | \frac{1}{r_{12}} | \psi_m \psi_\mu \rangle \right] . \end{aligned} \tag{2.18}$$

Therefore, to promote an electron from ψ_m to ψ_μ, one needs an energy equal to the difference between the two corresponding eigenvalues, minus the Coulomb and exchange energy between the "new" electron in ψ_μ and the "missing" one in ψ_m.

2.4 SUMMARY

Before proceeding to introduce methodologies beyond HF, it is useful to summarize here the advantages and the limitations of the aforementioned theory. Briefly speaking—besides the accuracy of the method in some cases—HF provides, in general, qualitatively useful results for a large number of problems. Also, the method presents an efficient scaling between $O(N^4)$ and $O(N^3)$, where N is a measure of the size of the system (the number of electrons or the basis functions). From a conceptual point of view, HF calculations represent an upper bound to the exact energies, with a "clean" separation between the exchange and the correlation effects. Moreover, the technical tools employed to solve the many-body problem are of a general utility in many other fields.

In the following chapters we will discuss the principal techniques used to go beyond the HF theory, however it is worth mentioning that, even at the level of HF calculations, approximations and technical elaborations are needed to perform actual calculations. One example of approximation is the Slater approximation, where the exchange integral is replaced with a local potential and the Fock operator becomes an ordinary differential operator. Second, a popular way to obtain a numerical solution is the method of Roothaan. In this method, each HF orbital is expanded into a (finite) sum of basis functions. Thus, the eigenvalue equations are converted into algebraic equations in the expansion coefficients, to be solved by matrix techniques. Clearly, the number and the type of basis influence the quality of the final result.

Finally, the determinant used to describe the ground-state can be built with restricted or unrestricted spin-orbitals. In the former case, a spatial orbital is *restricted* to be the same for each pair of spin functions (α, β), *i.e.* all electrons are paired in $N/2$ doubly occupied spatial orbitals. Intuitively, this choice is suitable to describe closed-shell determinants. With open-shell configurations, the situation often becomes more complicated and several spin-configurations produce very close energy levels. In these cases, one can resort to unrestricted determinants: the spatial orbitals are different for different spins. Usually, the unrestricted determinants are used to describe cases as radicals with one unpaired electron or in dissociation processes. During the dissociation of H_2, for example, the correct configuration at large distance should have one electron per atom, while the restricted configuration fixes the two electrons in the same spatial distribution.

2.5 CONFIGURATION INTERACTION

One solution to go beyond the Hartree-Fock method is to consider more than a single Slater determinant. Given a system of N-electrons and $2K$ spin-orbitals, it is possible to construct $\binom{2K}{N}$ different determinants. The name *Configuration Interaction* (CI) refers to the fact that each determinant corresponds to a specific electronic configuration. The

correlation energy is defined as

$$E = E_0 + E_{\text{corr}} \,, \tag{2.19}$$

where E is the exact ground-state energy and E_0 is the HF result. Following this separation, it is intuitive to write the CI wavefunction as an expansion of Slater determinant starting with the HF wave function Ψ_0, formed with the N lowest spin-orbitals. The other terms are the excited determinants of Ψ_0 and, in case of a complete basis, the resulting wavefunction would be the exact solution, giving not only the exact ground-state energy, but also the excited states energies. We can write the form of the full-CI wavefunction as

$$|\Psi\rangle = c_0|\Psi_0\rangle + \sum_{m}^{\mu} c_m^{\mu}|\Psi_m^{\mu}\rangle + \left(\frac{1}{2!}\right)^2 \sum_{\substack{mn \\ \mu\nu}} c_{mn}^{\mu\nu}|\Psi_{mn}^{\mu\nu}\rangle + \left(\frac{1}{3!}\right)^2 \sum_{\substack{mnl \\ \mu\nu\iota}} c_{mnl}^{\mu\nu\iota}|\Psi_{mnl}^{\mu\nu\iota}\rangle + \cdots \,, \tag{2.20}$$

the first excited determinant is the singly excited term, in which the spin orbital ψ_m is replaced by ψ_μ. Similarly, $|\Psi_{mn}^{\mu\nu}\rangle$ denotes doubly excited determinants and so on. The factor $(1/n!)^2$ takes care of the permutation of the indices and ensures that the n-tuply excited determinants are counted just once. For N electrons and $2K$ spin-orbitals there are $\binom{N}{n}\binom{2K-N}{n}$ n-tuply excited determinants, clearly indicating that the number of the excited determinants is extremely large even for small systems. One of the main advantage of the full-CI wavefunction is the flexibility, due to the presence of many determinants, which allows to describe changes in the electronic configuration. In case of dissociations, for example, a wavefunction as in Equation 2.20 contains the ground-state and the excited determinants. Thus, it is able to describe the change from bonding to antibonding orbitals as the distance increases.

The full-CI wavefunction is not normalized to one, in fact the product $\langle\Psi|\Psi\rangle = 1 + \sum_m^\mu (c_m^\mu)^2 + \cdots$ contains the sum of the coefficients. However, it has the property of intermediate normalization, taking the HF ground-state,

$$\langle\Psi_0|\Psi\rangle = 1 \,. \tag{2.21}$$

Now, the exact eigenvalue equation is written as

$$H_e|\Psi\rangle = E|\Psi\rangle \,, \tag{2.22}$$

the solution of the full-CI problem is obtained considering the expression above, multiplied by $\langle\Psi_0|$ and all the excited determinants $\langle\Psi_m^\mu|$, $\langle\Psi_{mn}^{\mu\nu}|$, etc. These are the elements of the hermitian full-CI matrix. The diagonalization procedure assigns a value for each coefficient of Equation 2.20.

Remembering that the correlation energy is defined as the difference between the exact solution and the HF ground-state energy, we can now write the expression for

E_{corr} and multiply the eigenvalue equation by $\langle\Psi_0|$:

$$\langle\Psi_0|H - E_0|\Psi\rangle = E_{\text{corr}}\langle\Psi_0|\Psi\rangle\,. \tag{2.23}$$

The left part can be easily simplified using the definition of intermediate normalization. The coupling between a Slater determinant and the full-CI expansion is constrained by the nature of the Fock operator. Mathematically, the mixing between determinants that differ by one or two columns is the only non-zero element. In particular, for the HF determinant, only the mixing with doubly excited states is admitted, see Theorem 2.

Theorem 2 (Brillouin's Theorem) *The singly excited determinants will not interact with the Hartree-Fock determinant.*

Therefore, almost all the products on the left side of Equation 2.23 vanish, only one term is kept

$$\left(\frac{1}{2!}\right)^2 \sum_{\substack{mn\\ \mu\nu}} c_{mn}^{\mu\nu}\langle\Psi_0|H_e|\Psi_{mn}^{\mu\nu}\rangle = E_{\text{corr}}\,, \tag{2.24}$$

suggesting that the correlation energy is determined only by the double excitations of the HF determinant. However, a careful observation reveals that the coefficients $\{c_{mn}^{\mu\nu}\}$ depend on other excitations, involving a large set of coupled equations.

The full-CI presents a scaling between $O(N^{2i+2})$ and $O(N^{i+2})$, where N is the number of orbitals and i is the excitation level. Therefore, the solution of the exact problem is computationally extremely demanding, being impractical for all but small molecules. Several approaches can be used to extend the applicability of the method. For example, the convergence can be reached more rapidly if the basis set used is the set of natural orbitals [20]. One can also use a limited number of configurations and optimize simultaneously both the expansion coefficients and the orbitals, this is the multiconfiguration self-consistent field (MCSCF), a truncated CI method particularly useful when the ground-state is described by nearly degenerate determinants. Another approximation is to neglect the core electrons and focus on the optimization of the valence states, as in the case of the generalized valence bond (GVB) method. In a more intuitive way, it is possible to simply truncate the full-CI expansion for the wavefunction, as for the doubly excited CI (DCI). The truncated CI expansions retain the variational property of the original formulation and can be used as a systematic procedure for improving the HF results. However, the size consistency is lost, meaning that the total energy of N noninteracting fragments is not the sum of N isolated fragment contributions. Unfortunately, the errors due to the lack of size consistency aggravate as the size of the system increases, with the surprising limit of zero correlation energy per monomer as $N \to \infty$, reducing the practical applicability of these approximations.

COUPLED CLUSTER

Another way to simplify the full-CI problem is *via* the coupled-pair approximations (CCA). As a first example, it is possible to write the total correlation energy as a sum of pair energies [21]. The full-CI wavefunction is reduced to a *pair function* with energy equal to the HF energy plus the pair correlation energy. Since the contributions of the electron pairs are considered separately, the method is called independent electron pair approximation (IEPA). Although the resulting pair energies are computed through the variational procedure, the method is not variational, *i.e.* the total correlation energy could be lower than the "true" energy. Unfortunately, the variational property is lost for all the pair approximations, including the coupled cluster method. The coupled cluster method gained popularity because the very accurate results are joined by an affordable computational price. Initially developed for nuclear physics studies in the 1950s [22], the coupled cluster approximation has been reformulated and popularized in quantum chemistry by Čižek in 1966 first and later together with Paldus [23, 24]. The idea of the CCA is to compute interactions among clusters of electrons and include the coupling between these clusters. This concept is motivated from the practical result that electron pair interactions are very important. Moreover, a large part of the contributions of quadruple excitations comes from the product of doubly excited determinants. The cluster interactions are introduced in term of the cluster operator that generates one-, two-electron, etc., clusters

$$T = T_1 + T_2 + T_3 + \cdots + T_N \,, \tag{2.25}$$

where N is the total number of the electrons. The action of T on the starting wavefunction of noncoupled electrons yields the various clusters

$$T_1|\Psi_0\rangle = \sum_{m\mu} c_m^\mu |\Psi_m^\mu\rangle \,, \tag{2.26a}$$

$$T_2|\Psi_0\rangle = \frac{1}{4} \sum_{\substack{mn \\ \mu\nu}} c_{mn}^{\mu\nu} |\Psi_{mn}^{\mu\nu}\rangle \,, \tag{2.26b}$$

$$\vdots \qquad .$$

The full-CI wavefunction can be rewritten in term of the cluster operator, if T is expressed as the argument of an exponential and a Taylor expansion of T is performed

$$e^T|\Psi_0\rangle = \left(1 + T + \frac{T^2}{2!} + \frac{T^3}{3!} + \cdots\right)|\Psi_0\rangle \,. \tag{2.27}$$

We can now substitute the definition of T, given in Equation 2.25, into the expression above and group the terms of each excitation

$$C_0 = 1 \tag{2.28a}$$

$$C_1 = T_1\,, \tag{2.28b}$$

$$C_2 = T_2 + \frac{1}{2!}T_1^2\,, \tag{2.28c}$$

$$C_3 = T_3 + \frac{1}{3!}T_1^3 + T_1T_2\,, \tag{2.28d}$$

$$C_4 = T_4 + \frac{1}{4!}T_1^4 + \frac{1}{2!}T_2^2 + T_3T_1 + \frac{1}{2!}T_1^2T_2\,. \tag{2.28e}$$

The sum of all the C_i operators, acting on $|\Psi_0\rangle$, would give the exact $|\Psi\rangle$. In other words, the action of C_0 on $|\Psi_0\rangle$ leaves the HF determinant unaffected, while C_1 gives the singly excited determinants, C_2 takes care of the doubly excited and so on. It is interesting to observe that, starting with C_2, the excited determinants are computed not only with "direct" contributions, *i.e.* T with the same index of C, but also some products of T with lower indices are included, *e.g.* T_1^2 in Equation 2.28c, the so-called disjoint clusters. As in the case of the CI methods, the set of coupled equations is obtained from the Schrödinger equation multiplied by the wavefunction

$$\langle\Psi_0|e^{-T}H_e e^{T}|\Psi_0\rangle = E\,. \tag{2.29}$$

The advantage of the coupled cluster formulation is that the operator T can be truncated to a certain order, using physical assumptions, without losing the property of size consistency. For example, looking at C_4, the quadruple excitations given by T_4 represent the case of four simultaneous excitations and are expected to be quite small. In comparison to that, the term T_2^2—a product of two disjoint clusters—is responsible for the interactions between two pairs of electrons and is usually considered to be the dominant one. Therefore, if we truncate at T_2 the coupled cluster expansion, the resulting wavefunction would contain not only the doubly excited determinant, but also contributions to higher excitations given by the products of disjoint clusters. Notably, the product of two T_2 is not a single quadruple excitation, but gives 18 distinct terms, counting all the possible permutations of the two coefficients of the doubles. It is the presence of these disjoint excitations that make CCA more complex than the truncated CI methodologies and guarantees the size consistency.

The name of a particular coupled cluster method is related to the index of the T_i considered in the truncation. Coupled cluster single, doubles (CCSD) scales as $O(N^6)$ and is the most popular variant, being the coupled cluster with triples (CCSDT) already computationally prohibitive. An alternative version is the single and doubles with the perturbative correction of the triples in the total energy, CCSD(T). This method is considered the "gold standard" of quantum chemistry because of the very accurate results, within the so-called chemical accuracy of 1 Kcal/mol (43 meV), for the correlation

energy of molecules [25]. The scaling of CCSD(T) is $O(N^6)$, as in the case of CCSD, plus the $O(N^7)$ scaling for the non-iterative step.

2.6 Perturbation Theory

The time-independent perturbation theory formalism is the basis for a post-Hartree-Fock method, different than CI, that allows to express the correlation energy as a sum of contributions of increasing complexity, eventually converging to the exact correlation. Unfortunately, as in the case of coupled-pair methods, this procedure is not variational and the approximations could give a correlation energy larger than the exact value. However, it has the advantage of being size-consistent at each step, giving the possibility to explore each order of the perturbation and to recursively increase the complexity.

The original formulation of perturbation theory in quantum mechanics was given by Schrödinger in 1926, inspired by works of Lord Rayleigh, and is commonly referred as RSPT. It is in 1955 that Brueckner explored the size consistency of the method and in 1957 Goldstone, adapting the diagrammatic formalism introduced by Feynman, assessed the validity of the size consistency for all orders. Using a diagrammatic representation of the different terms, he could prove, in the linked-cluster theorem [26], that all the disconnected diagrams always cancel. The graphic representation of Goldstone opened the way for a new set of approximations that sum up specific diagrams, going through all orders, instead of focusing on the truncation to a specific perturbative order.

In general, the total Hamiltonian for a system of N particles can be expressed as a sum of an unperturbed term H_0—whose eigenvalues and eigenfunctions are supposed to be known—plus a potential. The exact many-body problem is represented by the eigenvalue equation

$$H|\Psi\rangle = (H_0 + \mathcal{V})|\Psi\rangle = E|\Psi\rangle\,, \tag{2.30}$$

where the wavefunction of H_0, that corresponds to the ground-state energy, is written as $|0\rangle$. The intermediate normalization condition is considered here, as seen in Equation 2.21. The idea is to start with the known solution for H_0 and to improve step by step the eigenfunctions and the eigenvalues aiming to solve Equation 2.30. The procedure can be done if the additional term $\mathcal{V}$ is treated as a weak perturbation potential, that can be gradually turned on. This mean that the Hamiltonian is written as

$$H = H_0 + \lambda\mathcal{V}\,, \tag{2.31}$$

where the parameter λ ranges from 0 to 1, *i.e.* from no perturbation to the fully perturbed case. Now, the eigenvalues of the exact solution can be expanded in a Taylor series in λ, $E = E^{(0)} + \lambda E^{(1)} + \lambda^2 E^{(2)} + \cdots$ and a similar expansion is performed also for the eigenfunction. The superscript index refers to the degree of the perturbation. The first step is to use the two Taylor expansions in the eigenvalue equation (with $\lambda\mathcal{V}$) and equate

the terms with the same degree of λ

$$H_0|0\rangle = E^{(0)}|0\rangle\,, \tag{2.32a}$$
$$H_0|\Psi^{(1)}\rangle + \mathcal{V}|0\rangle = E^{(0)}|\Psi^{(1)}\rangle + E^{(1)}|0\rangle\,, \tag{2.32b}$$
$$H_0|\Psi^{(2)}\rangle + \mathcal{V}|\Psi^{(1)}\rangle = E^{(0)}|\Psi^{(2)}\rangle + E^{(1)}|\Psi^{(1)}\rangle + E^{(2)}|0\rangle\,, \tag{2.32c}$$
$$\vdots \qquad .$$

Each equation above defines the wavefunction at a specific order. As a second step, multiplying these equation by $\langle 0|$, remembering the intermediate normalization condition, allows to find an expression for the energy at each order

$$E^{(0)} = \langle 0|H_0|0\rangle\,, \tag{2.33a}$$
$$E^{(1)} = \langle 0|\mathcal{V}|0\rangle\,, \tag{2.33b}$$
$$E^{(2)} = \langle 0|\mathcal{V}|\Psi^{(1)}\rangle\,, \tag{2.33c}$$
$$\vdots \qquad .$$

From this set we see that the the first order correction of the energy is given solely by $|0\rangle$. In other words, the effect of the perturbation Hamiltonian is evaluated, as a first correction, considering the system fixed in the unperturbed ground-state. In order to evaluate the successive terms, one can express the perturbed wavefunctions as an expansion in terms of the eigenfunctions of H_0, which are a complete and orthogonal set of wavefunctions, with the condition that the zeroth-order energy level is not degenerate

$$|\Psi^{(1)}\rangle = \sum_{k\neq 0} |k\rangle\langle k|\Psi^{(1)}\rangle\,. \tag{2.34}$$

With the condition $k \neq 0$ the term $|0\rangle$ is excluded, since the product with the ground-state wavefunction vanishes. At this point it is possible to substitute the expansion written above in Equation 2.32b, to multiply by $\langle k|$ and to use the expression for $\langle k|\Psi^{(1)}\rangle$ inside Equation 2.33c in order to obtain the second-order energy

$$E^{(2)} = \sum_{k\neq 0} \frac{|\langle 0|\mathcal{V}|k\rangle|^2}{E^{(0)} - E_k^{(0)}}\,, \tag{2.35}$$

where the eigenvalue of H_0 corresponding to $|k\rangle$ is written as $E_k^{(0)}$. This procedure can be iterated to obtain the nth-order expression for both the energy and the wavefunction. The theory described above is of general validity and the mathematical derivation holds, with some extra precautions, also in case of two or more degenerate eigenvalues of H_0. We present now a special case of RSPT that links this formalism with the HF theory.

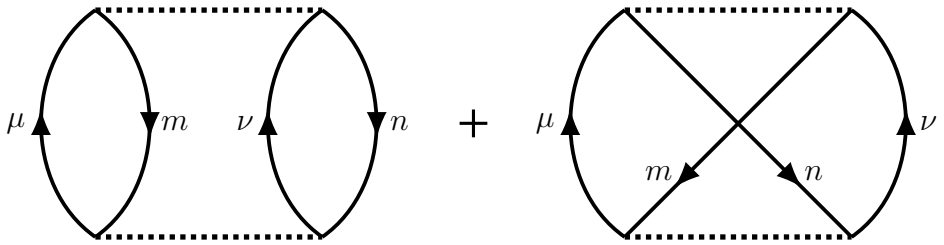

Figure 2.3: MP2 correlation energy represented with Goldstone diagrams. The direct Coulomb term is on the left, the exchange term is drawn on the right. The lines going up are associated with holes and the occupied orbital energies. The lines going down are associated with electrons and their unoccupied orbital energies. The bare Coulomb interaction is depicted by dotted horizontal lines.

Møller-Plesset Perturbation Theory

The RSPT can be used in the context of HF theory to calculate the correlation energy, defined as the difference between the exact energy and the ground-state HF energy, see Equation 2.19. This particular version of RSPT was proposed in 1934 by C. Møller and M. S. Plesset and is called Møller-Plesset Perturbation Theory (MP) [27]. In this context, H_0 is the HF Hamiltonian (H_e) and the unperturbed wavefunction $|0\rangle$ is now the HF wavefunction $|\Psi_0\rangle$. The perturbation potential is defined as

$$\mathcal{V} = \sum_{i<j} \frac{1}{|\mathbf{r}_i - \mathbf{r}_j|} - \sum_i \left[v_{\mathrm{H}}(\mathbf{r}_i) - v_{\mathrm{ex}}(\mathbf{r}_i) \right] , \tag{2.36}$$

where the second sum is the Hartree-Fock potential ($v^{\mathrm{HF}}(\mathbf{r}_i)$), exactly the same potential of H_0. From the definition of unperturbed energy, as written in Equation 2.33a, it appears that $E^{(0)}$ is just the sum over all the HF eigenvalues ϵ_i. The perturbation potential enters in the first-order correction. The two sums contain a two-electron operator and give two equal contributions (with opposite sign), namely the Coulomb repulsion and the exchange contribution, as seen in Equation 2.10. The only differences are the opposite sign and the factor $1/2$ in front of the first sum and absent in the case of $v^{\mathrm{HF}}(\mathbf{r}_i)$. It follows that the two terms can be simplified, giving

$$E^{(1)} = -\frac{1}{2} \sum_{m,n} \left[\langle \psi_m \psi_n | \frac{1}{r_{12}} | \psi_m \psi_n \rangle - \langle \psi_m \psi_n | \frac{1}{r_{12}} | \psi_n \psi_m \rangle \right] . \tag{2.37}$$

As a result, the total energy up to the first-order perturbation corresponds to the HF ground-state energy, seen in Equation 2.15, $E^{(0)} + E^{(1)} = E_0^{(\mathrm{HF})}$.

To improve the description already obtained within the HF approximation, one needs to consider, at least, the second-order perturbation correction. This method takes the name of MP2. An expression for $|k\rangle$, the eigenfunctions of H_0 used in the expansion in Equation 2.34, is necessary to compute the second-order correction of the correlation energy. The natural choice is represented by the excited determinants of the HF ground-state. This feature connects the perturbation theory with CI—more specifically, with

coupled pair and cluster approximations—in various way, some of them will be commented in the following. In order to determine the excited determinants participating in Equation 2.33c, the Brillouin theorem (Theorem 2) is used to exclude the singly excited determinants. Moreover, all determinants with more than two excitations do not mix with the ground-state $|\Psi_0\rangle$, because of the two-particle nature of the operator $\mathcal{V}$. Among all possible excited-state configurations, for the MP2 approximation, the doubly excited determinants $|\Psi^{\mu\nu}_{mn}\rangle$ are the only determinants considered. The eigenvalues of H_0 associated to these excited determinants are just the HF ground-state energy minus/plus the energies of the occupied/virtual spin orbitals. Now we have all the ingredients to write the expression for the correlation energy expanded at the second-order

$$E^{(2)} = \sum_{\substack{m<n \\ \mu<\nu}} \frac{\left|\langle\psi_m\psi_n|\frac{1}{r_{12}}|\psi_\mu\psi_\nu\rangle - \langle\psi_m\psi_n|\frac{1}{r_{12}}|\psi_\nu\psi_\mu\rangle\right|^2}{\epsilon_m + \epsilon_n - \epsilon_\mu - \epsilon_\nu}, \tag{2.38}$$

where the first term is the direct Coulomb repulsion and the second term is the exchange. These two terms are represented with two second-order Goldstone diagrams shown in Figure 2.3, called direct and exchange diagrams, respectively.

With respect to coupled-pair methods, the MP family of approximations have the advantage of scaling more efficiently. In particular, MP2 has a "modest" scaling of $O(N^5)$, that increases to $O(N^6)$ and $O(N^7)$ if we consider the third and fourth-order corrections, indicated by MP3 and MP4 respectively. In this sense, the MP2 expression can be rewritten as a sum of pair energies, where the pairs are the two electrons (m, n) in occupied orbitals. Therefore, there exists a link with the independent pair approximation, an approximation to the full-CI problem mentioned in Section 2.5.1. In detail, the MP2 expression is identical to the first-order pair energy[1] obtained with the IEPA. Furthermore, as mentioned above, the Goldstone diagrammatic techniques can be used to select and sum only particular types of diagrams. This allows us to recover, for example, the random-phase approximation (RPA), a very popular approach widely used for computing the correlation energy. The RPA can be interpreted starting from different theoretical frameworks. In the specific case of perturbation theory, it is obtained by considering the direct term in the MP2 approximation, see Figure 2.3, and summing up to infinity all the ring insets [28]. The RPA approximation is tightly related to density-functional theory and will be discussed in the next chapter.

[1] Meaning that the eigenvalue of the full Hamiltonian, given by the excited pair, is approximated as a difference between ground-state orbital energies.

3 Density-Functional Theory

In the previous chapter we presented the family of wave-function-based methods, where the solution of the many-body problem is given by developing a controlled hierarchy of approximations to the exact ground-state wavefunction $\Psi(\mathbf{r}_1\sigma_1, \ldots, \mathbf{r}_N\sigma_N)$, a function of $3N$ spatial coordinates, plus the spin. An alternative and popular approach is to recast the Schrödinger equation in terms of the electron density distribution $n(\mathbf{r})$, a much simpler function that has only 3 degrees of freedom. This idea dates back to the late 20s and is well known with the name of density-functional theory (DFT). The first clean mathematical proof of DFT has been provided by Hohenberg, Kohn, and Sham. Their seminal works significantly contributed to popularize DFT. At the time of writing, DFT represents the most popular *ab initio* method in quantum chemistry, with an incredibly wide range of applications and an increasing presence in scientific publications [29, 30]. An idea about the importance of DFT in modern science can be grasped by looking at Figure 3.1, where are reported the numbers of papers and patents that involve DFT, thorough the last 25 years. This impressive growth confirms the success of DFT, already rewarded with the 1998 Nobel prize in Chemistry, given to Walter Kohn, *"for his development of the density-functional theory"*. The prize was shared with a theoretical chemist, Sir John Anthony Pople, *"for his development of computational methods in quantum chemistry"*.

The key of the success of DFT resides in its favorable combination of accuracy and affordable computational cost. Within DFT, the reformulation of the many-body problem is not only conceptual, but also computational. In fact, in practice, the complex many-body effects are described solely by one term, called *exchange-correlation* (XC) energy. Formally, knowing the "real" form of the exchange-correlation term would determine the electron density and the ground-state of the system exactly. Unfortunately, as one can imagine, the form of such complex term is unknown and can only be constructed approximately. It follows that, many approximations have been proposed for the exchange-correlation functional to improve the general applicability of DFT, as for example to describe the long-range van der Waals interactions, and/or to treat particularly challenging phenomena as electronic energy level alignment, electron transport, strong correlation, etc. This subject attracted many efforts through the years, starting at the foundation of DFT, and still represents the main goal in current developments [31, 32].

In the following, the reader will be introduced to the fundamental concepts of DFT,

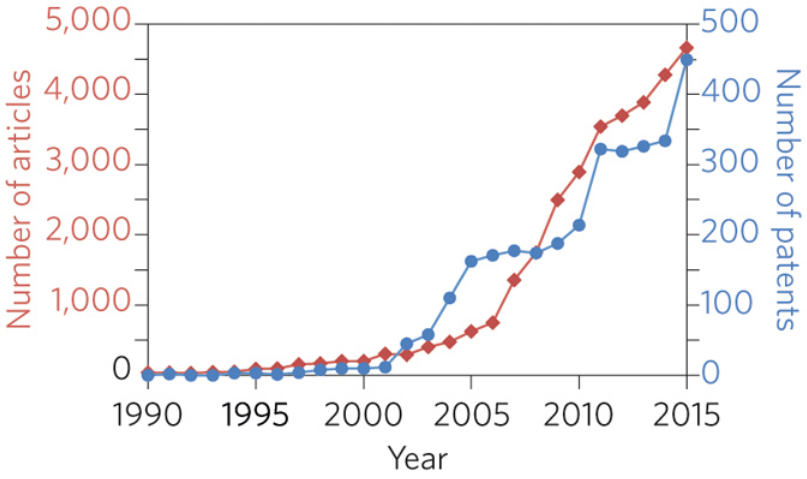

Figure 3.1: Number of articles and patents, in material science, that include the term "density functional theory". Source: Editorial, Nature Materials (2016) [29].

as well as the most used exchange-correlation functionals. Among all sources used, the matter below is based mainly on the texts by Parr and Yang [33] and Engel and Dreizler [34]. We suggest the reader to refer to these books and also to the classic book by Dreizler and Gross [35] to have a broader overview on DFT in all its flavors. The density-functional theory is particularly important for this thesis, in fact the large majority of the results presented here are indeed DFT calculations. Moreover, the van der Waals interactions, our central topic, are implemented within the DFT framework, as an extension of standard exchange-correlation functionals.

3.1 The Thomas-Fermi model

In this chapter we present the seminal idea of Thomas and Fermi, which is considered the precursor to DFT. They represented the ground-state electron energy as a functional of the density

$$E_0 = E[n_0(\mathbf{r})]\,. \tag{3.1}$$

From now on, the explicit dependency of the electron density on the coordinates will be omitted, unless necessary. The first model of Thomas and Fermi (TF) [36, 37] originates in 1927 and is based on the homogeneous electron gas (HEG). In this system the nuclei are replaced with a positive background charge density, which interacts with itself and the electrons. The electrons are approximated with a uniform distribution within small volumes (locally) and interact *via* the electrostatic repulsion term. The kinetic energy for the electrons is thus approximated as the one of the non-interacting electron gas. The space is divided in 3D cubic boxes with volume V and side L and periodic boundary conditions. With these assumptions one can write the normalized single-particle plane

wave as

$$\psi_{\mathbf{k}}(\mathbf{r}) = \frac{e^{i\mathbf{kr}}}{\sqrt{V}}\,, \quad \mathbf{k} = \frac{2\pi}{L}\mathbf{l}\,, \quad \text{with } l_i = 0, \pm 1, \pm 2, \dots\,, \tag{3.2}$$

where the index $\mathbf{l}$ includes all the periodic repetitions of the box. In the ground-state of the Fermi gas (free electron model), all the energetic levels are filled with both spin up and down. For this reason the spin part is omitted in the wavefunction above, keeping in mind that a summation/integration over space must include the factor 2, for the spin part.

Following the original TF formulation, the ground-state density (n_0) can be computed with an integration over the k-space or using the equivalent formulation in terms of the energy

$$n_0 = \left(\frac{L}{2\pi}\right)^3 \frac{2}{L^3}\int_0^{k_\mathrm{F}} 4\pi k^2 dk = \int_0^{E_\mathrm{F}} g(E)dE = \int_0^{E_\mathrm{F}} \frac{\sqrt{2E}}{\pi^2}dE\,, \tag{3.3}$$

where the first integral is performed using spherical coordinates, while $g(E) = \frac{1}{V}\frac{dN}{dE}$ is the density of states. In the same spirit, it is possible to evaluate the kinetic energy density

$$t_e[n] = \int_0^{E_\mathrm{F}} g(E)EdE = \frac{3}{10}(3\pi^2)^{2/3} n_0^{5/3} = C_k n_0^{5/3}\,, \tag{3.4}$$

with $C_k = 2.871$ Hartree. The energy is now written in terms of the ground-state electron density. In the TF approximation, the energy density expression for the inhomogeneous system is replaced by the expression obtained above, valid for the HEG. Thus, the electronic properties are functionals of the electron density, which is evaluated locally, resulting in

$$T_e^{\mathrm{TF}}[n] = C_k \int n(\mathbf{r})^{5/3} d\mathbf{r}\,. \tag{3.5}$$

This expression anticipates the concept of local-density approximation (LDA), the first exchange-correlation functional developed in DFT and one of the most important.

The total energy is computed, in general, using the definition of electronic Hamiltonian given in Equation 1.6. However, within the TF model, the exchange and correlation contributions are not taken into account. Only the classical Coulomb potential is considered,

$$E^{\mathrm{TF}}[n] = T_e^{\mathrm{TF}}[n] + \frac{1}{2}\int\int \frac{n(\mathbf{r})n(\mathbf{r}')}{|\mathbf{r}-\mathbf{r}'|} d\mathbf{r}\, d\mathbf{r}' + \int n(\mathbf{r})\, v_{\mathrm{ext}}(\mathbf{r})\, d\mathbf{r}\,. \tag{3.6}$$

The last term in the equation above introduces the external potential that, together with the electron density, form the term V_{e-n}. This new notation separates conceptually the functional of the electron density from the contribution coming from the nuclei, a function of the coordinates. Once the energy functional is known, assuming that the electron density minimizes it, one can proceed to derive the Euler-Lagrange equation, as previously seen in Section 2.2:

$$\mu^{\mathrm{TF}} = \frac{\delta E^{\mathrm{TF}}[n]}{\delta n(\mathbf{r})} = \frac{5}{3}C_k n^{2/3}(\mathbf{r}) + v_{\mathrm{ext}}(\mathbf{r}) + \int \frac{n(\mathbf{r}')}{|\mathbf{r}-\mathbf{r}'|}d\mathbf{r}'\,, \quad N[n] = \int n(\mathbf{r})d\mathbf{r}\,. \tag{3.7}$$

The total number of electrons N is used as a constraint and μ^{TF} is the Lagrange multiplier. This equation can be solved with the help of the constraint and the resulting electron density is inserted in Equation 3.6 to compute the TF total energy.

The first and most important step towards an improvement of this model is the inclusion of the exchange term. In 1930, Dirac followed the path of the TF model and derived [38] the exchange energy expression for the HEG in a cubic box,

$$E_x^{\mathrm{D}}[n] = -C_x \int n^{4/3}(\mathbf{r}) d\mathbf{r}\,, \tag{3.8}$$

with $C_x = 0.739$ Hartree. This expression is added to the total energy functional in Equation 3.6 and the sum takes the name of Thomas-Fermi-Dirac functional: $E^{\mathrm{TFD}}[n] = E^{\mathrm{TF}}[n] + E_x^{\mathrm{D}}[n]$.

A further improvement of the TF model is the von Weizsäcker functional for the kinetic energy, formulated in 1935. In the presence of a potential, observed von Weizsäcker, the single particle wavefunction can be considered real. The general expression for the kinetic energy is rewritten in term of the total density. Subsequently, the divergence theorem (or Green-Gauss theorem) is applied to the second term of $T_e[n]$ and it can be demonstrated [39] that such surface contributions vanish, since the real orbital decays exponentially, as $|\mathbf{r}| \to +\infty$,

$$T_e[n] = \frac{1}{8}\int \frac{|\nabla n(\mathbf{r})|^2}{n(\mathbf{r})} d\mathbf{r} - \frac{1}{4}\int \nabla^2 n(\mathbf{r}) d\mathbf{r} \implies T_e^{\mathrm{vW}}[n] = \frac{1}{8}\int \frac{|\nabla n(\mathbf{r})|^2}{n(\mathbf{r})} d\mathbf{r}\,. \tag{3.9}$$

The von Weizsäcker density functional is the exact non-interacting $T_e[n]$ functional in the case of single particle and spin-saturated pair of particles. Moreover, the $T_e^{\mathrm{vW}}[n]$ functional represents an important step beyond the TF model because it introduces the idea to use the gradient of $n(\mathbf{r})$ in order to improve the description of inhomogeneous systems.

Despite the attractiveness of a theory that reduces the many-body problem to a three-dimensional quantity, the TF-based models have been largely superseded. Many ingredients are still missing for accurate calculations and the model suffers severe approximations, for example the atomic shell structure is lost with a representation of the kinetic energy in terms of the density. We will introduce now, starting with the mathematical justification, another density-based theory: the DFT. In this case, the practical advantages stated above are joined with accurate results. The key concepts that led to the success of DFT will be the matter of the next sections.

3.2 The Hohenberg-Kohn Theorem

Let us consider an N-electron system with the electronic Hamiltonian of Equation 1.6, where the electronic–nuclear interactions are now called external potential: $H_e = T + V_{e-e} + V_{\mathrm{ext}}$. This Hamiltonian admits a ground-state Ψ_0, assumed to be nondegenerate

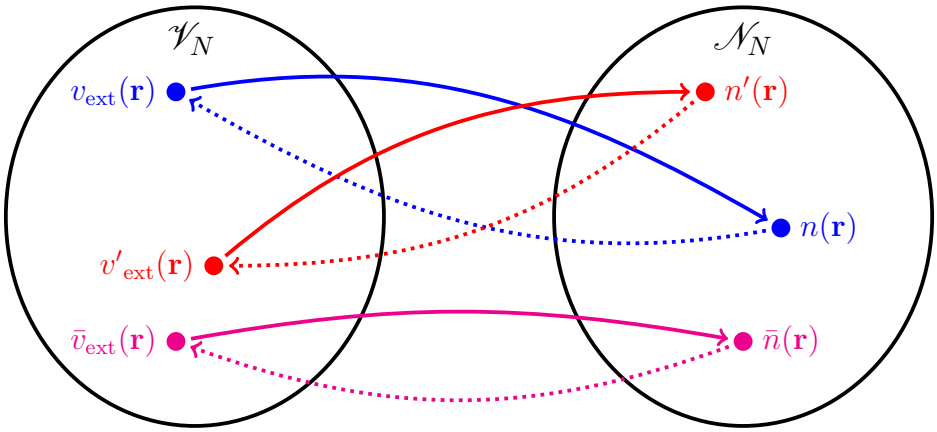

Figure 3.2: Representation of the Hohenberg-Kohn theorem. The set of external potentials and the set of electron densities are indicated with $\mathscr{V}_N$ and $\mathscr{N}_N$ respectively. Different external potentials must correspond to distinct ground-state densities and *vice versa*.

for simplicity. The ground-state is linked to the electron density and the external potential *via* the relations

$$n_0(\mathbf{r}) = N \int |\Psi_0(\mathbf{r}, \mathbf{r}_2, \ldots, \mathbf{r}_N)|^2 d\mathbf{r}_2 \ldots d\mathbf{r}_N \,, \quad \langle \Psi_0 | V_{\text{ext}} | \Psi_0 \rangle = \int n_0(\mathbf{r}) v_{\text{ext}}(\mathbf{r}) d\mathbf{r} \,, \tag{3.10}$$

where we omitted the spin dependency, unnecessary in the present formulation. The external potential determines the ground-state wavefunction, together with the constraint N, hence the electron density is a functional of $v_{\text{ext}}(\mathbf{r})$. In 1964 Hohenberg and Kohn demonstrated [40] that the opposite conclusion is also valid, a cornerstone of DFT.

Theorem 3 (Hohenberg-Kohn (HK) Theorem) *There is a one-to-one correspondence between the ground-state electron density of a N-electron system and the external potential acting on it* [15].

The schematic representation, a bijective map [1], is given in Figure 3.2. The demonstration is formulated as a *reductio ad absurdum*. In short, the hypothesis of two different external potentials with the same electron density can be confuted using the minimum property of the ground-state energy. In summary, we started knowing the relation $v_{\text{ext}}(\mathbf{r}) \Rightarrow \Psi_0[v_{\text{ext}}] \Rightarrow n_0(\mathbf{r})$ and now, thanks to the HK theorem, this relation can be inverted. The resulting map is injective up to a phase factor for the wavefunction and up to a constant for the external potential. An extended formulation of the HK theorem and the minimization procedure is given in Appendix B.1. In detail, the HK theorem links the ground-state wavefunction with a *v-representable* electron density. The *v-representability* guarantees the existence of an external potential associated with the ground-state electron density. The extensions of the HK theorem and the *v-representability*

[1] The map is bijective under the assumption of non degenerate ground-state. To include the degenerate case one needs to split the set of electron densities into an union of subsets. The density is a linear combination of degenerate ground-state densities.

are deeply discussed in the specialized literature [41], an introduction to the matter is given in the present Thesis in Appendix B.2. We invite the reader to refer to the books proposed at the beginning of this section for a more exhaustive documentation.

The most important consequence of the HK theorem is the existence of a variational principle for the energy that concerns the density.

Corollary 3.1 *The minimum of the total energy functional occurs when the electron density corresponds to the exact ground-state density of the system.*

The HK theorem can be used to demonstrated the statement above. We define the energy of a system of N interacting electrons in a given nuclear external potential v_{ext} as a functional of the electron density

$$E[n] = \langle \Psi | H_e | \Psi \rangle = T[n] + V_{\text{e}-\text{e}}[n] + V_{\text{n}-\text{e}}[n] = F[n] + \int v_{\text{ext}}(\mathbf{r}) n(\mathbf{r}) d\mathbf{r} \,, \tag{3.11}$$

where the dependence on $v_{\text{ext}}(\mathbf{r})$ is made explicit in the last passage and the electron density is allowed to vary. We note that the functional $F[n]$ is independent of the external potential and is a *universal* functional of the density. If we consider a trial density $\bar{n}(\mathbf{r})$, HK theorem links to it a potential $\bar{v}_{\text{ext}}$ and a wavefunction $\bar{\Psi}$. Clearly, the energy functional written above satisfies the inequality $E[\bar{n}] = \langle \bar{\Psi} | H_e | \bar{\Psi} \rangle \geqslant E[n_0]$, where $n_0(\mathbf{r})$ is the ground-state density.

In summary, a parallel with the variational principle for wavefunctions is traced, see Equation 2.7. Also, the Euler-Lagrange equation employed in the TF model (Equation 3.7) is now fully justified. The variational principle allows us to find the ground-state density *via* the stationary condition. The variation of $E[n]$, with the total number of particles N as a constraint, is set to zero, giving the Euler-Lagrange equation

$$\mu = \frac{\partial E[n]}{\partial n(\mathbf{r})} = \frac{\partial F[n]}{\partial n(\mathbf{r})} + v_{\text{ext}}(\mathbf{r}) \,, \tag{3.12}$$

where μ is the Lagrange multiplier. At this point, DFT is effectively a theory that reduces the N-body problem to the problem of finding a 3-dimensional function. It is important to stress that no approximations were introduced till now in the formulation of the theory, *i.e.* a hypothetical solution of Equation 3.12 would give the exact ground-state density of the system. Unfortunately, this task is far from being trivial, as the "true" form of $F[n]$ is unknown. In the following section, the difficulties concerning $F[n]$ will be tackled with the approach of Kohn and Sham. They successfully opened DFT for practical applications and their method represents the most widely used variant of DFT.

3.3 The Kohn-Sham Equations

The aforementioned formulation of DFT needs to be expanded with a specific shape for the kinetic energy term, following what has been done in the Thomas-Fermi model using the HEG. Unfortunately, the kinetic functional of the density is unknown and the

HEG represents a model with dubious applicability to real systems, where the electron density is nonuniform. To treat inhomogeneous systems of interacting electrons, one year after the original formulation of DFT, Kohn and Sham (KS) proposed in their seminal paper [42] to map the system of interacting electrons onto an auxiliary system of non-interacting electrons with the same ground-state density. For such fictitious system of N electrons, the density is given as a sum of single particle orbitals, called KS orbitals $\psi_i(\mathbf{r}, \sigma)$:

$$n(\mathbf{r}) = \sum_{i}^{N} \sum_{\sigma} \psi_i^*(\mathbf{r}, \sigma)\psi_i(\mathbf{r}, \sigma)\,, \tag{3.13}$$

where the ground-state wavefunction is, exactly as in the Hartree-Fock case (Equation 2.6), a Slater determinant of the N orbitals of lowest energy, $\Psi_0 = A\{\psi_1\,\psi_2\,\ldots\,\psi_N\}$. It is important to mention that the HK theorem applies to any electron system, therefore the existence of an external potential v_{ext}^0, that produces the ground-state density n_0 for non-interacting electrons, is guaranteed. Since the ground-state density n_0 and the density of the system of interacting electrons are taken to be equal, the decomposition into orbitals is valid also for the interacting system, even though the ground-state is not a Slater determinant of the orbitals.

With the decomposition of the density into a sum of single particle orbitals, shown in Equation 3.13, the total energy can be rewritten in term of one particle and two particles operators, see Equation 2.8 and 2.9. The one electron operator includes the kinetic energy for the non-interacting system and the electron–nucleus attraction, while the two-body operator corresponds to the Hartree term

$$T_0[n] + V_{\text{ext}}[n] = \sum_i \langle\psi_i| -\frac{1}{2}\nabla^2 + v_{\text{ext}}(\mathbf{r})|\psi_i\rangle\,, \tag{3.14a}$$

$$V_{\text{H}}[n] = \frac{1}{2}\sum_{i,j}\langle\psi_i\psi_j|\frac{1}{r_{12}}|\psi_i\psi_j\rangle = \frac{1}{2}\int\int\frac{n(\mathbf{r})\,n(\mathbf{r}')}{|\mathbf{r}-\mathbf{r}'|}d\mathbf{r}\,d\mathbf{r}'\,. \tag{3.14b}$$

The HK total energy functional in Equation 3.11 is rewritten as

$$E[n] = T_0[n] + V_{\text{H}}[n] + E_{\text{xc}}[n] + \int v_{\text{ext}}(\mathbf{r})n(\mathbf{r})d\mathbf{r}\,, \tag{3.15}$$

where the first three terms on the right side correspond to the functional $F[n]$. The complexity of the many-body problem is now described by one single term: the exchange-correlation functional, defined as

$$E_{\text{xc}}[n] = T[n] - T_0[n] + V_{e-e}[n] - V_{\text{H}}[n]\,. \tag{3.16}$$

Conceptually, the minimum of the energy functional above still represents the exact ground-state energy. Unfortunately, as one can easily imagine, the shape of $E_{\text{xc}}[n]$ is unknown and several different guesses have been proposed through the years in

order to improve the accuracy of DFT calculations [2]. The goal of finding the exact XC functional is far from being accomplished, however great progress has been made and DFT is now successfully applicable to a broad variety of different systems. The next section will be dedicated to introduce the most popular and used XC functionals.

The reformulation of the HK energy functional in terms of single-particle orbitals allows us to employ the method of the Lagrange multipliers to find the ground-state energy. The variation of the density is now translated into a variation of the orbitals and can be formally carried out exactly, as in the case of the Hartree (or Hartree-Fock) method (see Equation 2.3 and 2.11). The Lagrange function is built using the orthonormalization of the wavefunction as a constraint, more details can be found in Appendix A.2. Then the variation of the function leads to the KS eigenvalue equations

$$\left(-\frac{1}{2}\nabla^2 + v_{\mathrm{H}}(\mathbf{r}) + v_{\mathrm{xc}}(\mathbf{r}) + v_{\mathrm{ext}}(\mathbf{r})\right)\psi_i(\mathbf{r},\sigma) = \epsilon_i\psi_i(\mathbf{r},\sigma)\,, \tag{3.17}$$

where the terms on the left side are obtained analytically with a derivation of the functional expression with respect to the electron density

$$\frac{\partial V_{\mathrm{H}}[n]}{\partial n(\mathbf{r})} = v_{\mathrm{H}}(\mathbf{r}) = \int \frac{n(\mathbf{r}')}{|\mathbf{r}-\mathbf{r}'|}d\mathbf{r}'\,, \qquad \frac{\partial E_{\mathrm{xc}}[n]}{\partial n(\mathbf{r})} = v_{\mathrm{xc}}(\mathbf{r})\,. \tag{3.18}$$

In the literature, the three potentials on the left side of the KS equation are often collected in one single term, called Kohn-Sham potential or effective potential,

$$v_{\mathrm{eff}}(\mathbf{r}) = v_{\mathrm{H}}(\mathbf{r}) + v_{\mathrm{xc}}(\mathbf{r}) + v_{\mathrm{ext}}(\mathbf{r})\,. \tag{3.19}$$

The solution of the KS integro-differential eigenvalue equations is pursued in a self-consistent way. Usually, an initial guess for $n(\mathbf{r})$ is used to calculate the corresponding effective potential. Once the eigenvalue problem is solved for the orbitals ψ_i, a new electron density is constructed. This procedure is repeated until convergence is reached, *i.e.* the minimum value of the energy is approached sufficiently closely. Following the same steps of the HF theory (Section 2.15), the eigenvalues can be used to compute the total energy. The expression for the kinetic energy can be written in terms of the eigenvalues using Equation 3.17, however during the variational procedure, the factor $\frac{1}{2}$ in front of the Hartree term is lost, see Equation 3.18. For this reason, when the eigenvalues are inserted in the total energy functional, the external potential cancels out, while the Hartree term remains (with opposite sign), together with the XC functional

$$E[n] = \sum_i \epsilon_i - \frac{1}{2}\int\int \frac{n(\mathbf{r})\,n(\mathbf{r}')}{|\mathbf{r}-\mathbf{r}'|}d\mathbf{r}\,d\mathbf{r}' + E_{\mathrm{xc}}[n] - \int v_{\mathrm{xc}}(\mathbf{r})n(\mathbf{r})d\mathbf{r}\,. \tag{3.20}$$

From the eigenvalue equation written above, we note that the original formulation "orbital-free" of DFT, with a single equation for the density, is now significantly mod-

[2] Formally DFT is an exact theory.

ified. Indeed, the need to treat accurately the kinetic term brought us a set of N eigenvalue equations, corresponding to the N single-particle orbitals. On the other side, the KS eigenvalue problem is still computationally analogous to the Hartree theory and scales formally as $O(N^3)$ [3], better than the HF method, even though it contains (some) exchange and correlation effects.

As a conclusion of this section, before proceeding to introduce the reader to the most important XC functionals, it is worth to mention some extra technicalities. First, the single-particle orbitals that compose the ground-state electron density are, in principle, purely mathematical Lagrange multipliers. The physical meaning of the eigenvalues was provided by Janak in 1978 [43]. In Janak's theorem the eigenvalue is the derivative of the total energy with respect to the occupation of a state. As a result, the highest eigenvalue is associated to the energy necessary to add/extract one electron. This is in contrast with Koopmans' theorem for the HF orbitals, where an electron can be removed from/added to any orbital and the eigenvalues are related to the adiabatic ionization energies of the system. In practice, however, Janak's theorem is commonly used for arbitrary levels. Secondly, the present theory holds in case of spin-polarized systems. The operators are spin independent and the total electron density is just the sum of the two densities corresponding to the two spins: $n(\mathbf{r}) = n_\alpha(\mathbf{r}) + n_\beta(\mathbf{r})$. In case of restricted closed-shell calculations, the density is simply two times the sum over the orbitals $n(\mathbf{r}) = 2\sum_i^{N/2} |\phi_i(\mathbf{r})|^2$. Each energy eigenvalue is two-fold degenerate, meaning that for one spatial part there are two spins. In the ground-state, the singly occupied spatial orbitals, typically only one, are the highest occupied. The extension to spin-polarized functional is known for all the terms, including exact-exchange [44], written with the two spin channels as $E_\mathrm{x}[n_\alpha, n_\beta]$. The only term that can present a non-straightforward spin dependence is the (approximate) correlation functional. For this part, a general remedy is absent and the modifications necessary to introduce the spin variable depend on the particular functional.

Finally, we remind here that DFT is, by construction, an exact theory, thus the exact form of the XC functional can be formally derived. One way that can be used to obtain the exact XC part is through the adiabatic-connection (AC) procedure, in which the DFT formalism introduced above is derived starting from a system of non-interacting electrons and gradually turning on the Coulomb interaction [45]. The AC procedure is combined with the fluctuation-dissipation theorem (FD) and provides the ACFD formula, an expression for the exact XC functional in terms of the response functions of the system. This result can be used to study the approximations behind a particular XC functional and represents the starting point to improve its performances. The RPA, already introduced in the context of many-body perturbation theory, can be derived starting with the AC formalism. The ACFD formula can be conveniently partitioned, dividing the EXX part from the exact $E_\mathrm{c}[n]$ functional. For this reason, the ACFD formula will be mentioned also in the context of long-range correlation interactions

[3] In the following part of this chapter we will see that this scaling is not valid for advanced XC functionals.

(van der Waals), in Section 5.4 and 5.5. The ACFD theory is discussed in more detail in Appendix B.3. An alternative way to the AC procedure to derive the exact XC functional is the Kohn-Sham perturbation theory [46] (KSPT). Here, the Hamiltonian contains a perturbative term with the contributions of the fully interacting system. Formally, the AC and the KSPT lead to the same result, with the difference that in the latter case the electron density varies with the perturbation. On the other hand, within the AC formalism, the density is kept equal to the density $n_0(\mathbf{r})$ of the non-interacting system.

3.4 Exact-Exchange

Intuitively, the first step beyond the standard formulation of the KS problem, is the inclusion of the exact-exchange (EXX) effects in the total energy functional (Equation 3.15). In analogy with the step made to go from the Hartree to the Hartree-Fock theory. The exact-exchange (Equation 2.12) is defined as

$$E_{\mathrm{x}}^{\mathrm{EXX}}[n] = -\frac{1}{2}\int\int \frac{n_{\mathrm{x}}(\mathbf{r},\mathbf{r}')n_{\mathrm{x}}(\mathbf{r}',\mathbf{r})}{|\mathbf{r}-\mathbf{r}'|}d\mathbf{r}d\mathbf{r}' \,, \tag{3.21a}$$

$$\text{where} \quad n_{\mathrm{x}}(\mathbf{r}',\mathbf{r}) = \sum_{j}^{N}\sum_{\sigma}\psi_j^*(\mathbf{r}',\sigma)\psi_j(\mathbf{r},\sigma) \,. \tag{3.21b}$$

Thus, the XC functional is formally split in two parts and the inclusion of the term above would leave only the correlation as the unknown term. Naturally, the EXX has to be included self-consistently, *i.e.* the potential obtained from the functional derivative (see Equation 3.18) appears in the set of KS eigenvalue equations. Following the same procedure of the Hartree part, but with opposite sign, the EXX is thus contained in the ground-state total energy, see Equation 3.20.

The DFT theory with EXX scales, with respect to the number of particles, as the Hartree-Fock method, with the important difference that DFT includes some correlation effects. We remark here that the EXX term is non-local, thus the solution of the DFT many-body problem becomes much more demanding than the previous formulation. However, the combination of optimized implementations and modern computing resources have extended the applicability of EXX to very large systems.

The Self-Interaction Error

The exchange term represents an important contribution in all systems. In particular, the correct decay of the electrostatic potential, felt by an electron, should be $1/r$, while in the absence of exchange effects such potential would decay exponentially with distance. This well-known issue is one of the consequences of the "self-interaction" error (SIE) in DFT, *i.e.* the interaction of an electron with the field it generates. The SIE was early noticed by Amaldi and Fermi in 1934 during the development of the Thomas-Fermi theory. It originates from the fact that the Coulomb potential is approximated with the Hartree term, while the "exact" formulation should include the exchange term too. One

can easily see that the SIE is present even in the case of a single-electron system. In this case the Hartree term produces the spurious interaction of an electron with itself. For a one-electron system or a fully occupied orbital the requirement to solve the SIE is that the Hartree direct contributions and the XC energy cancel each other [47]. Namely, $V_{\mathrm{H}}[n_{i\sigma}] + E_{\mathrm{x}}[n_{i\sigma}, 0] = 0$ and $E_{\mathrm{c}}[n_{i\sigma}, 0] = 0$, where only one spin channel is present. Therefore, the inclusion of EXX term would solve completely the SIE. Nevertheless, for practical usage, approximations of the EXX term are typically employed in order to have faster calculations.

3.5 Approximate Exchange-Correlation Functionals

The problem of finding an accurate form for the unknown XC functional, defined in Equation 3.16, has been a central topic in DFT since its foundation. First, the straightforward inclusion of exact-exchange is not recommended, since it increases drastically the computational time, bringing a non-local term inside the KS eigenvalue equations. Second, the correlation term accounts for the fact that the electrons are not independent. From a parallel with the HF theory, the correlation can be defined as the energy contributions that are found when going beyond the HF solution. Unfortunately, the exact expression is unknown for $E_{\mathrm{c}}[n]$. Here, the most popular and successful approximations to the exact XC functional are discussed. In this survey, the different models are presented in order of increasing complexity, following the Jacob's ladder of density functional approximations [48], which ideally ends with the "heaven of chemical accuracy".

The Local-Density Approximation

In 1965 Kohn and Sham proposed the local-density approximation (LDA) to treat systems with slowly varying electron density. The idea goes back to the TF model and consists in approximating the density of an inhomogeneous electron gas as locally homogeneous, *i.e.* at every point $\mathbf{r}$ the XC density is considered to be the density of the HEG. Within the LDA, the XC functional is approximated in the form

$$E_{\mathrm{xc}}^{\mathrm{LDA}}[n] = \int \epsilon_{\mathrm{xc}}(n(\mathbf{r}))n(\mathbf{r})d\mathbf{r}\,, \tag{3.22}$$

where $\epsilon_{\mathrm{xc}}(n(\mathbf{r}))$ is *"the exchange and correlation energy per electron of a uniform electron gas of density* $n(\mathbf{r})$*"*. The XC potential, a fundamental ingredient of the KS equations, can be easily computed

$$v_{\mathrm{xc}}^{\mathrm{LDA}}(\mathbf{r}) = \frac{\delta E_{\mathrm{xc}}^{\mathrm{LDA}}[n]}{\delta n(\mathbf{r})} = \epsilon_{\mathrm{xc}}(n(\mathbf{r})) + n(\mathbf{r})\frac{d\epsilon_{\mathrm{xc}}(n(\mathbf{r}))}{dn(\mathbf{r})}\,. \tag{3.23}$$

The two terms above not only enter as a part of the effective potential (3.17), but have also an important role in determining the total ground-state energy. In particular, when $v_{\mathrm{xc}}^{\mathrm{LDA}}(\mathbf{r})$ is substituted into Equation 3.20, the first term simplifies with the XC energy $E_{\mathrm{xc}}^{\mathrm{LDA}}[n]$, leaving the integral of the second term as the only XC contribution to the total energy.

It is useful to partition the LDA energy density into a sum of an exchange and a correlation part, $\epsilon_{\mathrm{xc}}(n(\mathbf{r})) = \epsilon_{\mathrm{x}}(n(\mathbf{r})) + \epsilon_{\mathrm{c}}(n(\mathbf{r}))$. The expression for the exchange part, which is the exchange of the HEG, is taken from the contribution of Dirac to the TF theory [38], see Equation 3.8, and corresponds to $\epsilon_{\mathrm{x}}(n(\mathbf{r})) = -C_x n^{1/3}(\mathbf{r})$. The form of the correlation part, on the other hand, is in general unknown. Numerical results, obtained with Quantum Monte Carlo calculations, were employed to parametrize $\epsilon_{\mathrm{c}}(n(\mathbf{r}))$ [49, 50].

The local spin-density approximation (LSDA) represents the generalization of LDA to include electron spin. The exchange part is known analytically and can be easily extended to spin-polarized systems, as already mentioned in concluding Section 3.3. The spin-dependency of the correlation energy is introduced *via* a parametrization [49], interpolating a function of the spin, as the relative spin-polarization.

The LDA turned out to be much more accurate than could be expected from its initial approximations and is not confined to systems with approximately uniform electron density, as bulk metals. Even in atoms and molecules, the results obtained with LDA are comparable with HF, which is computationally much more demanding. In solids and surfaces, LDA give the best results and sometimes predicts accurate geometries and elastic properties. Since LDA is built upon a very simple approximation, these surprisingly good performances are attributed to an error compensation between the exchange and the correlation part. The shortcomings of LDA can be found, for example, by looking at atomization energies of molecules, where LDA overbinds by about 1 eV [51]. Typically, LDA overestimates also the bond strength in solids, producing an underestimation of the bond lengths. With these conclusions, extensions of the LDA functional become advisable, beyond the simple dependency on the local electron density.

The Generalized Gradient Approximation

The simplest extension of LDA to inhomogeneous systems are the generalized gradient-approximated (GGA) functionals. This family of XC functionals, also called semi-local functionals, emerged during the mid 1980s and, as the name suggests, they include the gradient of the electron density $\nabla n(\mathbf{r})$ to account for non-locality. The semi-local appellation comes from the fact that the non locality is only partially captured by the density gradient. The GGA XC functionals are written as a function of the density and its gradient

$$E_{\mathrm{xc}}^{\mathrm{GGA}}[n] = \int f(n, \nabla n) d\mathbf{r} = \int \epsilon_{\mathrm{xc}}(n(\mathbf{r})) F_{\mathrm{xc}}(n(\mathbf{r}), \nabla n(\mathbf{r})) n(\mathbf{r}) d\mathbf{r}\,, \tag{3.24}$$

where the GGA functional is expressed in term of $\epsilon_{\rm xc}(n(\mathbf{r}))$, the LDA exchange-correlation energy per particle, and $F_{\rm xc}$, a dimensionless enhancement factor that carries the information about the density gradient. Much work has been done in the past years on the development and parametrization of a number of GGA functionals. The most widespread and successful GGA functional is the one of Perdew, Burke and Ernzerhof (PBE) [52]. In general, the GGA functional parametrization is subjected to several exact conditions, as the sum rules for both the exchange end the correlation part. The PBE functional follows the construction of the functional of Perdew and Wang, PW91 [53]. The latter is designed to satisfy as many conditions as possible, but presents a long derivation and a complex and overparametrized analytical form which can lead to spurious fluctuations of the potential. On the contrary, PBE satisfies only the energetically significant conditions. PBE is a non-empirical functional, in the sense that all parameters are fundamental constants, without a dependency on experimental data.

The GGA functionals provide satisfactory results when applied to study the structure of molecules, although they significantly underestimate the binding of weakly bonded systems. In particular, the PBE bond lengths for diatomic molecules are in excellent agreement with the experimental results. The atomization energies are generally improved with respect to LDA, even though in the worst cases, the functional overbinds/underbinds by about 1 eV [54]. For solids, PBE is found to improve significantly the LDA cohesive energies and to describe well the lattice constants, but the functional presents a tendency to underbind [55], the opposite trend of LDA. Consequently, the bulk moduli are underestimated, matching the level of accuracy of LDA. In summary, the GGA functionals produce better results than LDA, with a similar computational cost. Unfortunately, the improvement is not uniform and some of the limitations of LDA are still present, as the SIE.

Hybrid Functionals

The idea behind a hybrid functional was proposed by Becke in 1993 [56] and consists of mixing a fraction of exact-exchange energy with the exchange (and the correlation) of a semi-local functional. The general form of a hybrid functional is written as

$$E_{\rm xc}^{\rm hybrid}[n] = \alpha E_{\rm x}[n] + (1-\alpha)E_{\rm x}^{\rm GGA}[n] + E_{\rm c}^{\rm GGA}[n]\,, \tag{3.25}$$

where the mixing is regulated by the coefficient α. Clearly, the limiting value of $\alpha = 0$ would recover the original GGA functional, on the other hand $\alpha = 1$ would employ 100% of EXX, limiting the GGA contribution only to the correlation part. Usually, the hybrids employ an $\alpha < 1$.

In the original idea of Becke, 50% of EXX was mixed with an equal 50% of XC contribution from LDA [56]. Successively, the method has been refined with a more complex mixing. Namely, the exchange is a mix of HF, LDA and the GGA functional called Becke88 [57]. The correlation part is obtained using the LDA correlation and the GGA functional of Lee, Yang and Parr [58], the two parts are weighted differently. This

is the popular B3LYP [59], a hybrid functional in which the amount of HF exchange, LDA exchange and the gradient correction to the correlation energy depend on a three parameters fit. The fit is introduced to reproduce important quantities as atomization energies, ionization potentials, etc., of the molecular G2 test set of Pople. B3LYP has been extremely successful in predicting a wide range of molecular properties, as the atomization energies. However, the accuracy of the results can be attributed also to a systematical cancellation of errors. In fact B3LYP tends to overestimate both exchange and correlation energies of atoms and molecules [60]. The functional is widely used in the chemistry community and a uniform improvement of its performances is a challenge for the present development of DFT functionals [32]. Because of the additional empirical parameters, that involve experimental data, the B3LYP is a semi-empirical functional. Another drawback is the increased computational cost, that restricts the applicability of the functional, when employed to study extended systems.

A second very popular hybrid functional is PBE0 [61, 62], where the XC functional is obtained using Equation 3.25 with a mixing coefficient $\alpha = 1/4$, *i.e.* 25% of EXX. This functional considerably improves the atomization energies of molecules with respect to PBE [54]. However, the binding distances display a comparable accuracy and the computational cost of a PBE0 calculation can be significantly higher than PBE, due to the fraction of EXX. For solids, PBE still represents a better method for computing the cohesive energies, while PBE0 improves the equilibrium lattice constants and the bulk moduli [63, 64]. Another type of hybrid functionals that emerged recently are the screened hybrids, as the HSE03 [65], proposed by Heyd, Scuseria and Ernzerhof in 2003. Here, the Coulomb interaction is partitioned into a short range (SR) part and a long range (LR) part. The inverse screening length ω, called also the range-separation parameter, is introduced to control the extent of the two parts. The error function is then used to determine the range separation. The partitioning is applied to the exchange terms in Equation 3.25. The purpose of this procedure is to approximate the EXX, the term responsible for a large part of the computational cost. EXX is a complex term to calculate because of the non-local and long-range contributions, therefore, for extended systems as solids, EXX limits the applicability of the hybrid functionals [65]. Considering, for example, the screened-hybrid functional HSE, the complicated long-range part of the EXX is neglected. To balance this choice, the long-range exchange of PBE is considered without the weight factor α. The expression for the HSE functional is

$$E_{\mathrm{xc}}^{\mathrm{HSE}}[n] = \alpha E_{\mathrm{x}}^{\mathrm{SR}(\omega)}[n] + (1-\alpha) E_{\mathrm{x}}^{\mathrm{PBE,SR}(\omega)}[n] + E_{\mathrm{x}}^{\mathrm{PBE,LR}(\omega)}[n] + E_{\mathrm{c}}^{\mathrm{PBE}}[n]\,, \qquad (3.26)$$

where the last term is the full PBE correlation. A popular version of the HSE functional is the HSE06 [66], a revision of the HSE03, where $\alpha = 1/4$ and $\omega = 11\,\mathrm{Bohr}^{-1}$. The screened-hybrid functionals have been employed extensively in the last years, resulting in performances similar to the hybrid functionals [63–66], but with a sensible reduction—about ten times less—of the computational cost. Considering solid systems, in particular semiconductors, HSE06 improves the PBE description of cohesive energies and band

gaps. On the other hand, in the case of metals, PBE performs much better than HSE06, which shows an overestimation of the cohesive energies (as with LDA), due to the presence of EXX [67]. The effects of EXX are reflected into the electronic properties too, lowering the molecular LUMO and increasing the band gap in semiconductors. For the same reason, the metallic bands are shifted down, in particular the fully occupied ones. As a consequence, other electronic properties can be affected, as the workfunctions, that are typically lowered [68]. All these effects are important in case of surfaces interacting with adsorbed molecules. For such complex systems, HSE06 performs well, similarly to PBE0, outperforming B3LYP. However, in comparison with PBE, which is devoid of such complex non-local and long-range contributions, the hybrid functionals can improve the adsorption distances, but can also lead to the wrong absorption site order and tend to overestimate the adsorption energies [68, 69].

The Meta-Generalized Gradient Approximation

The third rung of Jacob's Ladder of DFT is obtained by adding contributions beyond the density and the first-order density gradient, used in the GGA functionals. These functionals are called meta-GGA (MGGA) and contain higher-order density gradient, as well as other semi-local terms. The general form of a MGGA functional is

$$E_{\mathrm{xc}}^{\mathrm{MGGA}}[n] = \int \epsilon_{\mathrm{xc}}^{\mathrm{MGGA}}(n(\mathbf{r}), \nabla n(\mathbf{r}), \tau(\mathbf{r}), \mu(\mathbf{r}), \ldots, \gamma(\mathbf{r}))\, n(\mathbf{r})\, d\mathbf{r}\,, \tag{3.27}$$

where the terms after the gradient of the density are other semi-local terms that could be used in MGGAs. Among all terms, the first one, $\tau(\mathbf{r})$, is the non-interacting kinetic energy density, see the first term in Equation 3.14a. It has been demonstrated that, in the context of MMGA, $\tau(\mathbf{r})$ and the Laplacian of the density ($\nabla^2 n(\mathbf{r})$) carry the same contributions [70]. The construction of a MGGA functional is, in principle, subject to the same conditions of the GGA family. In addition to that, the presence of new terms leads to additional constraints. In particular, the presence of $\tau(\mathbf{r})$ adds the dependency on the kinetic energy density into the enhancement factor. This can be conveniently used to recover some conditions, as the limit of HEG in case of slowly varying density, absent in most semi-empirical functionals.

A well-known MGGA is the functional of Tao, Perdew, Staroverov and Scuseria (TPSS) [71], a non-empirical functional designed for both molecules and solids, which includes the contributions of the kinetic energy density. The TPSS functional provides results comparable with PBE0 [71], with the advantage of being easily evaluated for solids. The atomization energies and the properties of solids, as the lattice constants and the bulk moduli, can be improved with respect to GGAs. On the other hand, the cohesive energies of solids present the same accuracy of PBE [55]. Another example of MGGA is the M06-L [72, 73] functional, which has been widely employed, together with its numerous extensions [74]. The exchange part of the M06-L is based on the exchange energy density of both LDA and PBE, with the addition of mixing factors that depend

on the kinetic energy density $\tau(\mathbf{r})$. The uniform electron gas correlation energy density, modulated with functions of $\tau(\mathbf{r})$, is used to compute the correlation part. Several parameters are used in the M06-L functional and are optimized by fitting the data of a training set [72]. This functional yields good atomization energies, as well as bond lengths and cohesive energies of semiconductors and transition metals [73, 74]. In this regard, M06-L outperforms other meta-GGA and hybrid-GGA functionals, as B3LYP. The M06-L functional can be modified with the addition of the non-local HF exchange and a reparametrization of the M06-L exchange-correlation part, leading to the M06-HF [75] functional. The M06-HF is free of self-interaction error at long distances, *i.e.* the correct long-range asymptotic trend $1/r$ is guaranteed. MO6-HF established good performances in modeling the excited electronic states of well separated fragments [75]. Particularly successful results are found for charge-transfer states. However, the inclusion of the non-local exchange part increases the computational costs and limits the applicability of the functional. As a last example, we mention the recently developed strongly-constrained and appropriately normed semi-local density functional (SCAN) [76]. This meta-GGA obeys all the possible exact constraints and has been normed on rare-gas atoms and non-bonded interactions. The computational cost of SCAN, applied to molecular systems, is slightly higher than PBE. SCAN provides nearly exact results for rare-gas atoms and very good binding energies for various sets of interacting molecules, outperforming PBE and other computationally more expensive meta-GGA functionals [76]. For example, PBE yields a MAE for the S22 database of ~ 120 meV, while SCAN is below 40 meV. Moreover, SCAN describes well the energetics of both covalent and metallic solids and is also able to capture the vdW interactions [77]. This functional predicts, for example, the correct energetic ordering of the four low-energy water hexamers, with binding energies in good agreement with CCSD(T) calculations.

Despite the numerous and different XC functionals presented in the last two sections, a clear and uniform solution that improves the GGAs is absent. The overall good performances of GGAs, as PBE, still represent an attractive choice, especially because the modest computational cost, that allows to study very large systems, is joined with overall satisfactory results. On the other side, the approximations of GGAs XC functionals can lead to large errors. The SIE (Section 3.4.1) is probably the most important limitation, responsible for large errors in the electronic structure of systems with interactions between localized and delocalized states, as with rare earth metals. Also, the inclusion of EXX can be important in determining the band gap, affecting properties as the charge transfer between two fragments or between a surface and an adsorbate. Resorting to more complex functionals might help in some situations, as discussed above, but a general remedy for a systematic improvement is absent. First, the computational cost of a functional usually grows with its complexity. Second, several XC functionals beyond GGAs are parametrized with respect to reference experimental data. Thus, they can provide excellent results for specific classes of systems, but lack of a broad transferability. Moreover, it is important to keep in mind that the starting point of all the XC functionals presented above is the electron gas of slowly varying density. Therefore, the XC effects

cannot be correctly predicted where this assumption is essentially wrong. One well-known example are the van der Waals interactions between two non-overlapping fragments [78].

3.6 The Random-Phase Approximation

The good performances and the computational efficiency of some of the aforementioned XC functionals, as LDA or PBE, are the major contributions to the success of DFT as a prominent modeling method to investigate the electronic structure. Nevertheless, these functionals are built upon semi-local approximations, which have many known limitations. On the opposite, one can start the quest for the ideal functional by considering the formally exact expression for the exchange-correlation functional. This is the ACFD formula, discussed at the end of Section 3.3 (details in Appendix B.3). Alternatively, as also mentioned in the last part of Section 3.3, the formally exact representation of the many-body problem can be achieved from KSPT. However, within the ACFD formalism the ground-state electron density is kept constant along the adiabatic path, from the KS system to the fully interacting one. The exact XC expression can be formulated in term of the exchange-correlation hole (or also the pair-correlation function) that contains the fluctuation of the electron density $\delta\hat{n}(\mathbf{r})$ around the expectation value $n(\mathbf{r})$. The density fluctuations are then linked to the linear density response function $\chi(\mathbf{r},\mathbf{r}',\omega)$ of the system, which represents the response of the density at point $\mathbf{r}'$ due the presence of an electron at point $\mathbf{r}$. Such connection is obtained through the zero-temperature fluctuation-dissipation theorem (FDT), a technique developed in statistical physics. Finally, the combination of these two steps, gives the adiabatic-connection fluctuation-dissipation (ACFD) expression for the XC energy,

$$E_{\text{xc}} = \frac{1}{2}\int\int v(\mathbf{r},\mathbf{r}')d\mathbf{r}\,d\mathbf{r}'\int_0^1\left[-\frac{1}{\pi}\int_0^{+\infty}\chi_\lambda(\mathbf{r},\mathbf{r}',i\omega)-\delta(\mathbf{r}-\mathbf{r}')n(\mathbf{r})d\omega\right]d\lambda\,, \quad (3.28)$$

where $v(\mathbf{r},\mathbf{r}')=\frac{1}{|\mathbf{r}-\mathbf{r}'|}$ and $\chi_\lambda(\mathbf{r},\mathbf{r}',i\omega)$ is the imaginary part of the response function of the λ-scaled system. In this way the XC functional is rewritten in terms of the response function. The density response function χ_λ is related to the non-interacting response function $\chi_0(\mathbf{r},\mathbf{r}',\omega)$ *via* the self-consistent Dyson-like screening equation

$$\begin{aligned}&\chi_\lambda(\mathbf{r},\mathbf{r}',i\omega)=\chi_0(\mathbf{r},\mathbf{r}',i\omega)+\\&+\int\int\chi_0(\mathbf{r},\mathbf{r_1},i\omega)\left[\lambda v(\mathbf{r_1},\mathbf{r_2})+f_\lambda^{\text{xc}}(\mathbf{r_1},\mathbf{r_2},i\omega)\right]\chi_\lambda(\mathbf{r},\mathbf{r}',i\omega)d\mathbf{r_1}d\mathbf{r_2}\,, \quad (3.29)\end{aligned}$$

where f^{xc} is the exchange-correlation kernel, an unknown quantity which needs to be approximated.

Although exact, the ACFD formula depends on the response function along the adiabatic path (χ_λ), which is unknown. Therefore, at this stage, approximations of the response function should be introduced. In this context, the simple choice of setting

the XC kernel to zero, $f_\lambda^{\rm xc} = 0$, leads to the random-phase-approximation (RPA), the fifth rung of the Jacob's ladder. This idea was developed since the 1950s, in the field of quantum electrodynamics, in a series of seminal works of Bohm, Pines, Gell-Mann and Brueckner. RPA can be obtained, as already mentioned at the end of Section 2.6.1, using the RSPT or also with an approximation of the coupled-cluster method. The different derivations, along with the one mentioned above and related to DFT, give an idea about the versatility of this approximation. The RPA, employed within the DFT framework [79–81], offers several important features: i) the EXX is included, solving the SIE, ii) the screening is taken into account, iii) is a parameter-free approximation, iv) the energy is fully non-local and includes long-range van der Waals interactions between non-overlapped electron densities in a seamless way. In order to obtain the RPA expression from Equation 3.28, the XC energy is conveniently separated into an exchange part, written in terms of the non-interacting response function, and a correlation part. Naturally, the exchange corresponds to EXX, written in Equation 3.21. The Dyson-like equation without the XC kernel, is then inserted into the correlation part, which contains both χ_λ and χ_0. Finally, the integral over λ can be performed analytically, giving [28, 82]

$$E_{\rm c}^{\rm RPA} = \frac{1}{2\pi} \int\int d\mathbf{r} d\mathbf{r}' \int_0^{+\infty} \left[\ln\left(1 - \chi_0(\mathbf{r}, \mathbf{r}', i\omega) v(\mathbf{r}, \mathbf{r}')\right) + \chi_0(\mathbf{r}, \mathbf{r}', i\omega) v(\mathbf{r}, \mathbf{r}') \right] d\omega \,. \tag{3.30}$$

The form of the response function χ_0 for the system of non-interacting particles ($\lambda = 0$) is usually computed by considering the occupied and the unoccupied KS orbitals $\{\psi_i\}$, as well as their orbital energies

$$\chi_0(\mathbf{r}, \mathbf{r}', i\omega) = \sum_{ij} \sum_{\sigma,\sigma'} \frac{(f_i - f_j)\psi_i^*(\mathbf{r}, \sigma)\psi_j^*(\mathbf{r}', \sigma')\psi_i(\mathbf{r}', \sigma')\psi_j(\mathbf{r}, \sigma)}{\epsilon_i - \epsilon_j - i\omega} \,, \tag{3.31}$$

where f_i are the occupation factors.

The RPA performance has been extensively benchmarked for molecular systems, investigating not only the atomization energies [83, 84], but also other properties as the dissociation [85]. Specialized reviews on RPA are available, in which the theoretical background is presented along with exhaustive results and comparisons with other XC schemes. We refer, in particular, to the work of Ren *et al.* [28]. The RPA applied to solids, both semiconductors and metals, as well as surfaces, leads to remarkably good lattice constants and bulk moduli [86], improving the results of conventional semi-local XC functionals. Notably, excellent results are obtained for weakly bonded systems, like graphite [87], where the binding energy and the interplanar spacing predicted with RPA agree very well with the experimental data. Considering other weakly bonded systems, RPA yields good performances for the S22 database [88], a set that contains a variety of noncovalent interactions. Here, the RPA binding energies are underestimated [4], but improve significantly the performances of PBE or PBE0 [89], two functionals without vdW interactions. In general, the improvement over semi-local functionals is not guar-

[4] The reference values for the binding energies of the S22 database are obtained with the CCSD(T) method.

anteed in case of atomization energies [83], as well as cohesive energies [86], where RPA systematically yields underestimated values. This issue, known as "The RPA atomization energy puzzle", is mainly attributed to the fact that RPA is not accurate for short-range correlation. For this reason, several extensions have been proposed, *e.g.* the RPA+ [90]. In this scheme the correlation of a chosen semi-local functional is subtracted to the correlation of RPA, computed within that functional, in order to evaluate the missing short-range correlation in E_c^{RPA}. A second variation of standard RPA is obtained with the inclusion of the second-order screened exchange SOSEX [91], an infinite sum of diagrams that compensate for part of the short-range correlation problem of RPA. Another term that can be added is the single excitation (SE) [89], which is absent by construction in HF theory, but needs to be considered in DFT. Finally, we mention that approaches beyond the RPA approximation ($f_\lambda^{\mathrm{xc}} = 0$), have been considered as well [92]. Unfortunately, these remedies, although they improve certain properties, lead to a non-uniform behavior. For example, SOSEX improves the description of atomization energies, but worsens the dissociation of diatomic molecules [93].

In conclusion, RPA and its different flavors represent a very strong and reliable methodology that can be applied to systems of about hundred atoms. The technique provides high accuracy, without relying on some fortuitous cancellations between different errors, as can happen in some non-local XC functionals. Current studies are focusing on reducing the scaling of RPA and/or producing RPA-based schemes with good performances and a modest computational cost. On the other hand, even in the most efficient implementations, the correlation part of RPA, written in Equation 3.30, presents a $O(N^4)$ scaling. This factor needs to be added on top of the HF or DFT calculation, which is coupled with RPA. Moreover, there are other limitations due to practical constraints. First, RPA forces have been recently implemented in few electronic structure codes. However, their high computational complexity limits the geometry optimization to small systems. For this reason, it is a common practice to relax the geometries with other XC functionals. Second, RPA calculations are performed in a post-process way. In practice, the KS single-particle orbitals, obtained from a converged DFT calculation, are the input for a one-shot RPA calculation. Although self-consistent implementations are available, the numerical cost of such calculations is still prohibitive. Overall, the most popular and successful XC functionals remain competitive because of the possibility to treat large systems with a moderate cost.

As discussed above, RPA describes very well weakly bonded systems and captures vdW interactions. Inspired by this, many vdW-enabled functionals are essentially based on the RPA. One example is the van der Waals density functionals (vdW-DFs), discussed in Section 5.4. However, these functionals differ in their way to construct the response function.

3.7 Green's Functions

The many-body problem can be reformulated using the concepts of Green's function and self energy. This section is dedicated in particular to the GW method, a set of self-consistent equations employed to evaluate these two objects. The Green's function G is, in general, a solution to a linear ordinary differential equation. In particular, considering a differential operator L, a Green function is the solution of the equation $L(G) = \delta_s$, for each point (or point-like) source s. Then, the convolution of the Green's function G with the source f, gives u, the solution of the inhomogeneous differential equation $L(u) = f$. Even though Green's function methods are not strictly related to this work, later on we are going to present calculations obtained with the GW method. A brief introduction here would facilitate their analysis and comprehension. The overview on Green's functions given here is meant to provide to the reader the fundamental concepts and tools of this reformulation of the many-body problem, a popular alternative to the wavefunction- or density-based methodologies, illustrated in the previous chapters. More complete and rigorous treatments on this matter are found in textbooks specialized in many-particle physics, as the one of Fetter and Walecka [94]. We will also discuss, in the final part of this section, the tight connection between RPA and GW.

In many-body-theory, the single particle Green's function, called also propagator, describes the probability amplitude of the propagation of a particle in an N-particles system. The Green's functions are written in terms of annihilation ψ and creation $\psi^\dagger$ operators, within the second quantization formalism. Let Ψ_0 be the ground-state of a N-electron system with Hamiltonian H, the single-particle Green's function is defined as

$$iG(\mathbf{r}\sigma t, \mathbf{r}'\sigma' t') := \langle \Psi_0 | T\left[\psi(\mathbf{r}\sigma t)\, \psi^\dagger(\mathbf{r}'\sigma' t')\right] | \Psi_0 \rangle \,, \tag{3.32}$$

where T is the time-ordering operator: if $t > t'$ the ordering $\psi\, \psi^\dagger$ is kept, while if $t < t'$ a permutation is performed, with sign -1 to account for the fermionic nature of the particles. The creation and annihilation operators depend on time and are written here in the Heisenberg representation. The time-ordering can be written in terms of the Heaviside step functions $\Theta(t - t')$ and $\Theta(t' - t)$, instead of using the more compact form given above. At this point, it is possible to insert between ψ and $\psi^\dagger$ the complete set of eigenstates in the Fock space of the Hamiltonian H. The presence of creation and annihilation operators changes the inserted eigenstate by either adding or removing a particle. The completeness relation of the Fock space allows to simplify to zero the products between two different eigenstates. Consequently, apart from Ψ_0, only two eigenstates survive, associated with $N \pm 1$ Hilbert spaces. At this point one can consider the explicit form of ψ and $\psi^\dagger$ and write the eigenvalues associated to the Hilbert spaces, present in Equation 3.32. The Fourier transform of such expression gives an alternative

form of the single particle Greens' function, called Lehmann representation [95],

$$G(\mathbf{r}\sigma,\mathbf{r}'\sigma',\omega) = \sum_n \frac{\langle\Psi_0|\psi(\mathbf{r})|\Psi_n^{N+1}\rangle\langle\Psi_n^{N+1}|\psi^\dagger(\mathbf{r})|\Psi_0\rangle}{\omega - E_n^{N+1} + E_0 + i\eta} + \\ + \sum_n \frac{\langle\Psi_0|\psi^\dagger(\mathbf{r})|\Psi_n^{N-1}\rangle\langle\Psi_n^{N-1}|\psi(\mathbf{r})|\Psi_0\rangle}{\omega + E_n^{N-1} - E_0 - i\eta}\,, \tag{3.33}$$

following the definition of Fourier transform of $\Theta(t)$, η has to be considered in the limit $\eta \to 0^+$. The denominators in Equation 3.33 shows that the poles of the Green's function correspond to the energy differences between the ground-state energy E_0 and the energy of $N \pm 1$ electronic states. The four brackets contain a creation or annihilation operator and are called Lehmann amplitudes. They describe the probability amplitude related to the addition/removal of one electron to/from the ground-state of the N-particle system. The Lehmann (or spectral) representation is important also because connects the Green's function with measurable physical properties. For example, the spectral function is just the integrated imaginary part of the (contracted) Green's function. With the photoemission spectrum, one can obtain information about excitation processes, the energy of collective and quasi-particle excitations and their lifetime. The latter corresponds to the inverse of the broadening of the quasi-particle state.

Given a N-body system interacting with the electronic Hamiltonian H_e, it is possible to evaluate the equation of motion of the interacting Green's function. This procedure is known since early 50s and leads to the Schwinger-Dyson equations, the equivalent in quantum-field theories of the Euler-Lagrange equation. Since the Hamiltonian involves one and two bodies, the equation of motion contains both one- and two-particle Green's functions (G_2). This formulation can be simplified and the two-particle Green's function is removed with the introduction of an additional quantity, the self-energy (Σ). Briefly, the term that contains G_2 and the Coulomb potential is substituted with another one that depends on $G_0(\mathbf{r}\sigma t, \mathbf{r}'\sigma' t')$ and Σ (with the Hartree potential). The self-energy contains the many-body interactions expanded as an infinite series of several different diagrams, connected through unperturbed Green's functions G_0.

In this sense, this formalism traces a parallel with the perturbation theory, seen in section 2.6. We saw that in the RSPT the various interactions can be represented with Goldstone diagrams, as in the example of the MP2 approximation. Here, the Feynman diagrams [96] are employed to represent the self-energy processes. These famous diagrams can describe several different interactions and are widely used, for example, in quantum electrodynamics (QED). In the particular case of the many-body Hamiltonian with interactions between identical particles *via* a two-body potential, all diagrams are constructed using two basic components: arrows and wavy lines. The former indicates an unperturbed Green's function, the latter represents the electrostatic interaction. Among all diagrams, the disconnected ones cancel out as a consequence of the Wick's theorem [94]. We avoid now to go into further details about the rules of construction and evaluation of the Feynman diagrams.

At this point G, the Green's function of the interacting systems, is expressed in terms the unperturbed Green's function and the self-energy Σ, which contains all possible diagrams. As an alternative formulation, the self-energy can be expanded as an infinite sum of the same set of diagrams, the *proper* self-energy (Σ^*), connected through non-interacting Green's functions. In this way, G can be computed with the Dyson equation

$$G(x,x') = G_0(x,x') + \int\int G_0(x,x_1)\Sigma^*(x_1,x_1')G(x_1',x')dx_1dx_1' \,, \tag{3.34}$$

where the substitution $x = (\mathbf{r}\sigma, t)$ was used to simplify the notation. The integral is performed over space and time. One can notice that G is now present also on the right side of the equation. The validity of the Dyson equation written above can be verified by substituting the expression of G in the term on the right side. This leads to infinite repetitions of proper self-energy terms, connected through G_0, that sum up to Σ. Suppose now that, for a given system, the exact Green's functions is known, then the total energy can be computed. The formula for the total energy is not unique. However, it is possible to obtain a particularly useful expression that requires only the single-particle Green's function: the Galitskii-Migdal formula.

As one can easily guess, the exact analytical form of the (proper) self-energy is unknown. In 1965 Hedin proposed a recipe that allows the formally exact evaluation of G and Σ [97]. In practice, G depends on Σ and the latter is linked to the screened Coulomb potential and the vertex function. Another quantity, the polarization function, enters the definition of screened Coulomb potential. These five functions are determined with five corresponding equations—called Hedin equations—and are connected together with a complex interdependence. In other words, they are a set of self-consistent integro-differential equations. The solution of the problem is approached with an iterative calculation, starting with the non-interacting Green's function and computing the five equations following a cycle, called Hedin's pentagon. The criterion for convergence can be, for example, the total energy of the system.

The *GW* Approximation

The GW approximation consists in taking a particular approximation of the vertex function that effectively excludes its presence in the set of SC equations. Also, this approximation greatly simplifies the mathematical expression of the remaining four Hedin equations. The name of the approximation comes from the fact that the self-energy is defined as the product of G and the screened Coulomb term W. As mentioned before, the converged G can be obtained from the Hedin equation with a SC procedure, starting with the guess G_0. This method, known as self-consistent GW (sc-GW), has been tested on diatomic or small molecular systems with overall good performances. For example, for ground-state properties, as bond lengths and binding energies, sc-GW compares well with high accuracy methods as the RPA [98]. However, one should consider that sc-GW calculations describe also excited states and are computationally

much more demanding than a perturbative correction of the total energy, as in most of RPA approaches. Moreover, we have already mentioned, that some DFT XC functionals can capture quite well these ground-state properties (Section 3.5). It follows that sc-GW is not the preferred choice, if confined to these applications. On the other hand, a sc-GW implementation can express its full potential when is applied to study the changes in the electron density and the modifications of the electronic properties of ground- and excited-states. Moreover, a self-consistent implementation offers other important features. For example, sc-GW is independent of the initial reference, *i.e.* the starting guess of the SC calculation, which is often taken from a DFT calculation. An extended discussion about both the technical elements and the possible applications of sc-GW can be found in the doctoral thesis of Dr. Caruso [99].

A common practice is to reduce the theoretical consistency of the method and simply perform a one-shot calculation using the GW approximation. One starts with the guess G_0 and performs one single cycle to solve the remaining three Hedin equations. This method, called G_0W_0, turned out to be starting-point dependent, in contrast with sc-GW. Consequently, the accuracy of the results relies on the quality of the initial guess. Some hybrid XC functionals are able to provide remarkably good reference state for the perturbative G_0W_0 approach, giving results even better than sc-GW [100]. In conclusion, the GW method offers good performances with the attractive feature of a description of the excited-states. However, it is still too demanding and applications to large and complex systems are impractical.

GW AND RPA

In terms of Feynman diagrams, the GW approximation consists in the sum of ring diagrams up to infinite order, equivalent to the definition of RPA. However, the comparison between the diagrammatic representations of the two methods should be taken with care, in fact the evaluation of the Goldstone and the Feynman diagrams follows different rules. The expression for the total XC energy, obtained with the ACFD procedure, is written in Equation 3.28 and contains the response function $\chi_\lambda(\mathbf{r}, \mathbf{r}', i\omega)$. This expression can be reformulated in terms of Green's function. For example, the non-interacting response function can be computed as the integral of two non-interacting G_0. After some manipulations, the integrand of E_{xc} is rewritten as the product between the interacting Green's function and the proper self-energy $G(\mathbf{r}\sigma, \mathbf{r}'\sigma', i\omega)\Sigma^*(\mathbf{r}'\sigma', \mathbf{r}\sigma, i\omega)$ or equivalently $G_0(\mathbf{r}\sigma, \mathbf{r}'\sigma', i\omega)\Sigma(\mathbf{r}'\sigma', \mathbf{r}\sigma, i\omega)$. The imaginary part of the frequency is considered. The RPA formula—see Equation 3.30 for the correlation part—was obtained in Section 3.6 by setting the kernel of the response function equal to zero, f_λ^{xc}=0. Here, the equivalent energy expression is obtained by considering the non-interacting Green's function and the GW approximation of the self-energy [28, 101]

$$E_{\text{xc}}^{\text{RPA}} = \int\int d\mathbf{r}d\mathbf{r}' \sum_{\sigma,\sigma'} \int_0^1 \frac{d\lambda}{2\pi\lambda} \int_0^{+\infty} \left[G_0(\mathbf{r}\sigma, \mathbf{r}'\sigma', i\omega)\Sigma^{GW}(\mathbf{r}'\sigma', \mathbf{r}\sigma, i\omega, \lambda)\right] d\omega \,, \quad (3.35)$$

where the proper self-energy depends also on λ, the adiabatic parameter. The energy above contains both EXX and the RPA correlation energy. These two contributions are usually written separately, in this case Σ_{c}^{GW} refers only to the correlation part of the self-energy. By looking at Equation 3.35, one can see that the RPA XC energy is retrieved by considering the GW series of diagrams and omitting the dependency of the Green's function on λ. The energy formula in Equation 3.35 gives the perturbative XC correction energy. This term must be added to the other components of the total energy, obtained using a non-interacting Hamiltonian, such as with HF or KS-DFT. Self-consistent RPA calculations are obtained with a minimization of the total energy functional with respect to the non-interacting input, G_0, built using the KS orbitals. On the other hand, if the energy in Equation 3.35 is computed with the Green's function G and the proper self-energy (both depend on λ), then the sc-GW total energy can be rescued. The interacting Green's function is obtained *via* the Dyson equation, see Equation 3.34, starting from G_0. The total energy functional is then minimized with respect to G and the converged value differs from the one of RPA.

Part II

Van der Waals Interactions

4 Van der Waals Interactions in Atoms and Molecules

As evidenced in Chapter 3, the semi-local approximations underlying current state-of-the-art density functionals allow for a very favorable compromise between achievable accuracy and overall computational cost. At variance with high level quantum chemical approaches or RPA, semi-local DFT methods exhibit quasi-linear scaling with respect to the number of electrons, and are nowadays routinely applied to large scale systems, up to a few thousands atoms. A price to pay for the high efficiency of semi-local DFAs, however, is the lack of non-covalent vdW interactions. In fact, by construction, semi-local XC approximations can hardly capture correlation contributions between non-overlapping electron density fragments. The inherently non-local electronic correlation effects responsible for long-ranged vdW forces therefore demand an alternative description, beyond conventional *nearsighted* approaches.

The existence of non-covalent attractive forces acting between atoms and molecules at large distance is known since the pioneering work of J. D. van der Waals. By observing consistent experimental deviations from the ideal gas law, van der Waals proposed a modified equation of state, accounting for the excluded atomic volume and including an effective attractive interparticle potential. This attractive contribution was empirically shown to scale like R^{-6} in terms of the interparticle distance R, compatibly with the well-known Lennard-Jones expression. The physical origin of vdW forces, however, was explained starting in the second part of the 20's with the work of London, after the advent of quantum mechanics. The seminal work of London opened *de facto* a novel research field, and strongly influenced the later developments of such diverse areas as surface science, biophysics and nanoscience. Major contributions to this field came in the following decades also from other scientists—among the others Heitler, Wang, Casimir, Polder and Lifshitz—who explored dispersion interactions between atoms, molecules, surfaces and macroscopic systems, opening the way to the modern understanding of vdW forces. Clearly, the accurate treatment of dispersion forces is an extremely challenging task, which ideally requires the knowledge of all correlation effects arising in many-particle systems. In this context, the inclusion of vdW interactions within the DFA framework is highly desirable. This corresponds to augmenting approximate XC functionals via inherently non-local terms, as proposed by several authors in the last

years. In this Chapter we will present some of the most successful schemes, starting from the seminal formula proposed by London. More elaborate methods will be subsequently introduced, finally including those many-body effects that turn out to be crucial for a chemically accurate description of large-scale systems.

As first understood by London in the 30's, dispersion forces have a quantum mechanical origin, and arise from instantaneous fluctuations of the electronic clouds that surround atoms and molecules. For this reason, dispersion interactions are ubiquitous, and arise even in charge neutral systems in the absence of permanent electric multipoles [102], where classical electrodynamic interactions are vanishing. The general equations that describes intermolecular interactions for well-separated fragments can be straightforwardly derived from Rayleigh-Schrödinger perturbation theory (see Section 2.6). Considering two molecules/fragments A and B, the interaction energy at the second perturbative order contains three different terms, namely

$$E_{\rm int} = E^{(1)}_{\rm el} + E^{(2)}_{\rm ind} + E^{(2)}_{\rm disp} \,. \tag{4.1}$$

Here the first contribution describes the classical multipole–multipole electrostatic energy. The second and third terms, instead, represent the induced (Debye) interaction and London dispersion. Their expression is analogous to the second-order correction to the HF energy (Equation 2.38)

$$E^{(2)}_{\rm ind} + E^{(2)}_{\rm disp} = -\sum_{m,n} \frac{\left|\langle \Psi^A_0 \Psi^B_0 | \frac{1}{r_{12}} | \Psi^A_m \Psi^B_n \rangle\right|^2}{E^A_m + E^B_n - E^A_0 - E^B_0} \,, \tag{4.2}$$

where Ψ^A_0 is the ground-state of the molecule A, Ψ^A_m refers to the m-th excited state, and E^A_m is the corresponding eigenenergy.

The induced interaction energy is the part of Equation 4.2 that describes the interaction between a molecule A characterized by a permanent electric dipole (or multipole) in its ground-state, $\rho^A_0(1) = \langle \Psi^A_0(1) | \Psi^A_0(1) \rangle$ and a second non-polar molecule B. The static electric field generated by the dipole (or multipoles) of atom A, causes a transition to an excited state $\rho^B_{n0}(2) = \langle \Psi^B_n(2) | \Psi^B_0(2) \rangle$ (polarization) in B, resulting in a net attractive force. Without loss of generality, in this example the molecule A is kept in its ground-state, and the sum over its index m is suppressed. The denominator is simplified accordingly and only the difference $(E^B_n - E^B_0)$ survives.

We consider now the interactions between molecules at large distances. The energy can be conveniently represented by exploiting a multipolar expansion of the Coulomb potential, given in powers of $1/R$. For instance, the dipole-dipole induction interaction is obtained by substituting in Equation 4.2 the Coulomb interaction with the electrostatic potential of two interacting permanent dipoles. The resulting contribution is just the dipole–induced dipole interaction energy, averaged over space. Clearly, since all configurations are equally probable, a straightforward average over all possible dipole orientations would give a vanishing overall interaction. For this reason the probability of

each dipole orientation should be weighted according to the corresponding Boltzmann factor. In the limit of low energy, the average energy squared, *i.e.* the numerator of the above, reads: $\langle E^2_{\text{d–d}} \rangle = \frac{2}{3} |d^B_{n0}| \, |d^A_0| \, R^{-6}$, where d is the dipole moment.

The second term in Equation 4.2 is the dispersion contribution. This is defined as the interaction between mutually induced charge fluctuations arising from the instantaneous quantum mechanical excitations of the valence electrons. At large distances, the dispersion interaction can again be expressed via a multipolar expansion, as a series in inverse powers of R:

$$E_{\text{vdW}} = -\sum_{n=6}^{\infty} \frac{C_n}{R^n} \,, \quad \text{with only even values of } n \,. \tag{4.3}$$

The first term of the series, proportional to $1/R^6$, corresponds to the induced dipole–induced dipole interaction, and typically represents the leading contribution. The two following terms decay as $1/R^8$ and $1/R^{10}$. The former describes the mutually induced dipole–quadrupole interaction, while quadrupole–quadrupole and dipole–octopole interactions are accounted for in the latter. We note that the first term of the dispersion interactions is always proportional to $1/R^6$ for finite size fragments, which indicates the inherently quantum mechanical nature of dispersion. By considering for instance two molecules with no permanent dipole and quadrupole, the leading term in the electrostatic interaction will be at least the octopole–octopole ($\propto 1/R^7$). Similarly, the first non-zero term for induction interactions will be the dipole–octopole, which is proportional to $1/R^{10}$. In contrast, the transient quantum-mechanical fluctuations of the electron density will always induce a $\propto 1/R^6$ dipole–dipole interaction, regardless of the symmetry. We note in passing that it is also possible to express the dispersion interactions between separate fragments (Equation 4.2) with a perturbative expansion beyond the second order. For instance, the third order of the perturbation series relates three fragments through a $\sim R^{-9}$ power law expression, the so-called Axilrod–Teller–Muto term [103].

Coming back to the second order term of the dispersion interactions, it is interesting to express the leading dipole-dipole contribution in terms of the dipole matrix elements d_{n0}, in analogy to induction interactions. By assuming that the fragments A and B are isotropic, one derives the following formula

$$E^{(2)}_{\text{disp}} = -\frac{C_{6,AB}}{R^6} \,, \quad \text{with } C_{6,AB} = \frac{2}{3} \sum_{\substack{m\neq 0 \\ n \neq 0}} \frac{|d^A_{m0}|^2 \, |d^B_{n0}|^2}{\omega^A_{m0} + \omega^B_{n0}} \,, \tag{4.4}$$

where $\omega^A_{m0} = E^A_m - E^A_0$ is the transition frequency. From this expression (in the isotropic approximation), we observe that the key quantities for the computation of $E^{(2)}_{\text{disp}}$ are the excitation energies and the dipole oscillator strengths associated to transitions of the type $0 \rightarrow m$. Since the evaluation of $C_{6,AB}$ would require the knowledge of both ground and excited states, a straightforward application of the above formula

could be rather cumbersome in practical calculations. A more viable expression for the computation of the C_6 Hamacker constants is the Casimir-Polder formula [104]. The dynamic polarizabilities are used here to express the C_6 coefficients as a frequency integral [1]

$$C_{6,AB} = \frac{3}{\pi}\int_0^\infty \alpha_A(i\omega)\,\alpha_B(i\omega)d\omega\,, \quad \text{with } \alpha(i\omega) = \sum_{m\neq 0}\frac{2}{3}\frac{\omega_{m0}|d_{m0}|^2}{(\omega_{m0}^2+\omega^2)}\,. \tag{4.5}$$

The dynamic polarizabilities used in this definition are averaged and can be measured in experiments. Hence, this last formulation is much more versatile, and it is frequently employed as a starting point for the development of vdW functionals.

Before introducing some of the most popular vdW-corrected DFT-methods, we suggest the reader to refer to specialized literature [105–107], for a general and complete overview about intermolecular and vdW interactions.

4.1 Pairwise Methods

The first term ($n = 6$) in Equation 4.3 represents the starting point for all the *pairwise* vdW methods, where the total vdW energy is expressed as a sum over interatomic contributions and R is the distance between the two atoms. This is probably the simplest approach to describe the correct long-range asymptotic interaction for well separated particles. Within this framework, the vdW energy is simply added to the DFT energy

$$E_{\text{tot}} = E_{\text{DFA}} + E_{\text{vdW}}\,, \tag{4.6}$$

where E_{DFA} is the KS-DFT energy computed with the underlying approximate XC density functional. Pairwise methods differ one from the other in the approximations adopted to compute the C_6 coefficients. Also, each vdW scheme needs to be smoothly merged with the chosen XC functional and the divergence of E_{vdW} for $R \to 0$ has to be cured. These requirements can be handled in different ways. In this work we will largely employ the approach of Tkatchenko and Scheffler [108] (TS) to correct standard DFT XC functionals for the missing vdW interactions (vdW^{TS}).

In pairwise approaches the vdW energy is expressed according to the formula

$$E_{\text{vdW}} = -\frac{1}{2}\sum_A\sum_B \frac{C_{6,AB}}{R_{AB}^6} f_{\text{damp}}(R_{AB}, R_{AB}^0)\,, \tag{4.7}$$

where the indices A and B refer to two atoms and the sums involve the total number of atoms in the system. The interatomic distance between the atoms is R_{AB}, while $C_{6,AB}$ is the dispersion coefficient of the pair. The last term, $f_{\text{damp}}(R_{AB}, R_{AB}^0)$, is the damping function, introduced to avoid the divergence of R_{AB}^{-6} for small interatomic distances. In addition, the damping couples the long-range vdW energy to a given semi-local

[1] The identity $\frac{1}{a+b} = \frac{2}{\pi}\int_0^\infty \frac{ab}{(a^2+x^2)\,(b^2+x^2)}dx$, with $a, b > 0$ is used to rewrite the frequencies.

XC functional via the correlation length, R^0_{AB}, defined as the sum of the atomic vdW radii. The success of pairwise methods in the last years can largely be attributed to the pioneering work of Grimme and coworkers, who introduced the popular methods called DFT-D and DFT-D2 [109, 110]. In the DFT-D the damping function is a Fermi-type function. The C_6 coefficients are obtained assuming the additivity property and taking the average over the possible hybridization states of an atom, using accurate reference values [111]. The DFT-D2 coefficients are re-parametrized based on atomic ionization potentials and static dipole polarizabilities. In this way the number of parameters of the DFT-D method is reduced and the whole procedure loses part of its original empiricism. However, the very low computational cost and the accuracy for small molecules—between 10% and 30% of the interaction energy—are accompanied by two main disadvantages: i) the coefficients are kept fixed, independently of the chemical environment and ii) fitted parameters are present both in the C_6 coefficients and in the damping function.

The DFT-D3 method of Grimme [112] extends the previous functionals introducing the coordination number. The coefficients are computed with *ab initio* time-dependent DFT (TDDFT) calculations for each pair, taking into account the different hybridization states. Then the covalent radii are used to obtain the pair coordination numbers in the system. The reference C_6 of the pair is finally interpolated depending on the coordination numbers, providing the response of the atomic charge due to the environment that surrounds the atom. In the DFT-D3 method the damping function has been revised too and the vdW radii are used as cutoff parameters for the dispersion energy. A set of 174 pair coefficients of common molecules has been used to test the DFT-D3 method, giving a mean absolute relative error (MARE) of 8.4%.

An alternative approach that includes the dependence of the environment is the exchange-dipole moment (XDM) method proposed by Becke and Johnson [113–115]. In the XDM method the instantaneous dipole is computed as an asymmetry of the exchange hole, based on HF or KS orbitals and the electron density of the system. The C_6 coefficients are obtained combining the estimated dipoles with tabulated values for the isotropic polarizabilities. Finally the vdW energy is computed according to Equation 4.7. The Becke-Johnson scheme captures the effects of the environment directly, *via* the exchange hole. This method has the advantage of being free from empirical parameters and fitted coefficients. However, the quality of the results is greatly affected by the actual calculation of the exchange hole, which depends on the input orbitals. In this regard, HF orbitals turned out to be preferable [113] over LDA or GGA KS orbitals because of the lack of long-range effects of the latter. Consequently, the method requires a CPU time comparable to an HF calculation or to hybrid functionals. The method gives good performances for the molecular C_6 coefficients, with a MARE of 12.5%. An improvement of the performances of the Becke-Johnson scheme has been obtained with the inclusion of a damping function, based on atomic correlation energies, in the energy formula. The MARE is reduced to 11.1% for the C_6 coefficients of 174 complexes [114].

The last method that we mention here will be described in detail in the next section

and is the one proposed in 2009 by Tkatchenko and Scheffler [108]. In the TS method, the total vdW energy depends on the electron density $n(\mathbf{r})$ *via* the Hirshfeld weight ($w(\mathbf{r})$) [116], used to partition the total electron density into atomic components. The C_6 coefficients and the vdW radii are environment-dependent and scale accordingly to the Hirshfeld weight. Moreover, the TS functional is a proper functional of the electron density, which is a fundamental prerequisite for the self-consistent implementation, as we will see in the next chapter. The damping function depends only on a single parameter, which is adjusted depending on the XC functional used. The TS method is also very efficient, since all the quantities needed for the TS vdW energy are already computed in a regular DFT calculation. In addition, the TS shows good performances with a MARE of 5.5% for the C_6 coefficients of 1225 intermolecular complexes.

4.2 The Tkatchenko-Scheffler van der Waals Functional

The energy of the functional of Tkatchenko and Scheffler is a sum over pairwise interatomic C_6/R^6 terms computed as in the formula written in Equation 4.7. The method is built starting with the exact expression for the isotropic C_6 that describes the vdW interactions between two well-separated fragments: the Casimir-Polder formula, already introduced in Equation 4.5. In order to facilitate the reading of the following mathematical passages, we rewrite that definition of C_6 coefficient

$$C_{6,AB} = \frac{3}{\pi}\int_0^\infty \alpha_A(i\omega)\alpha_b(i\omega)d\omega\,, \tag{4.8}$$

where $\alpha_A(i\omega)$ is the average dynamic polarizability for atom A. As a second step, the polarizability is approximated by retaining only the leading term of the Padé [117] series

$$\alpha_A^1(\omega) = \frac{\alpha_A^0}{1-(\omega/\omega_A)^2}\,, \tag{4.9}$$

where α_A^0 is the static polarizability and ω_A is an effective excitation frequency. The frequency $\alpha_A(i\omega)$ in the Casimir-Polder formula can be replaced with the frequency $\alpha_A^1(\omega)$ (evaluated in the imaginary plane) and the integral is solved analytically. The C_6 coefficient for a pair AB is given by

$$C_{6,AB} = \frac{3}{2}\alpha_A^0\alpha_B^0\frac{\omega_A\omega_B}{(\omega_A+\omega_B)}\,. \tag{4.10}$$

Now, if we consider $A = B$, the effective excitation frequency of A is expressed in terms of the static polarizability and the homonuclear $C_{6,AA}$ coefficient

$$\omega_A = \frac{4}{3}\frac{C_{6,AA}}{(\alpha_A^0)^2}\,. \tag{4.11}$$

The corresponding expression for ω_B is obtained in the same way. Then, both ω_A and ω_B are substituted into the definition of $C_{6,AB}$ in Equation 4.10. In this way we can write a formula for the pair coefficient that depends only on homonuclear parameters

$$C_{6,AB} = \frac{2\, C_{6,AA} C_{6,BB}}{\left(\frac{\alpha_B^0}{\alpha_A^0} C_{6,AA} + \frac{\alpha_A^0}{\alpha_B^0} C_{6,BB}\right)} \,. \tag{4.12}$$

With this simple expression, the C_6 coefficients can be accurately computed using the free-atom parameters, α_A^0 and $C_{6,AA}$. In the TS scheme, these homonuclear values are taken from high-level self-interaction corrected TDDFT reference data [118], which provide an accuracy better than 3% for nonmetallic atoms.

The Hirshfeld Weight

The free-atom parameters can be adapted to model an atom inside a molecule or solid, making the TS an environment-dependent method. First, the free-atom quantities introduced earlier (static polarizability, C_6 and vdW radius) are explicitly renamed here as "free" quantities, while "eff" will refer to the *effective* quantities of an atom inside a molecule. Second, the volume depends linearly on the polarizability [119], where k is the proportional coefficient: $k_A^{\text{free}} \alpha_A^{\text{free}} = V_A^{\text{free}}$. In the TS the factor used to rescale the parameters is the ratio between the effective volume of an atom inside a molecule and its free value. The electron density of the system and the Hirshfeld partitioning of the density [116] are employed to compute the effective volume

$$\frac{k_A^{\text{eff}} \alpha_A^{\text{eff}}}{k_A^{\text{free}} \alpha_A^{\text{free}}} = \frac{V_A[n(\mathbf{r})]}{V_A^{\text{free}}} = \frac{\int r^3\, w_A(\mathbf{r}) n(\mathbf{r}) d\mathbf{r}}{\int r^3\, n_A^{\text{free}}(\mathbf{r}) d\mathbf{r}} = \gamma_A[n(\mathbf{r})] \,, \tag{4.13}$$

in which the free atom spherically averaged reference density is $n_A^{\text{free}}(\mathbf{r})$ and $r = |\mathbf{r} - \mathbf{R}_A|$ is the distance between the (nucleus of) atom A and the point $\mathbf{r}$. Of course the electron density $n(\mathbf{r})$ is taken from DFT calculations. The Hirshfeld partitioning weight of the total charge density into atomic component is defined as

$$w_A(\mathbf{r}) = \frac{n_A^{\text{free}}(\mathbf{r})}{\sum_{i=1}^{N} n_i^{\text{free}}(\mathbf{r})} \,, \tag{4.14}$$

where the sum goes over all atoms in the system. The domain of the integrals in Equation 4.13 can be defined as $\Omega_A := \{\mathbf{r} \mid n_A^{\text{free}}(\mathbf{r}) \geq \epsilon_A^{\text{threshold}}\}$. In practice, the integrals over the volume are performed by running over all grid points, $\mathbf{r} \in$ [Grid points], see last paragraph of Section 6.2. The ratio in Equation 4.13, shortly indicated with $\gamma_A[n(\mathbf{r})]$, takes into account hybridization, Pauli repulsion, and other semi-local XC effects in the construction of these effective quantities for a given "atom-in-a-molecule". Therefore, the inclusion of the electron density allows this method to effectively go beyond the pairwise approximation. Also, the direct dependence on the electron density allows the analytical derivation of the KS potential, employed in the self-consistent implementation,

see Chapter 7.

Additional approximations in the TS method regard the ratio between the free and effective proportional coefficients and the excitation frequencies, that are assumed to be unity. Thus, the effective quantities are determined from the free ones as

$$\alpha_A^{0,\text{eff}} = \gamma_A[n(\mathbf{r})]\,\alpha_A^{0,\text{free}}\,, \tag{4.15}$$

$$C_{6,AA}^{\text{eff}} = (\gamma_A[n(\mathbf{r})])^2\,C_{6,AA}^{\text{free}}\,, \tag{4.16}$$

$$R_A^{0,\text{eff}} = (\gamma_A[n(\mathbf{r})])^{1/3}\,R_A^{0,\text{free}}\,, \tag{4.17}$$

where the rescaling factors are just different powers of $\gamma_A[n(\mathbf{r})]$. The great accuracy of the intermolecular C_6 dispersion coefficients, obtained with the TS scheme, validates the assumptions mentioned above, which break down only with the H_2 molecule. A database of 1225 C_6 for the interaction between atoms and molecules has been considered and the TS scheme provides a MARE of 5.5%.

The Damping Function

The sum of pairwise C_6/R_{AB}^6 terms clearly diverges for small interatomic distances. For this reason the vdW energy formula written in Equation 4.7 includes a damping function $f_{\text{damp}}(R_{AB}, R_{AB}^0)$. Another motivation for using the damping is to minimize the overlap between the short-range correlation contributions of the semi-local XC functional and the ones of the vdW functional. Therefore, the damping function should assume the two liming values of one at large distances and zero at short distances. Several different functions are available in the literature, in the specific case of the TS method a Fermi-type function is chosen

$$f_{damp}^{AB}(R_{AB}, R_{AB}^0[n(\mathbf{r})]) = \frac{1}{1+\exp[-d(\frac{R_{AB}}{s_R R_{AB}^{0,\text{eff}}[n(\mathbf{r})]}-1)]}\,, \tag{4.18}$$

where R_{AB} is the interatomic distance and $R_{AB}^{0,\text{eff}} = R_A^{0,\text{eff}} + R_B^{0,\text{eff}}$ is the sum of the vdW radii associated with atoms A and B. Each vdW radius depends on the electron density through the Hirshfeld volume, as written in Equation 4.17. The simplest definition of vdW radius is to take half of the equilibrium distance of rare-gas dimers. For the other elements the definition can be extended by taking as a reference the rare-gas atom in the same row of the periodic table of elements. More precisely, the reference is the electron density contour of this rare-gas atom, evaluated at its vdW radius. Then, the vdW radius of the atom in question is defined as the distance where its electron density contour is equal to the reference.

In this damping function both d and s_R are empirical parameters that need to be determined. The parameter d affects the steepness of the damping. Even though it affects negligibly the results, the value $d = 20$, that corresponds roughly to the average of possible values, has been tested to be the most appropriate. The parameter s_R scales the vdW radii and regulates the extent of the vdW correction for a given XC

functional. In the TS scheme, the parameter is obtained for each functional by fitting the S22 database [88], which contains binding energies of weakly bonded systems. The reference values are computed with the coupled-cluster method with single, double and triple excitations CCSD(T) (see Chapter 2.5.1). The value of s_R associated with the PBE functional, the most frequently used XC functional in this thesis, is $s_R = 0.94$.

5 Van der Waals Interactions Beyond Pairwise Additivity

The vdW methods reviewed in the previous chapter are based on pairwise additivity and represent very efficient solutions for including the missing vdW contributions in the context of semi-local DFA. In addition, some of these methods capture effects beyond the pairwise approximation, such as the electronic hybridization of atoms in molecules, included in the TS [108] (and in the Becke-Johnson [114]) method *via* the Hirshfeld atomic partitioning weight. Nonetheless, all these pairwise methods are unable to capture the inherently many-body nature of vdW interactions, which can result in a strongly collective electronic response (screening).

Many-body vdW effects are commonly regarded as unimportant in small molecular systems. However, recent studies proved that a description of vdW interactions beyond the pairwise limit can have a key role, for example, in the structure, stability, and response properties of molecular crystals at finite temperature and pressure [120]. Moreover, many-body effects are essential in order to achieve chemical accuracy (1 Kcal/mol) for the binding energies of molecular crystals [121], organic molecules [3], or even supramolecular systems (host–guest complexes) [121]. Many-body vdW effects were also found to have a significant role in determining the cohesive properties of solids such as semiconductors and ionic solids [122], or even metals [123]. Moreover, recent calculations confirmed that the many-body effects can have very important role in the adsorption of atoms/molecules on metal surfaces [124, 125]. Also, the collective charge fluctuation modes of the substrate can couple to strongly non-additive vdW contributions at the molecular level, leading to a modification of the molecular polarizability as a function of the size of the molecule [8].

In principle, an accurate approach that describes vdW interactions beyond the pairwise approximation is the RPA, reported in Equation 3.28. As an example, the DFT functional EXX+cRPA combines exact-exchange and RPA correlation (see Equation 3.30). The EXX+cRPA method, when applied to solids, leads to accurate lattice constants and bulk moduli [9]. However, RPA results can exhibit non-trivial dependence on the input orbitals. The EXX+cRPA method is computationally very expensive and its applicability is currently limited to small and medium sized systems (< 100 atoms) [9]. Finally, numerical convergence can represent an issue in EXX+RPA, and the computation of

atomic forces appears rather complex. These issues are strongly alleviated in vdW-inclusive DFT methods. Moreover, recent benchmarking for hybrid molecules adsorbed on metals demonstrated that vdW-augmented DFT methods can provide very accurate equilibrium geometries and adsorption energies, outperforming EXX+cRPA [126, 127]. In addition to that, RPA implementations are, up to now, non self-consistent, *i.e.* the effects of RPA correlation on the electronic properties of the systems are totally neglected. As an alternative to the demanding RPA and RPA-based methods, one could extend the more efficient pairwise methods by including those many-body screening effects present in solids. For instance, the TS vdW functional was recently extended (see Section 4.2) to model ionic solids and semiconductors [122]. In practice, the polarizabilities (and the C_6 coefficients) are re-computed using the Clausius-Mossotti (CM) equation, which relates the polarizability to the dielectric function of the solid. In this way, the long-range electrostatic screening is effectively included into the TS functional. A complete description of the procedure can be found in the Ph.D thesis of Dr. Guo-Xu Zhang [128]. This method has been applied to several solids, as Si, GaAs and NaCl, providing substantial improvement over PBE (and HSE06) cohesive energies, lattice constants and bulk moduli [122].

A particularly relevant approach for this thesis is the extension of the TS pairwise vdW functional, presented in Section 4.2, to model bulk metals and adsorption of atoms/molecules on metallic surfaces, namely the $\mathrm{vdW}^{\mathrm{surf}}$ method [123]. To introduce this method, we will first focus on the vdW interactions arising in metals. Subsequently, we will introduce the theory developed by Lifshitz and by Zaremba and Kohn, which models the vdW interactions between an atom and a metallic surface. Finally, we will describe in detail the $\mathrm{vdW}^{\mathrm{surf}}$ method. In concluding this section, an overview will be given about the derivation of many-body vdW interactions within the adiabatic-connection fluctuation-dissipation (ACFD) theorem formalism (see Appendix B.3) [1], along with a brief description of the most popular vdW methodologies derived from it.

5.1 Van der Waals interactions in metals

The effects of vdW interactions between atoms in noble metals is a long-standing problem. Although the importance of vdW contributions to the cohesive energy is now broadly recognized, the quantitative estimates of their magnitude strongly depend on the adopted theoretical approach, and can typically vary from a few percent [122] up to above one third of the total cohesive energy [129–131]. In the seminal work of Rehr, Zaremba, and Kohn [130] on the vdW cohesive interactions in coinage metals, the ionic polarizabilities due to core states are disentangled from the response of delocalized s electrons, treated as a homogeneous electron gas. This choice yields a dynamically screened interaction between the ions, whose polarizabilities are modeled *via* the Lorenz-Lorenz relation.

[1] This theorem is introduced in the context of DFT in Section 3.6 and described in detail in Appendix B.3.

The starting point is the application of perturbation theory to treat the interactions between the ions and the electron gas, and between the ions only. Let us consider the case of two ions a and b separated by a distance R, immersed in a HEG (e). The total Hamiltonian is written as

$$H = H_0 + H_1 \,, \tag{5.1}$$

where the unperturbed Hamiltonian H_0 includes the two independent ionic contributions, plus a term describing the uncoupled HEG. The perturbation H_1, instead, contains the couplings between the ions and between the ions and the HEG

$$H_1 = H_{ab} + H_{ae} + H_{be} + H_{ee} \,. \tag{5.2}$$

Many-body perturbation theory [94] is then applied to evaluate the effective interaction energy between ions a and b. In the perturbative expansion only a limited set of diagrams is retained, namely the ones corresponding to the second order correlation between the ions, and the electrodynamic screening of inter-ionic interaction due to the surrounding electron gas. The corresponding expression for the dispersion energy is given by

$$E_{\rm disp}(R) = -\int_0^\infty \frac{d\omega}{2\pi} \int\int \chi_a(\mathbf{q},\mathbf{q}',i\omega) V(\mathbf{q}',i\omega) \chi_b(\mathbf{q}',\mathbf{q},i\omega) V(\mathbf{q},i\omega) \frac{d\mathbf{q}}{(2\pi)^3} \frac{d\mathbf{q}'}{(2\pi)^3} \,, \tag{5.3}$$

where $\chi_i(\mathbf{q},\mathbf{q}',i\omega)$ is the Fourier transform of the density-density response function. The contribution of electron–electron interactions in Equation 5.3 is given by $V(\mathbf{q},i\omega)$, which represents the frequency-dependent screened interactions of the form

$$V(\mathbf{q},i\omega) = \frac{v(\mathbf{q})}{\epsilon(\mathbf{q},i\omega)} \,, \tag{5.4}$$

where the numerator is the Fourier transform of the electrostatic Coulomb potential and the denominator is the dielectric function of the HEG, evaluated with the proper polarization insertion [94].

The time-ordered density-density response is now approximated by its leading order term, which is proportional to the ionic polarizability $\alpha_i(i\omega)$,

$$\chi_i(\mathbf{q},\mathbf{q}',i\omega) \simeq -\mathbf{q}\,\mathbf{q}'\, e^{i(\mathbf{q}-\mathbf{q}')R_i} \alpha_i(i\omega) \,. \tag{5.5}$$

Within this approximation only the dipole-dipole contribution of the response function are considered. This approximate expression for $\chi_i(\mathbf{q},\mathbf{q}',i\omega)$ is inserted into Equation 5.3 leading to the following expression for the dipole-dipole dispersion energy:

$$E_{\rm disp}(R) \simeq -\int_0^\infty \alpha_a(i\omega)\alpha_b(i\omega) \left[\left(\frac{\partial^2 V(R,i\omega)}{\partial R^2} \right) + \frac{2}{R^2} \left(\frac{\partial V(R,i\omega)}{\partial R} \right)^2 \right] \frac{d\omega}{2\pi} \,. \tag{5.6}$$

Here the screened Coulomb interaction $V(R, i\omega)$ is the Fourier transform of Equation 5.4,

$$V(R, i\omega) = \int \frac{4\pi}{q^2} \frac{e^{i\mathbf{qR}}}{\epsilon(\mathbf{q}, i\omega)} \frac{d\mathbf{q}}{(2\pi)^3} = \frac{2}{\pi} \int \frac{\sin(qR)}{qR} \frac{1}{\epsilon(\mathbf{q}, i\omega)} \, dq \,. \tag{5.7}$$

Notably, in the limit of very dilute electron gas (or very large frequencies), the dielectric function tends to 1, (absence of screening). Consequently, the expression in brackets in Equation 5.6 reduces to $6/R^6$ and the dispersion energy $E_{\rm disp}(R)$ tends to the pairwise formula for the vdW interactions between atoms and molecules, see Equation 4.4.

The first ingredient needed to evaluate Equation 5.6 is the screened Coulomb interaction, evaluated numerically with RPA calculations. The second ingredient is the frequency-dependent polarizability of the ions. Optical data have been employed to extract the values of $\alpha_i(i\omega)$ in noble metals from the long-wavelength limit of the dielectric function, by subtraction of the free electron contribution. Local field effects are taken into account by approximating the ionic polarizabilities with a Lorenz-Lorenz relation, where the magnitude of the ionic polarizabilities is large at low frequency, and decreases monotonically as a function of ω. An important observation is that the HEG screening is mostly relevant for small values of q, hence it can be well approximated by taking the limit $\epsilon(q \to 0, i\omega) = 1 + \omega_p^2/\omega^2$ [2]. The effect of the conduction-electron screening provides a reduction of a factor 2–3 in the dispersion interactions with respect to calculations with zero screening.

Using this approach, many-body dispersion interactions were evaluated for Cu, Ag and Au *via* Equation 5.6 and with the inclusion of higher-order terms in the expansion of the response function (Equation 5.5), beyond the dipole-dipole approximation. The contributions of higher-order terms were found to be roughly 20% of the leading dipole-dipole term. The calculated dispersion energies are 0.21, 0.42 and 0.63 eV respectively for Cu, Ag and Au [130]. These values corresponds to 6%, 14% and 17% of the total cohesive energy of Cu, Ag and Au, which clearly proves the importance of vdW interactions in the structural stability of coinage metals.

5.2 Atom-Surface van der Waals interactions

This section is dedicated to the theory of dispersion interactions between a neutral atom and a solid surface, also adopted in the $\mathrm{vdW}^{\mathrm{surf}}$ method [123]. In particular we will focus on the microscopic formulation first introduced by Lifshitz [132] and later developed by Zaremba and Kohn [133], generally known under the name of Lifshitz-Zaremba-Kohn theory (LZK). In the discussion below we will follow the formulation of the LZK theory proposed by the latter authors. The geometry under consideration is depicted in Figure 5.1. This corresponds to the physical adsorption of a small particle having negligible charge overlap with the underlying surface. Since relativistic effects become important only for a very large atom–surface distance, they can be safely neglected here.

[2] The plasma frequency is defined as $\omega_p = (4\pi n)^{1/2}$, where n is the electron density.

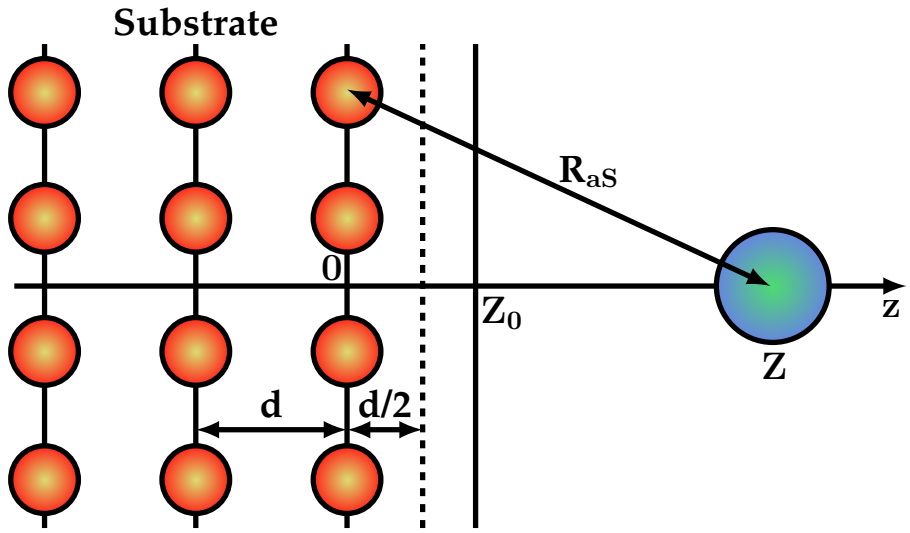

Figure 5.1: Sketched representation of the surface–atom system. The origin of coordinates is the center of the topmost metal layer, z is the axis perpendicular to the metallic surface. The distance atom-solid is indicated by R_{aS}.

The atom-surface system represented in Figure 5.1 is described by the following Hamiltonian

$$H = H_a + H_S + V_{aS}\,, \tag{5.8}$$

where the Hamiltonians of the isolated atom and the solid are H_a and H_S respectively, while the third term, V_{aS}, is the Coulomb interaction between the two subsystems. At this point the Coulomb interaction between the electron density of the atom and the solid is treated *via* a second order perturbative approach (see Equation 4.2). In analogy to Equation 5.3, the interaction energy can be expressed in terms of the density-density response functions, making use of the identity utilized in passing from Equation 4.4 to Equation 4.5 (see the footnote),

$$\begin{aligned} E^{(2)}_{\rm disp} = \; & - \int\int d\mathbf{r}\, d\mathbf{r}' \int\int v(\mathbf{R}+\mathbf{x}-\mathbf{r})\, v(\mathbf{R}+\mathbf{x}'-\mathbf{r}')\, d\mathbf{x}\, d\mathbf{x}' \\ & \times \int_0^{+\infty} \chi^{\rm R}_a(\mathbf{x},\mathbf{x}',i\omega)\chi^{\rm R}_S(\mathbf{r},\mathbf{r}',i\omega)\frac{d\omega}{2\pi}. \end{aligned} \tag{5.9}$$

The coordinate $\mathbf{R}$ indicates the position of the atomic nucleus and corresponds to $\mathbf{R} = (0,0,Z)$ in Figure 5.1, while $\mathbf{R}+\mathbf{x}$ refers to the position of the measured electron density. The Coulomb potentials can be expressed using the two-dimensional Fourier transform.

$$v(\mathbf{R}+\mathbf{x}-\mathbf{r}) = \sum_{\mathbf{q}} \frac{2\pi}{q} e^{i\mathbf{q}(\mathbf{R}+\mathbf{x}-\mathbf{r})}\, e^{-q|R_z+x_z-r_z|}\,, \tag{5.10}$$

where the wave vector $\mathbf{q} = (q_x, q_y, 0)$ is a 2D vector in the plane of the surface. Each one of the scalar products between the real space vectors and $\mathbf{q}$ in the first exponential

generates two terms, corresponding to the x and y directions along the surface plane. Having assumed no overlap between the atom and the solid, the Coulomb potential decays exponentially away from the surface.

At this point Equation 5.9 can be rewritten by expanding the exponentials of the two Coulomb potentials and defining the complex wave vector $\mathbf{k} = \mathbf{q} + iq\hat{z}$

$$E^{(2)}_{\text{disp}} = \int_0^{+\infty} \frac{d\omega}{2\pi} \sum_{\mathbf{q},\mathbf{q}'} \left(\frac{2\pi}{q}\right) \left(\frac{2\pi}{q}\right) e^{-Z(q+q')} e^{i\mathbf{R}(\mathbf{q}-\mathbf{q}')} A(\mathbf{x},\mathbf{x}',i\omega)\, S(\mathbf{r},\mathbf{r}',i\omega)\,. \quad (5.11)$$

Here $A(\mathbf{x},\mathbf{x}',i\omega)$ contains the response function of the adatom, together with the related exponentials and the double integration, while $S(\mathbf{r},\mathbf{r}',i\omega)$ is the analogous surface term. The periodicity of the surface allows to express $\mathbf{q}'$ as $\mathbf{q}' = \mathbf{q} + \mathbf{G}$, where $\mathbf{G}$ is the reciprocal lattice vector in the plane of the surface. For $\mathbf{G} \neq 0$, the first exponential in Equation 5.11 rapidly decays away from the surface, *i.e.* for large Z. The summation over $\mathbf{q}'$ can thus be restricted to the first Brillouin zone, where $\mathbf{G} = 0$. With the substitution $\mathbf{q}' = \mathbf{q}$ in Equation 5.11 the first exponential reads $\exp(-2qZ)$ and effectively cuts off the q summation at $q \sim 1/Z$. The second exponential, instead, reduces to 1 given that the corresponding exponent is equal to zero.

The exponentials in the integral over the atomic coordinates, included into $A(\mathbf{x},\mathbf{x}',i\omega)$, can be expanded if Z is much larger than the size of the adsorbate, leading to

$$A(\mathbf{x},\mathbf{x}',i\omega) = \int\int e^{i\mathbf{k}\mathbf{x}}\, e^{-i\mathbf{k}^*\mathbf{x}'} \chi^{\text{R}}_a(\mathbf{x},\mathbf{x}',i\omega)\, d\mathbf{x}\, d\mathbf{x}' = 2q^2\alpha(i\omega) + \mathcal{O}(q^4)\,, \quad (5.12)$$

where α is the frequency-dependent atomic polarizability. Higher order terms with even powers of q correspond to higher-multipole polarizabilities. On the other hand, the first order expansion brings a factor q^2 in Equation 5.11 which cancels out the two q factors coming from of the two Coulomb potentials.

The factor $S(\mathbf{r},\mathbf{r}',i\omega)$ is now written by separating the integral over z and z' from the two 2D integrals over the surface

$$S(\mathbf{r},\mathbf{r}',i\omega) = \int\int e^{qz}\, e^{qz'} \chi^{\text{R}}_S(z,z',\mathbf{q},\mathbf{q}',i\omega)\, dz\, dz'\,. \quad (5.13)$$

Remembering that the first exponential in Equation 5.11 cuts off the summation over q, it follows that $S(\mathbf{r},\mathbf{r}',i\omega)$ should be evaluated at small q. Before expanding Equation 5.13, we note that the response function of the surface describes the electron density induced by an external perturbation. More precisely, the induced density can be seen as the response to an external time-dependent charge distribution of the form $n_{\text{ext}}(\mathbf{r},t) = \delta(z-Z)e^{(i\mathbf{q}\mathbf{r})}e^{(\omega t)}$. This induced electron density, averaged over the surface of the solid ($\mathbf{G} = \mathbf{0}$), is expressed as a 2D Fourier transform of the product between the Coulomb

potential and the response function $\chi_S^{\mathrm{R}}(z, z', \mathbf{q}, \mathbf{q}', i\omega)$ [3].

$$S(\mathbf{r}, \mathbf{r}', i\omega) = \frac{q}{2\pi} \int e^{qz} \delta n(z, \mathbf{q}, i\omega)\, dz\,. \tag{5.14}$$

The equation above is just as an integral of the surface charge density with an exponential weight factor. The quantity $\delta n(z, \mathbf{q}, i\omega)$ represents the screening charge due to the non-local response of the bulk and is expected to be localized near the surface. We can now perform the expansion of Equation 5.14 for small q, retaining only the first order ($q = 0$). At this point, the integral in Equation 5.14 would provide the total screening charge of the surface and can be related to the current in the bulk *via* the continuity equation. Using this relation, the quantity $\delta n(z, \mathbf{q}, i\omega)$ is finally expressed in terms of the dielectric function of the solid

$$\int_{-\infty}^{+\infty} e^{qz} \delta n(z, i\omega)\, dz = \frac{\epsilon_S(i\omega) - 1}{\epsilon_S(i\omega) + 1}\,, \tag{5.15}$$

where $\epsilon(i\omega) = 1 + 4\pi\sigma(i\omega)/\omega$ and $\sigma(i\omega)$ is the bulk conductivity.

The results in Equation 5.15, Equation 5.14 and Equation 5.12 are now combined into the expression for the dispersion energy, Equation 5.11 (where the sum over $\mathbf{q}$ is turned into an integral in polar coordinates). After the integration, the complete formula for the dispersion energy reads

$$E_{\mathrm{disp}}^{(2)} = -\frac{C_3^{aS}}{Z^3} - \frac{C_4^{aS}}{Z^4} + \mathcal{O}(Z^{-5})\,, \tag{5.16}$$

where the coefficient in the first term is

$$C_3^{aS} = \frac{1}{4\pi} \int_0^{+\infty} \alpha(i\omega) \left[\frac{\epsilon_S(i\omega) - 1}{\epsilon_S(i\omega) + 1}\right] d\omega \tag{5.17}$$

and depends on the dipole polarizability of the adsorbed atom and the dielectric function of the solid. In order to obtain terms after the leading one in Equation 5.16, one needs to consider more terms in the expansion of $\delta n(z, \mathbf{q}, i\omega)$ (see Equation 5.14), beyond the first one. Unfortunately, the direct application of Equation 5.16 is not possible without a specific origin of coordinates. The information necessary to establish the reference plane is contained in the second term, of order Z^{-4}, which is the dominant correction. With some algebraic manipulation of the coordinates, the correction Z^{-4} can be absorbed in the first term of Equation 5.16. Finally, the dispersion energy can be approximated as

$$E_{\mathrm{disp}}^{(2)} \simeq -\frac{C_3^{aS}}{(Z - Z_0)^3} + \mathcal{O}(Z^{-5})\,, \tag{5.18}$$

where the position of the reference plane is

$$Z_0 \equiv \frac{C_4^{aS}}{3C_3^{aS}}\,. \tag{5.19}$$

[3] An identity taken from the linear response theory, see for example Reference [94].

Table 5.1: The free vdW parameters, obtained with the vdW$^{\mathrm{TS}}$ method, are compared with the screened parameters of the vdW$^{\mathrm{surm}}$ scheme. The lattice constants a_0 are obtained by coupling the vdW$^{\mathrm{TS}}$ method with the PBE functional. The C_6 are in [hartree Bohr^6], the vdW radii are in [Bohr], the polarizabilities are in [Bohr^3] and the lattice constants are in [Å]. All the values are taken from Reference [134].

	Free atom				Screened			
Substrate	C_6	R^0	α	a_0	C_6	R^0	α	a_0
Cu	253	3.76	42.0	3.543	59	2.40	10.9	3.572
Rh	469	3.95	56.1	3.773	84	2.42	13.0	3.765
Pd	158	3.66	23.7	3.913	102	3.07	13.9	3.949
Ag	339	3.82	50.6	4.071	122	2.57	15.4	4.007
Ir	359	4.00	42.5	3.844	98	2.71	13.2	3.873
Pt	347	3.92	39.7	3.939	120	2.80	14.5	3.979
Au	298	3.86	36.5	4.116	134	2.91	15.6	4.163

Notably, this approximation can fail for very small atom-surface distances. However in the typical case of physisorption the distance is large enough (~ 3 Å) and these equations are safely applicable. The jellium model can be applied to noble metals, yielding to an approximated reference plane (in the limit of high frequency) of $d/2$, where d is the interlayer distance, see Figure 5.1. This position of Z_0 is modified when local-field effects become large in the dielectric function. Therefore, the magnitude of the many-body effects in the potential between the atom and the surface can be evaluated by looking at the deviations in the approximation $Z_0 = d/2$.

5.3 Modeling Adsorption Phenomena with the Tkatchenko-Scheffler Functional

The LZK theory, discussed in the previous section, provides a definition of the C_3 coefficient, written in Equation 5.17. This result is of fundamental importance for the extension of the TS pairwise method to model adsorption on periodic surfaces. In fact, it is possible to relate the definition of the C_6 coefficient, used in pairwise methods, to the C_3 coefficient for the atom-surface vdW interaction. In 1937 Hamaker calculated the interaction between an atom a and a substrate S as an integration of the pairwise London formula (see Equation 4.3) over the volume of the solid Ω [135],

$$E_{\mathrm{disp}}^{(2)} = -\int_{\Omega} \frac{C_6^{as}}{R^6} n_S \, dV \,, \tag{5.20}$$

where dV is the volume element of solid and n_S is the number of atoms per volume in the bulk. From now on we will use the capital S to indicate the substrate. On the other hand, the lowercase s, as written in the C_6 in Equation 5.20, refers to a single atom of the substrate. The above formula can be equated to the known LZK expression for the

atom-surface dispersion energy, written in Equation 5.18. The equivalence is satisfied by setting the relation [135, 136]

$$C_3^{aS} = \frac{\pi}{6} n_S C_6^{as} , \tag{5.21}$$

where the surface is taken as an ideally half-spaced solid with constant density n_S.

The relation in Equation 5.21 can be derived by considering the dielectric function of the solid (Equation 5.17) with the approximated of the Clausius-Mossotti (CM) relation (or Lorenz-Lorenz relation)

$$\frac{\epsilon_S^{\mathrm{CM}}(i\omega) - 1}{\epsilon_S^{\mathrm{CM}}(i\omega) + 2} = \frac{4}{3}\pi n_s \alpha_s(i\omega) = \alpha_s^*(i\omega) , \tag{5.22}$$

where $\epsilon_S^{\mathrm{CM}}(i\omega)$ is the CM approximation of the dielectric function. The approximation is exact in case of cubic symmetry and if the constituents of the solid can be treated as point dipoles, *i.e.* with no overlap between the electronic charge distributions. In this case the total electric field, related to the dielectric function, is generated by i) the external source and ii) a macroscopic field due to the polarization of the solid, thus including the many-body effects of electromagnetic screening. The definition of $\epsilon(i\omega)$ as a function of $\alpha_s^*(i\omega)$, obtained from Equation 5.22, is then inserted into the $C_3^{aS}(i\omega)$ expression, see Equation 5.17. Finally, the relation between C_6^{as} and C_3^{aS} (Equation 5.21) is obtained by expanding $\alpha_s^*(i\omega)$ and retaining only the leading term [136]. We note that the second term in the expansion corresponds to the three-body dipole interactions, *i.e.* the Axilrod-Teller-Muto term [103].

We can now proceed to implement the LZK theory into the Tkatchenko-Scheffler vdW functionals (Section 4.2) with the following steps:

- For a specific solid S, the dielectric function $\epsilon_S(i\omega)$ is extracted from reflection electron energy-loss spectroscopy (REELS) experiments[4].The absorption spectra is used to obtain the imaginary part of the dielectric function. The real part is subsequently computed with a Kramers-Kronig transformation.

- The dielectric function is inserted into Equation 5.17, together with the polarizability of the adsorbed atom $\alpha_a(i\omega)$, to obtain the C_3^{aS} coefficient. Here the polarizability corresponds to the static polarizability, already introduced in the TS scheme (α_a^0) in Equation 4.9.

- The relation in Equation 5.21 is employed and the heteronuclear C_6^{as} coefficient is finally obtained.

- The heteronuclear coefficient is expressed in terms of homonuclear C_6 coefficients

[4]It is also possible to compute the dielectric function with first-principles calculations. Accurate DFT results reported a good agreement with REELS experimental data.

and polarizabilities (Equation 4.12), we report here the expression

$$C_{6,as} = \frac{2C_{6,aa}C_{6,ss}}{\frac{\alpha_s^0}{\alpha_a^0}C_{6,aa} + \frac{\alpha_a^0}{\alpha_s^0}C_{6,ss}} \,. \tag{5.23}$$

- The equation above presents two unknown parameters: the polarizability and the homonuclear coefficient of the substrate, α_s^0 and $C_{6,ss}$. It is sufficient to employ two different adsorbed atoms with the same substrate to have a solvable set of two equations with two unknown parameters.
- The value of α_s^0 is used to obtain the vdW radius for the atom-in-a-solid $R_s^0 = (\alpha_s^0/\alpha_s^{0,\text{free}})^{(1/3)} R_s^{0,\text{free}}$, where the superscript "free" indicates that the quantity has been computed for the free atom.

This new set of parameters $C_{6,ss}$, α_s^0 and R_s^0 for the atom-in-a-solid are used as input parameters in the TS vdW functional. Therefore, all the ingredients of the original TS functional are also used here. The only difference is that the effective quantities, which include the effects of polarization *via* the Hirshfeld weight (see Section 4.2.1), are built from the LZK parameters and not from the free atom reference. This extension of the TS is referred to as DFA+vdW$^{\text{surf}}$ method. The DFA+vdW$^{\text{surf}}$ method has been applied to a set of seven metal surfaces, using different kind of adsorbed atoms, such as H, C, Ne, Ar, Kr. The set of vdW parameters that include the screening for an atom-in-a-solid are reported in Table 5.1. From the comparison with the free-atom values, also reported in Table 5.1, it is evident that the inclusion of the collective response of the solid in the parameters cannot be neglected. The screened C_6 coefficients, for instance, display large reductions. In particular, the effective C_6 for Rhodium is reduced by a factor of 5.5 with respect to the C_6^{free}. More modest C_6 modifications, however, are found for some other metals, such as Au or Pd where the reduction factor is 2.2 and 1.55 respectively. The different magnitude in the renormalization of the parameters suggests that screening effects are strongly sensitive to the type of substrate. For what concerns the lattice constants, the values reported in Table 5.1 are obtained by coupling the vdW$^{\text{surf}}$ to the PBE functional. We remark that PBE reduces to LDA in the limit of homogeneous electron densities. Thus, it can provide a quite accurate description of metallic electrons. As a consequence, PBE+vdW$^{\text{surf}}$ can lead to a partial double counting of the interactions between electrons in the metal. This can lead, in some cases, to a tiny increase of the lattice constants with respect to the PBE ones [134]. Unfortunately, these overestimations can not be easily quantified and the inclusion of the full ions–metallic electrons interactions into the microscopic polarizability is a necessary step to improve the present model. We note here that the inclusion of the vdW$^{\text{TS}}$ energy on top of PBE always improve the lattice constants computed with PBE alone. These results might appear surprising if we consider that the vdW$^{\text{TS}}$ do not include any screening between the ions in a metal. However, the good performances of the vdW$^{\text{TS}}$ are the consequence of error cancellations between the overestimated C_6 coefficients and the large values for

the vdW radii [134].

An extensive and detailed description of the vdW interactions in metals and for adsorption phenomena on metal surfaces can be found in the Ph.D thesis of Dr. Ruiz [137]. In that work both technical aspects and numerical results for fourteen metallic substrates are reported. Also, the DFA+vdW$^{\mathrm{surf}}$ method is applied to study the adsorption of an atom/molecule on a metal surface, with a particular attention to PTCDA (see Section 10.4) on coinage metals. The DFA+vdW$^{\mathrm{surf}}$ method has been successfully employed to study a large number of different adsorbates on a variety of metallic surfaces [10, 123, 134, 138–140]. The adsorbates include small rare-gas atoms as the Xenon atom, small-medium sized organic molecules as benzene or azobenzene, as well as large molecules as PTCDA or the C_{60} buckyball. A broad review with several examples and a thorough discussion about the performances and the possible improvements of the DFA+vdW$^{\mathrm{surf}}$ method is available in Reference [127].

5.4 The Non-Local Density Functionals

In this section we give an overview of the so-called non-local vdW functionals. This family of popular vdW functionals originated from the vdW density functional (vdW-DF) of Dion *et al.* [141], however the seminal idea dates back to the work of Langreth and Lundqvist [142]. The vdW-DF will be used in this thesis and compared to the pairwise DFA+vdW$^{\mathrm{TS}}$ functional.

In vdW-DF the XC energy is given by

$$E_{\mathrm{xc}}^{\mathrm{vdW-DF}}[n] = E_{\mathrm{x}}^{\mathrm{GGA}}[n] + E_{\mathrm{c}}^{\mathrm{LDA}}[n] + E_{\mathrm{c}}^{\mathrm{nl}}[n]\,, \tag{5.24}$$

where, originally, the GGA exchange energy is taken from revPBE [143]. The non-local correlation energy functional $E_{\mathrm{c}}^{\mathrm{nl}}[n]$ is defined by introducing a two-point dependency on the electron density, which motivates the name "non-local":

$$E_{\mathrm{c}}^{\mathrm{nl}} = \frac{1}{2}\int\int n(\mathbf{r})\Phi(\mathbf{r},\mathbf{r}')n(\mathbf{r}')d\mathbf{r}d\mathbf{r}'\,. \tag{5.25}$$

Here $\Phi(\mathbf{r},\mathbf{r}')$ is the so-called non-local kernel, that reproduces the asymptotic behavior $\Phi(\mathbf{r},\mathbf{r}') \sim R^{-6}$ for $R \to \infty$. The double integral in Equation 5.25 has a higher computational cost compared with discrete post-processing pairwise methods. This drawback will be discussed in relation to calculations of metallic bulks and surfaces, see Section 7.3.

The starting point of vdW-DF is the exact ACFD equation, see Equation 3.28 (and Appendix B.3). In the vdW-DF, the ACFD formula is split into local and non-local contributions for the correlation energy. As a first step, the local part of the correlation is defined as the LDA correlation term, as written in Equation 5.24. Therefore, the non-local correlation should take into account the remaining piece of the correlation energy. Three approximations are then introduced in order to correct LDA correlation with a non-local dispersion contribution: 1) The first approximation of vdW-DF enters when

the integration over the adiabatic factor λ is carried out. That is, the interacting response function $\overline{\chi}_\lambda$ in the ACFD formula is substituted with the response function of the full electric potential ($\lambda = 1$). This is the so-called full potential approximation [142]. In this way, the integration over the switching parameter λ can be performed analytically. The quantity $E_c^{\mathrm{nl}}[n]$ is written as

$$E_c^{\mathrm{nl}} = \int_0^\infty \mathrm{Tr}\left[\ln\left(1 - V(\mathbf{r}-\mathbf{r}')\overline{\chi}(\mathbf{r},\mathbf{r}',i\omega)\right) - \ln\epsilon(\mathbf{r},\mathbf{r}'.i\omega)\right] d\omega\,, \tag{5.26}$$

where the response function used here can be expressed in terms of the dielectric constant ϵ. We consider now two separate fragments that are pushed close together. As the distance between them reduces, the density of the system is expected to become more and more uniform. At the same time, the effects of non-local correlation should gradually decrease to zero. This limit is included by construction in the vdW-DF functional. In fact, for a uniform system the relationship between $\overline{\chi}$ and ϵ becomes $\epsilon = 1 - V\overline{\chi}$ and the integral in Equation 5.26 vanishes. Also, a seamless connection with the LDA correlation is guaranteed, avoiding double counting. 2) The second approximation consists in a second order expansion of the term $S \equiv 1 - \epsilon^{-1}$ [141]. 3) Other approximations are necessary to write a form for the factor S (or $\overline{\chi}$). In the vdW-DF a plasmon-pole model was employed [141]. After some algebra, the functional in Equation 5.26 is finally rewritten as Equation 5.25. The non-local kernel is a function of the position, the density and the gradient of the density, evaluated simultaneously for two points ($\mathbf{r}$ and $\mathbf{r}'$).

The vdW-DF has been applied to a variety of systems where dispersion is an important component of the total energy. From the results it emerged that the functional tends to overestimate the long-range correlation, as we will see also in this thesis, in Section 8.2. For example, the vdW-DF yields a MAE for the S22 database of ~ 60 meV [88], outside the chemical accuracy of ~ 43 meV. These outcomes stimulated new proposals for improving the performances of the vdW-DF. Among the various ideas there are functionals with a modified version of the exchange functional, usually derived from PBE and/or revPBE. A popular variation is the vdW-DF2 [144], which employs an accurate semi-local exchange functional (PW86) in combination with a gradient correction in the kernel. The results for the S22 database show a significant reduction of the MAE and the chemical accuracy is reached for dispersion-dominated complexes [144]. Other examples are optPBE and optB88, where the exchange functional is a mixture of PBE and revPBE for the former, while the B88 functional is employed for the latter. The parameters of the exchange part were also optimized by fitting on the S22 database. We note here that, by construction, vdW-DF is not compatible with EXX and the use of hybrid functionals typically results into large overbind and less accurate values.

In concluding, we mention that other non-local functionals that substantially differ from vdW-DF are also available. One example is the non-local functional of Vydrov and van Voorhis, the VV10 (and VV09) [145]. The idea of the VV10 is to compute the kernel after a range separation between short- and long-range contributions, resulting in a rather simple mathematical expression. By controlling the two components via a

range-separating function, the VV10 functional can be coupled to other XC functionals. Moreover, the VV10 contains empirical parameters that are fitted to a set of reference C_6 coefficients. A detailed description of the different non-local vdW functionals and their performances is far beyond the scope of this work and we suggest the interested reader to refer to specific works, as the one in Reference [146]. In additioon to that, more general reviews are available, that describe the most popular vdW methodologies proposed in the literature [147, 148].

5.5 Summary

This chapter introduced the "classical" description of vdW interactions as the dispersion energy that is generated by the interaction between induced dipoles or multipoles. Following the idea of London, the dispersion interactions for non-overlapping fragments are defined as a sum of pairwise contributions. The leading term is the induced dipole–induced dipole contribution, computed within second order perturbation theory and a multipolar expansion of the Coulomb potential (dipole approximation). Approaches of increasing complexity are subsequently introduced in order to treat bulk periodic metals and physical adsorption. We note that, in principle, the vdW dispersion energy stems from the retarded electromagnetic interaction acting between the atoms, and its exact description would require a full many-body quantum mechanical approach. Due to the complexity of the problem, however, some simplifying approximations should be introduced.

In first place, we consider systems where the distance between the interacting bodies is sufficiently limited that the electromagnetic field can be treated as non-retarded. Second, in the case of physical adsorption we restrict to interacting fragments with non-overlapping electronic wavefunctions. At this point the problem of two interacting bodies can be treated within the LZK approach, as described by Equation 5.9. The equation depends on the Coulomb potential V, and the electron density-density response χ. Notably, by considering the leading order of a multipole expansion of the Coulomb potential, the classical London expression ($E^{(2)}_{\mathrm{disp},AB} = -C_{6,AB}/R^6_{AB}$) for the vdW energy is recovered.

The sum of pairwise contributions can be applied to a variety of systems. Great efforts were made in order to derive analytical expressions for the pairwise vdW energy of macroscopic objects with well-defined shapes, as thick/thin slabs, spheres, cylinders and many more. The typical strategy is to substitute the summation by a continuous space integration. In this way it is possible to obtain the analytical dependence of the vdW energy on the separation distance D between macroscopic fragments. A very large set of examples of this kind can be found in the book of A. Parsegian [107]. As clearly discussed in Section 5.1 and 5.2, the pairwise methods are unable to capture many-body effects, that stem from the screening of the Coulomb interaction between the fragments.

The dispersion interaction is part of the correlation energy and the exact form of

the latter is provided by the ACFD formula [5], see Equation 3.28. Therefore, the ACFD formula represents the proper starting point for vdW methods that includes many-body effects. In this regard, we discussed the derivation of the non-local vdW methods, such as vdW-DF, from the ACFD formula. Another popular approach is the RPA, see Equation 3.30, which provides an elegant expression for the many-body correlation energy. The RPA has been applied to several systems and the asymptotic behavior of the correlation energy has been compared to the "standard" results, obtained with pairwise methodologies [149, 150]. Deviations from the pairwise power laws are found, for example, for metallic and semi-metallic systems. In particular, large deviations from the standard asymptotics were observed in low-dimensional nanoscale systems, such as parallel metallic wires, carbon nanotubes or thin slabs.

We note here that within the ACFD framework one can also derive the LZK formula for atoms adsorbed on a metallic substrates. In Section 5.2 we have followed the "classical" derivation, which starts from a second-order perturbative approach for substrate-adsorbate coupling. As an alternative, one can start from the ACFD formula and follow the same steps used for deriving the RPA. In this way the dispersion energy is written in terms of the response function. Moreover, the total response function of the system can be factorized as a tensor product of two susceptibilities (χ_{12} and χ_{21}), relative to the two non-overlapping fragments. Perturbative diagrams can be summed up for intra-fragment interactions, leading to a renormalization of χ_{12} and χ_{21}. The two interacting susceptibilities, accounting for intra-fragment many-body effects, can finally be coupled via the interfragment Coulomb interaction. At second perturbative order in the inter-fragment Coulomb coupling —valid for sufficiently large interfragment separations—, the LZK is recovered. In conclusion, the ACFD formula provides a universal theoretical framework for the description of many-body long-range correlation interactions. The ACFD expression is not only exact, but it also allows for an insightful derivation of approximate methods, from pairwise approaches (second order perturbative approximation) and LZK theory (second order coupling between full many-body fragment susceptibilities), up to RPA (infinite summation of ring diagrams) and alternative many-body techniques.

[5] The ACFD formula is an exact expression for both the exchange-correlation part of the energy. The two components can be separated into two independent parts.

Part III

Implementation

6 Electronic Structure Methods

Now that the reader is more familiar with van der Waals interactions and the TS functional in particular, we can approach the core of the present thesis. This chapter is devoted to describe the details of the self-consistent (SC) implementation of the TS scheme in the Fritz-Haber-Institut *ab initio* molecular simulation package (FHI-aims) [151]. Here, we will present step-by-step the analytical derivation of the vdW potential. The working equations for the SC implementation will be shown and compared with the corresponding *a posteriori* scheme, in which the vdW interactions are treated in a non-self-consistent manner. Finally, the performance and the efficiency of the new implementation will be discussed using different test systems and convergence settings. However, before proceeding directly to the SC implementation, now we introduce the reader to the basic concepts of a real-space code with local orbitals, such as the FHI-aims. This will clarify the subsequent technical discussion of the implementation. It will help, in particular, to explain the reasons behind the efficiency/inefficiency and to illustrate the pathway for possible improvements and/or approximations. In passing, we will also discuss the comparison with another very popular family of electronic structure codes, which employ plane-waves basis sets.

Many different codes exist for performing electronic structure calculations. Each code provides a variety of computational methods (see some examples in Chapter 2 and Chapter 3) and presents specific characteristics, efficiency and accuracy. We can loosely distinguish two families depending on the basis set that is employed: plane-wave (necessarily combined with the pseudopotential approximation) and atom-centered orbital (typically all-electron) codes. To clarify the division above let us consider, as an example, the case of DFT. We saw in Chapter 3 that the solution of the many-body problem corresponds to the solution of the KS eigenvalue equations, written in Equation 3.17, $(t_0 + v_{\text{eff}})\psi_i(\mathbf{r}) = \epsilon_i\psi_i(\mathbf{r})\,, \forall$ particle i. To solve this set of single-particle equations, it is a common practice to use basis functions to expand the single-particle orbitals

$$\psi_i = \sum_n^{N_b} c_{ni}\phi_n(\mathbf{r})\,, \tag{6.1}$$

where the spin-polarized index is omitted in this chapter for a simplified notation. A basis set enables the reformulation of the differential equations into a generalized

eigenvalue problem

$$\sum_{n}^{N_b} h_{mn} c_{ni} = \epsilon_i \sum_{n}^{N_b} s_{mn} c_{ni} \,, \tag{6.2}$$

where the matrix element of the Hamiltonian is $h_{mn} = \langle \phi_m | t_0 + v_{\text{eff}} | \psi_n \rangle$, while $s_{mn} = \langle \phi_m | \phi_n \rangle$ is the overlap matrix element. The choice of the basis set determines some important properties of the code. The Gaussian basis set, for instance, are atom-centered orbitals with an analytical form. Any large enough gaussian basis is almost complete and can be used for different electronic structure methods. For this reasons they have been extensively used in the quantum-chemistry community—along with Slater-type orbitals—and are able to describe accurately the non-local correlation effects. The analytical form has the advantage to simplify the integrals in Cartesian coordinates. On the other hand, a large number of basis functions is often needed to obtain accurate results, leading to a slow convergence in term of total number of basis functions.

The plane-wave basis set is popular in solid-state physics and offers the advantage of describing the periodicity of the system by construction. This feature is reflected in particularly fast computation with plane-wave codes when studying periodic systems. However, since the plane-waves are defined all over space, this methodology is not particularly indicated for low dimensional systems, as surfaces, where the vacuum represents a large part of the unit cell. With plane-wave basis, the description of an atom becomes problematic in the region close to the nucleus, where the wave-functions present rapid oscillations. The orbitals that describe core electrons are in general very similar to the ones of the isolated atom. Therefore, a common procedure is to avoid an explicit description of core electrons and use effective core potentials, called pseudopotentials. The pseudopotential is associated to single-particle pseudo-wavefunctions that should replace the core states with smooth functions. Since the valence electrons feel the pseudopotential, the valence states result consequently modified in the vicinity of the nucleus. Beyond a certain cutoff, that separates the core from the valence states, the pseudopotential and the pseudo-wavefunctions become identical to the "original" all-electron potential and wavefunctions. The pseudopotentials allow to use a reduced number of basis functions, but extra care should be taken when partitioning the core and the valence region, in particular for heavier atoms.

6.1 Numeric Atom-Centered Orbitals

Since the large majority of the results presented in this work are obtained with the aforementioned FHI-aims code, we will focus mainly on this code in the following discussion. An extended discussion about all the technical details of the FHI-aims code is reported in Reference [151]. FHI-aims is an all-electron code that employs a numeric atom-centered orbitals (NAOs) of the form

$$\phi_i(\mathbf{r}) = \frac{u_i(r)}{r} Y_{lm}(\Omega) \,, \tag{6.3}$$

where the function $u_i(r)$ has radial symmetry and is numerically tabulated. The angular part is given by the complex spherical harmonics $Y_{lm}(\Omega)$, divided into real parts $(m = 0, \ldots, l)$ and imaginary parts $(m = -l, \ldots, -1)$. Similar to other atomic basis sets, the NAOs are centered on nuclei and have the advantage of retaining chemical bonding information of the system with an appropriate description of the atomic core electrons. The particular form of the NAOs allows to include the radial functions of free-atom orbitals and to describe well the inner electrons, near the nuclei. The flexibility of the radial function $u_i(r)$ comes from the fact that it can be constructed using a Schrödinger-like radial equation

$$\left[-\frac{1}{2}\frac{d^2}{dr^2} + \frac{l(l+1)}{r^2} + v_i(r) + v_{\text{cut}}(r)\right] u_i(r) = \epsilon_i u_i(r)\,, \tag{6.4}$$

where l is the angular quantum number. The potential $v_i(r)$ defines the shape of $u_i(r)$. The term $v_{\text{cut}}(r)$ is the confining potential, which guarantees a smooth decay to zero of the radial functions $u_i(r)$ outside a certain radius.

The analytical shape of the confining potential is not unique. Care must be taken to ensure, along with a smooth decay, the absence of discontinuities in the function and its derivatives. The confining potential in FHI-aims is given by

$$v_{\text{cut}}(r) = \begin{cases} 0 & r \leq r_{\text{onset}}\,, \\ \frac{s}{(r-r_{\text{cut}})^2}\exp(\frac{w}{r-r_{\text{onset}}}) & r_{\text{onset}} < r < r_{\text{cut}}\,, \\ +\infty & r \geq r_{\text{cut}}\,, \end{cases} \tag{6.5}$$

in which s is a global scaling parameter. The difference $w = r_{\text{cut}} - r_{\text{onset}}$ sets the width of the region in which the potential is defined and not divergent. The choice of these parameters is critical for both the accuracy of the results and the numerical efficiency of the code. In fact, if one chooses a very small r_{onset}, the radial functions would be confined in a very small region around the atom, leading to unphysical results. On the other side, a small r_{onset} and a large width would produce extended radial functions with very slow decay. This can significantly affect the CPU time, especially in case of densely packed solids. The values for a "safe" $v_{\text{cut}}(r)$ are tabulated[1] and correspond to $r_{\text{onset}} = 4.0\,\text{Å}$ and a width $w = 2.0\,\text{Å}$. As a general prescription, the potential cut-off can be responsible for changes in the properties, apart from the total energies. Therefore, the value of $v_{\text{cut}}(r)$ should always be tested to ensure an accurate convergence in all situations. In this work we will consider several different systems and present a study of their electronic properties. Our results will be supported by convergence tests, in particular for what concerns the confining potential.

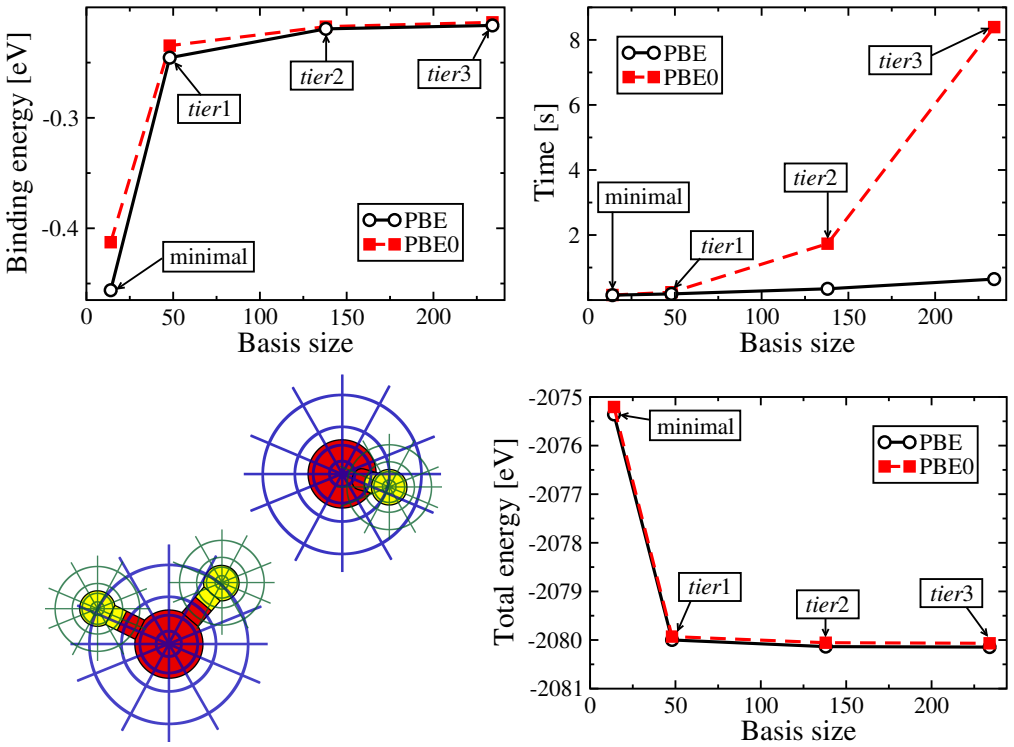

Figure 6.1: Top left: PBE and PBE0 binding energy of the water dimer as a function of the basis set. Top right: time employed for each dimer calculation. The values reported are the average time per self-consistent cycle, obtained with the code running with twelve processors in parallel. Bottom left: structure of the water dimer with a sketch of the atom-centered grids for the real space numerical integration. Bottom right: PBE and PBE0 total energy of a water molecule as a function of the basis set.

6.2 FHI-AIMS SETTINGS

The radial NAOs are obtained for each species with an iterative procedure that allows to gradually increase the accuracy. First, the so-called *minimal basis set* is constructed. It consists of the orbitals of the spherically symmetric free atoms and is obtained by setting the radial potential in Equation 6.4 equal to the free atomic potential. The minimal NAOs are exact for free atoms and provide both core and valence functions, which can be transferred to bonded systems. For the valence electrons, the minimal basis set describes well the regions close to the nuclei, because the nuclear potential dominates and the shape of the orbitals are similar to the free-atom case. Second, for each element a closed-shell optimization target is chosen, typically a dimer. The pool of candidate functions is tested and only the radial function that improve the most the total energy is retained. This procedure is then iterated until no further improvement is found. Of course, several variations can be applied to the schematic procedure described above, as the introduction of additional candidates in the initial pool, beyond

[1] We report here the two values suggested and tabulated as the default choice for the tight settings, the set of parameters typically considered to provide reliable accuracy.

the minimal basis set. The radial functions, selected in this way, are grouped together in *tiers* of different angular momenta and distributed with the FHI-aims code. Naturally, the first $tier$ improves significantly the minimal basis set and the correction reduces quantitatively as the rank of the $tier$ increases. An example is shown in Figure 6.1 top-left panel, where the binding energy of the water dimer is computed with PBE and PBE0 functionals and plotted in function of the different $tiers$ basis sets, see Appendix C.1 for the computational details. The cost of each calculation is plotted in the top-right panel of Figure 6.1. Unfortunately, it is a general fact that the speed of the calculations is reduced as the basis set increases. In this particular case, the PBE over-converged calculation with $tier3$ is about five times longer than the one with the minimal basis set. For PBE0 the scaling is much worse and the difference becomes more than fifty times. In conclusion, higher $tiers$ should be used only when really necessary. For example, $tier1$ is very likely to be enough in case of geometry optimizations, where the number of self-consistent calculations is definitely large. Then, for carefully converged total energies, one should consider $tier2$ or beyond.

An important quantity in a DFT calculation is the electrostatic (Hartree) potential. In FHI-aims, the charge density is partitioned on the atoms and decomposed in a multipole expansion. The multipole components are regulated by the parameter l that indicates the highest angular momentum. This parameter is very important for the computational efficiency of the code and should be carefully chosen. From the practical experience it emerged that a value of $l = 4$ is usually enough to give meV/atom-converged energy differences [151]. In the tight settings a value of $l = 6$ is used. The potential $v_{\mathrm{H}}(r)$ is then evaluated on a dense logarithmic grid. Outside the cut-off that limits the atom-centered electron density, the Hartree potential decays analytically as $\propto r^{-(l+1)}$. Therefore, the high multipole components decay very fast to zero at large distances. The long-range electrostatic potential (small l) can be efficiently computed, for periodic systems, using Ewald's method. The Hartree potential is split into a short-ranged part and a smooth long-ranged part. Then, the long-range part is evaluated in reciprocal space, using Fourier transforms.

The numerical integrations are evaluated in FHI-aims in a real-space mesh, that is created by overlapping atom-centered grids. The space around each atom is divided in shells, which are sampled with a certain amount of points, as sketched on top of the water dimer geometry in the bottom-left panel of Figure 6.1. The radial and angular integration points are created along with their respective tabulated integration weights. In practice, a Lebedev grid [152] is used to distribute the points on spherical shells. In the code, the number of shells and their density can be fully controlled, as well as the number of angular grid points distributed in a specific region. We note that inner shells requires fewer points than those, more extended in space, that are located far away from the nuclei.

6.3 Additional Features

In FHI-aims the spherical atoms are modeled including their valence functions in the basis set. However, the situation is different in all other possible cases, as non-spherical atoms, molecules, etc. Consequently, during the variational procedure, the basis set of a fragment can contribute to improve the energy of other fragments. This artificial effect is known as the basis set superposition error (BSSE) and leads to a lowering of the atomization or binding energies. One way to evaluate and correct the BSSE is the counterpoise (CP) correction: energy calculations are performed for each isolated fragment, with and without the basis set of the other fragments. The difference between the two values is the CP correction for the fragment. Once the CP energy value is known, it is possible to correct the BSSE by subtracting this number to the binding energy. In the FHI-aims, the magnitude of the BSSE has been extensively studied in relation to the number of basis functions. In conclusion, the BSSE turned out to be negligible for well converged energy calculations, in most DFT functionals. Already with a moderate basis size, as $tier2$, the BSSE becomes basically irrelevant. Exceptions exist, in particular for explicitly correlated methods [153], *e.g.* MP2.

The expansion of two-particle operators, as the Coulomb operator, in a single-particle basis is evaluated with four-center two-electron integrals. The Coulomb integral is written, using the decomposition of Equation 6.1, as

$$\langle ij|\frac{1}{|\mathbf{r}-\mathbf{r}'|}|kl\rangle = \int\int \frac{\phi_i^*(\mathbf{r})\phi_j^*(\mathbf{r}')\phi_k(\mathbf{r})\phi_l(\mathbf{r}')}{|\mathbf{r}-\mathbf{r}'|} d\mathbf{r}d\mathbf{r}' \,. \tag{6.6}$$

The exchange part is just the expression above with the sign minus and the two indices k and l interchanged. Once the integrals are computed, the single-particle orbitals are obtained using the expansion coefficients. Unfortunately, the CPU time necessary to compute the four-center integrals represents a large part of the total workload. Also, the memory required to store these integral can be a major bottleneck, with a scaling of $O(N^4)$, where N is the number of basis functions employed. The four-center integrals are relatively easy to compute with Gaussian basis functions. In fact, the product of two Gaussians centered in two different points has an analytic expression: it is just another Gaussian centered at a third point. In this way the four-center integrals are reduced to two-center integrals. In the case of FHI-aims, where NAOs are used, no analytical expression is available. Different methods have been proposed to reduce the numerical cost of the four-center integrals. The resolution of identity (RI), implemented in FHI-aims [153], reduces the four-center integrals to a series of two- and three-center integrals. Within the RI, the atomic basis functions $\phi_i(\mathbf{r})\phi_k(\mathbf{r})$ are written in term of an auxiliary basis:

$$\phi_i(\mathbf{r})\phi_k(\mathbf{r}) \simeq \sum_{\mu=1}^{N_{\text{aux}}} C_{ik}^{\mu} P_{\mu}(\mathbf{r}) \,, \tag{6.7}$$

where $\{P_\mu\}$ is the set of functions, called auxiliary basis functions (ABF), and C_{ik}^{μ} are the

expansion coefficients. In the limit of a complete auxiliary basis, the expression above would be an equality. However, the auxiliary basis is invariably incomplete and this is essential for obtaining increased computational efficiency. In other words, the number of ABFs, N_{aux}, can be kept always smaller than the number of NAO pairs, which scales as $O(N^2)$. On the other hand, the size of the basis set guarantees low errors in the expansion. A typical number for the ABFs is $\sim$ 3–6 times the NAOs [153].

The four-center integral in Equation 6.6 is now rewritten in terms of the ABFs

$$\langle ij|\frac{1}{|\mathbf{r}-\mathbf{r}'|}|kl\rangle \simeq \sum_{\mu\nu}^{N_{\text{aux}}} C_{ik}^{\mu} V_{\mu\nu} C_{jl}^{\nu}\,, \tag{6.8}$$

where $V_{\mu\nu}$ is the Coulomb potential, a two-center integral that involves two ABFs. From this definition, the method takes the name of "RI-V". Finally, the expansion coefficients can be determined in several ways. An option is to minimize the expansion error of the ABFs with respect to the NAOs. Here, the RI error of the four-center integrals is minimized, yielding to three-center Coulomb integrals that contain both NAOs (two functions per integral) and ABFs (one function per integral). A complete overview about the RI-V implementation in FHI-aims is available in Reference [153].

In concluding this chapter we mention that an all-electron self-consistent calculation embodies a series of operations that can considerably affect the computational efficiency. The improvement of the efficiency of electronic structure codes is a topic of great interest. In particular, an appropriate implementation leads to an applicability extended to large systems (hundred of atoms) along with an efficient computational cost. In FHI-aims, the key objects are the NAOs and the real-space grid, where all the operations are performed. Consider, for instance, the setup of the electron density, an operation required at each self-consistent cycle. The density is defined using pairs of orbitals and running over all the grid, giving a $O(N^3)$ scaling. Another important passage is the integration of the Hamiltonian, that gives the same $O(N^3)$ scale. Therefore, the computational efficiency depends on the shape and the total number number of NAOs as well as on the partitioning grid. The NAO, defined in Equation 6.3, can be taken in a localized form, using a cutoff potential, see Equation 6.5. We already mention that the real-space grid is composed of overlapping atom-centered grids, with shell-like distribution of points. At this stage, the quantity of interest is obtained with an integral over a discrete set of points, considering also that a weight function is assigned to each atom-center grid. However, several algorithms of different complexity can be used to efficiently partition the grid into batches, that are as localized as possible. This allows to split the original loop over the grid points into several smaller parallel jobs. Finally, the division in batches, together with the NAOs localization, yields to a small number of non-zero basis functions in each batch, speeding up the loops and the operations between matrices. All the details about the optimization of the scaling in FHI-aims are available in Reference [154]. In conclusion, a linear scaling $O(N)$ is achieved for several grid-based operations, resulting in a nearly linear total scaling.

7 Self-Consistent Tkatchenko-Scheffler van der Waals Functional

In this Chapter we discuss the details of our self-consistent (SC) implementation of the Tkatchenko-Scheffler van der Waals functional into the FHI-aims code. The first step is the introduction of the working equations, then the analytical derivation of the vdW potential will be presented. The chapter is concluded with illustrative convergence tests, analysis and optimizations of the computational efficiency of the SC implementation and comparisons between different XC functionals.

Before the actual implementation, we recall briefly some formulas that will be used in the following. The interatomic vdW functional of Tkatchenko and Scheffler [108] (TS) has already been described to the reader in Section 4.2. The total vdW energy formula with the effective quantities is written as

$$E_{\mathrm{vdW^{TS}}}[n(\mathbf{r})] = -\frac{1}{2}\sum_{A,B} E^{AB}_{\mathrm{vdW^{TS}}}[n(\mathbf{r})] = -\frac{1}{2}\sum_{A,B} f^{AB}_{damp}[n(\mathbf{r})] C^{eff}_{6,AB}[n(\mathbf{r})] R^{-6}_{AB}\,, \qquad (7.1)$$

in which the electron density enters the equation through the ratio $\gamma[n(\mathbf{r})]$ between effective and free volume, see Equation 4.13.

The $C_{6,AB}$ coefficient of a pair of atoms contains the polarizabilities and the homonuclear coefficients, redefined for the effective quantities in Equation 4.15 and Equation 4.16, respectively. We substitute those definitions into Equation 4.12 to compute the effective coefficient for each pair. After some algebraic manipulation, the factors $\gamma_A[n(\mathbf{r})]$ and $\gamma_B[n(\mathbf{r})]$ are regrouped and simplified,

$$\begin{aligned} C^{eff}_{6,AB}[n(\mathbf{r})] &= \frac{2C^{eff}_{6,AA}[n(\mathbf{r})]C^{eff}_{6,BB}[n(\mathbf{r})]}{\frac{\alpha^{0,eff}_B[n(\mathbf{r})]}{\alpha^{0,eff}_A[n(\mathbf{r})]}C^{eff}_{6,AA}[n(\mathbf{r})] + \frac{\alpha^{0,eff}_A[n(\mathbf{r})]}{\alpha^{0,eff}_B[n(\mathbf{r})]}C^{eff}_{6,BB}[n(\mathbf{r})]} = \\ &= \frac{2\,C^{free}_{6,AA}C^{free}_{6,BB}\,\gamma_A[n(\mathbf{r})]\,\gamma_B[n(\mathbf{r})]}{\frac{\alpha^{0,free}_B}{\alpha^{0,free}_A}C^{free}_{6,AA} + \frac{\alpha^{0,free}_A}{\alpha^{0,free}_B}C^{free}_{6,BB}} = C^{free}_{6,AB}\,\gamma_A[n(\mathbf{r})]\,\gamma_B[n(\mathbf{r})]\,. \qquad (7.2) \end{aligned}$$

Now the dependency on the electron density is found only in two factors at the numera-

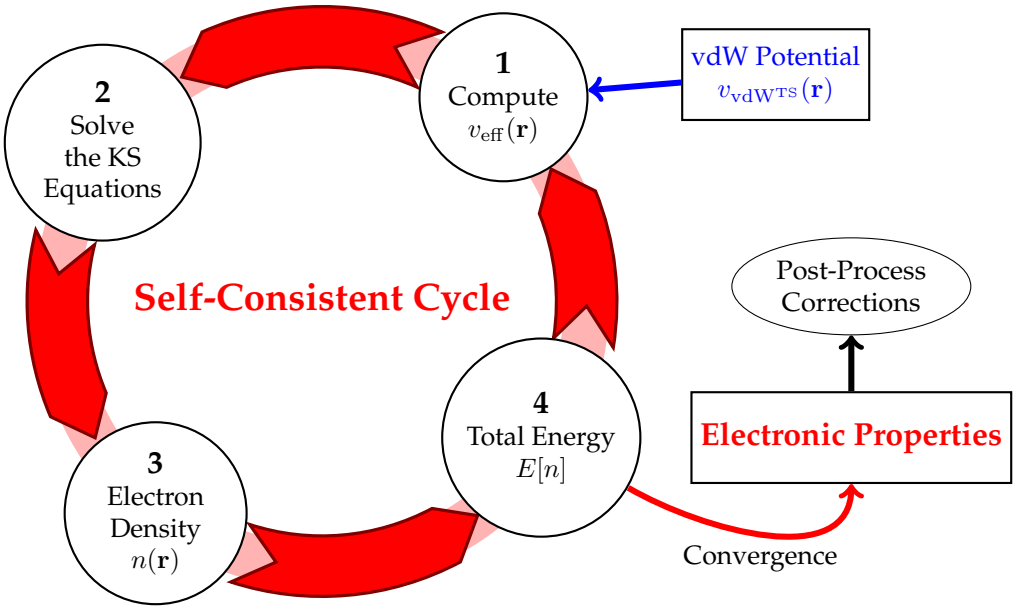

Figure 7.1: Schematic representation of the DFT self-consistent procedure with the four main steps. The figure also shows that the vdW potential is introduced at the beginning, where the cycle is initialized. Instead, the post-process operations are performed at the end.

tor, corresponding to the volume ratio of atoms A and B.

The Fermi-type damping function is defined in Equation 4.18. For each given pair, the damping depends on the electron density *via* the sum of the two effective vdW radii, $R_{AB}^{0,eff}[n(\mathbf{r})] = R_{A}^{0,eff}[n(\mathbf{r})] + R_{B}^{0,eff}[n(\mathbf{r})]$. The effective vdW radius is obtained using $\gamma[n(\mathbf{r})]^{1/3}$ as multiplicative factor of the free value, as written in Equation 4.17.

7.1 Kohn-Sham Equations with van der Waals Interactions

The long-range vdW energy typically represents only a small part (0.001%) of the total DFT energy. Hence, the influence of vdW on the electron density $n(\mathbf{r})$ and electronic properties, such as multipolar moments and orbital energy levels, is generally assumed to be rather small, if not negligible. For this reason, the majority of the popular vdW functionals employed within the framework of density-functional theory (DFT), are commonly approximated by an *a posteriori* perturbation (post-process correction) of the total energy. We have already mentioned this approach, for example, when talking about the coupled cluster approximation in Section 2.5.1. The CCSD(T) method is a famous variation that includes the triples wavefunction as a perturbative correction.

In practice, a DFT calculation is performed with a given XC functional and is iterated until convergence. The self-consistent solution gives a ground-state electron density

$n_0(\mathbf{r})$ and a total energy, functional of the density, $E[n_0(\mathbf{r})]$, see Equation 3.20. Then, in order to evaluate the TS vdW energy, the Hirshfeld ratio (Equation 4.13) is computed with the (converged) ground-state electron density. The effective quantities are obtained and used into the vdW energy formula (Equation 7.1), leading to the vdW energy $E_{\mathrm{vdW}^{\mathrm{TS}}}[n_0(\mathbf{r})]$. Finally, the DFT calculation is "corrected" adding the contribution that accounts for the missing long-range correlation to the total DFT energy value

$$E_{\mathrm{tot}}[n_0(\mathbf{r})] = E[n_0(\mathbf{r})] + E_{\mathrm{vdW}^{\mathrm{TS}}}[n_0(\mathbf{r})]\,. \tag{7.3}$$

Clearly, within an *a posteriori* scheme, the trivial modification of the standard DFT total energy formula is accompanied by a computationally very efficient "one-shot" correction, performed at the end of the calculation. However, only the total energy is modified by vdW interactions and no information is left about the effects on the electronic properties.

On the other hand, within a fully self-consistent scheme the contributions of the vdW functional would be directly added into the self-consistent KS equations through the vdW potential, *i.e.* the functional derivative of the vdW energy with respect to the electron density. The potential is added to the effective potential, see Equation 3.17, leading to modified ground-state eigenfunctions and eigenvalues. In Figure 7.1 is drawn a representation of the DFT self-consistent cycle showing at which point the vdW potential is inserted. Consequently, a SC scheme affects not only the total energy, but also the electron density $n(\mathbf{r})$ and the electronic properties. Beside that, the SC approach represents, from a theoretical point of view, the rigorous way of implementing a functional into DFT and can be used to validate the *a posteriori* results. The SC version of the TS functional will be referred from now on as $\mathrm{vdW}^{\mathrm{TS}}_{\mathrm{sc}}$.

Before proceeding into the description of the $\mathrm{vdW}^{\mathrm{TS}}_{\mathrm{sc}}$, it is important to mention that several self-consistent vdW-inclusive functionals have been already presented in the literature. One example is the non-local vdW-DF family of functionals [141, 142, 155–157], a result of the Chalmers/Rutgers collaboration, see Section 5.4. For this vdW functional, the potential is derived analytically [155], as in our case. The vdW-DF SC implementation has been tested on different systems, from small molecular dimers and rare gas dimers to bulk silicon and molecules adsorbed on metal surfaces [155, 158]. Another SC implementation is available for the density-dependent dispersion correction (dDsC) of Steinmann and Corminboeuf [159, 160]. Also in this case the potential is analytical and the SC implementation was employed to study small molecular systems [161]. These studies indicate that self-consistency is responsible for small effects on the electron density and tiny modifications of the structure and stability [155, 158, 161]. However, SC vdW is expected to produce tiny modifications in the structure of small molecular systems, while an exhaustive investigation of the effects of self-consistency on the electron density and properties is still absent up to date. In this work we will apply our SC implementation to a large variety of systems, with particular interest in vdW bounded molecular complexes or larger and more challenging systems as metallic

surfaces and organic/inorganic interfaces.

The Self-Consistent Equations

We consider a set of N interacting particles and the associated HK energy functional, rewritten making explicit the XC energy term, see Equation 3.15. In principle, the long-range correlation interactions are absent in standard XC functionals and the term $E_{\mathrm{vdW^{TS}}}[n]$ should be added to the HK functional. Formally, the vdW functional is a part of the given XC functional,

$$E'_{\mathrm{xc}}[n] = E_{\mathrm{xc}}[n] + E_{\mathrm{vdW^{TS}}}[n]\,, \tag{7.4}$$

defined (in Equation 3.16) as the sum of the kinetic energy and the Coulomb potential, minus the kinetic term of the non-interacting system and the Hartree potential. The derivation of the KS eigenvalue equations can follow step-by-step the derivation performed in standard DFT, with the difference that we have now the long-range correlation term, besides the semi-local one. The variational method for N single-particle orbitals is now applied. Requiring the stationary of $E[n]$ with respect to variations of ψ_i, *i.e.* the variation of the energy equals zero, leads to the set of N one-electron equations

$$\left[-\frac{1}{2}\nabla^2 + v'_{\mathrm{eff}}(\mathbf{r})\right]\psi_i(\mathbf{r}) = \epsilon_i\psi_i(\mathbf{r})\,, \tag{7.5}$$

which need to be solved iteratively. As previously seen in Equation 3.17, the first term corresponds to the variation of $T_0[n]$, the kinetic energy of N non-interacting particles. The effective potential, $v'_{\mathrm{eff}}(\mathbf{r})$, sums all other contributions and is defined as

$$v'_{\mathrm{eff}}(\mathbf{r}) = v_{\mathrm{H}}(\mathbf{r}) + v_{\mathrm{ext}}(\mathbf{r}) + v'_{\mathrm{xc}}(\mathbf{r})\,, \tag{7.6}$$

where the first term is the Hartree potential and the second is the electron–nuclei electrostatic potential. The third term contains the potential of the standard exchange-correlation term, plus a new term: the vdW potential,

$$v'_{\mathrm{xc}}(\mathbf{r}) = v_{\mathrm{xc}}(\mathbf{r}) + v_{\mathrm{vdW^{TS}}}(\mathbf{r}) = \frac{\partial E_{\mathrm{xc}}[n]}{\partial n(\mathbf{r})} + \frac{\partial E_{\mathrm{vdW^{TS}}}[n]}{\partial n(\mathbf{r})}\,. \tag{7.7}$$

The vdW potential is thus obtained *via* the derivative of the vdW energy with respect to the electron density. The derivation has been performed analytically for the TS formula in Equation 7.1. All the terms will be shown afterward, in the next section (Section 7.1.2). The solution of a set of N equations with a modified effective potential, as the one in Equation 7.6, brings a different set of eigenvalues $\{\psi_i\}$ and eigenfunctions $\{\epsilon_i\}$, compared to those obtained with the effective potential without $v_{\mathrm{vdW^{TS}}}(\mathbf{r})$. Since the electron density is defined from the eigenfunctions as $n(\mathbf{r}) = \sum_i f_i\psi_i^*(\mathbf{r})\psi_i(\mathbf{r})$, it results directly modified by the "new" vdW term.

The total energy expression, previously introduced in Equation 3.20, is now adapted

to the SC vdW$^{\mathrm{TS}}$ implementation and takes the form

$$E[n] = \sum_i f_i \epsilon_i - \frac{1}{2}\int\int \frac{n(\mathbf{r})n(\mathbf{r}')}{|\mathbf{r}-\mathbf{r}'|} d\mathbf{r}d\mathbf{r}' + E_{\mathrm{xc}}[n] - \int v_{\mathrm{xc}}(\mathbf{r})n(\mathbf{r})d\mathbf{r} + \\ + E_{\mathrm{vdW^{TS}}}[n] - \int v_{\mathrm{vdW^{TS}}}(\mathbf{r})n(\mathbf{r})d\mathbf{r} + E_{n-n}\,, \tag{7.8}$$

in which the first line was also present in the "original" formula. However, the first term contains the eigenvalues and is directly affected by the modification of the KS eigenvalue equations (Equation 7.5). The second term, the Hartree potential (or electrostatics), together with the two XC terms are affected by vdW interactions *via* modifications in the electron density $n(\mathbf{r})$. The first two terms in the second line are the vdW$^{\mathrm{TS}}$ energy and the integrated vdW potential, respectively. These two additional contributions appear only in the SC implementation of the vdW$^{\mathrm{TS}}$ functional and exhibit similarity with the two XC terms. At last we find the nucleus–nucleus Coulomb repulsion, which is not dependent on the electron density and is left unaffected. It is important to remember that this expression is not only valid for the ground-state (converged) energy, but needs to be computed at each self-consistent cycle, as sketched in Figure 7.1. From the same figure, one can clearly see the differences with the simpler *a posteriori* vdW correction. The latter is performed just once, on top of the converged value and contains only the total vdW energy, without the integrated potential term, as written in Equation 7.3.

In practice, in the FHI-aims, during the iterative procedure, the energy is computed with a more efficient method, which involves the eigenvalues, obtained from the solution of KS equations, and the electron density of the previous SC cycle. Apart from the sum of the eigenvalues, all other quantities are already prepared at the beginning of the cycle. With this alternative formula, called Harris functional and discussed in more detail in Appendix C.2, the evaluation of the total energy becomes much faster. The convergence is checked by measuring the variation of the Harris energy between two successive iterations.

Self-Consistent van der Waals Forces

Beside the SC implementation of the vdW energy into the DFT, it is possible to derive and implement self-consistently the vdW forces too. At the present stage, the forces are computed using the formula $\partial E^{AB}_{\mathrm{vdW^{TS}}}[n]/\partial R_{AB}$ and are associated with the *a posteriori* implementation. Looking at the TS formula in Equation 7.1, the partial derivative above is performed by deriving the two factors that contain the interatomic distance: R_{AB}^{-6} and the damping function. In principle, for a "complete" derivation of the forces, one should consider the total derivative with respect to a nuclear displacement of atom A along the x-direction, $\mathrm{d}E_{\mathrm{KS+vdW^{TS}}}[n]/\mathrm{d}R^x_A$. Following this derivation, one finds the contribution coming from the partial derivative with respect to R^x_A, plus two extra terms. These two terms, called also Pulay forces, are the derivative of the orbitals, see Equation 6.1, with respect to the nuclear coordinate. One term comes from the derivative of the coefficients

and the other of the basis set. Under the condition of self-consistent energy and with an ideally complete basis set, the Hellmann-Feynman [162, 163] (H-F) theorem can be applied, leading to the simple formula for the forces: $\partial E_{\mathrm{KS+vdW^{TS}}}[n]/\partial R_A^x$, without involving the basis functions. Moreover, the TS vdW scheme introduces other factors that depend on the atomic position *via* the Hirshfeld partitioning of the density, written in Equation 4.13. In this regard, one should differentiate $\gamma_A[n]$ and $\gamma_B[n]$ with respect to R_A to obtain new terms, in addition to the partial derivatives. Nevertheless, the derivatives of the Hirshfeld volume are much smaller than the partial derivatives and are thus neglected. Also, in the *a posteriori* scheme, the derivatives of the basis set should be both present, but they effectively cancel each others. In conclusion, the implementation of the vdW forces with the partial derivatives (called H-F forces) and no Pulay forces is well suited within the *a posteriori* scheme.

At self-consistency, the energy is minimized with respect to the electron density, *i.e.* by solving the eigenvalue problem in Equation 6.2. It follows that the derivatives of the coefficients with respect to the nuclear coordinates are zero by definition. On the contrary, the derivative of the basis set would be zero only with a complete basis or if the dependence on the atomic positions is absent. Of course, a true completeness is never achieved in practical calculations. However, to cancel the Pulay terms, it is only necessary that the incompleteness is equal for all atomic positions. This condition is matched, for instance, using plane-wave. Thus, the Pulay forces vanish for the plane-waves basis set. We consider now the SC implementation of the TS energy in FHI-aims. In this case, only the derivative of the coefficients with respect to the atomic position vanishes. Therefore, the simple H-F forces can not be implemented alone, but the *implicit* derivative of the basis set should be included as well. A more complex implementation is always associated with a reduced computational efficiency, which needs to be summed on top of the cost of the self-consistent energy. The appeal of the SC forces is reduced also because the effects of self-consistency on the structure of materials is expected to be very small. In this thesis we will go through this claim and prove, for example, that the *a posteriori* cohesive energy calculations are indeed almost indistinguishable from the SC ones. In conclusion, due to the additional computational cost and the small effects, the TS SC forces are not (yet) available in FHI-aims.

The Tkatchenko-Scheffler vdW Potential

This section contains the analytical derivation of the vdW potential for the TS functional. Here, we follow the derivation by Robert A. DiStasio Jr., which has been originally implemented in the plane-wave pseudopotential code Quantum ESPRESSO [164, 165]. After introducing the basic equations, we will focus on the implementation into the all-electron code FHI-aims [151], which has been employed for all the calculations presented in this work.

As pointed out in Equation 7.7, the vdW potential is the derivative of the energy with respect to the electron density. Therefore, we consider now the derivative of Equation 7.1,

the TS energy formula

$$v_{\mathrm{vdW^{TS}}}[n(\mathbf{r})] = \frac{\partial E_{\mathrm{vdW^{TS}}}[n]}{\partial n(\mathbf{r})} = -\frac{1}{2}\sum_{AB}\left[\left(\frac{\delta C_{6,AB}^{eff}[n(\mathbf{r})]}{\delta n(\mathbf{r})}\right) R_{AB}^{-6} f_{damp}^{AB}[n(\mathbf{r})] + \right.$$
$$\left. + C_{6,AB}^{eff}[n(\mathbf{r})] R_{AB}^{-6}\left(\frac{\delta f_{damp}^{AB}[n(\mathbf{r})]}{\delta n(\mathbf{r})}\right)\right]. \quad (7.9)$$

Before analyzing the derivative of the two terms, we note that in the TS formula the electron density affects only the effective volume. Thus, the core quantity necessary for computing the vdW potential is the functional derivative of the factor $\gamma[n(\mathbf{r})]$, see Equation 4.13. In particular, the analytical expression is obtained by deriving the Hirshfeld volume $V_A[n(\mathbf{r})]$ with respect to the electron density:

$$\frac{\delta\gamma_A[n(\mathbf{r})]}{\delta n(\mathbf{r})} = \frac{1}{V_A^{free}}\frac{\delta V_A[n(\mathbf{r})]}{\delta n(\mathbf{r})} = \frac{1}{V_A^{free}} r^3 w_A(\mathbf{r})\,. \quad (7.10)$$

This result allows us to write the functional derivatives of all the three effective quantities: the polarizability, the homonuclear C_6 coefficient and the vdW radius, written in Equation 4.15, Equation 4.16 and Equation 4.17, respectively,

$$\frac{\delta\alpha_A^{0,eff}[n(\mathbf{r})]}{\delta n(\mathbf{r})} = \frac{\alpha_A^{0,free}}{V_A^{free}} r^3 w_A(\mathbf{r}) = \left(\frac{\alpha_A^{0,eff}[n(\mathbf{r})]}{V_A[n(\mathbf{r})]}\right) r^3 w_A(\mathbf{r})\,, \quad (7.11)$$

$$\frac{\delta C_{6,AA}^{eff}[n(\mathbf{r})]}{\delta n(\mathbf{r})} = \left(\frac{2V_A[n(\mathbf{r})]C_{6,AA}^{free}}{(V_A^{free})^2}\right) r^3 w_A(\mathbf{r}) = \left(\frac{2C_{6,AA}^{eff}[n(\mathbf{r})]}{V_A[n(\mathbf{r})]}\right) r^3 w_A(\mathbf{r})\,, \quad (7.12)$$

$$\frac{\delta R_A^{0,eff}[n(\mathbf{r})]}{\delta n(\mathbf{r})} = \left(\frac{R_A^{0,free}}{3(V_A[n(\mathbf{r})])^{2/3}(V_A^{free})^{1/3}}\right) r^3 w_A(\mathbf{r}) = \left(\frac{R_A^{0,eff}[n(\mathbf{r})]}{3\,V_A[n(\mathbf{r})]}\right) r^3 w_A(\mathbf{r})\,. \quad (7.13)$$

With these expressions in hand, we can now proceed to tackle the two derivatives in Equation 7.9 and write the analytical formula of $v_{\mathrm{vdW^{TS}}}[n(\mathbf{r})]$.

The effective C_6 coefficient for a pair of atoms is defined in a convenient form in Equation 7.2. The derivative of that expression is computed using the product rule for the derivatives of the two $\gamma[n(\mathbf{r})]$, see Equation 7.10,

$$\frac{\delta C_{6,AB}^{eff}[n(\mathbf{r})]}{\delta n(\mathbf{r})} = C_{6,AB}^{free}[n(\mathbf{r})]\left(\frac{\delta\gamma_A[n(\mathbf{r})]}{\delta n(\mathbf{r})}\gamma_B[n(\mathbf{r})] + \gamma_A[n(\mathbf{r})]\frac{\delta\gamma_B[n(\mathbf{r})]}{\delta n(\mathbf{r})}\right) =$$
$$= C_{6,AB}^{free}[n(\mathbf{r})]\left[\left(\frac{r^3 w_A(\mathbf{r})}{V_A^{free}}\right)\left(\frac{V_B[n(\mathbf{r})]}{V_B^{free}}\right) + \left(\frac{V_A[n(\mathbf{r})]}{V_A^{free}}\right)\left(\frac{r^3 w_B(\mathbf{r})}{V_B^{free}}\right)\right]. \quad (7.14)$$

Alternatively, one can obtain the same result by using the derivative of the effective polarizability and homonuclear C_6 coefficient, written in Equation 7.11 and Equation 7.12. Then substitute those expressions, for a pair of atoms, into the "original" definition of $C_{6,AB}^{eff}$, given in Equation 4.12. With the derivative of $C_{6,AB}^{eff}$, the first term of the vdW

potential is now completely defined.

The second term contains the derivative of the damping function, $f_{damp}^{AB}(R_{AB}, R_{AB}^{0}[n(\mathbf{r}])$, which depends on $n(\mathbf{r})$ via $R_{AB}^{0,eff}[n(\mathbf{r})] = R_{A}^{0,eff}[n(\mathbf{r})] + R_{B}^{0,eff}[n(\mathbf{r})]$, the effective vdW radii of atoms A and B. Therefore, the derivative is computed using the chain rule for the composition of two functions,

$$\frac{\delta f_{damp}^{AB}(R_{AB}, R_{AB}^{0,eff}[n(\mathbf{r}])}{\delta n(\mathbf{r})} = \left(\frac{\delta f_{damp}^{AB}(R_{AB}, R_{AB}^{0,eff}[n(\mathbf{r}])}{\delta R_{A}^{0,eff}[n(\mathbf{r})]}\right)\left(\frac{\delta R_{A}^{0,eff}[n(\mathbf{r})]}{\delta n(\mathbf{r})}\right) +$$
$$+ \left(\frac{\delta f_{damp}^{AB}(R_{AB}, R_{AB}^{0,eff}[n(\mathbf{r}])}{\delta R_{B}^{0,eff}[n(\mathbf{r})]}\right)\left(\frac{\delta R_{B}^{0,eff}[n(\mathbf{r})]}{\delta n(\mathbf{r})}\right) =$$
$$= \left(\frac{\delta f_{damp}^{AB}(R_{AB}, R_{AB}^{0,eff}[n(\mathbf{r}])}{\delta R_{A}^{0,eff}[n(\mathbf{r})]}\right)\left[\left(\frac{\delta R_{A}^{0,eff}[n(\mathbf{r})]}{\delta n(\mathbf{r})}\right) + \left(\frac{\delta R_{B}^{0,eff}[n(\mathbf{r})]}{\delta n(\mathbf{r})}\right)\right]. \quad (7.15)$$

In the last passage we used the fact that the derivative of the damping function with respect to $R_{A}^{0,eff}[n(\mathbf{r})]$ is identical to the one with respect to $R_{B}^{0,eff}[n(\mathbf{r})]$ by symmetry:

$$\left(\frac{\delta f_{damp}^{AB}(R_{AB}, R_{AB}^{0,eff}[n(\mathbf{r}])}{\delta R_{B}^{0,eff}[n(\mathbf{r})]}\right) = \left(\frac{\delta f_{damp}^{AB}(R_{AB}, R_{AB}^{0,eff}[n(\mathbf{r}])}{\delta R_{A}^{0,eff}[n(\mathbf{r})]}\right). \quad (7.16)$$

Let us consider the derivative of the damping function with respect to $R_{A}^{0,eff}[n(\mathbf{r})]$. Using the definition of $f_{damp}^{AB}(R_{AB}, R_{AB}^{0,eff}[n(\mathbf{r}])$, given in Equation 4.18, we obtain

$$\left(\frac{\delta f_{damp}^{AB}(R_{AB}, R_{AB}^{0,eff}[n(\mathbf{r})])}{\delta R_{A}^{0,eff}[n(\mathbf{r})]}\right) = \frac{-dR_{AB}\exp[-d(\frac{R_{AB}}{s_R R_{AB}^{0,eff}[n(\mathbf{r})]-1})]}{s_R(R_{AB}^{0,eff}[n(\mathbf{r})])^2(1+\exp[-d(\frac{R_{AB}}{s_R R_{AB}^{0,eff}[n(\mathbf{r})]-1})])^2} =$$
$$= \frac{-dR_{AB}\exp[-d(\frac{R_{AB}}{s_R R_{AB}^{0,eff}[n(\mathbf{r})]-1})]}{s_R(R_{AB}^{0,eff}[n(\mathbf{r})])^2}\left(f_{damp}^{AB}(R_{AB}, R_{AB}^{0,eff}[n(\mathbf{r})])\right)^2. \quad (7.17)$$

The symmetry property can now be easily verified by repeating the steps above and evaluating the derivative with respect to $R_{B}^{0,eff}[n(\mathbf{r})]$. The second component of the total derivative, the derivative of the effective radius with respect to the electron density, has been already shown in Equation 7.13. Therefore, the second term of the vdW potential is finally obtained with the combination of Equation 7.17 and Equation 7.13 (evaluated for atom A and B), into Equation 7.15. The analytical derivation of the $\mathrm{vdW}^{\mathrm{TS}}$ potential is now complete.

7.2 Numerical Implementation

The technical details about the SC implementation of the $\mathrm{vdW}^{\mathrm{TS}}$ functional into the code will be now discussed. First, FHI-aims is an all-electron code that uses a real-space numerical integration. In other words, all quantities are obtained with an integration performed over a set of points distributed in a real-space grid, as discussed in Section 6.2.

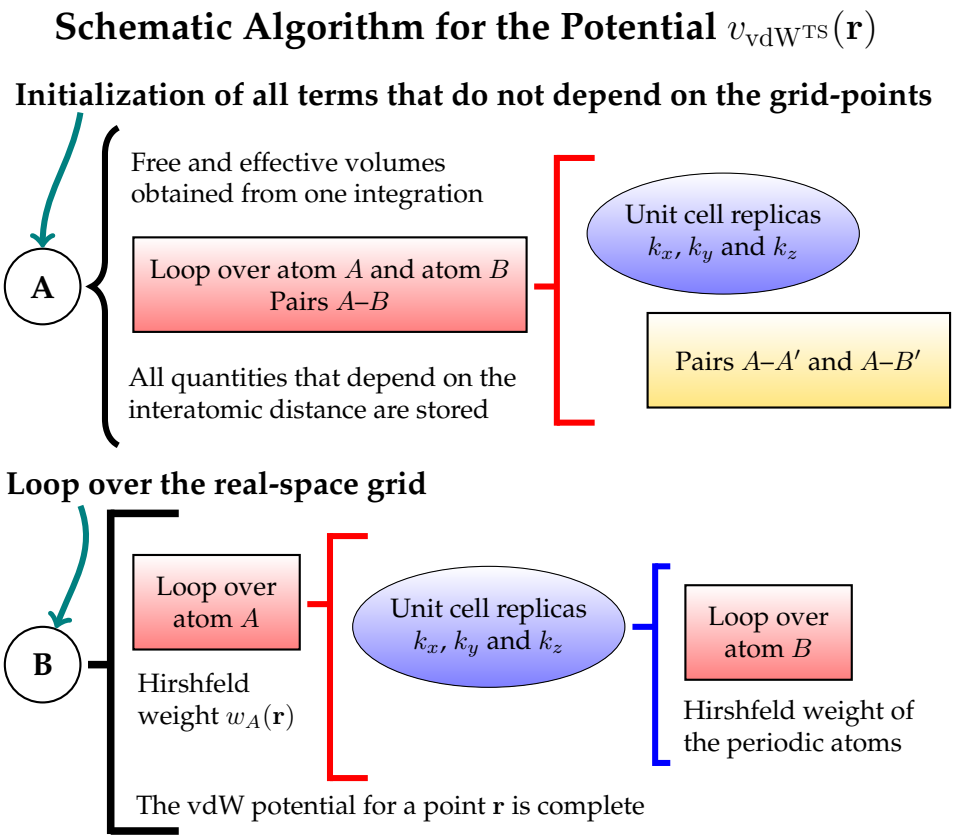

Figure 7.2: Schematic representation of the main steps employed in the algorithm of the vdW potential. In part **A**, the initial integrated quantities are manipulated with a loop over the atomic pairs (rectangle in red), and a loop over the periodic images of the unit cell (ellipse in blue). At this stage, the atom-atom distance is computed for each pair and all the terms that do not depend on the grid-points are build and stored in a table. In part **B**, the black square bracket refers to the loop over the real-space integration grid. This loop is necessary to evaluate the distance between a specific grid-point and an atom and to compute its Hirshfeld partitioning weight $w_A(\mathbf{r})$. Rectangles (in red) and ellipses (in blue), are associated respectively with loops over atoms and over the periodic repetitions of the unit cell.

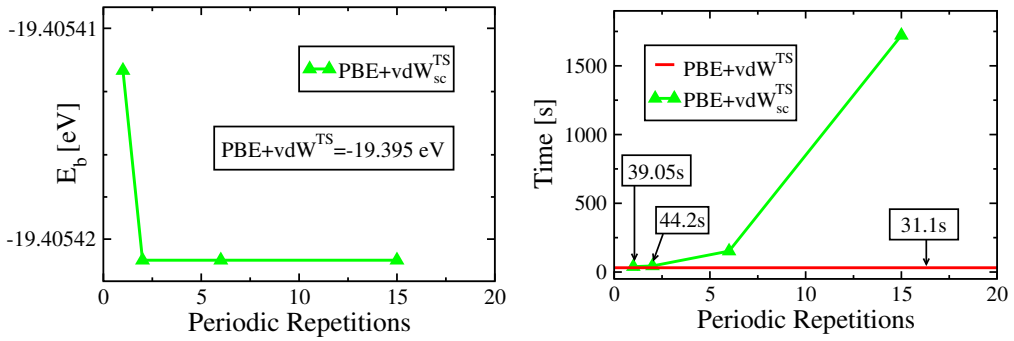

Figure 7.3: Silver (111) surface with six metal layers. Left panel: PBE+vdW$^{\mathrm{TS}}_{\mathrm{sc}}$ binding energy in function of periodic repetitions, per unit vector, of the unit cell. The inset reports the value obtained with the (non-SC) PBE+vdW$^{\mathrm{TS}}$ method. Right panel: the time consumed for a calculation is plotted as a function of the periodic replica. The values are the average time per self-consistent cycle. The horizontal line at the bottom indicates the time spent for one cycle in the *a posteriori* calculation. All the computational details are reported in Appendix C.3.

In our vdW potential, the integrals are used to compute only the quantities that depend on the electron density $n(\mathbf{r})$. The other quantities depend only on the type of atoms and their total number and are kept fixed during the convergence. Meaning that, they can be constructed with rather fast operations at the beginning of each calculation. By looking at the equations that form the vdW potential, one can see that the Hirshfeld volume needs to be computed through an integration over the grid points. Consequently, all the effective quantities are obtained after this operation. Given a system of N atoms, we consider the Hirshfeld ratio (Equation 4.13) for an atom A. Clearly, the electron density enters the integral in the numerator. For this reason the effective volume must be evaluated at each self-consistent cycle. On the other hand, the Hirshfeld weight and the free volume carry a dependence on the grid points, but are derived from the "free" non-interacting density $n^{free}(\mathbf{r})$, *i.e.* the density of an atom considered as isolated. In principle these terms can be computed with just one single integration performed at the beginning, when the calculation is initialized. After that, they can be stored in a vector with N entries, used to build the potential in each self-consistent cycle.

The vdW potential is, by construction, derived from the vdW energy, which is a property of the whole system. On the contrary, the derivative of $E_{\mathrm{vdW^{TS}}}[n]$ with respect to the electron density is evaluated at each point of the grid, as it is done for the electron density itself. In practice, one loop over the grid is performed and a value of the potential $v_{\mathrm{vdW^{TS}}}(\mathbf{r})$ is assigned for each grid-point. Since the potential is computed with pairs of atoms, if follows that, for each grid-point a loop over all atomic pairs is performed. Of course, one can easily see how this operation consumes most of the CPU time in our implementation. There are many grid points (≈ 500 points per atom with light settings) and a first and easiest optimization of the code is to avoid to recompute every time the quantities that do not depend on the grid.

We start the routine with two vectors of N components, that contain the Hirshfeld

free and effective volumes. Before entering the loop over the grid, all the quantities that depend on the interatomic distance R_{AB} can be computed and stored in a table of $N_A \times N_B \times k_x \times k_y \times k_z$ components. The two N corresponds to the pairs and the three k are introduced in the periodic case for storing the atoms of the supercell. The schematic representation of these passages is sketched in Figure 7.2, upper part (A). For what concerns the derivative of the damping function, all terms in Equation 7.17 are available and also part of Equation 7.13. The only missing parts are the two derivative of the effective vdW radii, that contain the Hirshfeld partitioning weight, as well as the cube of the distance r^3. Both terms depend on the specific grid-point and must be computed inside the loop over the grid, indicated in part B of Figure 7.2 with the external square bracket. All terms are also available for the derivative of $C_{6,AB}^{eff}$, in Equation 7.14, except for the two terms: $r^3 w_A(\mathbf{r})$ and $r^3 w_B(\mathbf{r})$. These are coming from the two derivatives of the Hirshfeld ratio, see Equation 7.10. Therefore, the loop over the points of the grid is performed to compute the three ingredients left and combine them with the data stored in the table. As drawn in Figure 7.2, this operations require additional loops over the atoms and the periodic images of the unit cell. In summary, the introduction of a table reduces the CPU time, but increases the required memory. However, considering all the calculations performed during the extensive tests of the implementation, the higher memory requirements were never found to be an issue.

A way of reducing the computational cost would be to employ a distance cut-off. For instance, we can set a limit on the number of periodic repetitions of the unit cell. Another cut-off can be used to decide the maximum allowed distance between two atoms or between the grid-point and an atom. In the case of finite systems, no cut-off has been introduced in our implementation of the vdW potential. On the other hand, in order to treat periodic systems one needs to choose how many repetitions of the unit cell are considered. In this regard, the vdW energy has to be computed at each cycle and is converged using a supercell. In other words, the unit cell is replicated until the contributions of an atom A (in the unit cell) interacting with its images A' and other atoms B' become negligible. This happens because of the large distances between the pairs. In our vdW potential, we use the same number of replica of the energy calculation. Thus, the three loops with indices k_x, k_y and k_z, see Figure 7.2 part A, replicate the unit cell, reaching the supercell of the energy calculation. The second set of loops involving the periodic repetition of the unit cell is located inside the loop over the grid, part B of Figure 7.2.

Our first choice for the second loop over the periodic repetitions was to compute only the contributions inside the unit cell and in the first replicas. This decision could appear exaggerated, however one should remember that in this last step we compute only the cube of the distance r^3 and the Hirshfeld partitioning weights. The latter is a quantity localized roughly in the vicinity of an atom, while the points of the grid are always located inside the unit cell. Therefore, when is evaluated on the grid, the partitioning weight of an atom that belongs to a periodic image of the unit cell decays very quickly to zero. This conclusion has been assessed with actual calculations, as shown in Figure 7.3.

There, we plot the cohesive energies of a six-layered Ag(111) surface in function of the number of periodic repetitions. We choose the smallest possible unit cell, with one single atom per layer, in order stress the approximation introduced above. In fact, the atoms in the second repetitions, which are not considered in the cut-off, are separated from the grid-points of about 3–6 Å only. In this particular system, the binding energy is indeed slightly modified, by about 2×10^{-3} meV, when the second repetitions are included. In conclusion, the choice to consider up to one repetition of the unit cell shows its limitations only in the case of a very small unit cell. However, these systems contain a small number of total atoms and the second replicas of the unit cell contribute with a negligible correction of the energy. Moreover, additional repetitions of the unit cell vectors, at this stage, would cause only a significant slow down of the overall performance, without any effect on the energy. An idea can be grasped by considering the right panel of Figure 7.3, where we report the average time per SC cycle, with different repetitions of the unit cell. Even with such a small unit cell, the performance is highly affected when large supercells are considered. It is also important to mention that this particular example is a surface, hence the periodicity expands in two directions only, k_x and k_y. The increasing of the CPU time for a 3D periodic system would be even worse. In conclusion, the SC scheme has a computational cost, for very large periodic systems, comparable to a DFT calculation with a GGA functional. The applicability of the implementation presented above has the same limits of standard DFT, even though an improvement of the efficiency would be highly desirable. This issue will be discussed with more details in the next section, where we will present a new and improved version of the implementation and compare it with the "standard" one.

7.3 Optimization of the Implementation

A first modification of the implementation presented before is the introduction of a "smart" cut-off for the periodic repetition of the unit cell. We are referring to the second loop over the indices k, indicated in part B of Figure 7.2 (the ellipse). Even though our tests confirmed that the effects of the cut-off are negligible for the energy, see Figure 7.3, we decided to improve the previous choice ($k_x = k_y = k_z = 1$) with a value that adjusts itself, depending on the dimensions of the cell. The number of replicas is determined by the ratio between a limiting value, set equal to 10 Ångstrom, and the vector of the unit cell: $k = 1 + 10/(\text{Primitive vector})$. Naturally, when the vector is larger than 10 Ångstrom, only one replica is considered. This solution offers a safe remedy in case of small unit cells and recovers the previous cut-off with large systems. Looking at the Ag(111) surface, the example in Figure 7.3, the periodic repetitions obtained with the new cut-off are $k_x = k_y = 4$ and $k_z = 1$.

In the case of finite systems, the loops over the indices k, see the two ellipses in part A and B of Figure 7.2, are simply removed from the algorithm. Moreover, the columns of the table (where the quantities are stored) are now significantly reduced to only two

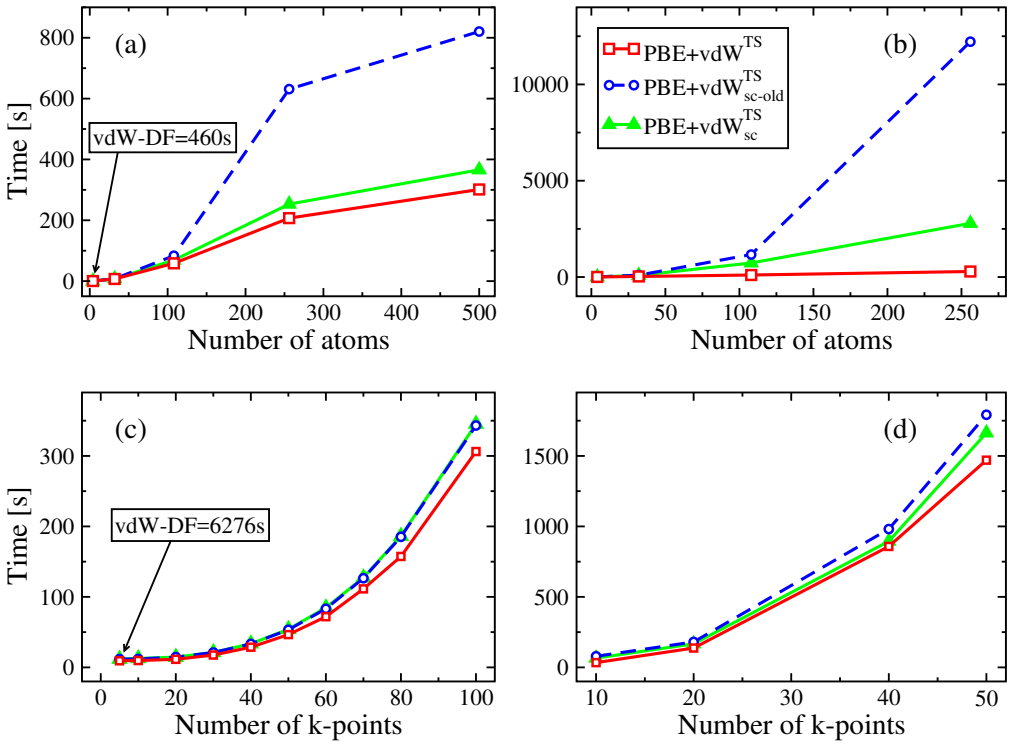

Figure 7.4: Average time consumed for a self-consistent cycle of copper bulk, obtained with different implementations of the TS functional. Top left and right: scaling of the non-periodic in (a) and the periodic in (b) as the number of atoms increases. Bottom left and right: periodic Cu bulk with a unit cell of 4 atoms in (c) and 32 atoms in (d), which are sampled with an increasing number of k-points. The results obtained with SC vdW-DF are reported in the two insets in panel (a) and (c). All the computational details are available in Appendix C.3.

columns with N elements each. Another advantage is that the contribution of a given pair of atoms can be conveniently partitioned back into atomic contributions. By looking at Equation 7.14 and Equation 7.15 one can see that most of the terms referring to atom A are uncoupled to atom B. Of course the interatomic distance depends on both A and B. Also, in the derivative of the C_6 coefficients, the Hirshfeld ratio of atom B is multiplied by the free volume of atom A. However, as previously discussed,the dependence on the grid-points is absent in these quantities. Therefore, the contribution of atom A to $v_{\mathrm{vdW^{TS}}}(\mathbf{r})$, due to the interaction A–B, can be computed before the loop over the grid and stored in a single vector of N components. This implies a reduction in the memory usage, which is joined by a lower CPU time. In fact, the loop over the grid-points contains a double loop over the pairs A–B, see the two rectangles in Figure 7.2 part B, which is now reduced to a single loop over all atoms (without the factor $1/2$ in front of the potential). Unfortunately, in the case of periodic systems, these optimizations are not available straightforwardly. Hence, the scaling of the method is for now visibly worsened by the periodicity, with respect to non-periodic systems.

A reformulation of the original algorithm is necessary to enable the same simplifi-

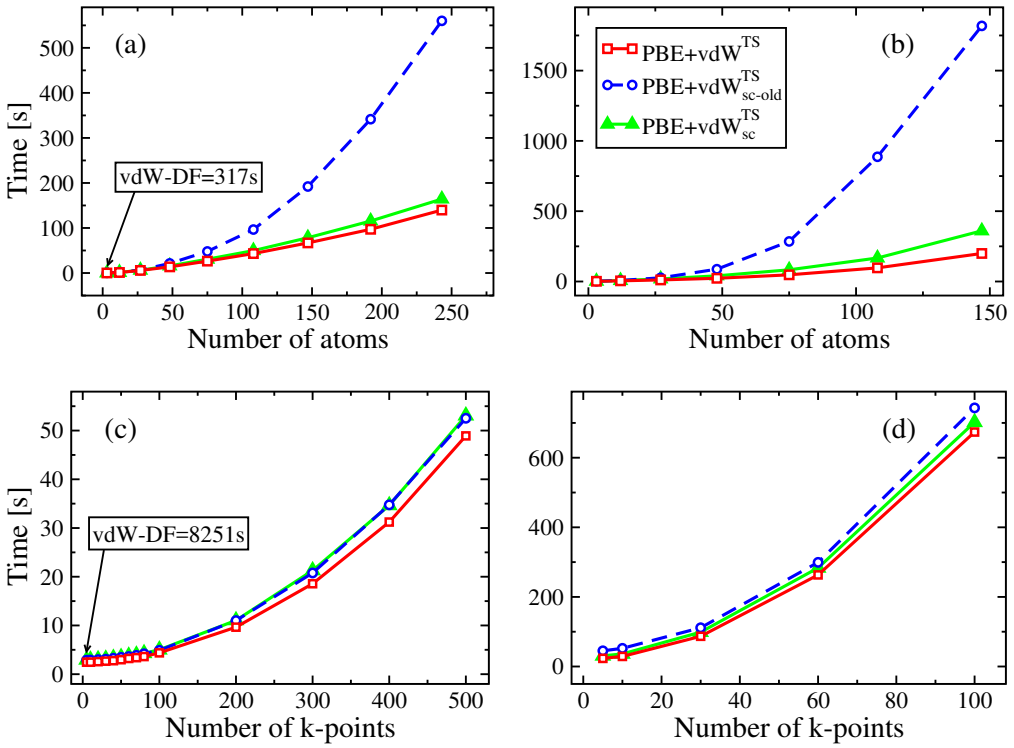

Figure 7.5: Silver surface (111). In the four plots are reported the performances of the *a posteriori* TS scheme, along with the two SC implementations. Panel (a): non-periodic systems with different number of atoms. Panel (b): periodic system tested with several unit cells. Bottom panels: periodic surface with a unit cell of 3 atoms (c) and 27 atoms (d). An increasing number of k-points is employed. In the insets are reported the performances of SC vdW-DF. All the settings used in these simulations are available in Appendix C.3.

cation for periodic systems. Instead of writing a table with $N_A \times N_B \times k_x \times k_y \times k_z$ components, it is possible, with a reorganization and optimization of the loops, to store all necessary quantities using "only" $N_B \times k_x \times k_y \times k_z$ elements. The reduced memory consumption, due to the lower dimensionality of the table, is associated with a modification in the algorithm. Looking at part B in Figure 7.2, the first loop over the atoms, the rectangular box on the left, is simply removed from the code. Since we managed to remove a factor of N, the CPU time employed for the SC scheme results visibly reduced, in particular for systems with a large number of atoms. Most importantly, the table of data stored in the memory is called at each loop over the grid (part B of Figure 7.2). Calling a matrix of stored elements is an operation that can significantly slow down the efficiency of an algorithm. In this regard, the optimized scheme yields a considerable reduction of the total number of calls, which is the main reason behind the improved computational performances.

As a first test we employed the copper bulk, considered with different number of atoms in the unit cell and varying the samplings of the reciprocal space. The perfor-

mance of the improved implementation ($\mathrm{vdW}^{\mathrm{TS}}_{\mathrm{sc}}$) is compared with the one without any optimization ($\mathrm{vdW}^{\mathrm{TS}}_{\mathrm{sc-old}}$) and with the standard *a posterior* approach ($\mathrm{vdW}^{\mathrm{TS}}$). As we can see from Figure 7.4 (a), simply increasing the number of atoms, with no periodicity, drastically reduces the efficiency of the scheme. The CPU time of the original algorithm in Figure 7.2 is, at least, 50% longer than a regular DFT calculation. For very large systems, it becomes about four times more expensive than the *a posteriori* calculation. The new implementation, instead, scales much better. The time needed for a calculation with the $\mathrm{PBE} + \mathrm{vdW}^{\mathrm{TS}}_{\mathrm{sc}}$ functional ranges between 15 and 25% more than the one of $\mathrm{PBE} + \mathrm{vdW}^{\mathrm{TS}}$. This improvement is the direct consequence of the simplification introduced in the algorithm for finite systems, as described above. The second simplification that we have introduced in the algorithm, valid for periodic systems, is tested in panel (b) of Figure 7.4. The time for a self-consistent cycle is plotted as a function of the number of atoms in the unit cell. Similarly as before, the scaling results much improved with the new version of the code. Considering for instance the system with 108 atoms, the time for a SC calculation is almost halved, becoming more than three times less, in the last case tested.

In the bottom of Figure 7.4, both graphs report the CPU time per self-consistent cycle as the number of k-points increases. The smallest unit cell, only 4 atoms, is considered in panel (c). One can see that, in this case, the number of k-points is not affecting the scaling of both SC implementations. The computational time of $\mathrm{vdW}^{\mathrm{TS}}_{\mathrm{sc-old}}$ and $\mathrm{vdW}^{\mathrm{TS}}_{\mathrm{sc}}$ is practically the same and differs from the *a posteriori* calculations by roughly 15%, independently of the number of k-points. In panel (d) the same test has been performed using a larger unit cell, that contains 32 atoms. Also in this case, the scaling is not significantly affected by the different number of k-points employed. However, the number of atoms is now increased with respect to the previous system. This has the effect of slowing down the non-optimized implementation, that costs roughly 20–30% more than the $\mathrm{PBE} + \mathrm{vdW}^{\mathrm{TS}}$. The performance of $\mathrm{vdW}^{\mathrm{TS}}_{\mathrm{sc}}$ fits in between the two other schemes. The CPU time is up to 20% more than the *a posteriori* one, but this difference stays below 15% in most cases. In figure (a) and (c) there is an inset reporting the time taken by the SC vdW-DF, applied to the smallest system. Clearly, the absolute numbers are much larger with respect to the TS ones, severely limiting the applicability of the functional to large systems. Apart from that, the resulting scaling laws, restricted to the data available, are similar to the ones found with the TS functional. For example, considering the non-periodic cluster, going from 4 atoms to 32, increases the CPU time by a factor of ~ 6, while ~ 5 was found with both the SC and non-SC version of the TS. We note that the current implementation of the SC vdW-DF in FHI-aims is probably suitable for optimizations, that would lead to faster performances.

The second test system is a metal surface: Ag(111). The surface has three metal layers and is computed, as for bulk Cu, considering several unit cells with a different number of atoms, see Figure 7.5 (a) and (b). In both non-periodic and periodic case, the scaling of the optimized SC method follows quite closely the path of the non-SC scheme. Marked differences emerge only for very large and periodic systems, see panel (b). For the

non-periodic geometries in (a), the CPU time of $\mathrm{vdW}_{\mathrm{sc}}^{\mathrm{TS}}$ is up to 20% more than the *a posteriori* one. Nevertheless, this value is reached only with very large unit cells. On the other hand, when $\mathrm{vdW}_{\mathrm{sc-old}}^{\mathrm{TS}}$ is used, the time for a calculation increases, already for medium-sized systems, by 80–100%.

We consider now the same unit cell, tested with different meshes of k-point. The difference between the two SC implementations become significantly less marked. In panel (c), the chosen unit cell contains only 3 atoms. We can see that the two schemes are basically indistinguishable. We remind the reader that an equal CPU time is not an obvious result since the cut-off in the $\mathrm{vdW}_{\mathrm{sc}}^{\mathrm{TS}}$ includes, for this particular system, 4 repetitions of the unit cell along two directions (x and y). On the other hand, only one replica per unit vector is considered in the $\mathrm{vdW}_{\mathrm{sc-old}}^{\mathrm{TS}}$ scheme. The situation changes in panel (d), where we employed a unit cell composed by 27 atoms. The number of repetitions with $\mathrm{vdW}_{\mathrm{sc}}^{\mathrm{TS}}$ is reduced to $k_x = k_y = 2$. In this case, a factor of N (spared with $\mathrm{vdW}_{\mathrm{sc}}^{\mathrm{TS}}$) has a sensible weight on the total algorithm and a clear difference emerges between the two schemes. The optimized SC implementation is located roughly in between $\mathrm{vdW}_{\mathrm{sc-old}}^{\mathrm{TS}}$ and $\mathrm{vdW}^{\mathrm{TS}}$. Initially, self-consistency increases the time of a calculation of about 10–25%, while after the optimization the algorithm reduces the workload to a factor of 5–10%.

In conclusion, the algorithm employed in the $\mathrm{vdW}_{\mathrm{sc}}^{\mathrm{TS}}$ implementation delivers satisfactory computational performances and can be coupled with standard XC functionals, as PBE or PBE0, without limiting the applicability of DFT. Apart from the necessary cut-off, that regulates the number of periodic repetitions, the SC equations have been implemented without any approximation so far. In this regard, it is possible to further speed up the efficiency of the algorithm adding, for example, a cut-off that sets the maximum allowed distance between a grid-point and an atom. This type of cut-off would enter the computationally expensive loop over the grid, see part B of Figure 7.2, leading to further improvements in the efficiency of $\mathrm{vdW}_{\mathrm{sc}}^{\mathrm{TS}}$. However, the idea of approximating the interactions with a cut-off on the distance might cause some underestimation of the vdW contributions, which are long-ranged by definition. The risk of altered results and the necessity of careful extra tests is not balanced with an urgent need of a more efficient implementation. For these reasons, we have decided to avoid any additional cut-off in the present version of the $\mathrm{vdW}_{\mathrm{sc}}^{\mathrm{TS}}$. From now on, every time the TS SC implementation will be mentioned, we will automatically refer to the optimized $\mathrm{vdW}_{\mathrm{sc}}^{\mathrm{TS}}$ version, unless stated otherwise.

Another way to speed up the implementation, only in the case of surfaces, would be to avoid the periodic replicas along the direction of the vacuum slab. Usually, a very large vacuum is employed to effectively reduce these unphysical interactions to zero. Hence it would be faster to introduce an approximation *ad hoc* simply to avoid to compute and store these data. A simple implementation of this feature can be done with the introduction of a flag, which indicates the presence of a surface and the orientation of the vacuum.

Part IV

Applications

8 Molecular Complexes

Here we present the results of the DFA + $\mathrm{vdW}_{\mathrm{sc}}^{\mathrm{TS}}$ method applied first to small dimers such as noble-gas dimers and molecular complexes such as water dimer, carbon dimer, naphthalene dimers among other systems. The acronym DFA stands for an approximate XC density functional and refers here to PBE [52] in particular. The others XC functionals used in this section, coupled with $\mathrm{vdW}_{\mathrm{sc}}^{\mathrm{TS}}$, are HF and PBE0 [62], see Section 3.5.2 and Section 3.5.3. The $\mathrm{vdW}^{\mathrm{TS}}$ has been successfully tested and applied to a large range of molecular systems, starting at the point of its formulation [108], with extensive benchmarks and applications [166, 167]. Therefore, such large set of data available and already established for the *a posteriori* TS, represents the natural starting point for our comparison using the new SC scheme. Subsequently we will investigate the role of $\mathrm{vdW}^{\mathrm{TS}}$ on the electron density $n(\mathbf{r})$ and the electronic properties. The main findings reported in this section are taken from reference [168].

8.1 Total Energy

First, we consider the binding energies of two sets of systems, the S22 [88] database and the S66 [169] database. The S22 contains complexes of different interaction strengths, from hydrogen-bonded to weakly dispersion-bonded. The S66 provides a variety of systems relevant to organic molecules and biomolecules. The binding energy (E_b), for a

Table 8.1: Mean absolute error (MAE) and mean absolute percentage error (MAPE) for the S22 [88] and S66 [169] databases, tested with the PBE and PBE0 functionals. Both the SC and non-SC flavors of the TS are coupled with the two XC functionals. Extra details are available in Appendix D.1.

	S22 MAE [meV]	S22 MAPE	S66 MAE [meV]	S66 MAPE
PBE	115.94	57.80	93.79	57.23
PBE+$\mathrm{vdW}^{\mathrm{TS}}$	12.90	9.81	21.60	13.24
PBE+$\mathrm{vdW}_{\mathrm{sc}}^{\mathrm{TS}}$	12.96	9.85	21.64	13.25
PBE0	106.32	55.22	89.56	55.85
PBE0+$\mathrm{vdW}^{\mathrm{TS}}$	14.21	8.02	18.64	10.38
PBE0+$\mathrm{vdW}_{\mathrm{sc}}^{\mathrm{TS}}$	14.25	8.05	18.68	10.40

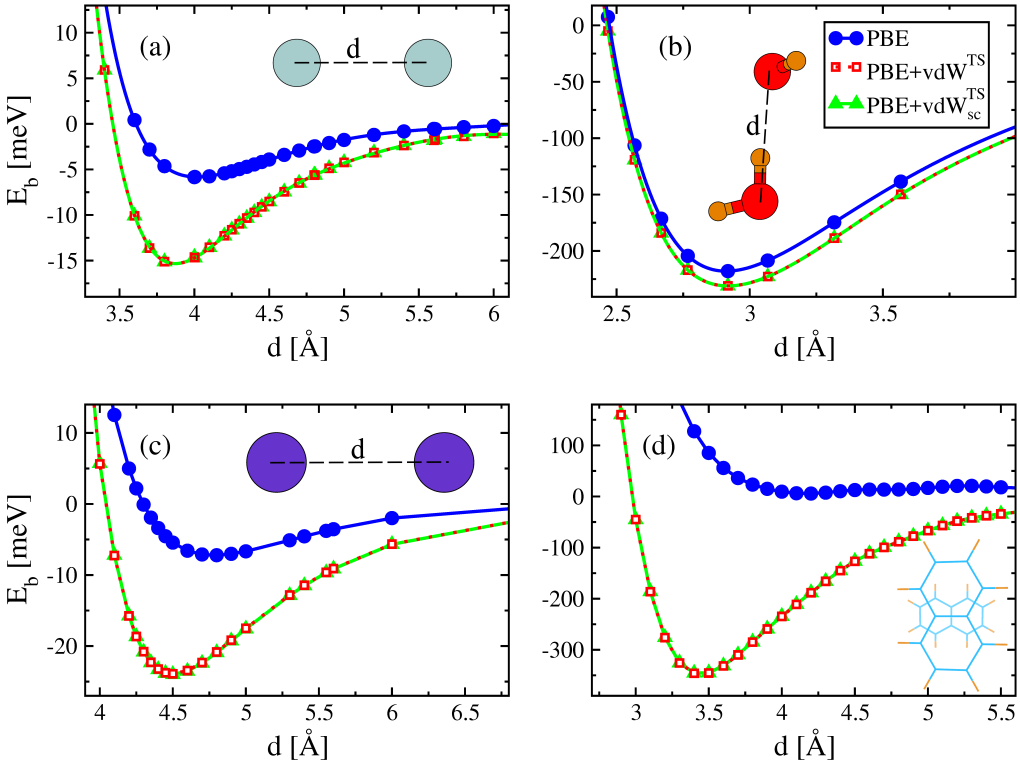

Figure 8.1: Binding energy curves computed with PBE, PBE+vdW$^{\mathrm{TS}}$ and PBE+vdW$^{\mathrm{TS}}_{\mathrm{sc}}$. Panel (a): Argon dimer. Panel (b): water dimer. Panel (c): Xenon dimer. Panel (d): naphthalene dimer considered with the cross-shaped configuration (c-dimer). The insets represent the structures used. The distance d between the two atoms/molecules is sketched with a black dashed line.

system composed of N molecules, is computed with the formula

$$E_b = E_{\mathrm{tot}} - \sum_{i=1}^{N} E_i \,, \tag{8.1}$$

where E_{tot} is the energy of the whole systems and E_i is the energy of a single fragment. From the results, summarized in Table 8.1, one can see that the TS method brings a great improvement in the performances of both the PBE and the PBE0 functionals. On the other hand, the inclusion of self-consistency provides only tiny modifications of the *a posteriori* binding energies, leaving the results practically unaffected. The interested reader can consult, in Appendix D.1, the complete set of numbers for the S22 database and verify the conclusion above.

Other tests systems have been employed to check whether self-consistency has any effect on the binding energies or not. We analyzed, for example, noble-gas dimers and molecular dimers. The binding energy E_b has been investigated not only at the equilibrium distance d_{eq}, but also a large number of different configurations are considered, ranging from small to very large interatomic/intermolecular distances. Four

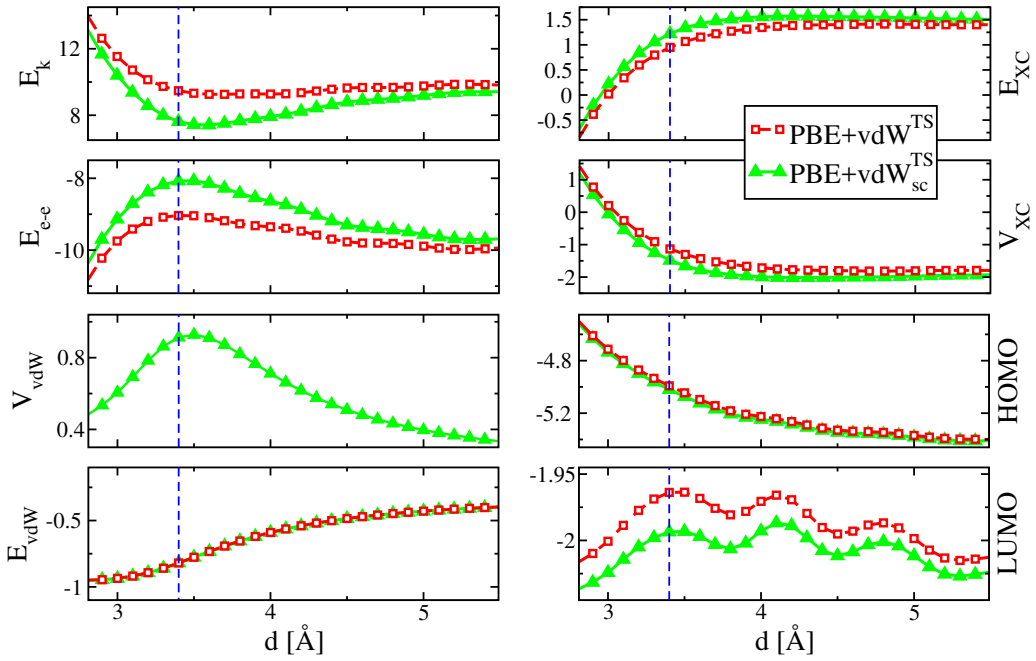

Figure 8.2: Naphthalene c-dimer: different components of the total energy, plotted as a function of the intermolecular distance d. In the panels are compared the results of the PBE+vdW$^{\mathrm{TS}}$ and the PBE+vdW$^{\mathrm{TS}}_{\mathrm{sc}}$ schemes. The potential is by definition available only with the SC vdW functional. The vertical (blue) dashed lines indicate the equilibrium distance. All values are in [eV].

selected systems, are reported in Figure 8.1. Two noble-gas dimers, Ar and Xe, are in panel (a) and (c). The noble-gas dimers have been studied also with PBE0 and HF, see Appendix D.1. These systems are characterized by a weak bonding and the vdW correlation is responsible for almost the total binding energy in the long-range part of the curve. The water dimer, plotted in panel (b), shows a much larger E_b. For this system the H $\cdots$ O hydrogen bond determines the binding and is well captured by PBE alone. The last system is slightly larger, two naphthalene molecules with parallel and crossed-shaped orientation, also called c-dimer. Since the naphthalene molecule contains two aromatic rings, the c-dimer is a non-covalent π-stack dimer. From the graph we can see that the binding is obtained only with the inclusion of dispersion interactions. Several different stable configurations can be formed with two naphthalene molecules. Two of these are plotted in Figure D.2. In the t-dimer, for instance, one molecule is rotated by $90°$ and the rings are not parallel. The consequence is a reduced E_b and a much larger equilibrium distance, with respect to other naphthalene dimers. Overall, for all the systems in Figure 8.1, the SC results overlap very well with the *a posteriori* binding energy curves. The very small differences in the binding energy ΔE_b between the two approaches are always below 1 meV. In detail, ΔE_b spans from a negligible 0.001% for the Argon dimer, to about 0.1% (~ 0.5 meV).

Since the *a posteriori* vdW correction is not affecting the electron density, the values of

the energy components—with the exception of $E_{\mathrm{vdW}^{\mathrm{TS}}}$—obtained with PBE+vdW$^{\mathrm{TS}}$ and PBE are exactly the same by definition. On the other hand, the total energy formula with SC vdW effects, written in Equation 7.8, suggests that the contributions of vdW interactions should be included in all the different terms, through the electron density and the eigenvalues. An idea of that can be grasped by looking in Figure 8.2, where we consider the naphthalene c-dimer and plotted the different components of the binding energy. At first glance, one can see that the curves obtained with PBE+vdW$^{\mathrm{TS}}$ and PBE+vdW$^{\mathrm{TS}}_{\mathrm{sc}}$ are not completely overlapping. However, the SC and non-SC vdW energies (E_{vdW}), shown in Figure 8.2, display a perfect agreement. We remind the reader that, in the case of vdW$^{\mathrm{TS}}_{\mathrm{sc}}$, an additional term exists: the integrated vdW potential (V_{vdW}), which is the sixth term in Equation 7.8. From Figure 8.2 it emerges that V_{vdW} is positive and counterbalances the vdW energy in the total energy formula, see the last two electronic terms in Equation 7.8. On the other hand, the *a posteriori* total energy, written in Equation 4.6, contains just the vdW energy. It follows that the "direct" vdW contributions to the energy of a system are different in the two schemes. In particular, considering the naphthalene c-dimer at the equilibrium distance, the V_{vdW} term reduces the binding by 0.9 eV. For what concerns the other terms, self-consistency decreases the kinetic energy of about 1.75 eV ($\sim 20\%$), while the electrostatic energy increases by 1 eV ($\sim 11\%$), see top-left panels in Figure 8.2. Smaller changes are also found in the XC energy and the integrated potential, shown in the top-right panels of Figure 8.2. All these different modifications of the energy components are summed up in the total energy and cancel out. It is indeed this balance that yields to a total negligible difference in the binding energies, which is, for the c-dimer, below 1 meV. In the same figure, on the bottom-right side are reported the changes in the HOMO and the LUMO. Also in this case, the effects of SC vdW are different for the two orbitals and change accordingly to the intermolecular distance. At the equilibrium distance, vdW$^{\mathrm{TS}}_{\mathrm{sc}}$ reduces the HOMO by 25 meV and the LUMO by 28 meV. The two modifications compensate, and the HOMO-LUMO gap is only 3 meV larger.

The effects on the different components of the total energy are a general feature of the SC vdW approach. A second example, the Xenon-Xenon dimer, is reported in Figure D.3 (Appendix D.1) to support our discussion on the naphthalene c-dimer. We focus now in particular on the difference between E_{vdW} and V_{vdW}, shown in Figure 8.3 for the argon, krypton and xenon dimers. Of course, for these systems the absolute values are much smaller than the ones found with the naphthalene dimer. However, as previously seen, the vdW potential is responsible for a reduction of E_b with a magnitude comparable to $E_{\mathrm{vdW}^{\mathrm{TS}}}$. In conclusion, SC effects are found to be responsible for large changes, typically on the order of 5%, in all the components of the total energy. Still, in most cases, the sum of the different terms results in a negligible difference in ΔE_b, as shown in Figure 8.1. In other words, these remarkable agreements fully validate the *a posteriori* results for binding energies between relatively weakly polarizable atoms and molecules and support the choice of such vdW scheme, which is computationally cheaper than the SC one.

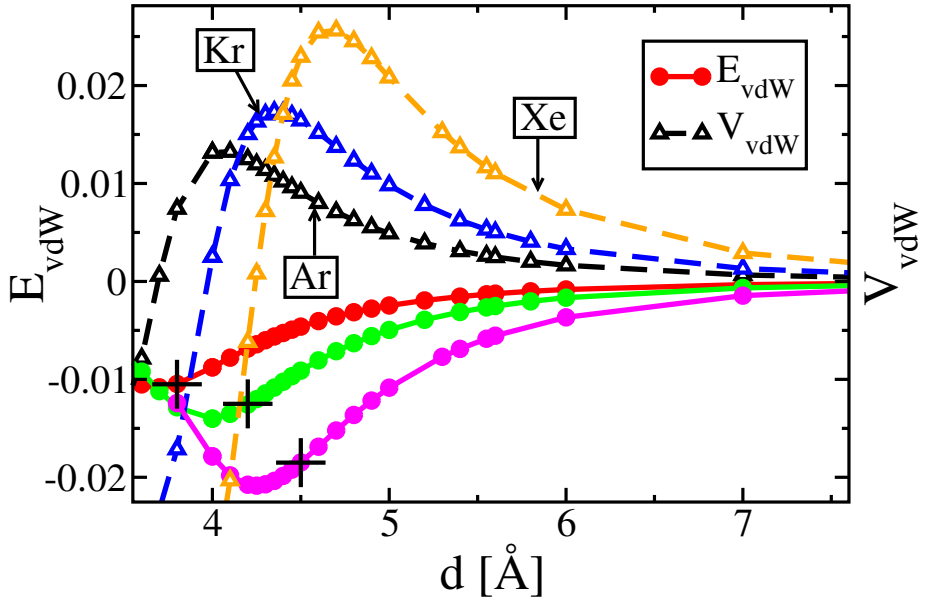

Figure 8.3: Comparison between the vdW energy (in dots) and the integrated potential (in triangles). The data are shown for three noble-gas dimers: Ar, Kr and Xe. The energies and the integrated potentials, reported in [eV], are plotted as a function of the interatomic distance d. For each dimer, the equilibrium distance is marked with a cross on the binding energy curve.

During our extensive tests we encountered some specific classes of systems that are particularly sensitive to SC effects. In the following sections we will analyze such systems in detail. As for now, following up with finite systems, in Figure 8.4 are sketched three different structures representing some systems with a non-negligible influence of self-consistency in the vdW energy and in the electronic properties. In (1) there is the $Li(NH_3)_4Na$ molecule, which belongs to the so-called metal-ammonia alkalides. In this family the number of NH_3 groups can vary, as well as the type of alkali metal atoms used, *e.g.* Li, Na and K. These molecules generally possess a considerable polarizability, first hyperpolarizability and dipole moment [170], which is oriented along the z-axis indicated in the figure, *i.e.* the direction that connects the two alkali metal atoms. In the particular case of $Li(NH_3)_4Na$, self-consistency increases by 0.25 Debye (D) ($\sim 3\%$) the total dipole moment. Considering that the effect on the dipole moment is about 0.01–0.05 D for systems as the naphthalene t-dimer or the endohedral fullerenes, which are fullerenes (C_{60}, C_{70}, etc.) with additional atoms (noble-gas or alkali-metal atoms) or small molecules inserted within their spheres, the value found for $Li(NH_3)_4Na$ is noteworthy. We will see similar effects in Section 8.3, when we will discuss the "special" case of the alkali metal dimers. The second system in Figure 8.4 is a complex with the fullerene C60 [171] and the buckyball catcher [172]. This system is composed by 148 atoms (C and H) and presents a non-zero dipole moment along the vertical direction, indicated as the z-axis in the figure. Here, self-consistency enhances the binding energy by 5 meV and increases the dipole moment by 0.05 D, that corresponds to the 5.5% of

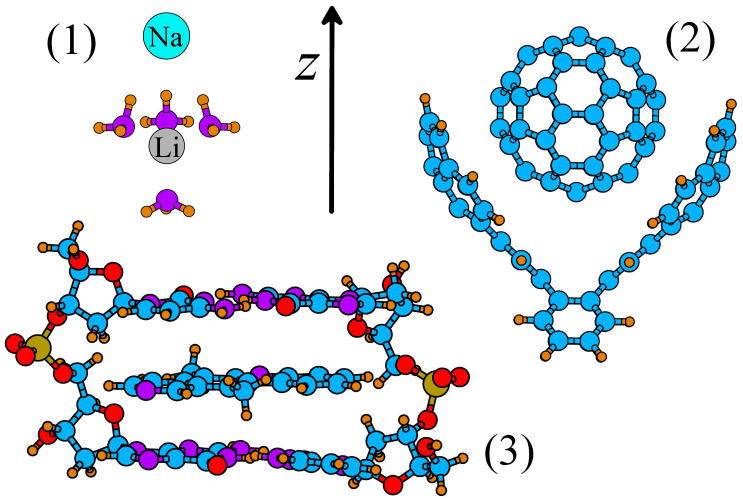

Figure 8.4: Three examples of finite structures particularly sensitive to SC vdW effects. The structure in (1) is the $Li(NH_3)_4Na$, a metal-ammonia alkalide. (2) The buckyball catcher-C60 complex. (3) A DNA-ellipticine complex. The z-axis is drawn in the middle of the figure.

the PBE value. In this system, two main factors contribute to increase the SC effects: the anisotropy in the polarizability and the large number of atoms. Very similar results are obtained with the Cyclo[n]paraphenylenes (abbreviated [n]CPP), where n indicates the number of molecules, in complexes with fullerenes, as the C60 and C70. The system (3) in Figure 8.4 contains an ellipticine molecule combined with two cytosine-guanine base pairs (C-G) attached to their sugar-phosphate. Ellipticine is an alkaloid, first synthesized in 1959 [173], which exhibits a particularly interesting anti-tumor activity. For this reason, its interactions with DNA are of great importance and have been widely investigated both experimentally and theoretically. The SC effects increase the binding energy of the complex by 4 meV. The total dipole moment is reduced by 0.1 D ($\sim 3\%$). One component (along y, which corresponds roughly to an horizontal line in the figure) is slightly increased, while two components (x and z) are reduced. In particular, the dipole along the z-axis is reduced by 0.07 D (8%). Again, the complexity of the geometry and the high number of atoms (157) are enhancing factors for the SC effects. Moreover, in the systems (2) and (3), we found modifications in the quadrupole moment on the order of 0.5–2 eÅ^2, that correspond to 2–6% of the PBE values. These changes in the electronic properties imply that self-consistency is directly affecting the electron density, as we will analyze in more detail in the next section.

8.2 Electron Density Rearrangements

Even though the differences between $\mathrm{vdW}^{\mathrm{TS}}$ and $\mathrm{vdW}^{\mathrm{TS}}_{\mathrm{sc}}$ in the cohesive energies of small molecules are rather small, as clearly shown in the previous section, the modifica-

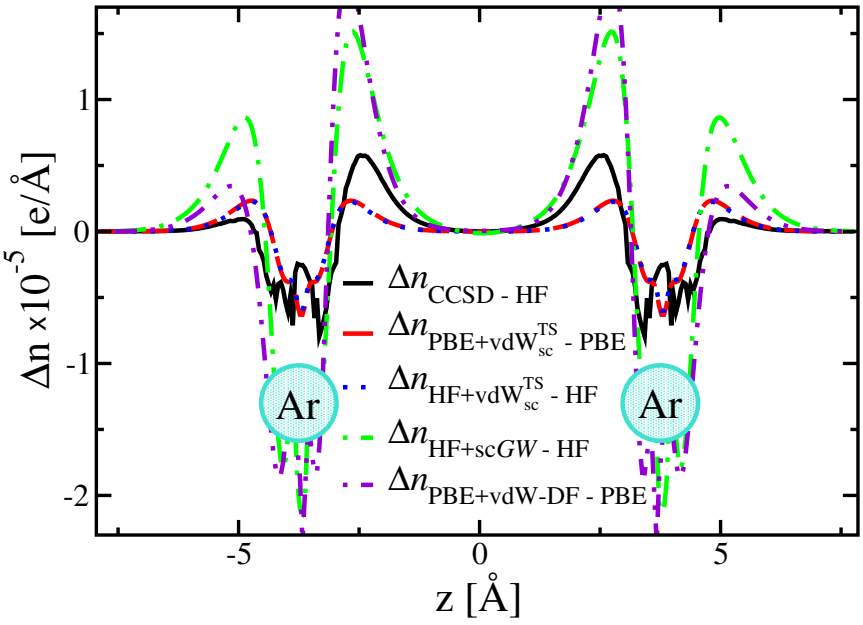

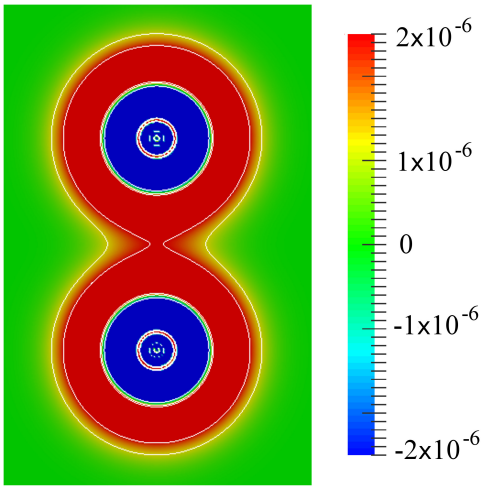

Figure 8.5: Top: integrated electron density differences $\Delta n(z)$ for the argon dimer, taken at a distance of 7.5 Å. The equilibrium distance is 3.8 Å. The positions of the Ar atoms are sketched in the figure. The $\Delta n_{\mathrm{PBE+vdW\text{-}DF-PBE}}(z)$ extends up to 2×10^{-5} and down to -2.5×10^{-5}. Right: 2D plot of $\Delta n_{\mathrm{PBE+vdW_{sc}^{TS}-PBE}}(\mathbf{r})$ for the xenon dimer, separated by an interatomic distance of $5.45 = \mathrm{d_{eq}} + 1$ Å. The scale is in $[e/\text{Å}^3]$ and the isosurfaces correspond to 1×10^{-6} and $\pm 2 \times 10^{-6}$ $[e/\text{Å}^3]$.

tions in the various energy components indicate that vdW self-consistency is affecting the electronic properties. Aiming to understand the non-trivial modifications of the electron density, we applied the SC scheme to several dimers, where the intermolecular distance has been taken to be somewhat larger than the equilibrium one, in order to highlight the role of long-range correlation effects. The density response due to SC vdW is evaluated by taking the electron density difference $\Delta n_{M1-M2}(\mathbf{r})$, where $M1$ and $M2$ refer to the two different electronic structure methods chosen, *e.g.* PBE+vdW$_{\mathrm{sc}}^{\mathrm{TS}}$ and PBE. The density difference is subsequently integrated over the corresponding orthogonal x-y planes

$$\Delta n_{M1-M2}(z) = \int\int \left[n_{M1}(\mathbf{r}) - n_{M2}(\mathbf{r}) \right] dx\, dy\,, \tag{8.2}$$

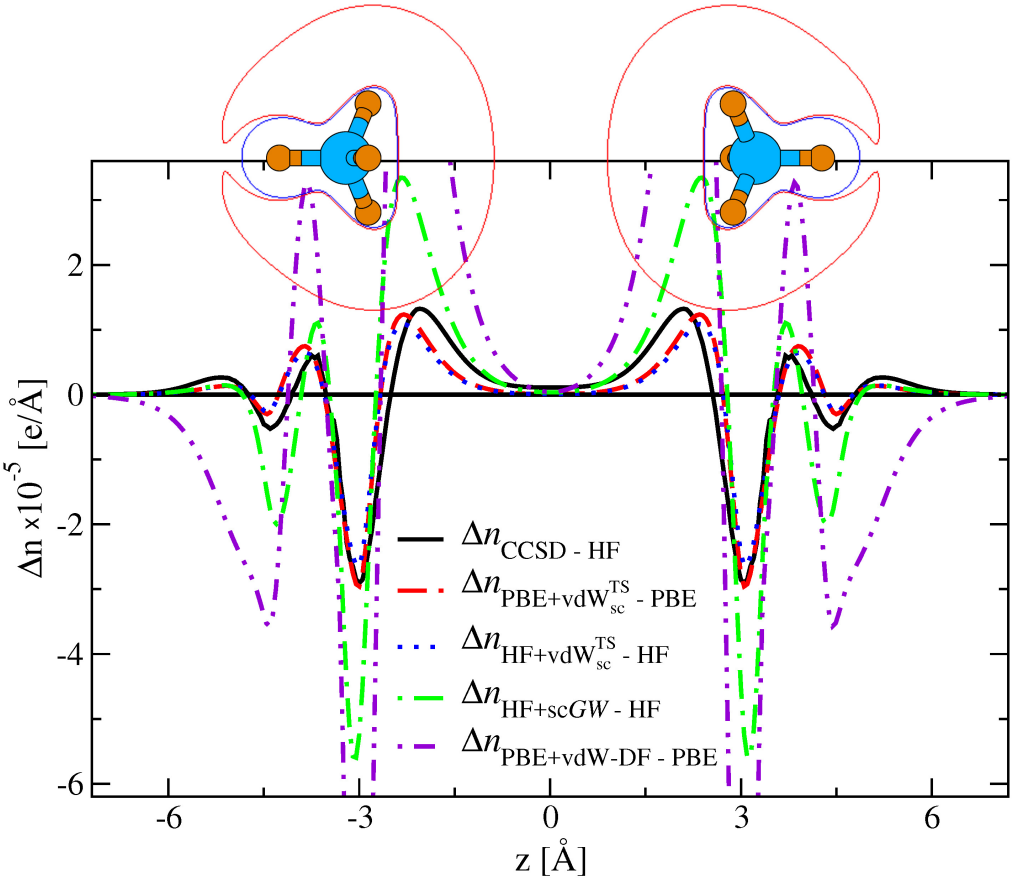

Figure 8.6: Integrated electron density differences $\Delta n(z)$ for the methane (C_4H_4) dimer. The carbon-carbon distance is $6.72 = d_{\text{eq}} + 3$ Å. In figure the structure of the dimer is sketched along with two isosurfaces produced from $\Delta n_{\text{PBE+vdW}^{\text{TS}}_{\text{sc}}-\text{PBE}}(\mathbf{r})$. The outer contour delimits a region of electron density accumulation of 1×10^{-7} [e/Å]. The inner isosurface corresponds to a region of depletion of -1×10^{-7} [e/Å]. The whole extension of the curve $\Delta n_{\text{PBE+vdW-DF}-\text{PBE}}(z)$ is from -14×10^{-5} to 9×10^{-5} e/Å. This figure is taken from reference [168].

where z is defined as the direction that connects the centers of the two atoms/molecules considered. The integral in Equation 8.2 conveniently reduces the (3D) density redistribution due to SC effects to a 1D projection, function of the distance between the fragments. The same formula can be applied to different functionals and quantum-chemical methods. This results can be used as a reference or for comparisons. Our reference for the long-range correlations effects on the density is the difference $\Delta n_{\text{CCSD}-\text{HF}}(z)$, the integrated electron density difference between the coupled-cluster single and double excitations level of theory (CCSD) and the Hartree-Fock (HF) approximation [174]. We remark that the energies are usually computed with the CCSD(T) method, which includes the contribution of the triples with a perturbative correction, see Section 2.5.1. However, for what concerns the electron density and electronic properties, CCSD(T) and CCSD are expected to be of similar accuracy.

The first example is the argon dimer, taken at a distance of 7.5 Å. The performances of different functionals are plotted in the left panel of Figure 8.5. In solid black line, is drawn the reference curve $\Delta n_{\mathrm{CCSD-HF}}(z)$, which displays peaks of density accumulation on both sides of each atoms, with higher concentrations in between the dimer. Our SC functionals, coupled with PBE and HF, overall reproduce the reference curve. However, the two peaks of density accumulation in between the two Ar atoms are only slightly larger than the peripheral ones. This is due to the fact that, at the starting point, the Ar atom is constructed spherically symmetric and the Hirshfeld partitioning of the electron density can not describe anisotropic densities. A second observation is that the two curves, $\Delta n_{\mathrm{PBE+vdW_{sc}^{TS}-PBE}}(z)$ and $\Delta n_{\mathrm{HF+vdW_{sc}^{TS}-HF}}(z)$, overlap perfectly. The predominance of the $\mathrm{vdW_{sc}^{TS}}$contributions over the underlying XC functionals, at such large interatomic distances, confirms the ability of the TS vdW method to capture long-range correlation interactions. In the same figure is plotted the density rearrangement obtained with the self-consistent GW (sc-GW) method [175] (Section 3.7.1). The shape of $\Delta n_{\mathrm{HF+sc}GW-\mathrm{HF}}(z)$ replicates the qualitative feature of the reference curve. Still, the sc-GW method overestimates the accumulation/depletion peaks and the density modifications decay faster than the reference CCSD method. In particular, in the center of the picture, the $\Delta n_{\mathrm{HF+sc}GW-\mathrm{HF}}(z)$ is even below 0. The second SC functional used as a comparison is the vdW-DF, see Section 5.4. The density difference of vdW-DF, coupled with PBE, reproduces the shape of $\Delta n_{\mathrm{CCSD-HF}}(z)$. On the other hand, the functional further increases the quantitative overestimation of the charge rearrangement found with sc-GW. The reasons behind the different performances of the SC functionals will be analyzed in detail in the last paragraph of this section.

All of the functionals used in Figure 8.5 show a redistribution of $n(\mathbf{r})$ where the region with the largest accumulation of density is located between the two atoms. This concentration of charge, driven by long-range correlation effects, implies a modification of the electrostatics between the two atoms. A second example, that supports this conclusion, is reported in the right panel of Figure 8.5. We consider a 2D slice of $\Delta n_{\mathrm{PBE+vdW_{sc}^{TS}-PBE}}(\mathbf{r})$, that cuts both atoms in half. Similarly as before, the distance between the two atoms is one Ångstrom larger that d_{eq}. The $n(\mathbf{r})$ is clearly delocalized, by vdW interactions, with a dominant spherical shape around the atoms. Nevertheless, in the middle of the figure, the electron density shows a larger concentration and the shape of the external isosurface (1×10^{-6} $e/\mathrm{Å}^3$) clearly confirms this feature. This accumulation of charge density induces an electrostatic attraction between a nucleus and its own distorted electronic cloud, leading to an effective attraction between the nuclei. Hence, the inclusion of SC vdW effects establishes a connection between the London approach, in which the long-range correlation stems from the electrodynamic coupling between fluctuating dipoles, with the Feynman picture of vdW interactions. In the second part of his seminal paper about molecular forces [163], Feynman proposed a "classical electrostatic" picture of the intermolecular forces. Then, in the last paragraph, he extended this interpretation to vdW interactions too. We quote his words: "*Van der Waals' forces can also be interpreted as arising from charge distributions with higher*

concentration between the nuclei". Concluding that, it is not the interaction between the induced electronic dipoles that yields to the vdW forces. Rather, each nucleus is attracted towards the displaced center of charge of its own electrons.

In concluding this section we present a last example and discuss in more detail the differences between the three SC approaches previously seen in Figure 8.5. We choose the methane dimer, with a carbon-carbon distance, along the z-axis, of 6.72 Å. This system is bigger than the Argon dimer and is expected to display quantitatively larger correlation effect. Moreover, it is not spherically symmetric. For this dimer, we computed $\Delta n(z)$ using the same functionals employed to study the Argon dimer. The complete set of integrated density differences is plotted in Figure 8.6. Overall, the shape of the reference curve, $\Delta n_{\mathrm{CCSD-HF}}(z)$, is qualitatively similar to the one of Figure 8.5, with a predominant accumulation of charge density in between the two molecules. Here, the absolute values are larger and the density rearrangement presents several positive and negative peaks. The performances of the PBE and HF methods coupled with our $\mathrm{vdW}^{\mathrm{TS}}_{\mathrm{sc}}$ are indistinguishable and match almost exactly with the reference curve $\Delta n_{\mathrm{CCSD-HF}}(z)$. The agreement is a strong indication that the $\mathrm{vdW}^{\mathrm{TS}}$ correction to standard DFT XC functionals, more precisely the first term in Equation 7.9, is indeed able to capture the long-range correlation effects on $n(\mathbf{r})$ properly. On the other hand, sc-GW captures the qualitative trend, but still exhibits quantitative differences with an overestimation of the charge rearrangements and steeper peaks. While such differences might be attributed to the overestimation of C_6 coefficients at the sc-GW level of theory, these discrepancies are indicative of the high level of accuracy that is required in order to correctly capture the non-trivial density modifications induced by long-range correlation effects. Similar to the sc-GW method, the SC vdW-DF functional also reproduces the shape of the $n(\mathbf{r})$ redistribution, as in the case of the Argon dimer, but yields much larger charge rearrangements than the CCSD reference. Since the vdW-DF C_6 coefficient for the methane dimer is accurate [145], this overestimation must stem from the large-gradient behavior of the vdW-DF kernel.

8.3 Alkali-Metal Dimers

In the analysis of SC vdW effects discussed above we concluded that, in general, the effects on the binding energy between small organic molecules are negligible. However, at the end of Section 8.1, we have introduced some small and mid-size organic molecules which display larger SC vdW effects. In detail, small contributions to the energetics are found (still below 1%), together with modifications of the electronic properties, as the dipole and quadrupole moments (few %). Apart from those examples, the alkali-metal dimers represent another family of systems in which the SC vdW effects are found to be particularly large. These small systems (diatomic dimers) are characterized by a very large vdW energy, which is a fundamental component of E_b. In fact, some of these dimers, when calculated with HF or other hybrid XC functionals could be even un-

Table 8.2: The equilibrium distance d_{eq} of the Cesium-Cesium dimer is reported together with d_{eq} and the dipole moment of the Sodium-Cesium dimer. The HF method is employed and also coupled with vdW$^{\mathrm{TS}}$ and vdW$^{\mathrm{TS}}_{\mathrm{sc}}$. The distances are in [Å], the dipole moments are in Debye [D].

	HF	HF+vdW$^{\mathrm{TS}}$	HF+vdW$^{\mathrm{TS}}_{\mathrm{sc}}$	Experiment
$d_{\mathrm{eq}}(\mathrm{Cs_2})$	5.02*	4.50	4.58	4.61-4.65[a]
$d_{\mathrm{eq}}(\mathrm{NaCs})$	4.08*	4.33	4.24	3.85-4.00[b]
Dipole moment NaCs	6.18		5.44	4.75[c]

$*$: Not "real" equilibrium distances, the binding energies are always positive.
a: Reference [176].
b: Reference [177, 178].
c: Reference [179].

bound, without the inclusion of long-range correlation interactions. From the electronic structure point of view, these systems are very difficult to model accurately because of i) the weak bonding between the two atoms due to the diffuse ns valence orbitals and ii) the easily polarizable core of the atoms which yields to important intershell correlation effects. Thus, the full spectra of electronic properties is hard to capture with *ab initio* methodologies. This fact and the small size of the systems suggest to tackle the alkali-metal dimers with very accurate schemes, as the configuration interaction (see Section 2.5). Even for such small dimers, the core electrons can be too many (Cs for instance) to be treated with full CI. In practice, pseudopotentials are employed to simulate core-polarizations effects, while the valence electrons can be treated at the CI level of theory [180–182]. In our case, we are interested in measuring how much the electronic properties of these polarizable systems are affected by the "simple" inclusion of long-range correlation interactions. The simulations have been performed with the "really tight" settings, that include *tier*3, an angular momentum $l = 8$ and the cut-off potential is taken with an over-converged $r_{\mathrm{onset}} = 10$ Å (5–6 is tight). Since the outermost electron shell of the alkali atoms can decay very slowly to zero, a particularly large cut-off value is chosen to ensure extended radial functions. Refer to Section 6.1 and 6.2 for an overview of the settings available in FHI-aims.

First, we analyzed the binding energy curves, using the HF methods coupled with our TS vdW in both the *a posteriori* and SC flavors. In Figure 8.7 we can see the binding energies plotted as a function of the interatomic distance. Considering the left panel, the equilibrium distance d_{eq} for $\mathrm{Cs}\cdots\mathrm{Cs}$ obtained with HF+vdW$^{\mathrm{TS}}_{\mathrm{sc}}$ is 4.58 Å, a value slightly different—0.08 Å larger—than the one given without the SC approach. The binding distance obtained with HF+vdW$^{\mathrm{TS}}_{\mathrm{sc}}$ compares well with 4.61 Å, the results of an accurate (all-electron) pseudopotential valence CI calculation with core-polarization potential [181]. Also, the absolute value of the binding energy is not exactly coincident, but SC vdW increases E_b by 12 meV ($\sim 4.2\%$). The binding energy curves for $\mathrm{Na}\cdots\mathrm{Cs}$ are drawn in the right panel of the same figure. In this case, the inclusion of SC effects reduces d_{eq} by the same 0.08 Å and adds 7 meV (4%) to the binding energy. In summary,

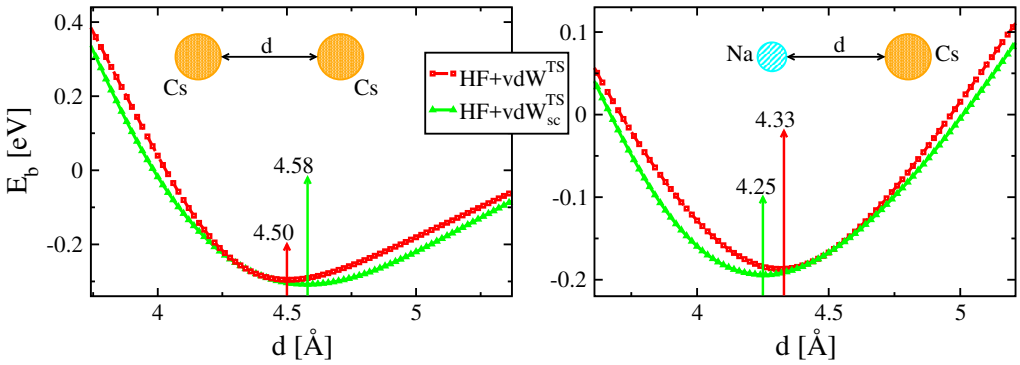

Figure 8.7: Binding energy curves plotted as a function of the interatomic distance. The functionals used are HF+vdW$^{\mathrm{TS}}$ and HF+vdW$^{\mathrm{TS}}_{\mathrm{sc}}$. Left panel: Cesium-Cesium dimer (Cs_2). Right panel: Sodium-Cesium dimer (NaCs). The two insets represent the geometries used.

we found that self-consistency can indeed affect both the structures and the binding energy of alkali dimers. For the two dimers considered here, the two modifications of d_{eq} have opposite directions, nevertheless improve the non-SC results with respect to the experimental data, as reported in Table 8.2.

As a second step, we look at the integrated density difference $\Delta n(z)$ (Equation 8.2) to study the electron density rearrangements driven by the SC vdW interactions. The density differences between HF with and without vdW$^{\mathrm{TS}}_{\mathrm{sc}}$ are plotted (solid lines) in Figure 8.8 for Cs_2 and NaCs. The dimers are now taken with the experimental binding distances (see Table 8.2). The density of the dimer is significantly displaced when SC vdW is taken into account and the effects of self-consistency on the binding energy are even larger than before. Considering $\mathrm{Cs}\cdots\mathrm{Cs}$, HF+vdW$^{\mathrm{TS}}_{\mathrm{sc}}$ gives $E_b = -0.305$ eV, a value 25 meV (9%) larger than the *a posteriori* one, while simple HF provides a positive energy (no binding). A similar result is found for the heteronuclear $\mathrm{Na}\cdots\mathrm{Cs}$, where SC vdW increases the E_b by 34 meV, which corresponds to $\sim 45\%$ of the HF+vdW$^{\mathrm{TS}}$ value. Moreover, the quantitatively large density rearrangement of $\Delta n(z)_{\mathrm{HF+vdW^{TS}_{sc}-HF}}$ is a very strong indication of possible modifications of the electronic properties. In fact, looking at the right panel in Figure 8.8, the density is redistributed to form a dipole in the region between the two nuclei. Close to the Na atom there is an accumulation in $n(\mathbf{r})$, while a depletion is present in the vicinity of Cs. The consequence is a reduction of 0.74 D ($\sim 12\%$) in the dipole moment of NaCs with respect to the value obtained with HF alone. The resulting dipole of 5.44 D improves the agreement with the experimental measurement of 4.75 D (Table 8.2).

The effects reported above are found also when the hybrid PBE functional is used instead of the HF method. For example, the $\Delta n(z)$ obtained with PBEh(1)+vdW$^{\mathrm{TS}}_{\mathrm{sc}}$ is drawn in the two panels of Figure 8.8 in dashed lines. The letter h in PBEh(1) stands for "hybrid", while (1) means that the mixing parameter is $\alpha = 1$, see Section 3.5.3. This functional corresponds to the hybrid with 100% of EXX included. In other words,

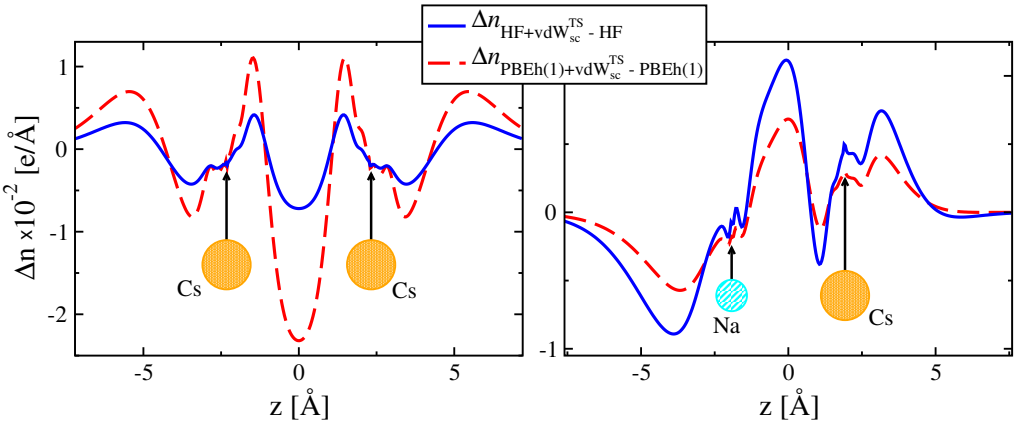

Figure 8.8: Panel left: the integrated density difference for the Cesium-Cesium dimer. Panel right: $\Delta n(z)$ computed for the Sodium-Cesium dimer. The two structures are taken at the experimental binding distances and the densities are computed with HF and PBEh(1), with and without $\mathrm{vdW_{sc}^{TS}}$. The insets in the figure indicate the positions of the different nuclei.

it combines the HF exchange with the PBE semi-local correlation part. The shape of the integrated density differences are comparable with the ones obtained with HF and produce similar modifications in the binding energy and dipole moment. However, we found that the inclusion of semi-local PBE correlation only worsens the agreement with experiment for the electronic properties of these alkali-metal dimers. With this section our study of SC effects in finite systems is concluded. The next parts will be dedicated to condensed systems, including interfaces between molecules and metal surfaces.

9 METAL SURFACES

In this second part dedicated to the applications of the vdW$_{\text{sc}}^{\text{TS}}$ functional, the attention is focused on extended systems, in particular metal (111) surfaces. The three indices (111) are called Miller indices and denote the lattice plane used to cut the metal bulk to form the surface. The combination (111) means that the x, y and z axis are intersected by the cleavage plane at the same value. The direct application of the vdW$^{\text{TS}}$ scheme would lead to large overestimation of the vdW interactions within the surface [134], as well as the surface-adsorbate interactions, as shown for example with azobenzene adsorbed on metal surfaces [183]. Therefore, to study these extended systems we employed the extension of the vdW$^{\text{TS}}$ method to model adsorbates on surfaces [123] (vdW$^{\text{surf}}$), discussed in Section 5.2. From a practical point of view, in the vdW$^{\text{surf}}$ method the collective response of the substrate is included *via* a renormalization of the vdW parameters. In other words, the SC implementation introduced in Section 7 still holds and can be directly extended to the vdW$^{\text{surf}}$ variant. Here we employ the screened set of vdW parameters, summarized in Table 5.1 for several metallic substrates, instead of the free-atom parameters. The PBE+vdW$^{\text{surf}}$ method has been already applied to several bulk metals to calculate the lattice constants. The overall performances are on the same level or better than the PBE accuracy [134]. The metal (111) surfaces presented in this work are build using the PBE+vdW$^{\text{surf}}$ lattice constants. All the settings and the details used to obtain the results presented in this section are reported in Appendix D.2.

In analogy to the analysis already shown for the Argon and the methane dimers in Section 8.2, we consider the electron density difference integrated $\Delta n_{\text{PBE+vdW}_{\text{sc}}^{\text{surf}}-\text{PBE}}(z)$ for the (111) surfaces of the three most common coinage metals: Cu, Ag and Au. The z-axis is defined here as the direction normal to the (111) surface. The first point to highlight is that the modifications of $n(\mathbf{r})$ for the three metal (111) surfaces, shown in Figure 9.1, are about three orders of magnitude larger than those of molecular dimers, see Figure 8.6. This feature is a strong indication of the importance of SC vdW effects for these periodic systems.

For Cu(111) and Ag(111), self-consistency yields an accumulation of $n(\mathbf{r})$ in between the metal layers and in the vacuum region. On the contrary, for Au(111), self-consistency produces an accumulation of $n(\mathbf{r})$ at the metal layers and a net depletion in the interstitial and vacuum regions. These two qualitatively opposite effects are caused by the balance between the vdW radius R^0 and the interatomic distance $a_{0,111}$ of the metal surface in

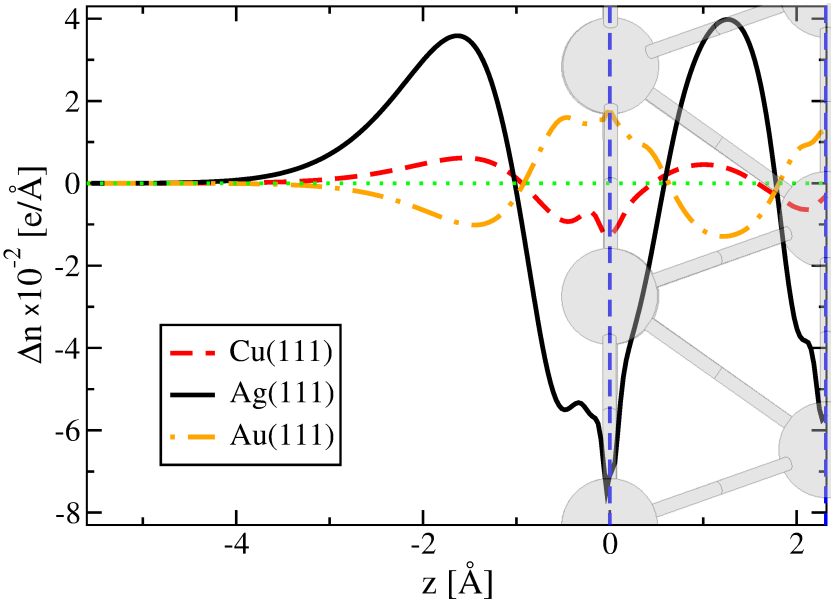

Figure 9.1: Integrated electron density differences $\Delta n(z)$ for the three coinage metal (111) surfaces. The $\Delta n(z)$ is computed between the PBE+vdW$^{\mathrm{TS}}_{\mathrm{sc}}$ and the PBE methods and is plotted along the z-direction, perpendicular to the (111) surfaces. The vertical dashed line at $z = 0$ represent the position of the topmost metal layer. The vacuum is on the left side. The metal surface is sketched in the background as a guide to the eye. This figure is taken from Reference [168].

question.

- When $R^0 < a_{0,111}$, the dominant term in the vdW potential is the first one written in Equation 7.9, *i.e.* the derivative of the C_6 coefficients. In this case the density is redistributed by spreading the electron density from the regions with a large concentration, as the metal layers. This effect is similar to what has been previously found for molecular dimers. In the case of Cu and Ag, the lattice constants are $a_0 = 3.57$ and 4.007 Bohr, see Table 5.1, that lead to an interatomic separation within the (111) surface of $a_{0,111} = a_0/\sqrt{2} = 2.52$ and 2.83 Bohr, respectively. The vdW radius for Cu is 2.40 Bohr, while 2.57 Bohr is the value for Ag. It follows that both surfaces satisfy the inequality $R^0 < a_{0,111}$.

- When $R^0 \geq a_{0,111}$, an opposite behavior is found. In this case the damping regime plays a more important role. The second term of Equation 7.9 becomes larger and eventually results in a switch of the accumulation and depletion regions. One can see that this condition is satisfied by Au(111). In fact, the surface lattice constant is $a_{0,111} = 2.94$ Bohr and the vdW radius is 2.91 Bohr.

Notably, the effects of the vdW potential on the electron density at large distances from the metal surface, i.e. well into the vacuum region, recover the decay predicted by the LZK theory [132, 133] (see Section 5.2) of $1/(R - R_0)^3$, where R_0 is the reference plane.

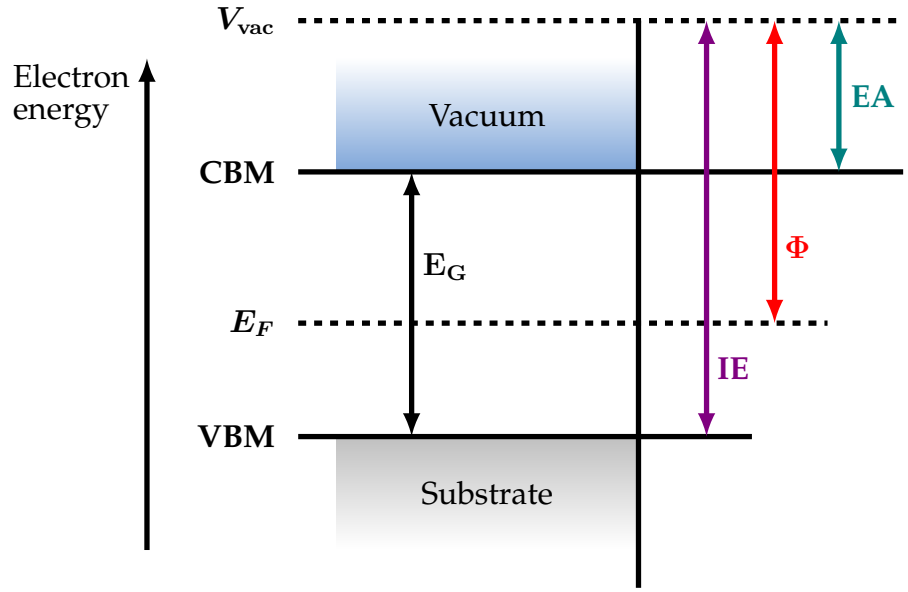

Figure 9.2: General representation of the energy diagram of a semiconductor with the approximation of flat bands to the surface. The important energy levels are the maximum of the valence band (VBM), the minimum of the conduction band (CBM), the Fermi energy E_{F} and the vacuum level V_{vac}. Some electronic properties are measured as energy differences between two of these levels. For example, the gap between the VBM and the CBM is called energy gap (E_G). The ionization energy (IE) is the difference between the VBM and V_{vac}, while the electronic affinity is the difference between the CBM and V_{vac}. The workfunction Φ is defined as the difference between the Fermi level and the vacuum potential. For the systems of our interest, metal (111) surfaces, the Fermi energy and the VBM overlap and the same definition of Φ holds.

9.1 Workfunctions with van der Waals Interactions

The SC effects are particularly pronounced at the metal layers and in the vacuum region, as clearly depicted in Figure 9.1. This situation suggests that the vdW effects are modifying, with sizable contributions, the dipole of these metals at the surface level. In this regard, the workfunction (Φ) is an observable electronic property, directly related to the surface dipole. The workfunction is defined as *the minimum energy required to remove an electron from the metal surface to the vacuum region*. The definition of Φ is sketched in Figure 9.2 for the general case of a semiconductor with the approximation of flat bands at the surface level. Following the definition written above, the workfunction corresponds to the difference between the energy of the vacuum level and the Fermi energy (E_F). In semiconductors, the Fermi level, which depends on several factors as the temperature and the doping, is generally unoccupied and the value of Φ has to be probed in a statistical way [184]. The workfunction is generally determined *via* photoemission spectroscopy experiments. The same definition of Φ is valid for metal

Table 9.1: Workfunctions in [eV] of various metal (111) surfaces obtained from experiment [185–187] and theory, using the PBE and PBE+vdW$_{\text{sc}}^{\text{surf}}$ functionals. In the second column the period in the periodic table of elements is associated to each metal. The experimental methods used to obtain the workfunctions are denoted by PE (photoelectric effect) or FE (field emission). Particularly large vdW$_{\text{sc}}^{\text{surf}}$ effects are marked with underlined values. This table is taken from Reference [168].

Metal (111) surface	Period	Experiment [Method]	PBE	PBE+vdW$_{\text{sc}}^{\text{surf}}$
Cu	4	4.94 [PE]	<u>4.89</u>	<u>4.95</u>
Rh	5	5.60 [PE]	<u>5.26</u>	<u>5.55</u>
Pd	5	5.60 [PE]	5.30	5.28
Ag	5	4.74 [PE]	<u>4.44</u>	<u>4.74</u>
Ir	6	5.76 [PE]	5.66	5.64
Pt	6	5.93 [FE]	5.76	5.73
Au	6	5.32 [PE]	5.18	5.14

surfaces too, with the simplification that the Fermi energy corresponds to the highest energy available for an electron in the solid and marks the division between occupied and unoccupied states. In other words, in metals the three energy differences IE, Φ and EA coincide [184]. Looking at Figure 9.2, the workfunction can be seen as the smallest energy barrier that prevents an electron from escaping the metal.

In practice, the workfunctions are computed with the formula

$$\Phi = V_{\text{vac}} - E_F \,, \tag{9.1}$$

where V_{vac} is the electrostatic potential in the vacuum region. The second term, the Fermi energy, is a bulk-related quantity and is the dominant term in the equation. The other value, the potential in the vacuum, is the energy that an electron assumes when is placed, at rest, in the vacuum region nearby the surface. Thus, the energy V_{vac} is a surface-dependent quantity. It originates from a potential step at the surface level of the system in question, driven by a redistribution of charges. This definition of Φ appears to be closely related to the electron density redistributions shown in Figure 9.1, which affect both the atoms belonging to the metal layers and the vacuum region. At this point, one can expect that the effects of SC vdW could have a role in the determination of both E_F and V_{vac}.

We compute all the workfunctions presented in this work using the FHI-aims [151] code. The values were carefully screened through a long process of convergence of i) the number of k-points used to sample the reciprocal space, ii) the extension of the cut-off potential, discussed in Section 6.1 and iii) the number of layers. As an example, the convergence procedure for the three settings listed above is summarized in Figure 9.3. The three coinage metal surfaces Cu(111), Ag(111) and Au(111) are considered, taken with a $(1 \times 1 \times 1)$ unit cell. The three panels in the first column show the convergence of Φ with respect to an increasing density of k-points. The fastest convergence is obtained

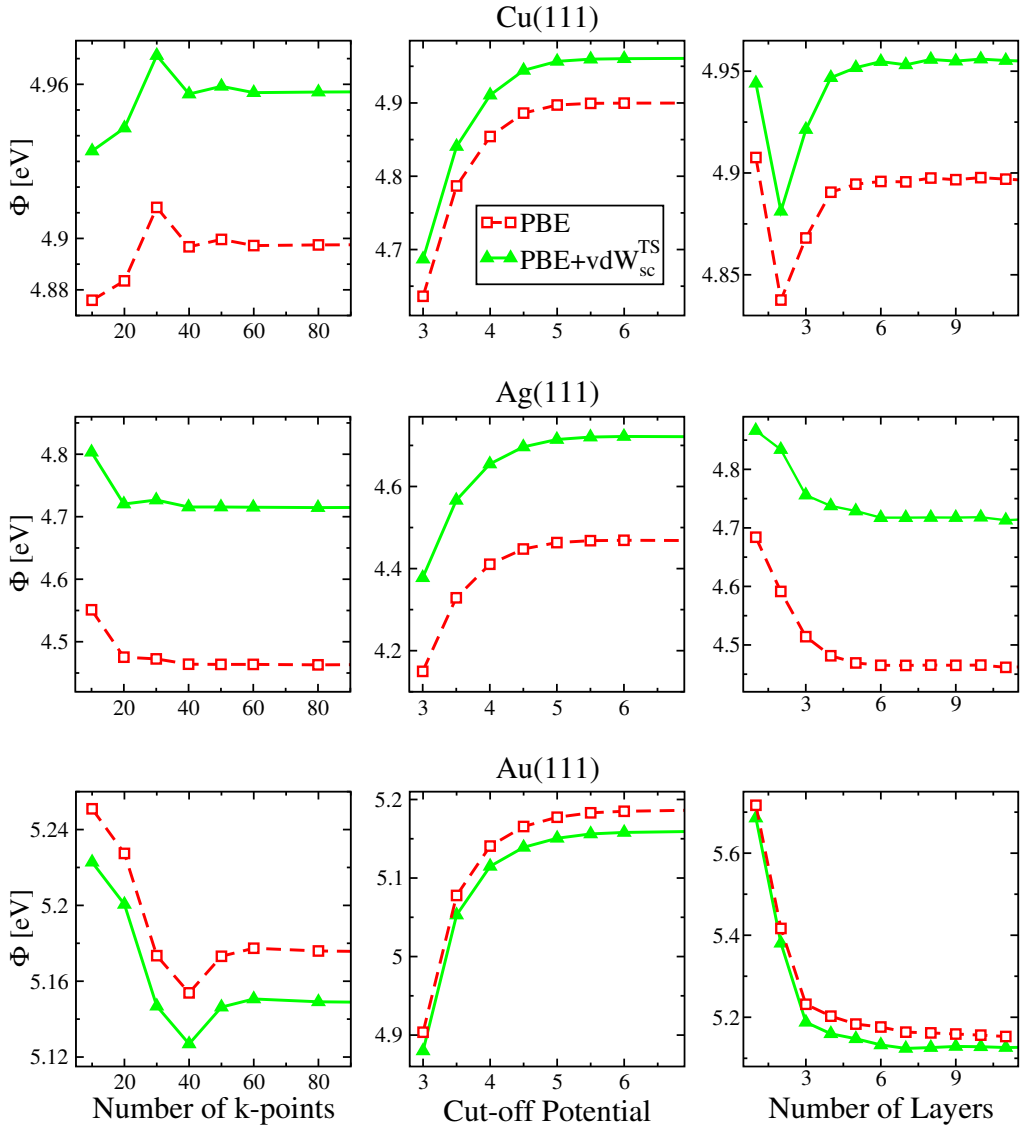

Figure 9.3: Convergence tests for the workfunctions of coppper, silver and gold (111) surfaces. Each row corresponds to one metal surface, Cu(111) is on top, Ag(111) is in the central row and Au(111) is found at the bottom. In the first column are plotted the variation of Φ for the three metals due to an increasing mesh of k-points. The central row shows the important role of the cut-off potential on the workfunctions. The values of the parameter r_{onset}, which regulates the cut-off potential, are in [Å]. The third row reports the relation between the workfunctions and the number of metal layers used in the unit cells.

with Ag(111), starting with a grid of $(40 \times 40 \times 1)$ k-points. The other two surfaces are safely converged with a minimum of 60 points per side. Similarly, the panels in the second column represent the variation of Φ with respect to the value r_{onset}, which regulates the extension of the cut-off potential. For the three systems, a minimum of $r_{\text{onset}} = 5\,\text{Å}$ is necessary to ensure converged workfunctions. In the column on the right, we converged the workfunctions with respect to the number of metal layers. For such small surfaces, the addition of one layer can significantly change the value of Φ, in particular for surfaces with less than 5 layers. The fastest convergence is obtained for Cu(111) with five metal layers, while the Ag(111) surface is converge starting with six layers. Finally, after nine metal layers, also the workfunction of the gold (111) surface reaches convergence.

Other important factors that can adjust, with small variations, the value of Φ are the dimension of the unit cell, the number of layers relaxed during the optimization procedure and the extension of the vacuum region. In this regard FHI-aims utilizes atom-centered basis functions, that are absent in the space dedicated to the vacuum. Consequently, one can extend the vacuum region as much as needed to avoid any spurious interactions between a surface and its periodic repetitions above and below, without affecting the CPU time of a calculation. On the other hand, since the structures are periodic, the increasing of k-points and/or large unit cells can have a severe impact on the computational performance of the code. We have already discussed these issues in Section 7.3 and some examples of the increasing workload are reported in Figure 7.5. In addition to that, we report in Figure D.4 the computational time as a function of the cut-off potential. All the details about the structures and the computational settings employed in this section are reported in Appendix D.3.

The workfunctions for seven different metal (111) surfaces are reported in Table 9.1. Our results, obtained with PBE and PBE+vdW$^{\text{surf}}_{\text{sc}}$, are listed and compared with the experimental data. Well converged Φ were computed using structures build with the PBE+vdW$^{\text{surf}}$ lattice constants, reported in Table 5.1. The vacuum level is always set to values larger than 50 Å. The surfaces have a minimum of six metal layers, two of which were allowed to relax during the geometry optimization, performed at the PBE+vdW$^{\text{surf}}$ level of theory [1]. The zeroth-order regular approximation (ZORA) [188] is included in our calculation to account for relativistic effects. The settings employed herein are validated also by looking at the resulting PBE workfunctions, which display a good agreement with previously obtained results [189, 190].

In order to analyze the different effects of self-consistency on the workfunctions, the metal surfaces are now separated in two different groups, depending on their period in the periodic table of elements. For those metals belonging to the fourth and fifth periods, the vdW$^{\text{surf}}_{\text{sc}}$ method increases the magnitude of Φ with respect to "standard" PBE results. Overall, for these systems the contributions of self-consistency improve the agreement with experiment, with particularly large changes found for both Rh and Ag.

[1] We have already discussed in Section 7.1.1 that the forces are available within the *a posteriori* vdW correction.

Following the discussion on the density rearrangements, Rh(111) satisfies the condition $R^0 < a_{0,111}$. As a consequence, the same qualitative behavior found for Cu and Ag, shown in Figure 9.1, is found. Namely, the density $n(\mathbf{r})$ accumulates in the vacuum and in the space between the metal layers, while a depletion is found within the layers. The effect is a lower Fermi energy, due to the attractive electrostatic interaction between the metal layers and the interstitial regions. Besides, the spillage of electron density into the vacuum increases the dipole at the surface level, thus increasing V_{vac}. These two effects lead, combined, to an increase of the workfunctions for Cu, Rh and Ag, see Table 9.1. For the most sensitive case, Ag(111), the Fermi energy is modified by 6% with respect to the PBE value and V_{vac} by 40%. The combination of these two effects is a significant increase of Φ of more than $0.30\,\text{eV}$ (7.2%).

The exception in this group is Pd(111), wherein the SC effects are rather small and in contrast with the other elements belonging to the fourth and fifth periods. In this case the relation is $R^0 > a_{0,111}$ and a modest accumulation of $n(\mathbf{r})$ is found at the metal layers, similarly to the Au(111) situation, drawn in Figure 9.1. For this system, E_F slightly increases and a nearly negligible reduction of the PBE workfunction is found. However, both the PBE and the PBE+vdW$_{\text{sc}}^{\text{surf}}$ workfunctions are 0.3 eV lower than the experimental data. We note here that Pd has a fully occupied valence electron shell: $[\text{Kr}]4\text{d}^{10}$. For such localized states, self-interaction error can become increasingly more deleterious. For this reason, we computed the Φ using PBE0 [61, 62] and HSE06 [66] hybrid functionals, described in Section 3.5.3, which add 25% of EXX. Indeed, the inclusion of a fraction of EXX is reflected into a Φ increased by 0.2 eV with respect to PBE, a value obtained with both functionals. Thus, the discrepancy between the computed and the experimental values is now within 0.1 eV. In particular, the EXX increases E_F and decreases V_{vac}, but the modification of the Fermi energy is much more pronounced, because of the relatively low density of states (DOS) at the Fermi level. The other metals in the fourth and fifth periods present incomplete valence shells and therefore significantly higher DOS at the Fermi level. The effect of hybrid functionals, for these metals, is an increase of E_F with a further underestimation of the PBE Φ with respect to experiment. We note in passing that the hybrid functionals are known to perform comparably or worse than PBE for metals [60], with a particular emphasis on transition metals. The reason is probably due to an overestimation of the exchange splitting in d-block elements, that leads, for instance, to an underestimation of the atomization energies [63].

For the remaining three metals belonging to the sixth period (Ir, Pt and Au), the workfunctions computed at the PBE lever are slightly reduced when vdW$_{sc}^{\text{surf}}$ is included, see Table 9.1. These three surfaces satisfy the relation $R_0 \geq a_{0,111}$ and the rearrangements of $n(\mathbf{r})$ follow the behavior discussed above for Au and shown in Figure 9.1. Similarly to Pd(111), we observe a slightly increased E_F coupled with an increased V_{vac}. The combination of these two effects is a reduction of the PBE workfunctions by 0.02–$0.04\,\text{eV}$ (see Table 9.1). For these metal surfaces the workfunctions computed with the hybrid functionals are comparable with those obtained with PBE. Therefore, the average

discrepancy of 0.2 eV between theory and experiment still remains. However, we note here that the hybrid XC functionals applied to Pt(111) seem to display a trend similar to Pd(111). The performances of the hybrid XC functionals on the workfunctions of all seven metal (111) surfaces presented in this section are reported in Table D.3. Since these functionals are only a secondary topic in the present thesis, we left a brief discussion about these results in the last part of Appendix D.3.

It is well known that effects beyond the scalar relativistic approximation become increasingly more important in computing the electronic properties for such heavy metals. In this regard, the spin-orbit coupling (SOC) is found to stabilize the Fermi level of bulk Au by ~ 0.4 eV [191]. This effect will consequently lead to an increase of Φ in Au. Therefore, we suggest, for an improved quantitative prediction of Φ in these surfaces, to perform self-consistent calculations which include the van der Waals interactions and full relativistic effects.

In concluding, the performances of PBE+vdW$_{\rm sc}^{\rm surf}$ have been compared with another SC vdW scheme, the vdW-DF, coupled with the PBE functional. The Cu, Ag and Au (111) surfaces, tested with PBE+vdW-DF, lead to results similar to the ones found with PBE+vdW$_{\rm sc}^{\rm surf}$. Namely, the workfunctions are increased upon the inclusion of SC vdW effects. The values obtained with the vdW-DF method are 5.10, 4.78 and 5.40 for the Cu, Ag and Au surfaces, respectively. These workfunctions are slightly overestimated with respect to experiments. In this regard, they are consistent with our analysis of the vdW-DF effects on the electron density of the Argon and the methane dimers (Figure 8.5 and 8.6). Overall, these findings assess a general validity to the results found with the PBE+vdW$_{\rm sc}^{\rm surf}$ method.

10 Hybrid Inorganic-Organic Systems

This last section of results is dedicated to the application of the SC vdW approach to hybrid inorganic/organic systems (HIOS). In optoelectronics, multi-layered materials attracted much attention because of the wide range of promising practical applications, for instance as components of transistors or light-emitting devices. A nanoscale interface, created by joining two or more materials with different properties, involves complex interactions between the different parts and may exhibit interesting phenomena, linked to new functionality. Of course, these features are not present when the different components are considered separately [11]. Among all the interfaces, the hybrid systems are composed by an organic molecular monolayer/monolayers and an inorganic substrate. Thus, with these systems it is possible to combine, for example, the high electrical conductivity of a metal substrate with the tunable structure and electronic properties of organic molecules. The resulting interfaces show interesting applications, for example as diodes, switches, sensors, photovoltaic cells [192, 193].

From a practical point of view, these interfaces are complex and large systems. Therefore, DFT is the favorite *ab initio* methodology to tackle HIOS because of i) its computational efficiency, which enables the study of relatively large compounds and ii) the accuracy in the prediction of the electronic properties of these systems. Nevertheless, as one can imagine, standard DFT XC functionals, as LDA or PBE, might be suitable for treating large systems, but include only a semi-local dependency on the electron density. In this regard, the absence of the long-range correlation interactions can be particularly troublesome for some HIOS [139, 194]. In fact, the distance between the substrate and the monolayer is often around 3 Å, the typical range of weakly bounded systems, at the edge between chemisorption and physisorption. The PBE functional typically overestimates the binding distances (the distance between the molecule/monolayer and the substrate) and underestimates the binding energies. The opposite behavior, with large underestimation of the binding distances, is found with LDA [195, 196]. If follows that, in order to predict the structure and the cohesive properties of these complex systems, many efforts have been dedicated in the last years to include vdW interactions within the DFT framework. Different methodologies were proposed (see Section 5), among all functionals we have already mentioned the DFT-D of Grimme [110], the vdW-DF [141]

and the TS [108], discussed respectively in Section 4.1, 5.4 and 4.2. These remedies show a great improvement with respect to standard DFT functionals, when applied to layered systems and molecules adsorbed on surfaces [196–201]. However, the results tend to overestimate/underestimate either the binding distance or the energy. Even very expensive calculations that employ EXX with the correlation at the RPA level of theory (cRPA) can fail to reach a discrepancy in the binding distance within 0.1 Å with respect to experimental data [126]. Hence, the accurate prediction of the structure and the energetic of these systems remains an open challenge.

The vdW method employed to model the HIOS in this work is the vdW$^{\mathrm{surf}}$ [123], the extension of the TS, described in Section 5.2. With this approach, the TS vdW functional for intermolecular interactions is combined with the LZK theory [132, 133] (see Section 5.2), which includes, in the vdW energy, the non-local collective response of the substrate. This scheme has been applied to a large variety of HIOS, starting with atoms, as Xenon, to molecules of different size, as benzene, azobenzene, naphthalene, the C_{60} buckyball and many more [127, 134, 200]. The vdW$^{\mathrm{surf}}$ method, coupled with PBE, leads to remarkably good results in comparison to experimental measurements. Overall, the binding distances are found with a MAE of 0.06 Å and the adsorption energies are within 0.16 eV [127]. These numbers represent, up to now, the benchmark in the *ab initio* description of HIOS. The substrates used are mainly metal (111) surfaces, but the functional shows the same level of performances also for adsorbates on (110) and (100) metallic surfaces [140].

The correct prediction of the structure is a fundamental prerequisite in order to characterize the properties of HIOS. This step is achieved in this work *via* structure relaxations performed with the PBE+vdW$^{\mathrm{surf}}$ functional. At this point it is possible to go beyond the cohesive properties and investigate the electronic structure and properties of HIOS. The workfunction, for example, is an experimentally measurable quantity. Hence the comparison between the simulated and the measured workfunction (or workfunction shift) is an important reference to assess the accuracy of the electronic structure calculations. Moreover, it is also possible to study the phenomena behind the modifications of the electronic properties upon molecular adsorption. We will apply this recipe to study the role of vdW interactions, included *via* vdW$^{\mathrm{surf}}_{\mathrm{sc}}$, in the electronic properties of HIOS. The analysis of SC effects is motivated by the fact that vdW interactions proved to be very important for the cohesive properties of HIOS and for the workfunctions of some metal surfaces. In the literature there are already few SC implementation available for HIOS, one example is the vdW-DF (see Section 5.4). This functional has been employed with layered systems as NTCDA and PTCDA on gold (111) surface [158], but no particular attention was given to SC effects. In conclusion, a study regarding the specific role of long-range correlation interactions on the electronic structure of HIOS is still absent up to date. In the next sections will study the SC effects for a series of selected HIOS of increasing complexity and size. Following our previous results for metal (111) surfaces (Table 9.1), the majority of the systems considered will contain Ag(111), the surface with the largest SC effects. Our analysis starts with the

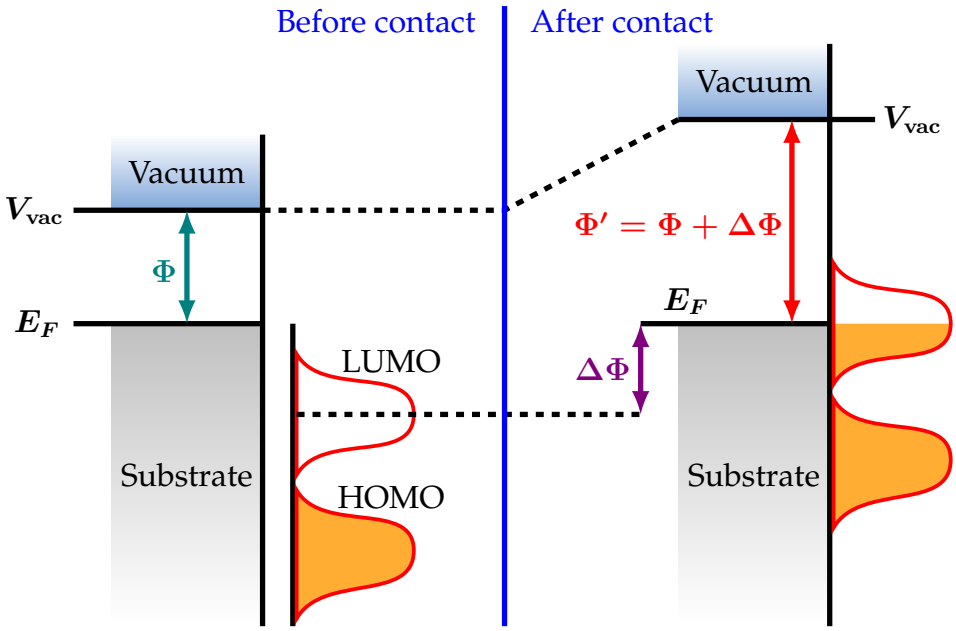

Figure 10.1: Schematic representation of the shift of the workfunction driven by charge transfer. In this figure the charge flows from the metal substrate to the molecule. On the left side are represented the surface, with its initial Φ, and the molecule as two separate systems. After contact, on the right side, the molecular LUMO is filled with electrons. The consequence of this charge transfer is an induced interface dipole, which increases the initial workfunction with a positive shift ΔΦ. The opposite situation, a transfer of charge from the molecule to the substrate, would imply a negative ΔΦ.

investigation of electron density rearrangements, comparing PBE and PBE+vdW$^{\text{surf}}_{\text{sc}}$ functionals. Then, we will proceed to study the effects on the electronic properties, with particular attentions devoted to the workfunctions.

10.1 The Workfunction Shift

The interesting features of HIOS are due to the fact that when a molecule/monolayer is adsorbed on a surface the electron density undergoes a complex rearrangement connected to the formation of intrinsic dipoles and, consequently, to electrostatic interactions at the interface. Therefore, for this class of systems, the potential importance in practical applications is joined by the possibility to model the electronic properties, as the band gap or the metal workfunction, in order to improve the performances [6, 202] and/or expand the functionality in organic electronic devices [203]. In particular, depending on the magnitude and the type of interfacial interactions, the workfunction of the surface, defined in Equation 9.1, shifts (ΔΦ). We can separate three main electrostatic effects behind the shift of Φ:

- The Pauli push-back or pillow effect, *i.e.* the repulsion between the electrons belonging to the metal surface and those of the adsorbed molecule.

- The presence of a charge transfer between the surface and the monolayer. As sketched in Figure 10.1, upon contact a flow of charge can travel from the substrate to the molecule or *vice versa*. Of course, this means a rearrangement of $n(\mathbf{r})$ that produces a dipole at the interface.

- The intrinsic electronic dipole moment of the monolayer. Since the molecules often become distorted upon adsorption, this term can be present even in molecules which have no dipole in gas phase.

The first two effects are correlated and can also concur in the so-called Fermi-level pinning or workfunction pinning phenomenon [204]. Considering a clean metal surface, part of the electron density is located above the topmost metal layer. In Figure 9.1 we show that SC vdW effects enhance this density for Cu and Ag (111) surfaces. When a molecule is adsorbed, the pillow effect, the overlap between the molecular and the metal wavefunctions, pushes back the electron density of the metal into the surface. Thus, the Φ of the clean metal is reduced (negative $\Delta\Phi$). At this point, if the molecular LUMO—which is renormalized accordingly to the interface dipole—is below the Fermi energy of the surface, then a charge transfer is established from the metal to the molecule. In this regime, the workfunction of the HIOS (Φ') is pinned, independent of the distance between surface and molecule [204, 205]. Even the inclusion of an extra dipole between surface and monolayer leads only to a charge rearrangement at the interface that keeps $\Delta\Phi$ constant. This happens because the charge transfer and the Pauli push-back balance each other, until the LUMO can be filled. When the molecule is too close to the surface, for example, the strong charge transfer fills the whole LUMO and $\Delta\Phi$ is unpinned again. Of course, the Fermi-pinning is not present without charge transfer.

The molecular geometries can distort during the adsorption process and provide an additional molecular dipole, the third phenomenon that affects $\Delta\Phi$. The workfunction shift can be indeed modified by the molecular dipole too, beyond Fermi-pinning, depending on the spatial location of the dipole. If the dipole is introduced above the monolayer, *i.e.* above the region where the electron density can rearrange to keep the workfunction pinned, it would create an additional potential step that contributes to the final workfunction Φ' [206].

The different types of substrates and molecules available open the possibility to create a countless number of interfaces with many different properties. Moreover, the control of the factors stated above allows to widely tune the electronic and optical properties of hybrid systems. For example, a chemisorbed monolayer with a pronounced polar orientation or a strong electron acceptor are usually associated with large $\Delta\Phi$, on the order of 2–3 eV [207]. On the contrary, weakly bounded interfaces, as in the case of noble gases, produce much less pronounced modifications of about 0.5 eV [208]. Naturally, a fundamental factor is the type of substrate. The same monolayer adsorbed on a metal surface and a semiconductor, can result in substantially different interactions at the interface, with large differences (40%) in the two $\Delta\Phi$ [209]. Also, the workfunction exhibits a non-trivial relationship with structural modifications. For instance, the deposition of

Table 10.1: Summary of binding distances, binding energies and workfunction shifts for Benzene adsorbed on Cu(111) and Ag(111). The results listed here are obtained with PBE+vdW$^{\text{surf}}$, PBE+vdW$^{\text{surf}}_{\text{sc}}$ and from experiments. The average distance between the carbon atoms and the topmost metal layer (d_{C}) are reported in [Å]. The binding energies E_b and the $\Delta\Phi$ are in [eV].

	Benzene/Cu(111)			Benzene/Ag(111)		
	d_{C}	E_b	$\Delta\Phi$	d_{C}	E_b	$\Delta\Phi$
PBE+vdW$^{\text{surf}}$	2.79[a]	-0.79	-1.07	2.96[a]	-0.74	-0.72
PBE+vdW$^{\text{surf}}_{\text{sc}}$	2.79	-0.79	-1.07	2.96	-0.73	-0.86
Experiment		-0.71[b]	-1.09[c]		-0.69[b]	-0.94[d]

a: Reference [134].
b: Reference [224].
c: Reference [225].
d: Reference [226].

a second monolayer, although visibly changes the geometry of this HIOS can result in modest workfunction reductions (~ 0.1 eV) [210].

The process of carefully tailoring the electrostatics at the interface includes a variety of different techniques, from doping methods [211, 212] to charge carrier injector/acceptor layers [213–215] and stacking layers [210, 216]. In summary, the characterization of HIOS and the understanding of the main processes behind the electronic properties represent formidable challenges, deeply investigated with both experimental [216–219] and theoretical [199, 206, 220–223] approaches.

10.2 Benzene on metals

As a first example, we start with a small molecule: Benzene (Bz) adsorbed on copper and silver (111) surfaces. The Bz molecule is adsorbed in a flat configuration on both Cu(111) and Ag(111) [226–229]. We consider the most stable structure, in which the molecule is adsorbed on a bridge site and is 30° tilted with respect to the high symmetry sites (bri30°). Refer to Appendix D.5 for additional details about the geometry and the settings employed. First, we compute the workfuncion shift of both structures using PBE[1] and PBE+vdW$^{\text{surf}}_{\text{sc}}$. From the results for Bz/Cu(111), summarized in Table 10.1, we can conclude that the SC effects are not important in determining $\Delta\Phi$. Although PBE and PBE+vdW$^{\text{surf}}_{\text{sc}}$ produce the same $\Delta\Phi$, one should keep in mind that the workfunctions of the clean substrate and the interface are different with the two functionals. The two values for Cu(111) are in Table 9.1. For the systems Bz/Cu(111), PBE gives a $\Phi' = 3.82$ eV, while 3.88 eV is found with SC effects. Both functionals agree well with the experimental value $\Phi' = 3.85$ eV [225].

The second case, Bz/Ag(111), displays a modification of the PBE $\Delta\Phi$, when SC effects are included. With self-consistency, the PBE workfunction decreases by 0.14 eV,

[1] We remind the reader that, for what concerns the electronic properties, PBE and PBE+vdW$^{\text{surf}}$ are the same functional. Hence, we decided to use the simplest notation.

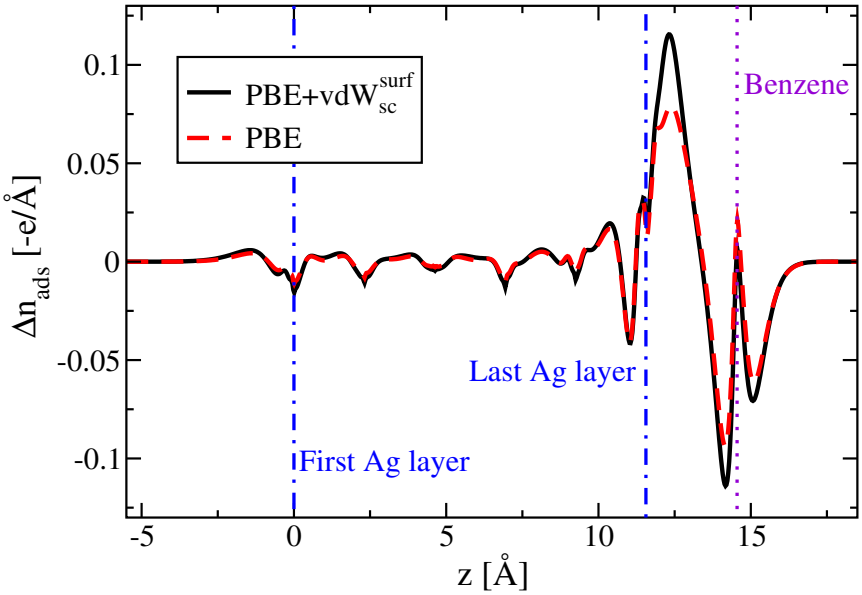

Figure 10.2: Bz/Ag(111). PBE and PBE+vdW$_{sc}^{surf}$ induced electron density integrated and plotted as a function of z, the axis perpendicular to the metal surface. The vertical dotted-dashed lines indicate the upper and lower limits of the silver slab. The vertical dotted line refers to the position of the Bz molecule.

improving the agreement with the experimental data. In order to understand the reasons behind this larger $\Delta\Phi$, we performed a in-depth analysis of the electronic structure. The interface Bz/Ag(111) is characterized by a rather weak interaction between the surface and the molecule. The binding distance (Table 10.1) is typical of a physisorption. Within this type of bonding, no substantial charge transfer between the interface is expected to take place. Therefore, the only physical phenomenon involved in the change of the workfunction is Pauli push-back [230]. During the adsorption, the electron density of the substrate and the one of the monolayer overlap. However, as the overlap increases, a repulsion between the two electron densities arises because of the Pauli exclusion principle. As a result, the electron density (in the vacuum) of the metal withdraws in a region close to the surface, thus creating a dipole that points toward the surface and reducing, consequently, the metal workfunction.

We define now the electron density modification induced by molecular adsorption as

$$\Delta n_{\rm ads}(\mathbf{r}) = n(\mathbf{r})_{\rm system} - (n(\mathbf{r})_{\rm surf} - n(\mathbf{r})_{\rm mol}) \ , \tag{10.1}$$

where $n(\mathbf{r})_{\rm mol}$ is the density of the isolated molecule or monolayer. The induced density can be subsequently integrated over x–y planes

$$\Delta n_{\rm ads}(z) = \int\int \Delta n_{\rm ads}(\mathbf{r})\, dx\, dy \, , \tag{10.2}$$

where z is defined as the axis perpendicular to the metal surface. The $\Delta n_{\rm ads}(z)$ for

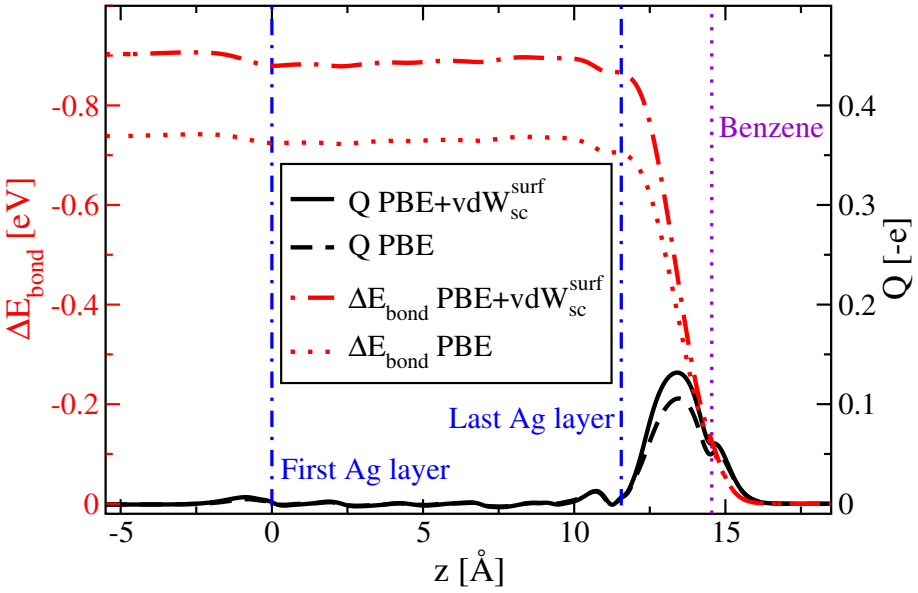

Figure 10.3: Bz/Ag(111). The delocalized charge $Q(z)$, computed with PBE and PBE+vdW$_{\rm sc}^{\rm surf}$, are plotted together with the change of the potential energy $\Delta E_{\rm bond}(z)$. The vertical dotted-dashed lines indicate the upper and lower limits of the silver slab. The vertical dotted line refers to the position of the Bz molecule. The values of the fully integrated $\Delta E_{\rm bond}(z)$ correspond to the BD.

Bz/Ag(111), computed with PBE and PBE+vdW$_{\rm sc}^{\rm surf}$, are plotted in Figure 10.2. In both curves it is clearly visible that, when the molecule adsorbs, a dipole is formed at the interface level. Also, the magnitude of the charge rearrangement is larger with PBE+vdW$_{\rm sc}^{\rm surf}$ (solid line). The inclusion of vdW interactions produce a delocalization of electron density above the metal surface and around π-conjugated molecules. This increases the overlap between electronic wavefunctions and triggers a larger Pauli push-back effect. As a result, the dipole at the interface can be estimated to be 1.22 D with PBE, which increases to 1.46 D when SC vdW effects are included. The consequence is a reduction of nearly 20% (0.14 eV) of the PBE $\Delta\Phi$, reaching an agreement between theory and experiment better than 0.1 eV. We also observe that the absence of charge transfer is confirmed in Figure 10.2, where the density rearrangements are not involving the density located at the level of the molecular plane.

The workfunction shifts reported in Table 10.1 are computed with the formula $\Delta\Phi = \Phi' - \Phi$. To further establish the role of SC vdW in HIOS, a simple electrostatic model can be used to partition the workfunction shift into two separate contributions. First, we define the delocalized charge as the integral of the induced density

$$Q(z) = \int \Delta n_{\rm ads}(z)\, dz\,. \tag{10.3}$$

Since the total charge is conserved, the full integral, performed along the z-axis of the unit cell, should give zero. A positive value of $Q(z)$ is connected to a transfer of electrons

from the molecule (right side) to the surface (left side). Considering the two $Q(z)$ plotted in Figure 10.3, it appears that the inclusion of SC vdW (solid line) gives rise to a larger rearrangement of charge with respect to PBE alone (dashed line), confirming the larger Pauli push-back effect previously described. We can measure the magnitude of the delocalized charge by considering the global maximum of the two $Q(z)$. The values are $Q_{\text{peak}} = -0.106\,e$ and $-0.130\,e$, with an increasing of $-0.024\,e$ (22%) due to SC vdW. The plateau in at the level of the Bz plane (dotted line), found in both schemes, indicates qualitatively the absence of charge transfer.

A second integration of $\Delta n_{\text{ads}}(z)$ [2] is linked to a modification of the electrostatic potential upon bond formation. In other words, the potential energy is obtained by solving the Poisson equation in 1D (along the z direction)

$$\frac{d^2}{dz^2}\Delta E(z)_{\text{bond}} = \frac{e}{\epsilon_0}\Delta n_{\text{ads}}(z)\,, \tag{10.4}$$

where the change in the potential energy is defined as: $\Delta E_{\text{bond}} = -e\Delta V_{\text{bond}}$. The net change in the potential energy (the full integral) represents the total change due to the formation of dipoles at the interface, called bond dipole (BD). At this point we can compute $\Delta\Phi$ with an alternative definition

$$\Delta\Phi = \Delta E_{\text{mol}} + \text{BD}\,, \tag{10.5}$$

in which the first term refers to the molecular contribution. As previously mentioned (Section 10.1), ΔE_{mol} originates solely from the adsorption-induced geometric distortion (bending and stretching phenomena) of the monolayer.

For Bz/Ag(111), we measured $\Delta E_{\text{mol}} = 0.037$ eV with no sensible modifications due to SC vdW. The two curves corresponding to ΔE_{bond} are drawn in Figure 10.3. Clearly, the potential energy is larger when SC effects are included, giving a BD$= -0.90$ eV. This contribution, combined with the molecular dipole, produces a $\Delta\Phi = 0.863$ eV. On the other hand, the change in the potential energy for PBE alone is -0.75 eV, -0.15 eV less ($\sim$ 20%), resulting in $\Delta\Phi = 0.713$ eV. The two workfunction shifts are in good agreement with the number reported in Table 10.1 and reflect the difference between the two approaches. Of course, the $\Delta\Phi$ obtained with Equation 10.5 are affected by numerical errors and should be regarded only as a test that confirms the validity of our analysis on the electronic structure. The $\Delta n_{\text{ads}}(\mathbf{r})$ are obtained from DFT calculations and saved in files as grid points. Therefore, the precision of the grid is very important in determining the integrated quantities as $Q(z)$ and $\Delta E_{\text{bond}}(z)$. For this reason, one should always refer to the values reported in the tables, *e.g.* Table 10.1, as the "true" $\Delta\Phi$. These numbers are computed within the FHI-aims code, which provides a much higher accuracy than the numerical integration of a file wrote for visual purposes.

[2] First we compute $Q(z)$, then we obtain $\Delta V(z)_{\text{bond}}$ with the integration of $Q(z)$.

Table 10.2: Binding distance, binding energy and workfunction shift for DIP/Ag(111), considered with two different monolayers. The PBE+vdW$^{\text{surf}}$ and PBE+vdW$^{\text{surf}}_{\text{sc}}$ results are compared with experimental measurements. The distances are in [Å], the energies and the workfunctions are in [eV].

	Herringbone DIP/Ag(111)			Brick-wall DIP/Ag(111)		
	d_C	E_b	$\Delta\Phi$	d_C	E_b	$\Delta\Phi$
PBE+vdW$^{\text{surf}}$	2.99^a	-6.45	-0.16	3.00^a	-3.22	-0.18
PBE+vdW$^{\text{surf}}_{\text{sc}}$	2.99	-6.38	-0.38	3.00	-3.18	-0.39
Experiment	3.01^a		-0.44^b	3.01		-0.44

a: Reference [138].
b: Private communication.

10.3 Diindenoperylene on Ag(111)

The analysis and the results presented above can be expanded by considering another well characterized HIOS: Diindenoperylene (DIP) ($C_{32}H_{16}$) adsorbed on Ag(111). DIP is a π-conjugated semiconductor and has a relatively simple chemical structure: is a planar hydrocarbon. This molecule has excellent optoelectronic device performances [231, 232] and, during the last years, it has been extensively studied in monolayer on coinage metal surfaces [233–235]. The comparison between the equilibrium distance d_C (defined in Table 10.1) obtained with PBE+vdW surf and with X-ray standing waves experiments (XSW) shows an almost perfect agreement [138]. The agreement in the structure is found also for Cu(111) and Au(111). However, with these two substrates, the contributions of SC vdW are basically absent, similarly to the example of Bz/Cu(111). For this reason, from now on, we focus only on HIOS with silver as a substrate.

The "best match" with the experimental d_C is obtained with two orientations of a close-packed DIP monolayer, already observed in STM and LEED experiments [234]. In the first case the monolayer is arranged in a herringbone shape with two molecules per unit cell. The second structure is a brick-wall monolayer and only one DIP molecule is included in the unit cell. More details about the geometries and the settings are available in Appendix D.5. For what concerns E_b, self-consistency gives a tiny reduction, of about 1.0–1.25%, of the PBE+vdW$^{\text{surf}}$ values. The binding distances, reported in Table 10.2, indicate a rather pronounced physisorption. Thus, vdW interactions are of great importance for this structure. Since the two monolayers produce basically the same results, we will describe here only the brick-wall arrangement.

DIP on Ag(111) differs from Bz/Ag(111), in fact the latter presents a net charge transfer from the metal to the molecule, following the representation in Figure 10.1. Within this regime, the Pauli push-back effect, that reduces the metal work function, is counterbalanced by the charge transfer, see Figure 10.1. On the contrary, a flow of charge from the HOMO of the molecule to the substrate would enhance the reduction of the workfunction due to the pillow effect [236]. Specifically, in the case of DIP/Ag(111), the charge transfer is modest and the $\Delta\Phi$ remains negative, see the results reported in

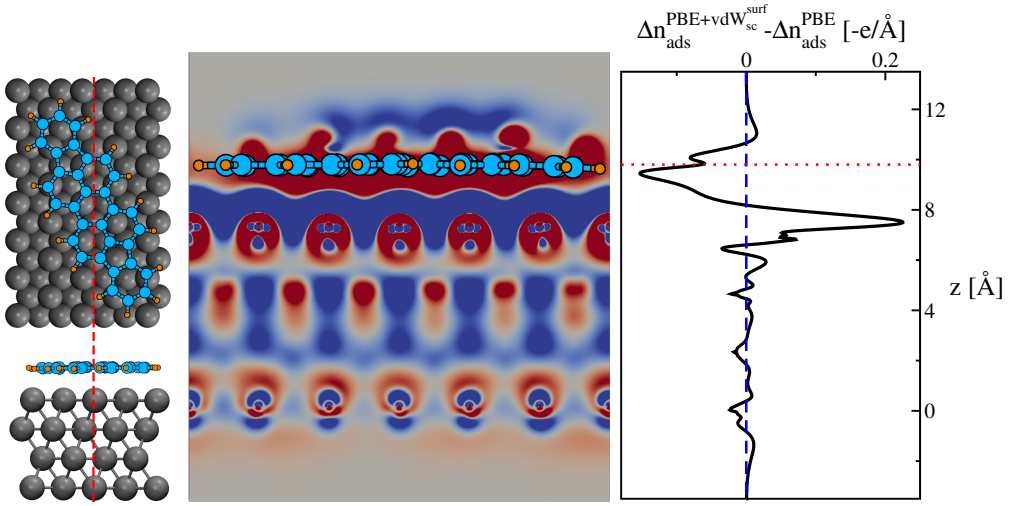

Figure 10.4: DIP on Ag(111). On the left panel are reported the top and side view of the unit cell with one DIP molecule in the brick-wall arrangement. The red dashed line defines the x-z plane used to plot the 2D slice of $\Delta n_{\text{ads}}^{\text{PBE+vdW}_{\text{sc}}^{\text{surf}}}(\mathbf{r}) - \Delta n_{\text{ads}}^{\text{PBE}}(\mathbf{r})$. In the center a 2D isosurface of $\Delta n(\mathbf{r})$ is plotted. The regions with excess of electron density are indicated in blue, the regions of depletion are in red. The limiting values are set to $\pm 2.0 \times 10^{-4}$ e/Å^3. The profile of the DIP molecule is sketched as a guide to the eye. The difference between the induced electron densities integrated over x-y planes, $\Delta n_{\text{ads}}^{\text{PBE+vdW}_{\text{sc}}^{\text{surf}}}(z) - \Delta n_{\text{ads}}^{\text{PBE}}(z)$, is plotted on the right panel. The plot is vertically aligned to match with the z coordinates of the figure in the central panel.

Table 10.2. Even though both functionals provide a negative workfunction shift, when SC interactions are taken into account the shift increases by 0.21 eV, doubling the PBE value, with a significant improvement in the agreement between theory and experiment.

This large change in $\Delta\Phi$ is analyzed by looking at the difference in the induced electron density between PBE+vdW$_{\text{sc}}^{\text{surf}}$ and PBE: $\Delta n_{\text{ads}}^{\text{PBE+vdW}_{\text{sc}}^{\text{surf}}}(\mathbf{r}) - \Delta n_{\text{ads}}^{\text{PBE}}(\mathbf{r})$. We consider a 2D slice of the induced electron density, taken along an x-y plane that cuts the unit cell (and the DIP molecule) in half, as indicated in the left panel of Figure 10.4. The 2D plot of such density difference is in the central panel of Figure 10.4. From the figure it emerges that self-consistency entails a depletion of density at the monolayer plane and at the metal layers. Conversely, the accumulation regions are located mainly at the interface and between the silver atoms. A quantitative inspection of these effects is provided with the integrated density, defined in Equation 8.2. The integrated density difference for DIP/Ag(111) is plotted in the right panel of Figure 10.4. The curve presents the shape of a dipole, with the negative pole located at the interface and the positive pole just above the topmost metal layer. Such density rearrangement is a clear indication of the pillow effect that pushes the density closer to the surface, reducing the metal workfunction. Having examined the electron density, we now show the total delocalized charge $Q(z)$, defined in Equation 10.3 as the integral of $\Delta n_{\text{ads}}(z)$. Since the rearranged density is already discussed above, we avoid to show here the two $\Delta n_{\text{ads}}(z)$ and move

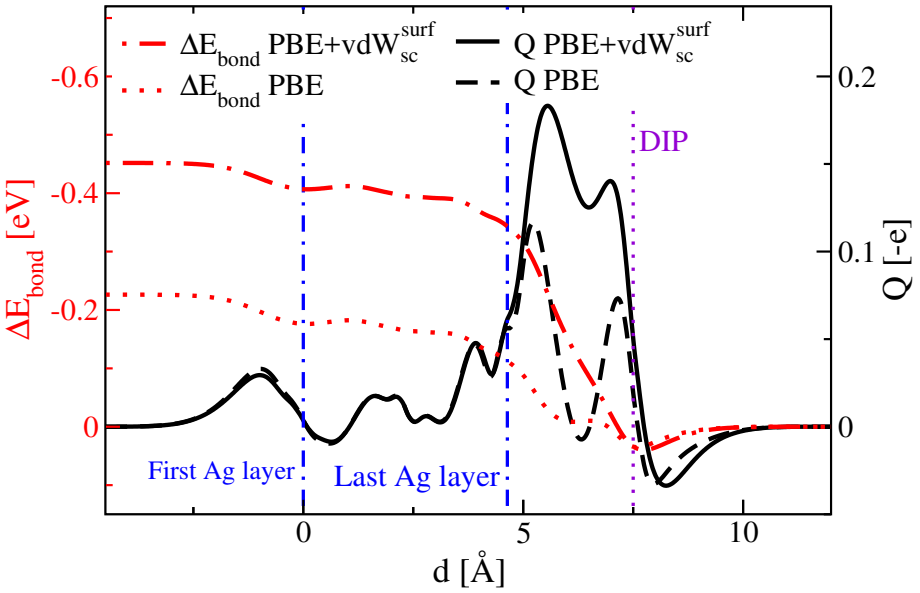

Figure 10.5: DIP/Ag(111). The PBE and PBE+vdW$_{\text{sc}}^{\text{surf}}$ delocalized charge $Q(z)$ are plotted together with the corresponding change of the potential energy $\Delta E_{\text{bond}}(z)$. The vertical dotted-dashed lines indicate the upper and lower limits of the Ag(111) surface. The vertical dotted line corresponds to the position of the DIP molecule.

directly to the analysis of the charge. Nevertheless, the plot of $\Delta n_{\text{ads}}(z)$ for DIP/Ag(111) is reported and discussed in Appendix D.5.

The delocalized charge is drawn in Figure 10.5 for PBE+vdW$_{\text{sc}}^{\text{surf}}$ and PBE alone, in solid and dashed lines respectively. The two curves show large differences in the region between the topmost metal layer and the monolayer plane, see in Figure 10.5 the region between the vertical dotted-dashed line (on the right side) and the vertical dotted line. Self-consistency enhances the charge redistribution at the interface of about $0.2\,e$. The higher positive peak of $Q(z)$, just above the Ag(111) surface, indicates the Pauli push-back effect and is roughly 40% higher when SC vdW effects are included. From the figure we can also grasp a qualitative estimation of the charge transfer by looking at the downward slope of $Q(z)$, located at the interface. Here, PBE+vdW$_{\text{sc}}^{\text{surf}}$ presents a less marked steepness and a higher local minimum with respect to the PBE curve, which even reaches negative values. Therefore, from this analysis, it emerges that SC effects increase the pillow effect and decrease the flux of charge from the metal to the molecule.

The change in the potential energy represents a quantitative estimation of the effects of self-consistency and can be computed by solving the 1D Poisson equation (see Equation 10.4). As expected, the ΔE_{bond} with SC effects, see the dotted line in Figure 10.5, is larger than the one of PBE, drawn in dotted-dashed line. The result is a BD of $-0.45\,$eV and $-0.23\,$eV for PBE with and without SC vdW, respectively. We note that the inclusion of SC effects doubles the PBE value. The flat relaxed geometry of the monolayer provides a small change in potential energy of $\Delta E_{\text{mol}} = 0.042\,$eV found in both schemes. At this point, the workfunction shift is computed *via* Equation 10.5. The sum of ΔE_{bond} and

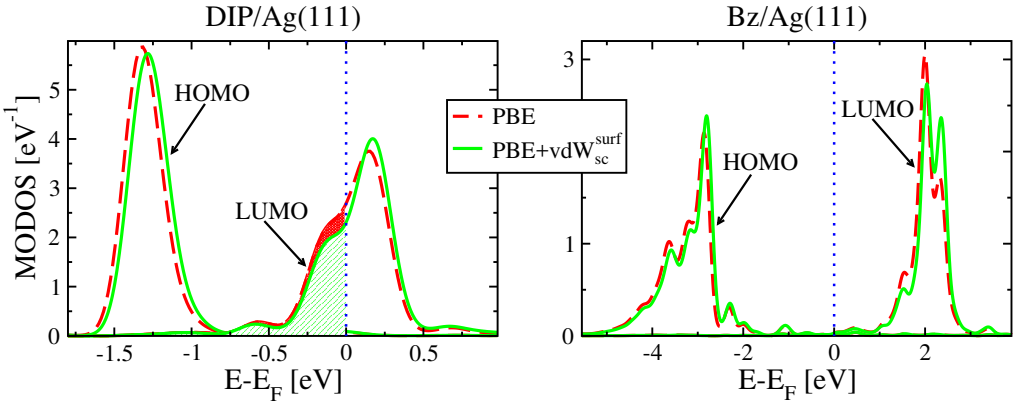

Figure 10.6: Molecular orbital density of states computed with PBE and PBE+vdW$_{sc}^{surf}$. The orbitals plotted in the two panels correspond to the HOMO and LUMO molecular levels of the adsorbate molecules. On the left panel are plotted the orbitals for DIP/Ag(111). Bz/Ag(111) is considered on the right panel. The energy axis is rescaled with respect to the Fermi energy, indicated with the vertical dotted lines.

ΔE_{mol} gives a large shift of -0.408 eV for PBE+vdW$_{sc}^{surf}$, while $\Delta\Phi = -0.188$ eV with PBE alone. These values nicely confirm the results reported in Table 10.2 and obtained from Equation 9.1.

We can give an estimation of charge loss/gain of the molecule adsorbed on the surface by summing over all the occupied molecular orbitals. When the molecule is adsorbed, the molecular orbitals (MOs) interact with the orbitals of the metal surface and can result broadened and shifted, depending on the "strength" of the interaction. The MOs are simulated by projecting the density of states (DOS) of the hybrid system onto the MOs of the isolated molecule (taken in gas phase). This Mulliken-like population analysis [237] allows to assess quantitatively the amount of electrons transferred to the molecule *via* the projected DOS [238], called MODOS. The occupation of a single MODOS is obtained with an integral over the energy that spans up to the Fermi energy. Subsequently, the total occupation is simply the sum of all the occupied MODOS. Then, the charge transfer is computed as the difference between the total occupation and the charge of the isolated molecule. More details on the MODOS analysis are included in Appendix D.4.

Considering DIP/Ag(111), self-consistency halves the charge transfer, starting from $0.2\,e$ with PBE to $0.09\,e$ with PBE+vdW$_{sc}^{surf}$ and a reduction of $0.11\,e$ (55%). Moreover, from the MODOS we can define the charge donation as the filling of the LUMO alone, while the occupation of all other orbitals higher in energy—the other empty molecular orbitals of the molecule in gas phase—is called back donation. The effect of self-consistency is to reduce the charge donation by 10% ($0.06\,e$), as well as a quantitatively similar increasing of back donation. A plot of the HOMO and LUMO of the adsorbate DIP molecule is drawn in the left panel of Figure 10.6. The effect of self-consistency on the HOMO is a simple rigid shift towards the Fermi energy, which has been rescaled in the figure and corresponds to the value zero. On the other hand, the LUMO overlaps the Fermi level, thus it is filled by the electrons of the substrate up to E_F. This observation

Table 10.3: PTCDA and CuPc adsorbed on silver (111) surface. The binding energies, the binding distances and the workfunction shifts computed with PBE+vdW$^{\rm surf}$ and PBE+vdW$^{\rm surf}_{\rm sc}$ are reported and compared with the experimental data. The distances between the topmost metal layer and the average position of the carbon atoms $d_{\rm C}$ and the nitrogen atoms $d_{\rm N}$ are reported in [Å]. The binding energies E_b and the workfunction shifts are in [eV].

	PTCDA/Ag(111)			CuPc/Ag(111)			
	$d_{\rm C}$	E_b	$\Delta\Phi$	$d_{\rm C}$	$d_{\rm N}$	E_b	$\Delta\Phi$
PBE+vdW$^{\rm surf}$	2.84[a]	-3.06	0.33	3.00	2.99	-4.085	-0.22
PBE+vdW$^{\rm surf}_{\rm sc}$	2.84	-3.00	0.11	3.00	2.99	-4.012	-0.41
Experiment	2.86[b]		0.06[c]-0.16[d]	3.08[e]	3.04[e]		-0.44[f]

a: Reference [123]; b: Reference [239]; c: Reference [240]; d: Reference [241]; e: Reference [242]; f: Reference [210].

is true for both PBE and PBE+vdW$^{\rm surf}_{\rm sc}$ and indicates the presence of a charge transfer between the metal and the molecule. However, when SC vdW interactions are included the LUMO is slightly distorted and the area available to be filled by the electrons of the substrate (left of zero) is reduced, as shown in Figure 10.6. This effect is the reason behind the reduction of $0.06\,e$ in the charge donation. As a comparison, we plotted on the right panel of Figure 10.6 the HOMO and LUMO of Bz adsorbed on Ag(111). Clearly the HOMO and LUMO are separated by a gap and the Fermi level is located in between the two orbitals. In this situation a transfer of charge between the substrate and the organic molecule is substantially absent ($\sim 0.01\,e$). Therefore, for Bz/Ag(111), even though self-consistency induces modifications of the orbitals, in particular for the LUMO, they have no relevant impact in the ground-state electronic properties.

10.4 PTCDA on Ag(111)

The study is now extended to another large and flat molecule, PTCDA ($C_{24}H_8O_6$), which shortly refers to *Perylenetetracarboxylic dianhydride*. The molecule forms a commensurate monolayer on Ag(111), as observed in STM experiments [243, 244]. The unit cell contains two molecules in a herringbone configuration and non-equivalent adsorption geometries, see Figure D.8. The binding distance of the structure, relaxed with PBE+vdW$^{\rm surf}$, is reported in Table 10.3 and displays an almost perfect agreement with the data extracted from XSW experiments [239]. Further details of the structure and the calculations presented here are available in Appendix D.5. The performances of PBE+vdW$^{\rm surf}$ with PTCDA/Ag(111) are discussed in detail in the References [123, 127, 140].

The main difference between PTCDA and the DIP is the presence of the functional group O=C−O−C=O on both sides of PTCDA. This leads to a different behavior with respect, for example, to perylene-like molecules, that is enhancing the bonding with the surface and the charge transfer [241, 245]. In this HIOS, a net charge transfer is present, from the substrate to the molecules, as sketched in Figure 10.1. The magnitude of the charge transfer is roughly three times larger than DIP/Ag(111). Consequently,

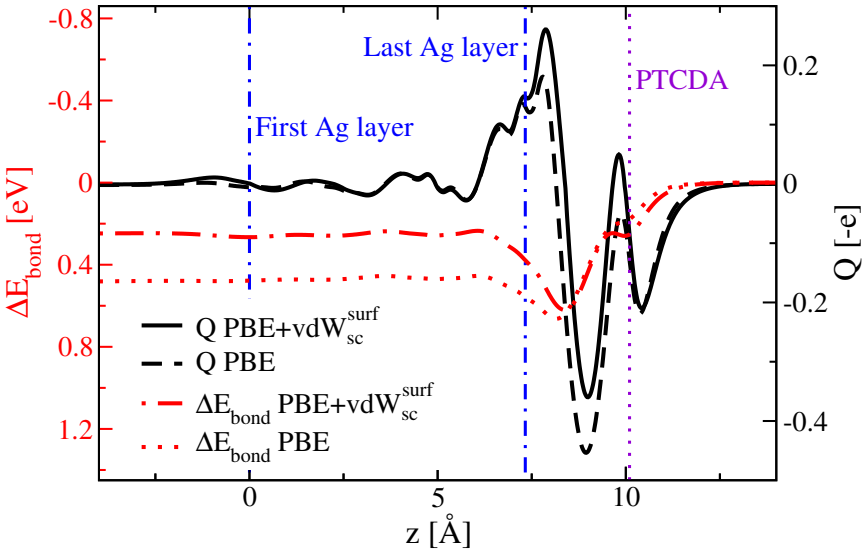

Figure 10.7: PTCDA/Ag(111). In the figure are reported the charge rearrangements upon molecular adsorption ($Q(z)$) and the corresponding variations of potential energy ($\Delta E_{\rm bond}(z)$) obtained with PBE and PBE+vdW$_{\rm sc}^{\rm surf}$. The two vertical dotted-dashed lines indicate the bottommost and topmost metal layers, while the vertical dotted line corresponds to the PTCDA monolayer.

the pillow effect is overturned and the pristine metal workfunction increases upon molecular adsorption. The positive $\Delta\Phi$ has been measured in experiments [240, 241], as well as predicted in previous theoretical studies [199, 205, 223]. As seen before in the case of DIP on Ag(111), the inclusion of vdW effects enhances the Pauli push-back and damps the (large) charge transfer. Consequently, with PBE+vdW$_{\rm sc}^{\rm surf}$ the positive shift $\Delta\Phi$ is reduced to one third of the PBE value. The results are reported in Table 10.3. Once again, the inclusion of vdW effects in the electronic properties significantly improves the agreement with experiments.

The delocalized charge, $Q(z)$, computed with PBE and PBE+vdW$_{\rm sc}^{\rm surf}$, is plotted in Figure 10.7 together with the corresponding change in the potential energy $\Delta E_{\rm bond}(z)$. The $Q(z)$ with SC vdW effects presents a higher peak located just above the topmost metal layer, suggesting a larger Pauli push-back. At the same time, self-consistency lessens the negative peak at the interface, a qualitative indication of the reduction in the charge transfer. From the comparison between the $Q(z)$ of DIP and PTCDA on Ag(111), Figure 10.5 and 10.7 respectively, we can see that the overall shapes are rather similar. However, with PTCDA/Ag(111) the magnitude of the displacements is larger. In particular, the downward peak at the interface is much more pronounced and both PBE and PBE+vdW$_{\rm sc}^{\rm surf}$ produce a $Q(z)$ that falls in the negative values. This feature is a clear evidence of the large charge transfer of PTCDA/Ag(111). Similar conclusions can be obtained from the analysis of $\Delta n_{\rm ads}(z)$, which are reported and described in Appendix D.5.

The effects of such large charge transfer can be seen in $\Delta E_{\rm bond}(z)$, *i.e.* the integral

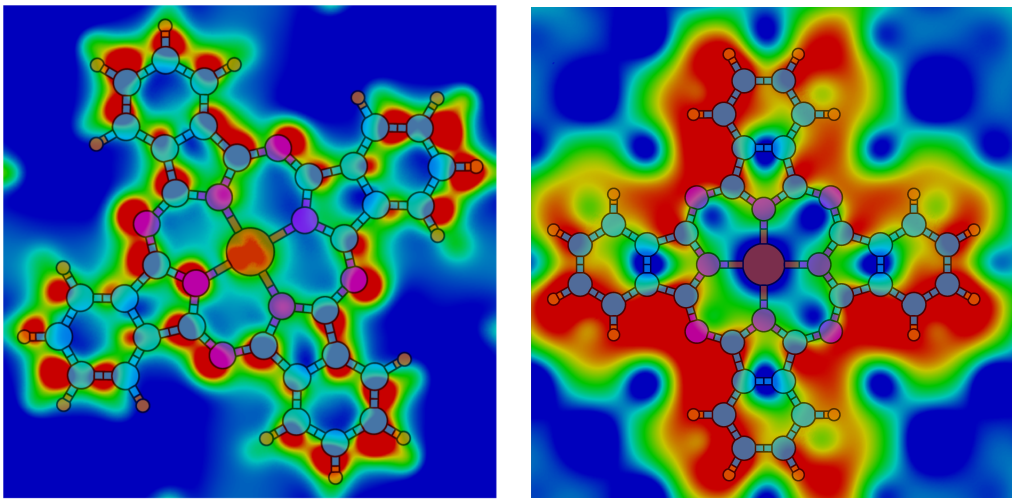

Figure 10.8: 2D slice of induced electron density difference $\Delta n_{\mathrm{ads}}^{\mathrm{PBE+vdW_{sc}^{surf}}}(\mathbf{r}) - \Delta n_{\mathrm{ads}}^{\mathrm{PBE}}(\mathbf{r})$. The regions of electron density accumulation are in blue, while red indicates depletion. The slice is taken at the interface, between the metal and the molecule. Left panel: Top view of CuPc on Ag(111). The limiting values are set to $\pm 5.0 \times 10^{-4}$ e/Å^3. Right panel: Top view of CuPc on Ag(100). The limiting values are set to $\pm 4.0 \times 10^{-4}$ e/Å^3. In both figures the CuPc molecule is sketched as a guide to the eye.

of $Q(z)$, see Equation 10.4. In fact, the two $\Delta E_{\mathrm{bond}}(z)$, plotted in Figure 10.7 for PBE and PBE+vdW$_{\mathrm{sc}}^{\mathrm{surf}}$, remain in the bottom side of the plot, leading to a positive BD. The shift in the workfunction can be computed *via* Equation 10.5, by adding to the BD the contribution of the molecular dipole, which is -0.17 eV for both functionals. We note in passing that the changes in the PTCDA geometry, during adsorption, produce a ΔE_{mol} roughly four times larger than the one of DIP (0.042 eV). The resulting $\Delta\Phi$ are $-0.17 + 0.48 = 0.31$ eV for PBE and $-0.17 + 0.26 = 0.09$ eV for PBE+vdW$_{\mathrm{sc}}^{\mathrm{surf}}$, in good agreement with the values reported in Table 10.3.

The quantitative estimation of the charge transfer, performed *via* the MODOS, reveals that self-consistency entails a robust reduction of the transfer of charge of about $0.10\,e$ (15%) per molecule. The transfer is $-0.68\,e$ per molecule with PBE and reduces to $-0.58\,e$ with PBE+vdW$_{\mathrm{sc}}^{\mathrm{surf}}$. In detail, charge donation, *i.e.* the filling of the LUMO, is affected by a reduction of $0.054\,e$ (3.7%). This charge is redirected as backdonation, which displays an increase of 6%.

10.5 Further Examples

In concluding the chapter of the applications we leave the reader with some extra examples of HIOS that have been successfully investigated with SC vdW interactions. The first system contains a large and flat aromatic molecule of the family of metal-phthalocyanines (MePc), CuPc, adsorbed on Ag(111) and Ag(100). This class of organic

semiconductors is characterized by the presence of a metal atom in the center of the molecule. The molecular geometry assumes a planar or non-planar configuration, depending on the atomic species of the metal atom. It can also display different electronic properties, e.g. the vertical dipole. Therefore, the substitution of the metal atom opens many possibilities for a controlled and efficient tuning of the electronic properties. This feature is combined with a high thermal stability of CuPc and makes these class of molecules particularly interesting for applications in organic electronics such as in photovoltaic cells, sensors, LED. CuPc on coinage metal surfaces has been characterized with several experimental techniques as STM, X-ray standing wave (XSW) and ultraviolet photoelectron spectroscopy UPS [242, 246]. Recently, this molecule has been utilized in a multi-component blend with perfluoropentacene (PFP) adsorbed on Cu and Ag (111) surfaces. The study investigates the modification of the interfacial properties with respect to the single-component system [210].

The CuPc molecule is weakly bonded on Ag(111) and the vdW dispersion interactions are of primary importance for a correct description of the geometries. A confirmation of this can be seen in Table 10.8, where both the binding distances d_{C} and d_{N} (computed by taking the average position of the carbon and nitrogen atoms) are around $3.0\,\text{Å}$. The values of d_{C} and d_{N} predicted by PBE+vdW$^{\mathrm{surf}}$ are in remarkably good agreement with the experimental data. The inclusion of SC effects produces only a negligible difference in the binding energy. However, a large density rearrangement is found. We consider now, for CuPc/Ag(111), the density difference between the induced density of PBE+vdW$^{\mathrm{surf}}_{\mathrm{sc}}$ and the one of PBE. A 2D slice of this density difference, taken at the interface, is plotted in the left panel of Figure 10.8. Clearly, self-consistency displays collective, pronounced and complex redistributions at the organic/metal interface. The depletion regions nicely overlap with the footprint of the CuPc molecule, while the accumulation areas are found in proximity of the carbon rings and and around the molecule. These effects are reflected in a reduction of the workfunction shift of $-0.19\,\text{eV}$, doubling the PBE value and significantly improving the agreement with experiment, see Table 10.8. We have already seen before that self-consistency reduces the charge transfer that flows from the substrate to the molecule. Here, the reduction is of about $0.14\,e$ (80%), going from the PBE value of $0.165\,e$ to the PBE+vdW$^{\mathrm{surf}}_{\mathrm{sc}}$ value of $0.025\,e$. The MODOS analysis reveals that the LUMO is not the only orbital that crosses the Fermi level, hence the reduction of the charge donation is rather modest ($0.013\,e$, $\sim 3\%$). For instance, the reduction of charge transfer in the filling of the second lowest unoccupied orbital is two times larger, $0.028\,e$ (11%). On the contrary, the backdonation increases of about $0.123\,e$ (51%).

Another example taken into consideration is CuPc on Ag(100). The 2D slice of density difference is drawn on the right panel of Figure 10.8 and can be easily compared with CuPc/Ag(111). Because of the different surface, the molecule adsorbs with the Cu atom aligned above a silver top atom, while the hollow site is found for CuPc/Ag(111). Therefore, in the case of CuPc/Ag(100) the density accumulates in the center of the molecule and results depleted around the borders. Notably, for CuPc/Ag(100) the

Table 10.4: Workfunctions Φ of the clean silver (100) surface (first column) and three hybrid systems. The values obtained with the two functionals PBE and PBE+vdW$^{\text{surf}}_{\text{sc}}$ are reported along with the experimental measurements, obtained with ultraviolet photoelectron spectroscopy (UPS). All the workfunctions are reported in [eV].

	Ag(100)	CuPc/Ag(100)	PYTON/Ag(111)	F4TCNQ/Ag(111)
PBE	4.30	4.16	4.82	5.046
PBE+vdW$^{\text{surf}}_{\text{sc}}$	4.59	4.37	4.897	5.112
Experiment	4.64[a]		4.88[b]	5.15[c]

a: Reference [185].
b: Reference [223].
c: Reference [247].

values of the density displacements are even larger than CuPc/Ag(111). Of course, these effects on the electron density are reflected on the workfunction. Self-consistency enhances the reduction of Φ of the pristine surface, leading to $\Delta\Phi = -0.22$ eV. A smaller shift, $\Delta\Phi = -0.14$ eV, is found with PBE. The values of the workfunctions are reported in Table 10.4, the shifts can be computed by subtracting the workfunction of the clean silver (100) surface to the one of the hybrid system. It is worth mentioning that PBE predicts a $\Phi = 4.30$ eV for the workfunction of the clean Ag(100) surface. On the other hand, the PBE+vdW$^{\text{surf}}_{\text{sc}}$ value is $\Phi = 4.59$ eV, once again in better agreement with the experimental number of $\Phi = 4.64$ eV. The charge transfer computed with PBE corresponds to $0.26\,e$. On the other hand, a modest value of about $0.046\,e$ is found with PBE+vdW$^{\text{surf}}_{\text{sc}}$, meaning that a pronounced reduction of $0.213\,e$ ($\sim 82\%$) is driven by SC vdW effects. The LUMO of CuPc/Ag(100) is not the only orbitals filled with the electrons from the substrate, similarly to what found above for CuPc/Ag(111). It follows that the charge donation is reduced by a tiny $0.01\,e$ ($\sim 1\%$). The second lowest unoccupied orbital presents, instead, a larger reduction of $0.068\,e$ (24%). The charge redirected as backdonation is about $0.2\,e$ (175%), a large contribution in the total reduction of charge transfer.

The last examples presented as a conclusion of this chapter are two prototypical organic acceptor, F4TCNQ (3,5,6-tetrafluoro-7,7,8,8-tetracyano-quinodimethane) and PYTON (4,5,9,10-pyrenetetraone, a pyrene with four oxygen atoms) adsorbed on Ag(111). These two molecules have been studied, in both theory and experiments, adsorbed on the three coinage metal (111) surfaces [223, 247, 248]. They are able to form hybrid systems with densely packed and ordered monolayers and are characterized by a large charge transfer, that fills the empty molecular orbitals. Hence, the workfunction of the clean metal increases, as in the case of PTCDA/Ag(111). In particular, F4TCNQ/Ag(111) presents a charge transfer approximately 2–3 times larger than the one of PTCDA/Ag(111). The consequence is a high workfunction of the hybrid system, as reported in Table 10.4. The shift measured in experiments is a large $\Delta\Phi = 0.41$ eV. The PBE functional, coupled with SC vdW effects, provides a shift of $\Delta\Phi = 0.372$ eV, which agrees well with the experimental value. In this regard, the inclusion of self-consistency provides the same qualitative effects already seen with PTCDA/Ag(111),

resulting in a reduction of the overestimated shift of PBE ($\Delta\Phi = 0.606\,\text{eV}$). In the last case, PYTON/Ag(111), the workfunction shift of PBE ($\Delta\Phi = 0.38\,\text{eV}$) is almost three times larger than the one obtained from experiments, $\Delta\Phi = 0.14\,\text{eV}$. On the contrary, the shift obtained with the PBE+vdW$_{\text{sc}}^{\text{surf}}$ functional, $\Delta\Phi = 0.157\,\text{eV}$, displays an almost perfect agreement with the measured value.

Overall, the inclusion of vdW effects in the electronic structure of HIOS, in particular with silver as a substrate, always brings an improvement in the description of the electronic properties, with respect to the performances of the PBE functional alone. In this chapter, we have employed several different examples to corroborate our results and conclusions. The detailed analysis presented here provides a clear overview about the fundamental contributions of vdW interactions in the regulation of the electronic properties of HIOS. In particular, self-consistency is found to affect the different physical phenomena that determine the value of the workfunction, an experimentally measurable quantity. In conclusion, our study demonstrates that vdW interactions can be a key factor for correctly predict and control the electronic properties of HIOS. As such, a refined description of the electronic structure of hybrid systems is achieved only with the inclusion of vdW interactions into standard XC functionals.

11 Summary and Outlook

The long-range correlation interactions are well known to be of fundamental importance in the structure and in the cohesive energy of a wide variety of different systems. However, little is know about their role on the electronic structure and properties of materials. In this doctoral work we tackled this open question with a numerical implementation of the self-consistent Tkatchenko-Scheffler method for including the van der Waals interactions into the DFT framework.

The self-consistent equations reported here have been derived analytically. Their implementation within the FHI-aims code has been presented and discussed, along with the necessary technical details. Part of the thesis has been dedicated to the assessment of the computational costs of self-consistency and the comparison with the more conventional *a posteriori* correction of the total energy. In this regard, the aim of our work has been focused on improving the efficiency of the implementation, without introducing approximations or cut-offs. The successful optimization procedure leads, in most of the cases, to a scaling comparable to the faster *a posteriori* scheme. The scaling worsens and the calculations become computationally expensive only in case of very large periodic systems with hundreds of atoms. Nevertheless, all the calculations tested with the "fast" implementation could reach convergence. Completely different performances were obtained with the unoptimized scheme, which presents much worse scaling for both periodic and non-periodic systems as the number of atoms increases. To further improve the efficiency of the code, one solution could be the introduction of a cut-off that limits the distance of the interactions. However, since we are dealing with long-range correlation effects, such approximations should be managed with care. Moreover, we consider the present level of efficiency as satisfactory since it allows to apply our implementation with the same size limit of a standard DFT functional.

With this tool in hand we have performed fully self-consistent calculations employing a wide variety of systems of different complexity and size, starting from small dimers, as rage-gas dimers, to large periodic systems, as molecules adsorbed on metal surfaces. The accuracy of our results has been benchmarked and compared with the more conventional *a posteriori* implementation as well as other popular approaches. From the comparisons between our results and the "gold-standard" coupled-cluster calculations it emerges that self-consistency provides a very accurate description of the effects of long-range correlation interactions on the electron density. Notably, the analysis of the SC effects on

rare-gas dimers and small molecular dimers allowed us to reconcile two different views on vdW interactions: (i) Feynman's view that claims that vdW stems from changes in the local electron density and (ii) atoms separated by infinite barrier. In the former picture, the vdW interactions are viewed as an electrostatic attraction between perturbed electron densities. The latter is the more conventional London approach, in which vdW interactions result from the electrodynamic coupling between fluctuating molecular dipoles.

Overall, for the large majority of the cases tested, the SC cohesive energies display an almost perfect agreement with the results of the *a posteriori* vdW scheme. The exceptions include systems with high polarizability and/or low dimensionality. However, the changes in the energy for large and periodic systems are still on the order of few percentage points. On the other hand, for systems characterized by very large vdW energy, as the alkali-metal dimers, self-consistency is found to affect the structural properties, with changes in the equilibrium distances, improving the agreement with the experimental data. In addition to that, SC effects can be responsible for exceptionally large contributions (up to $\sim 40\%$) to the cohesive energies.

The displacements of the electron density, driven by vdW interactions, can lead to substantial modifications in the electronic properties. Considering finite systems with strong vdW effects, as the alkali-metal dimers, we found that the dipole moment is increased/decreased by vdW interactions, with changes up to 10-15% of its value without SC effects. For periodic transition metal surfaces, the inclusion of self-consistency triggers a rearrangement of electron density which involves primarily the topmost metal layer and the vacuum region above the surface. Consequently, the surface dipole of these metal surfaces results significantly modified, leading to changes in the workfunction. In particular, vdW effects are found to change both i) the Fermi energy and ii) the electrostatic potential in the vacuum region. The combination of these two effects is reflected in large changes of the workfunctions, up to 0.2 eV (6%) for Ag(111), the most sensitive case.

To further assess the general validity of our findings for molecules and metal surfaces, in the last part of this thesis we extended the application of the SC implementation to complex hybrid inorganic/organic systems. Similarly to what was found for metal surfaces, vdW interactions are connected with sizable density rearrangements, characterized by particularly large effects between the last metal layer and the adsorbed molecule or monolayer. The workfunctions of surfaces can be tuned by molecular adsorption and they are connected with the density rearrangement at the interface. Therefore, the electron density displacements induced by vdW interactions are reflected into modifications of the workfunction shifts. For all the systems presented in this work, the addition of vdW interactions improves the agreement between the theoretical predictions and the experimentally determined data. For the most sensitive cases, DIP and PYTON on Ag(111), self-consistency entails a modification in the workfunction shift of about 0.22 eV, which consists in a reduction of the shift to one third of its value computed without vdW effects.

For hybrid inorganic/organic systems, unlike clean metal surfaces, the underlying mechanism responsible for the workfunction modifications stems from an interplay between two effects: i) The Pauli push-back, *i.e.* the repulsion between the electrons of the metal surface and those of the adsorbed molecule, ii) The charge transfer between the molecule and the surface. All the hybrid systems tested show that self-consistency enhances the Pauli push-back and reduces the charge transfer. It is indeed the combination of these two opposite effects that leads to the large reductions of the workfunction shifts mentioned above. Moreover, the quantitative analysis of the transfer of charge, performed with a Mulliken-like population analysis, revealed that SC vdW can be responsible for very large reductions of the charge transfer, up to 80% ($\sim 0.2\,e$) for CuPc on Ag(111) and Ag(100).

In summary, the extended analysis performed in this work discloses the important role of vdW interactions on the electronic properties of molecules and materials. From the results it emerged that the long-range correlation interactions are particularly important in systems with high polarizability density and in low dimensional materials. Along with these findings, several possible extensions are available for future works to further benchmark the role of vdW interactions.

First, in addition to the silver (111) surface, it is possible to employ other surfaces as the (100) and the (110), similarly to the example of CuPc/Ag(100), presented in Section 10.5. The PTCDA molecule, for example, has been already characterized on these two surfaces with the PBE+vdW$^{\text{surf}}$ functional [140]. The relaxed structures yield binding distances in a very good agreement with the experimental numbers, the differences—computed by taking the average distance of the carbon atoms—are ≤ 0.06 Å. Besides, different types of surfaces imply different coordination numbers and bond lengths. As a consequence, depending on the surface, the PTCDA monolayer displays different configurations. We already saw that PTCDA/Ag(111) is ordered in a herringbone structure. In addition to that, PTCDA on Ag(100) presents a T-shaped orientation (two molecules per unit cell), while PTCDA forms a brick-wall adsorption pattern on Ag(110) (one molecule per unit cell). Therefore, these systems could be conveniently employed to study the different effects of vdW interactions depending on the type of surface and monolayer.

Another group of organic molecules on metal surfaces, not considered in this work, is the one characterized by a charge transfer directed from the HOMO of the molecule to the substrate. In these systems the workfunction of the interface typically displays large reduction with respect to the one of the bare metal surface. These reductions are the result of the combined effect of Pauli push-back and the charge transfer. In fact, the presence of a flux of charge from the monolayer towards the metal surface would enhance the reduction of Φ due to the Pauli push-back effect. A suitable candidate for our implementation could be viologen adsorbed on coinage metal (111) surfaces. This molecule has already been studied with the PW91 [249] XC functional[1] and a

[1]The PW91 functional was the first successful GGA. The PBE functional is simplified version of the PW91. The results of these two XC functionals should be very similar.

loosely packed monolayer. The results indicate that the occupation of the HOMO of the molecule is reduced roughly by 30-40% during the adsorption and the total $\Delta\Phi$ are on the order of -1.0 eV [236]. It would be very interesting, for example, to check whether the effect of self-consistency enhances or lessens such charge transfer.

The results shown in our study for metal surfaces can be expanded by considering other materials as a substrate, for instance ionic and semiconductor surfaces. In this case the parameters of the vdW functional for the polarizabilities and the C_6 coefficients are obtained *via* the Clausius-Mossotti equation. With the CM equation the dielectric function of a solid, computed with time-dependent density-functional theory (TDDFT) calculations, is connected with its dynamic polarizability. This version of the TS vdW functional has already been applied to ionic and semiconductor solids showing an improvement in the cohesive properties as the bulk modulus, the lattice constant and the cohesive energy, with respect to PBE and HSE06 results [122]. These promising results are good motivations for further investigating the possible effects of vdW on the electronic properties. Also, good performances with semiconductor surfaces would open the possibility to test additional examples of complex hybrid systems as semiconductor-semiconductor interfaces or hybrid systems with molecules adsorbed on semiconductors. In this family of hybrids, unlike molecules on metals, the electronic properties are mainly determined from the alignment between the conduction and the valence bands of the semiconductor surface and the molecular HOMO and LUMO levels [209]. Preliminary calculations on Si(111), reconstructed with the well-known (7×7) supercell, suggest that self-consistency increases the workfunction of PBE and PBE0 of about 0.1 eV. The final values are 4.63 eV for PBE+vdW$^{\mathrm{TS}}_{\mathrm{sc}}$ and 4.51 eV for PBE0+vdW$^{\mathrm{TS}}_{\mathrm{sc}}$, showing a slight improvement in the agreement with the experimental workfunction of 4.60 eV [185]. The next step will be the study of other semiconductor surfaces as the Si(100), which reconstructs with a (2×1) unit cell.

The vdW interactions have been included into the electronic properties *via* the TS functional, which is based on a summation of pairwise contributions. The TS functional captures effects beyond the pairwise additivity as the charge polarization for atoms-in-a-molecule (Hirshfeld partitioning) and the collective electrodynamic response of the solid ($\mathrm{vdW}^{\mathrm{surf}}$). In this regard, the full treatment of the many-body effects represents the next step for improving the accuracy in the description of the vdW effects. However, accurate quantum-chemistry methods as the EXX+cRPA, where the correlation is computed at the RPA level and summed to the exact-exchange, imply prohibitive computational costs and are (still) too expensive to be applied to extended systems. The recently developed DFT+MBD method [250] consists of a dipole approximation of the RPA formula, which includes the long-range many-body effects as an infinite series. Within the MBD methods the response function is approximated with atom-centered quantum harmonic oscillators (QHO) interacting through a dipole-dipole potential. Under this assumption the MBD is equivalent to RPA [251]. The MBD method has already been successfully applied to adsorbates on metal surfaces, as Xe, benzene and PTCDA on Ag(111) [124, 125]. The MBD typically reduces the adsorption energies of $\mathrm{vdW}^{\mathrm{surf}}$, which

shows a tendency to overbind, yielding to an improvement in the adsorption energies and geometries. Very recently, the MBD was made available also in a self-consistent flavor, thus the role of the many-body effects can be tested on the electronic properties. In this regard, we expect effects on the electronic properties of HIOS quantitatively similar to the ones obtained with DFA+$\mathrm{vdW}_{\mathrm{sc}}^{\mathrm{surf}}$ calculations. The MBD method has been developed to describe the correlation of finite gap materials. Without the addition of delocalized oscillators for every atom, the localized QHO would not include the delocalized plasmonic response of free electrons in the metal substrate. A solution to induce the correct delocalization of the polarizability is to use the screened $\mathrm{vdW}^{\mathrm{surf}}$ parameters as a starting point in the calculation. Nevertheless, the challenge to include a simultaneous description of localized and metallic states remains open for future works.

Before concluding we mention here a couple of possible future projects. 1) The vdW interactions can display relativistic effects, for example in case of very large interatomic distances, where the power law of the interaction exhibits a R^{-7} decay, instead of the "usual" R^{-6} [252]. Once again, the role of these relativistic effects on the electron density and properties could be investigated with a self-consistent implementation. 2) So far our findings have been restricted to ground-state properties, but they are strongly suggestive of the potential importance of long-range vdW effects in properties beyond the electronic ground-state. In order to investigate electronic properties as the optical spectra one could, for example, perform TDDFT calculations. However, the implementation of the vdW effects into the TDDFT framework requires the second derivative of the vdW potential with respect to the electron density. This derivation presents a rather simple analytical form and all the different terms are already available in the code. In fact, they are necessary components of the vdW potential. On the other hand, the second derivative would introduce another space variable $\mathbf{r}'$, in addition to $\mathbf{r}$. This means that, with a straightforward implementation, the number of loops used to compute the potential would be doubled in this case. Therefore, this implementation would require a clean optimization procedure to reach a reasonable efficiency and enhance its practical applicability.

In conclusion, the implementation presented in this doctoral work represents an efficient and accurate scheme which provides electronic structure calculations with self-consistent vdW interactions. Our results demonstrated that self-consistency can bring sizable effects on the binding energies and molecular multipoles for polarizable fragments. Moreover, surface dipoles and workfunctions for inorganic substrates can display large modifications due to vdW interactions, as well as interface dipoles and charge transfer phenomena for hybrid inorganic/organic systems. Hence, a non-trivial connection between electrostatics and long-range correlation effects was revealed.

Part V

Backmatter

Appendices

A VARIATIONAL METHOD

A.1 THE VARIATIONAL PRINCIPLE

Given a Hilbert space and a Hermitian operator $\mathcal{H}$ and the corresponding eigenfunctions and eigenvalues, considering discrete spectrum, the i-th equation is written as

$$\mathcal{H}|\Psi_i\rangle = \mathcal{E}_i|\Psi_i\rangle\,. \tag{A.1}$$

with a set of exact solutions that follow the ordering

$$\mathcal{E}_0 \leq \mathcal{E}_1 \leq \mathcal{E}_3 \leq \cdots \leq \mathcal{E}_i \leq \cdots\,. \tag{A.2}$$

The variational principle assures that the expectation value of an eigenstate is an upper bound to the ground-state value

$$\langle\Psi_j|\mathcal{H}|\Psi_i\rangle = \mathcal{E}_i\delta_{i,j} \geq \mathcal{E}_0\,, \quad \text{with the ortonormal relation } \langle\Psi_j|\Psi_i\rangle = \delta_{ij}\,. \tag{A.3}$$

This conclusion can be proved, supposing that we know the eigenstate that corresponds to $\mathcal{E}_0$, we consider a normalized wavefunction $|\Psi\rangle$

$$\begin{aligned}\langle\Psi|\mathcal{H}|\Psi\rangle &= \sum_{i,j}\langle\Psi|\Psi_i\rangle\langle\Psi_i|\mathcal{H}|\Psi_j\rangle\langle\Psi_j|\Psi\rangle = \\ &= \sum_i \mathcal{E}_i|\langle\Psi_i|\Psi\rangle|^2 \geq \sum_i \mathcal{E}_0|\langle\Psi_i|\Psi\rangle|^2 = \mathcal{E}_0\,,\end{aligned} \tag{A.4}$$

where the equality is found only when Ψ_0 is considered. In the passage from the first to the second line, we used the completeness and orthonormal relations. The last passage combines again these two relations and can be written out explicitly

$$\begin{aligned}\langle\Psi|\Psi\rangle &= 1 = \sum_{i,j}\langle\Psi|\Psi_i\rangle\langle\Psi_i|\Psi_j\rangle\langle\Psi_j|\Psi\rangle = \\ &= \sum_i\langle\Psi|\Psi_i\rangle\langle\Psi_i|\Psi\rangle = \sum_i |\langle\Psi|\Psi_i\rangle|^2\,.\end{aligned} \tag{A.5}$$

From the variational principle it follows that a lower energy is associated with a better wavefunction, or, in other words, that the energy associated with an approximate wave-

function will always be too high. In the specific case of the wavefunction composed by a single Slater determinant, we can vary the set of spin-orbitals $\{\psi_i\}$ until the expectation value in Equation A.3 reaches its minimum, which is higher or equal than the exact ground-state energy.

A.2 Lagrange Multipliers

The minimization of the energy, a functional of the wavefunctions, is obtained within the linear variational method, *i.e.* a small variation of the function produces a variation in the energy too and the stationary point is imposed with the condition of a variation equal to zero: $\delta E = 0$. The stationary condition is not automatically assumed to guarantee a minimum. This needs to be verified, but is usually the normal outcome in practical calculations.

The stationary point is obtained *via* the method of Lagrange functions $\mathcal{L}$, defined in this case as the difference between the energy—functional of the wavefunctions—and the constraint of orthogonal and normalized wavefunctions

$$\mathcal{L} = \langle \Psi | H_e | \Psi \rangle - \lambda \left(\langle \Psi | \Psi \rangle - 1 \right) , \tag{A.6}$$

where λ is the Lagrange multiplier, whose physical meaning could be already guessed. The value of the Lagrange multiplier is found by varying the Lagrange function and equating the variation to zero. This condition means that the value of the Lagrange multiplier is associated with the stationary point of the function $\langle \Psi | H_e | \Psi \rangle$.

In the specific case of the HF theory, the ground-state wavefunction is a Slater determinant of N spin-orbitals and the constraint assumes the form

$$\int \psi_i^*(\mathbf{r}) \psi_j(\mathbf{r}) d\mathbf{r} = \delta_{ij} , \tag{A.7}$$

where the Lagrange multipliers are now a sum of terms over the indices i, j. The variation of the Lagrange function with respect to a spin orbital ψ_i leads to

$$\delta\mathcal{L} = \sum_i \int \delta\psi_i^*(\mathbf{r}) \left[\Big(h(\mathbf{r}) + v_{\mathrm{H}}(\mathbf{r}) - v_{ex}(\mathbf{r}) \Big) \psi_i(\mathbf{r}) - \sum_j \epsilon_{ij} \psi_j(\mathbf{r}) \right] + \mathrm{c.c} = 0 . \tag{A.8}$$

Given that the variation is arbitrary, the quantity in the square brackets should be zero for all i. Thus we obtain the expression for the eigenvalue equation, written in Equation 2.11 and the three terms between round brackets are just the Fock operator. The only differences between the expression above and the canonical HF equations are the Lagrange multipliers with two indices and the presence of the factor ψ_j, instead of ψ_i. A unitary transformation is necessary to eliminate the mixing among spin-orbitals and recover the "standard" eigenvalue equations.

B Extra Details in Density-Functional Theory

B.1 Hohenberg-Kohn Variational Principle

The central quantity in DFT is the electron density, defined in general as $n : \mathbb{R}^3 \to \mathbb{R}$. We define the set of all the ground-state densities for a N-body system as

$$\mathscr{N}_N := \{n \mid \text{function of the ground-state } \Psi[v_{\text{ext}}],\, v_{ext} \in \mathscr{V}_N\}\ ,$$

where the external potentials admit a minimizer, or a ground-state wavefunction, for the given Hamiltonian. The external potential, together with the number of particle N, determines the Hamiltonian. Therefore each potential is associated with a different electron density:

the map $v_{\text{ext}} \in \mathscr{V}_N \to n \in \mathscr{N}_N$ is injective .

Once the nuclear framework is fixed, the ground-state energy is minimized using the wavefunctions $\Psi[v_{\text{ext}}]$, see Equation 2.7.

Now, the Hohenberg-Kohn theorem inverts the relation above. Thus, the external potential is determined by the density,

the map $n \in \mathscr{N}_N \to v_{\text{ext}} \in \mathscr{V}_N$ is injective, v_{ext} is determined up to a constant .

As a consequence of the theorem, it is possible to express the ground-state energy as a functional of the ground-state density. First, we can define the functional $F[n]$ as

$$F : n \in \mathscr{N}_N \to \langle \Psi | T + V_{e-e} | \Psi \rangle$$

and the total energy results

$$E[n] = F[n] + \int v_{ext}(\mathbf{r}) n(\mathbf{r}) d\mathbf{r}\,. \tag{B.1}$$

Finally, given an external potential, the ground-state total energy is the minimum of the functional $E[n]$,

$$E_0 = E[n_0] = \min_{n \in \mathscr{N}_N} \left\{ F[n] + \int v_{ext}(\mathbf{r}) n(\mathbf{r}) d\mathbf{r} \right\}\ , \tag{B.2}$$

where the minimizer is the electron density. This is the Hohenberg-Kohn variational principle, which grants the stationary condition for the ground-state energy. In other words, the variation of the energy, subject to the constraint that the total number of particles is N, is equal to zero. Therefore, it possible to use the Lagrange multipliers technique in order to minimize the total energy

$$\partial \left\{ E[n] - \mu \left[\int n(\mathbf{r}) d\mathbf{r} - N \right] \right\} = 0 \,, \tag{B.3}$$

where μ is the Lagrange multiplier and the Euler-Lagrange equation is given by

$$\mu = \frac{\partial E[n]}{\partial n(\mathbf{r})} = \frac{\partial F[n]}{\partial n(\mathbf{r})} + v_{\text{ext}}(\mathbf{r}) \,, \tag{B.4}$$

recovering exactly the same result introduced at the end of Section 3.2.

B.2 Constrained Search Formulation

The HK theorem establishes a one-to-one correspondence between the ground-state electron density n_0 and the ground-state wavefunction Ψ_0. However, there can be several different wavefunctions that produce n_0. A way to distinguish the true ground-state is given by the Levy-Lieb constrained-search formulation [253, 254].

Suppose that Ψ_{n_0} is associated with n_0, but differs from the ground-state Ψ_0. The ground-state energy is the minimum value

$$E_0 = \langle \Psi_0 | H_e | \Psi_0 \rangle \leqslant \langle \Psi_{n_0} | H_e | \Psi_{n_0} \rangle \,. \tag{B.5}$$

The external potential is a simple function of the density,

$$\langle \Psi_0 | T + V_{e-e} | \Psi_0 \rangle + \int v_{\text{ext}}(\mathbf{r}) n_0(\mathbf{r}) d\mathbf{r} \leqslant \langle \Psi_{n_0} | T + V_{e-e} | \Psi_{n_0} \rangle + \int v_{\text{ext}}(\mathbf{r}) n_0(\mathbf{r}) d\mathbf{r} \,, \tag{B.6}$$

therefore the inequality simplifies. We observe also that the first term on the left side corresponds to $F[n_0]$,

$$\langle \Psi_0 | T + V_{e-e} | \Psi_0 \rangle = F[n_0] \leqslant \langle \Psi_{n_0} | T + V_{e-e} | \Psi_{n_0} \rangle \,, \tag{B.7}$$

concluding that the functional is found with the minimization

$$F[n_0] = \min_{\Psi \to n_0} \langle \Psi | T + V_{e-e} | \Psi \rangle \,, \tag{B.8}$$

where the set of possible wavefunctions is restricted only to those wavefunctions that are associated with n_0, hence the name of the method. The constrained-search method eliminates the problem of degenerate ground-state. In fact, considering a set of degenerate wavefunctions, with this method only the one that corresponds to n_0 is selected.

Also, this formulation extends the domain of definition for $F[n]$ from *v-representable* to *N-representable*, *i.e.* to any antisymmetric wavefunction for N electrons.

B.3 The Adiabatic-Connection Fluctuation-Dissipation Theorem

In this section we will discuss the derivation of the adiabatic-connection fluctuation dissipation (ACFD) formula, which represents the exact expression of the exchange-correlation energy $E_{\rm xc}[n]$. From the ACFD result one can, for example, derive the RPA XC energy formula, as shown in Section 3.28. We mention here that the exact expression for $E_{\rm xc}[n]$ can be derived with two different paths. Apart from the adiabatic-connection it is possible to employ the perturbation theory in the context of Kohn-Sham orbitals (KSPT) [34]. Briefly, a term in the Hamiltonian is written as the difference between the full electron–electron interaction and the Hartree potential and is treated as a perturbative term with a multiplicative coupling constant λ. In this way the value $\lambda = 0$ gives the noninteracting Hamiltonian, while $\lambda = 1$ corresponds to the fully interacting one. At this point the energy is written as a function of the parameter λ, which can be removed from the Hamiltonian with a simple derivation with respect to λ and the application of the H-F theorem for the normalized eigenfunctions. After that, the integration over λ for the energy can be carried out straightforwardly and the fully interacting energy $E_0(1)$ is expressed in terms of the response function of the electron density. A very similar derivation is performed for the adiabatic-connection, as we will see below. However the main difference is that, in the latter case, the whole Hamiltonian is considered in passing from non-interacting to fully-interacting. On the contrary, with the perturbative approach, only the part of the Hamiltonian responsible for the electron–electron interaction is considered. The drawback is an electron density that depends on λ, which means that the ground-state wavefunction is also varying. Hence, the expression obtained with the KSPT is hardly applicable for practical calculations.

Before starting our short discussion on the ACFD theorem, we suggest the reader that the present matter has been the subject of a number of thorough reviews. The ACFD theorem, related to the exact expression of the EX functional, can be found in textbooks [34] as well as in the literature [28, 45]. In the latter reference the ACFD formula has been derived and used as a starting point to derive the RPA.

In the adiabatic-connection the total Hamiltonian contains the full electron–electron Coulomb potential and another potential that depends on the switching factor λ. The dependence of the ground-state energy on λ is obtained with the expression

$$E_0(\lambda) = \langle \Psi_0(\lambda) | H(\lambda) | \Psi_0(\lambda) \rangle = T[n] + \int v_\lambda(\mathbf{r}) n(\mathbf{r}) d\mathbf{r} + \lambda W[n] \,, \tag{B.9}$$

where $\Psi_0(\lambda)$ is the ground-state corresponding to $H(\lambda)$. The assumption in the AC is that the ground-state density is kept fixed during the adiabatic switching from $\lambda = 0$

to $\lambda = 1$, *i.e.* it is always possible to find an external potential ($v_\lambda(\mathbf{r})$) that guarantees a constant $n(\mathbf{r})$ for any value of $\lambda \in [0, 1]$. The external potential is defined as

$$v_\lambda(\mathbf{r}) = \begin{cases} v_{\text{eff}}(\mathbf{r}) & \lambda = 0\,, \\ \text{unknown} & 0 < \lambda < 1\,, \\ v_{\text{ext}}(\mathbf{r}) & \lambda = 1\,, \end{cases} \tag{B.10}$$

in which $v_{\text{eff}}(\mathbf{r})$ corresponds to the effective potential, defined in Equation 3.19 as the sum of the Hartree, the external and the XC potentials. Naturally, the case $\lambda = 0$ gives the standard DFT Hamiltonian with XC interactions. In the opposite case, with $\lambda = 1$, the term $W[n]$ provides the full electron–electron interaction.

The derivative of Equation B.9 leads to

$$\frac{d}{d\lambda}E_0(\lambda) = E_0(1) - E_0(0) = \int_0^1 \langle\Psi_0(\lambda)|\frac{d}{d\lambda}H(\lambda)|\Psi_0(\lambda)\rangle d\lambda\,, \tag{B.11}$$

where the derivative of the ground-state wavefunction is zero because of the H-F theorem (orthonormalization of the wavefunction). The derivative of the Hamiltonian with respect to λ can be written as

$$\begin{aligned} E_0(1) =& E_0(0) + \int_0^1 \left[\int \frac{dv_\lambda(\mathbf{r})}{d\lambda} n(\mathbf{r})\, d\mathbf{r} + W[n]\right] d\lambda = \\ =& E_0(0) + \int \left[v_{\text{ext}}(\mathbf{r}) - v_{\text{eff}}(\mathbf{r})\right] n(\mathbf{r}) d\mathbf{r} + \int_0^1 W[n] d\lambda\,, \end{aligned} \tag{B.12}$$

in which the derivative of the kinetic term is zero. At this point we consider the three terms inside $v_{\text{eff}}(\mathbf{r})$ (Equation 3.19) and use the definition of the ground-state energy for $\lambda = 0$, $E_0(0) = T_0[n] + V_{\text{H}}[n] + V_{\text{xc}}[n] + \int v_{\text{ext}}(\mathbf{r}) n(\mathbf{r}) d\mathbf{r}$, written in Equation 3.15. On the other hand, the full interacting ground-state energy $\lambda = 1$ is expressed as, $E_0(1) = T[n] + V_{e-e}[n] + \int v_{\text{ext}}(\mathbf{r}) n(\mathbf{r}) d\mathbf{r}$. After a simple manipulation of these two terms inside Equation B.12, it is possible to express the exchange-correlation energy as

$$T[n] - T_0[n] + V_{e-e}[n] - V_{\text{H}}[n] = V_{\text{xc}}[n] = \int_0^1 W[n] d\lambda - V_{\text{H}}[n]\,, \tag{B.13}$$

see the definition of $E_{\text{xc}}[n]$ in Equation 3.16.

The integral of $W[n]$, in the equation above, is now written in the expanded form and reads

$$\int_0^1 W[n] d\lambda = \frac{1}{2}\int\int w(\mathbf{r}, \mathbf{r}') d\mathbf{r}\, d\mathbf{r}' \int_0^1 \left[\langle\Psi_0(\lambda)|n(\mathbf{r})n(\mathbf{r}')|\Psi_0(\lambda)\rangle - n(\mathbf{r})\delta^{(3)}(\mathbf{r} - \mathbf{r}')\right] d\lambda\,, \tag{B.14}$$

where the interaction $w(\mathbf{r}, \mathbf{r}')$ has not been specified in detail. Before using the fluctuation-dissipation theorem, we can employ the definition of $V_{\text{H}}[n]$ (see Equation 3.14b) into the expression for the exact XC functional (Equation B.13) and obtain an expression for the

exact XC function which is often found in the literature

$$E_{\mathrm{xc}}[n] = \frac{1}{2}\int\int n(\mathbf{r})w(\mathbf{r},\mathbf{r}')n(\mathbf{r}')h_{\mathrm{xc}}(\mathbf{r},\mathbf{r}')d\mathbf{r}d\mathbf{r}'\,, \tag{B.15}$$

where the last term is the so-called exchange-correlation hole

$$\begin{aligned} h_{\mathrm{xc}}(\mathbf{r},\mathbf{r}') =& \frac{\langle\Psi_0(\lambda)|n(\mathbf{r})n(\mathbf{r}')|\Psi_0(\lambda)\rangle - n(\mathbf{r})\delta^{(3)}(\mathbf{r}-\mathbf{r}')}{n(\mathbf{r})n(\mathbf{r}')} - 1 = \\ =& \frac{\langle\Psi_0(\lambda)|\tilde{n}(\mathbf{r})\tilde{n}(\mathbf{r}')|\Psi_0(\lambda)\rangle}{n(\mathbf{r})} - \delta(\mathbf{r},\mathbf{r}')\,. \end{aligned} \tag{B.16}$$

The two lines above are equivalent expressions, but two different terms are highlighted. In the first expression we used the pair-correlation function (minus one). In the second line we have grouped into the brackets the density operator minus its expectation value, $\langle\Psi_0|\tilde{n}(\mathbf{r})|\Psi_0\rangle = \langle\Psi_0|n(\mathbf{r})|\Psi_0\rangle - n(\mathbf{r})$, this is defined as the fluctuation of the density.

The fluctuation-dissipation theorem states that the response of a system (in thermodynamic equilibrium) to a small external perturbation corresponds to the response to the spontaneous internal fluctuation. Therefore, it is related to the fluctuation of the density defined above. In short, the consequence of the theorem is that the density–density fluctuations can be expressed in terms of the density–density response function

$$\langle\Psi_0|\tilde{n}(\mathbf{r})\tilde{n}(\mathbf{r}')|\Psi_0\rangle = -\frac{1}{\pi}\int_0^\infty \mathrm{Im}\,\chi(\mathbf{r},\mathbf{r}',i\omega)d\omega\,, \tag{B.17}$$

where $\chi(\mathbf{r},\mathbf{r}',i\omega)$ is the linear response function. The substitution of the response function into Equation B.15 leads to the ACFD formula, written in Equation 3.28, and can be used to derive the RPA equation for the (exchange-)correlation energy.

C FHI-aims Convergence Tests for Benchmark Calculations

C.1 Basis Set Convergence

Here, the details about the settings used to compute the convergence of the binding energy of the water dimer, presented in Figure 6.1, are given. The geometry is taken from the Benchmark Energy & Geometry Database (BEGDB) [255]. The structure has been obtained with an accurate coupled-cluster geometry optimization [88], which employs the CCSD(T)/cc-pVQZ basis set. We used the same structure and the tight settings for all the calculations. Apart from PBE and PBE0, also the LDA and HF methodologies have been tested. The data for the water monomer total energy and CPU time are reported in Figure C.1. The time reported in this plot is the average time per self-consistent cycle of a water molecule, computed using twelve processors in parallel. From these results, LDA turned out to be comparable with PBE, in term of computational efficiency, while HF scales similarly to PBE0. This suggests that the exchange integrals are the dominant part in the increasing of the CPU time associated with a large number of basis.

A second case tested is the ethene dimer (C_2H_4). The structure has been obtained from the same source of the water dimer and is optimized with the CCSD(T)/cc-pVQZ noCP basis set. The results for the binding energies of PBE and PBE0 are presented in Figure C.2, left panel. Both functionals converge the binding energy quit fast, already

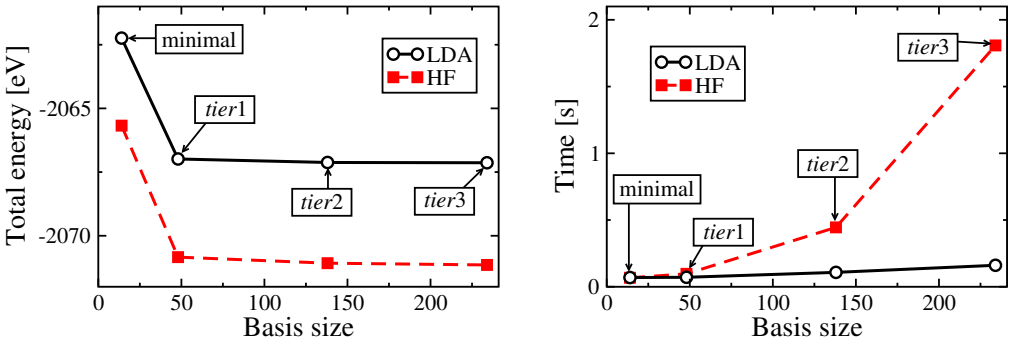

Figure C.1: Left: LDA and HF total energy of a water molecule as a function of the basis set. Right: time employed for each self-consistent calculation of the molecule.

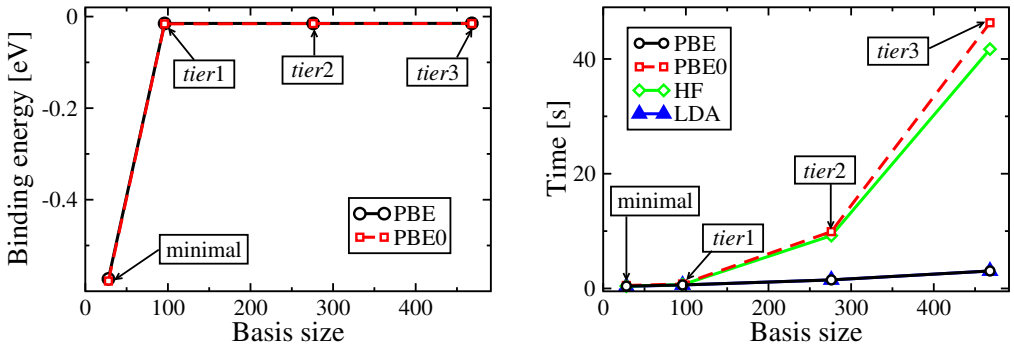

Figure C.2: Left: PBE and PBE0 binding energy of the ethene dimer as a function of the basis set. Right: time employed for each dimer calculation, the performances of PBE and PBE0 are joined here by HF and LDA.

at $tier1$ the two values overlap and are basically converged. This behavior can be qualitatively explained by considering the number of basis at each step, which is double the number of basis used in the case of the water dimer. This fact is combined with a tiny binding energy, meaning weak intermolecular interactions. Therefore, the binding energy is basically converged once the basis are enough to describe well the monomer. The efficiency of the different methods is compared by computing the average time needed for a single self-consistent cycle. The calculations were performed using twelve parallel CPUs. Once again, PBE and LDA present basically the same values and scale better that PBE0 and HF, as plotted in the right panel of Figure C.2. We note that the PBE calculation with $tier3$ is roughly five times longer than the one with the minimal basis. For PBE0 this factor is ninety.

C.2 Harris Functional

A simplified version of the density-functional scheme of KS was first used by Wendel and Martin and then has been reintroduced independently by Harris, Matthew and Foulkes [256]. This approach was developed in order to calculate an approximation of the total energy and is applicable in case of weakly interacting system. The basic idea is to calculate the total electron density, using a superimposition of frozen fragments. This approximation is applicable successfully to those systems in which the electron density of the coupled fragments is not deviating too markedly from a sum of isolated fragment densities. Mathematically speaking one constructs the total density as:

$$n(\mathbf{r}) = n_f(\mathbf{r}) + \delta n(\mathbf{r})\,, \tag{C.1}$$

where $n_f(\mathbf{r})$ is given by a sum over the frozen fragments. In this way the resulting $v_{\text{eff}}(\mathbf{r})$ is different from the true self-consistent potential and this affects the total energy, giving a dependency on $n_f(\mathbf{r})$. As one can easily see, the Harris scheme can be successfully used in case of small $\delta n(\mathbf{r})$.

Apart from the original motivations, the total energy expression derived from the Harris scheme, referred as Harris functional, can be conveniently used in a standard DFT calculation, during the approach to self-consistency. In the AIMS code the Harris functional is used to improve the efficiency of the total energy calculation and to speed up the self-consistent convergence [151]. The code generates, via the self-consistent iteration, a set of eigenvalues and eigenfunctions linked to the electron density. Then, the total energy is computed with the Harris functional:

$$\begin{aligned} E^{\mu}_{\text{Harris}}[n] &= \sum_i f_i^{\mu}\epsilon_i^{\mu} - \frac{1}{2}\int d\mathbf{r}\, n^{(\mu-1)}(\mathbf{r}) v_{\text{ext}}^{(\mu-1)}(\mathbf{r}) + \\ &+ E_{\text{xc}}[n^{(\mu-1)}] - \int d\mathbf{r} n^{(\mu-1)}(\mathbf{r}) v_{\text{xc}}[n^{(\mu-1)}] + E_{n-n}\,, \end{aligned} \tag{C.2}$$

where μ refers to the electron density computed after the self-consistent cycle, while $(\mu-1)$ is the density used to set up the Hamiltonian, the output of the previous self-consistent cycle. This scheme is faster than the regular energy expression, because in each cycle the energy and potential terms are available anyway for $(\mu-1)$. They are necessary terms in order to build the quantities that are used as initial guess. Thanks to Equation C.2, a second evaluation of such terms, this time for $n^{\mu}(\mathbf{r})$, is avoided. Moreover, it has been shown that Equation C.2 converges faster for large systems than the original KS total energy form.

The Harris functional (Equation C.2) is naturally extended to our scheme for the self-consistent vdW implementation. The final equation for the total energy is modified with two additional terms $+E_{\text{vdW}^{\text{TS}}}[n^{(\mu-1)}] - \int d\mathbf{r} n^{(\mu-1)}(\mathbf{r}) v_{\text{vdW}^{\text{TS}}}[n^{(\mu-1)}]$.

C.3 The Implementation: Computational Details

In this section are reported all the important settings used in our "test" calculations of the vdW potential. The results and the performances of our implementation will be frequently compared with the *a posteriori* scheme, as well as other DFT functionals. The silver Ag(111) surface employed to obtain the data in Figure 7.3 is built with six metal layers, a (1×1) unit cell with one atom per layer and a vacuum of 60 Å. The calculations are obtained by coupling our $\text{vdW}^{\text{TS}}_{\text{sc}}$ functional with the one of Perdew, Burke and Ernzerhof [52] (PBE). The reciprocal space is sampled with a Monkhorst-Pack grid [257] of $(20\times 20\times 1)$ k-points. We used the tight settings with a cut-off potential (see Equation 6.5) of 5.0 Å. These settings guarantee converged quantities and correspond to the ones employed in this thesis to study the electronic properties, beyond the total energy. The cohesive (or binding) energy is computed with the formula

$$E_b = E_{\text{tot}} - NE_{\text{Atom}}\,, \tag{C.3}$$

where N is the total number of atoms in the unit cell. The energy of the isolated atom is considered in a finite system. Twelve processors running in parallel are used for all the

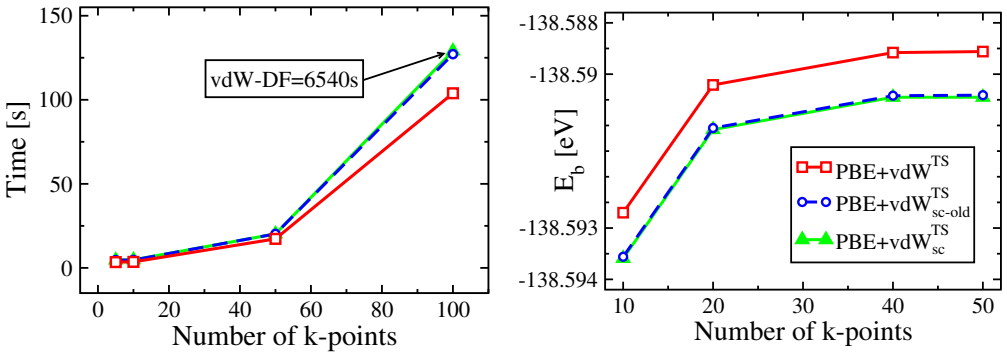

Figure C.3: In the figures are reported calculations of copper bulk made with the TS *a posteriori* method and the two SC implementations. Panel left: the average time per self-consistent cycle is plotted as a function of the k-points. This system contains 4 atoms in the unit cell. The inset reports the vdW-DF CPU time for 100 k-points per unit vector. Panel right: cohesive energies computed as a function of the number of k-points for a system of 32 copper atoms.

calculations in Figure 7.3. The performances are measured as the ratio between the total time spent for a converged calculation and the number of self-consistent cycles.

For what concerns the Cu bulk, the cells used in the two plots on top of Figure 7.4 contain an increasing number of atoms, obtained using different replicas of the unit vectors. For the plot (a), 96 cores in parallel are employed. Top right panel: we used 192 cores and a mash of $(2 \times 2 \times 2)$ k-points. The data in (c) is obtained with 64 cores. The smallest possible unit cell (4 atoms) is considered, with different k-point grids. In the bottom right panel we used 192 cores to study the unit cell obtained with the first repetition of the unit vectors (32 atoms), evaluated with an increasing mash of k-points. All calculations reported are obtained with the tight settings.

In Figure C.3 are reported two extra plots, in addition to Figure 7.4. The plot on the left is the same as Figure 7.4 (c), but in this case we used 192 cores instead of 64. As a consequence, the absolute numbers of all the three curves are now reduced by a factor of 3, confirming that the SC scheme has no issue in the parallelization. The cohesive energy, computed using the formula in Equation C.3, is reported in the second plot (right). From this figure we can conclude that the *a posteriori* and the SC energy converge similarly with respect to the number of k-points. The two SC schemes give the same numbers, as it should be. From the figure we see that the energy produced with the inclusion of self-consistency differs from the *a posteriori* one, the small variation is on the order of 1–2 meV.

We list here the settings of the Ag(111) calculations shown in Section 7.3. The surface is modeled with 3 metal layers and a vacuum of 60 Å in the z-axis. The tight settings were employed in all calculations. The four graphs in Figure 7.5 are obtained using 64 cores. In panel (a) we used non-periodic systems with an increasing number of atoms. In panel (b), the same cells of (a) are considered, but with the periodicity and a $(5 \times 5 \times 1)$ mesh of k-points. In (c) and (d) two surfaces with 3 and 27 atoms in the unit cell are

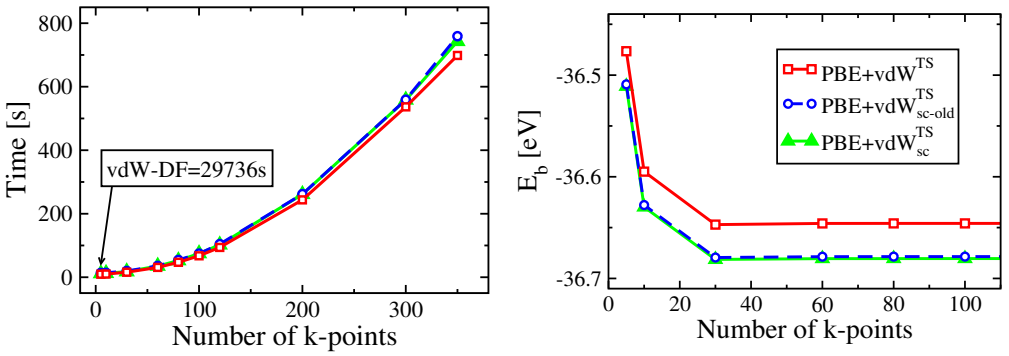

Figure C.4: Silver surface (111) tested with the post-process and the two self-consistent implementation of the TS scheme. Panel left: the average CPU time for a surface of 3 atoms in computed with an increasing number of k-points. The vdW-DF performance, obtained with 5 k-points per direction, is reported in the inset. Panel right: the binding energies of Cu(111) plotted against the number of k-points.

employed. The data in Figure C.4 are obtained with a cell of 12 atoms, computed with 64 cores. In the plots are reported the average time, left panel, and the binding energy, right panel, with respect to the number of k-points. On the left we see that since the unit cell is small (12 atoms) the two SC schemes perform very similarly, as in Figure 7.5 (c). The binding energies, computed with Equation C.3, are reported in the panel on the right. The values are well converged—beyond the meV—after 30 k-points per per unit vector (z-direction excluded). The difference in the energy between the *a posteriori* and the SC schemes is on the order of 35 meV, much more than what found for the Cu bulk, see Figure C.3.

D Detailed Results and Settings

In this appendix are reported all the settings and the details used to perform the calculations reported in the Chapter Results IV. Along with tests calculations that benchmark our convergence settings, we will report also additional calculations. These are not included in the part of this thesis dedicated to applications, but can support the general message. One should consider that the quest for finding sizable SC effects passed though a large number of different systems, tested with various XC functionals, many of which were actually found not relevant for the purpose of this work.

D.1 Finite Systems

The tight settings were employed for all the FHI-aims calculations concerning the S22 and S66 databases and all the other calculations reported in Section 8.1 and 8.2. The convergence criteria of 10^{-5} electrons for the electron density, 10^{-6} eV for the total energy and 10^{-3} eV for the sum of eigenvalues. The converged criterion of 0.01 eV/Å for the maximum final force was used for all structure relaxations. The relativistic effects were included *via* the zeroth-order regular approximation (ZORA) [188]. The mean

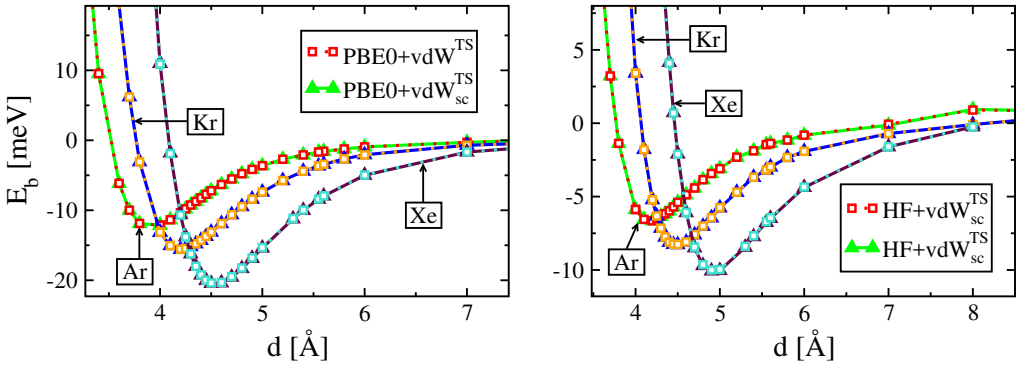

Figure D.1: Rare-gas dimers. The TS vdW method, taken in both *a posteriori* and SC versions, is coupled with PBE0 (left panel) and HF (right panel) to compute the binding energy curves for Argon, Krypton and Xenon dimers.

Table D.1: S22 database computed with PBE and PBE plus the TS vdW correction in both the SC and non-SC vdW flavors. The values are in [kcal/mol].

	CCSD(T)	PBE	PBE+vdW^{TS}	PBE+vdW$^{TS}_{sc}$
1	-3.150000	-2.819920	-3.250960	-3.251080
2	-5.070000	-4.939490	-5.242010	-5.242030
3	-18.810000	-18.278300	-19.445100	-19.445100
4	-16.110000	-14.810400	-16.106000	-16.106100
5	-20.690000	-18.590200	-20.644200	-20.645200
6	-17.000000	-15.394400	-17.931900	-17.933300
7	-16.740000	-14.397200	-17.298200	-17.299400
8	-0.530000	-0.095852	-0.814843	-0.815730
9	-1.480000	-0.324762	-1.836380	-1.836420
10	-1.450000	-0.050189	-1.649590	-1.650420
11	-2.620000	1.858110	-3.534770	-3.542190
12	-4.200000	0.694326	-4.442250	-4.447190
13	-9.740000	-2.731950	-9.835130	-9.840360
14	-4.590000	2.188720	-5.583660	-5.593560
15	-11.660000	-1.398930	-11.677800	-11.684200
16	-1.500000	-1.169980	-1.848230	-1.848390
17	-3.290000	-2.018250	-3.517010	-3.518180
18	-2.320000	-0.931321	-2.460420	-2.461510
19	-4.550000	-2.829110	-4.451890	-4.452680
20	-2.710000	-0.124476	-2.745070	-2.747260
21	-5.620000	-2.043700	-5.606420	-5.609750
22	-7.090000	-3.893230	-6.964010	-6.965100

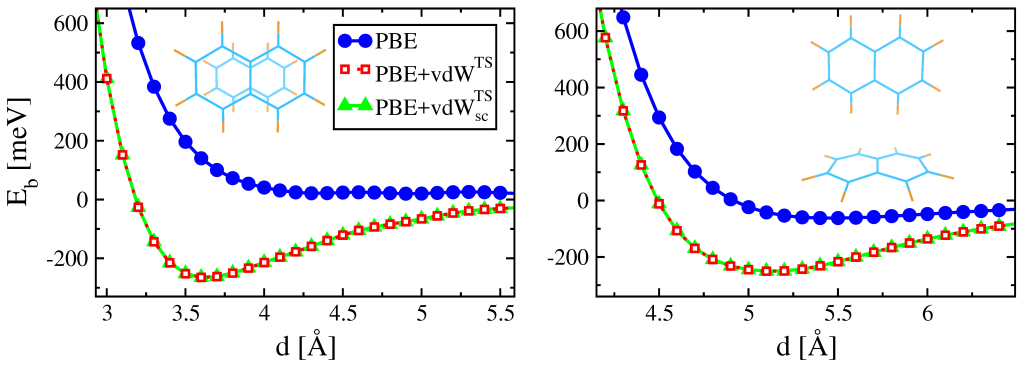

Figure D.2: Binding energy curves of two naphthalene dimers, computed with PBE with and without the inclusion of vdW interactions. The *a posteriori* and the SC results are shown. On the left side, the two naphthalene molecules are taken with a parallel orientation (p-dimer). On the right panel a perpendicular t-shaped configuration is considered (t-dimer). The structures are sketched in the two insets.

Table D.2: S22 database computed with PBE0 and PBE0 coupled with both the SC and non-SC vdW TS method. The values are in [kcal/mol].

	CCSD(T)	PBE0	PBE0+vdW$^{\mathrm{TS}}$	PBE0+vdW$^{\mathrm{TS}}_{\mathrm{sc}}$
1	-3.150000	-2.740560	-3.123120	-3.123220
2	-5.070000	-4.942710	-5.205770	-5.205790
3	-18.810000	-19.028100	-20.066200	-20.066200
4	-16.110000	-15.374000	-16.552900	-16.553000
5	-20.690000	-19.285700	-21.206300	-21.207000
6	-17.000000	-15.465800	-17.844100	-17.845300
7	-16.740000	-14.601400	-17.309700	-17.310500
8	-0.530000	-0.041536	-0.736706	-0.737442
9	-1.480000	-0.339527	-1.705290	-1.705360
10	-1.450000	-0.092646	-1.567480	-1.568200
11	-2.620000	1.810910	-3.344130	-3.349560
12	-4.200000	0.543216	-4.222840	-4.225810
13	-9.740000	-3.289000	-9.873010	-9.876290
14	-4.590000	2.038000	-5.267700	-5.274020
15	-11.660000	-2.141110	-11.516300	-11.519800
16	-1.500000	-1.178840	-1.814900	-1.815070
17	-3.290000	-2.182600	-3.561090	-3.561990
18	-2.320000	-1.026590	-2.434880	-2.435810
19	-4.550000	-3.264170	-4.763310	-4.763870
20	-2.710000	-0.281028	-2.786200	-2.788200
21	-5.620000	-2.350710	-5.734840	-5.737370
22	-7.090000	-4.183680	-7.028120	-7.028930

absolute error (MAE) is defined as

$$\mathrm{MAE} = \frac{1}{n}\sum_{i=1}^{n} |x_i - y_i| \ , \tag{D.1}$$

where x_i is the predicted value, y_i is the reference and n is the total number of data. The mean absolute percentage error (MAPE) is defined as

$$\mathrm{MAPE} = \frac{100}{n}\sum_{i=1}^{n} \left| \frac{x_i - y_i}{y_i} \right| \ , \tag{D.2}$$

where x_i is the predicted value, y_i is the reference one.

The reference data in Table D.1 and D.2 are CCSD(T) calculations performed with the limit of complete basis set (CBS) and counterpoise correction (see Section 6.3). The geometries are relaxed using either the MP2 method with cc-pVTZ CP basis set or CCSD(T) with cc-pVQZ noCP basis set. These basis set are developed by Dunning [258] and coworkers. The "cc-p" at the beginning means correlation-consistent polarized, while V stands for valence-only basis sets. Then, DZ, TZ and QZ refer respectively to double-zeta, triple-zeta and quadruple-zeta. The term "aug" can be found in front of the name and means an augmented version of the set with additional diffused functions.

The effects of self-consistency on the rare-gas dimers, already analyzed in Figure 8.1, panels (a) and (c), have been investigated with PBE0 and HF, instead of PBE. The results obtained with these XC functionals are plotted, for three dimers, in Figure D.1. With these data, we confirm that self-consistency is responsible for negligible differences in the binding energies of these small systems. A conclusion valid not only near the equilibrium geometry, but also for distances in the long-range. In this regard, it should be noted that, in particular with the HF functional, the differences in the energy increase a little when large interatomic distances are explored. Considering for instance the Ar dimer, the difference ΔE_b between HF+vdW$^{\mathrm{TS}}$ and HF+vdW$^{\mathrm{TS}}_{\mathrm{sc}}$ is typically < 0.01 meV. This number increases by five to ten times with an $\mathrm{Ar}\cdots\mathrm{Ar}$ distance larger than 6–7 Å.

We report in Figure D.2 two possible configurations of the naphthalene dimer in addition to the one of Figure 8.1 (d). The effects of vdW on top of PBE improve the binding of the systems, which are almost unbound without the inclusion of dispersion interactions. However, in both cases, the effects of self-consistency are in perfect agreement with the *a posteriori* curves. The tiny differences in the binding energies of the two vdW schemes are around 0.1–0.5 meV. We include here the changes due to SC effects on the different components of the energy of the Xenon dimer. The different components of the total energy are plotted, as a function of the interatomic distance, in Figure D.3, where the PBE+vdW$^{\mathrm{TS}}_{\mathrm{sc}}$ results are compared with the *a posteriori* ones. As we can see from the figure, the changes previously shown in Figure 8.2 for the naphthalene c-dimer are also visible here. This second example fully supports the analysis and the conclusions of Section 8.1. Here, however, the differences are quantitative smaller. In particular, the effects of self-consistency are clearly present for the kinetic and electrostatic energy terms.

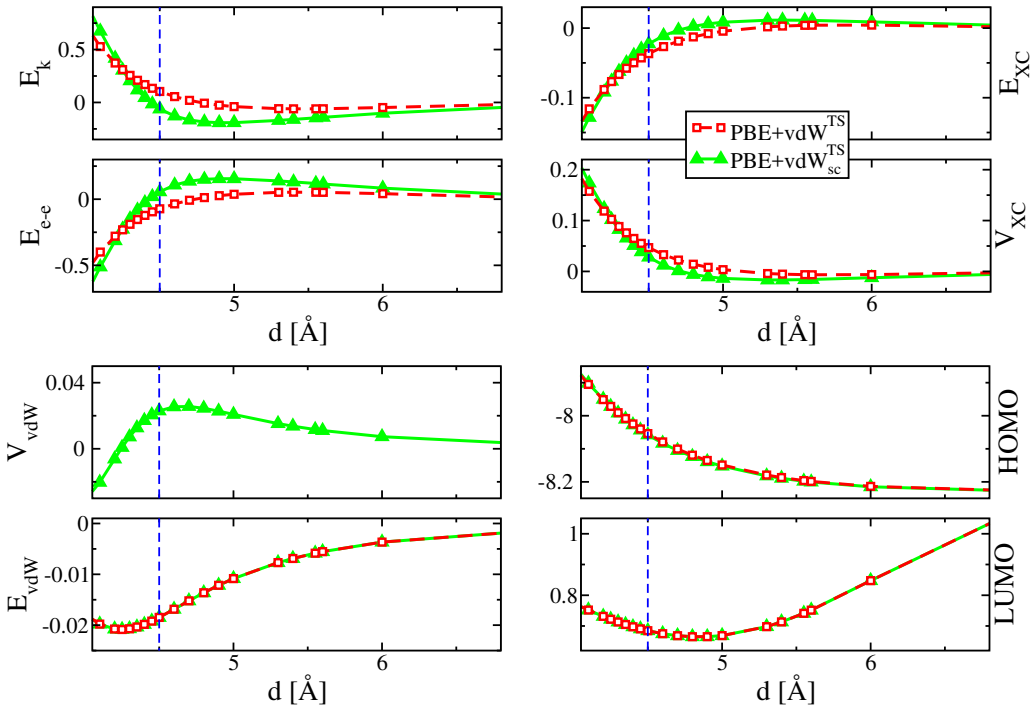

Figure D.3: Xenon dimer: different components of the total energy, plotted as a function of the intermolecular distance d. In the panels are compared the results of the PBE+vdW$^{\mathrm{TS}}$ and the PBE+vdW$^{\mathrm{TS}}_{\mathrm{sc}}$ schemes. The potential is by definition available only with the SC case. The blue dashed lines indicate the equilibrium distance (4.5 Å). All values are in [eV].

Also, for the XC energy and integrated potential the differences between the *a posteriori* and the SC curves are visible. As already mentioned in our analysis in Section 8.1, it is the balance between the different components that sums up to a negligible difference ($\sim 0.001\%$) in the total binding energy between PBE+vdW$^{\mathrm{TS}}_{\mathrm{sc}}$ and PBE+vdW$^{\mathrm{TS}}$. On the other hand, the HOMO and the LUMO appear to be not affected by SC vdW at all, a result that suggests the absence of SC effects on the electronic properties for these small dimers.

D.2 Periodic Systems

All the metal surfaces presented in Section 9 have been tested using different settings and various possible geometries. The results can be sensitive, for example, to the dimension of the unit cell, the number of metal layers and the number of layers allowed to relax. From our experience we can conclude that well converged electronic properties are obtained with $(2 \times 2 \times 1)$ unit cells and six metal layers. Typically, only the two layers on top are relaxed, while the other atoms are kept fixed in their initial positions. For what concerns the k-point sampling, it clearly depends on the extension of the unit vectors, *i.e.* the element and the number of replica of the unit cell. For a $(1 \times 1 \times 1)$ unit cell we

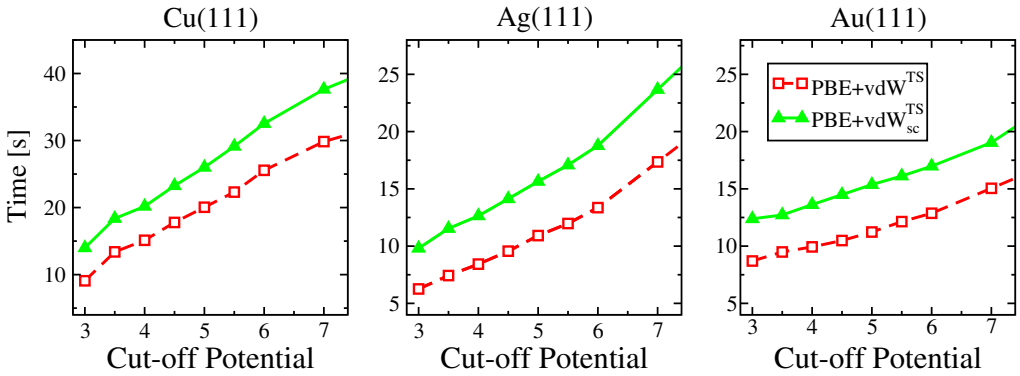

Figure D.4: The average time consumed in a self-consistent cycle is plotted against the cut-off potential for the PBE+vdW$^{\text{surf}}$ and the PBE+vdW$^{\text{surf}}_{sc}$ schemes. The performances for Cu, Ag and Au (111) surfaces are reported in the three panels from left to right. The values of r_{onset} appear on the x-axis and are in [Å] .

suggest to sample the reciprocal space with a mesh of $(60 \times 60 \times 1)$ Monkhorst-Pack grid [257] for a safely converged calculation. For the $(2 \times 2 \times 1)$ cell the largest sampling was $(30 \times 30 \times 1)$ k-points. We employed the tight settings to compute the density differences $\Delta n(\mathbf{r})$ and the electronic properties. In particular, the workfunctions are greatly affected by the tails of electron density that extends in the vacuum region, above the surface. For this reason, the surfaces are build with a "safe" value of minimum 50 Å of vacuum, *i.e.* the distance between the topmost metal layer and the periodic repetition of the bottommost layer. Another very important parameter for capturing the effects of the electron density tail into the vacuum is r_{onset}. This parameter regulates the cut-off potential, written Equation 6.5. The value of r_{onset} has been carefully tested and $r_{\text{onset}} = 5$ Å turned out to be a safe choice for all the metals tested.

All the surfaces were built with the lattice constants determined from the PBE+vdW$^{\text{surf}}$ method [134]. The convergence criteria employed are 10^{-5} electrons for the electron density, 10^{-3} eV and 10^{-6} eV respectively for the sum of eigenvalues and the total energy. A criterion of 10^{-2} eV/Å is used to converge the maximum final forces. The ZORA approximation [188] is employed to include the relativistic effects in our calculations.

D.3 The Workfunctions

The workfunctions presented in this thesis are all computed by means of the FHI-aims [151] code. In order to compute the electrostatic potential in the vacuum region V_{vac} one needs to set a distance above the last metal layer. In the code, the vacuum level is determined automatically from the geometry input. The vacuum is set as half of the distance between the topmost metal layer and the bottommost metal layer of the periodic repetition, above the vacuum. For this reason, it is highly recommendable to use always large values of the vacuum in the unit cell. Also, a large vacuum avoids situations where the surface interacts with its repetitions above and below, leading

to unphysical results. In this regard, one perk of using numeric atom-centered basis functions is that the vacuum space is basically computed for free, while plane waves are defined over the entire 3D space.

Once the vacuum level is set, the electrostatic potential can be computed. The Hartree potential is solved using Ewald's method, *i.e.* the potential is split into a short-ranged and a long-ranged part [151, 259]. Then, the former term can be computed in real space, while the latter is conveniently treated in reciprocal space using a Fourier transform. In this way the less favorable scaling due to the slow convergence of the long-ranged contributions is eliminated. Moreover, it can happen that the two sides of a surface present two different values of the long-range Hartree potential, for example in case of non-symmetric slabs. Consequently, a dipole field is present between the slab and its periodic repetitions above and below. If the discrepancy between the potentials of the two sides is within 10%, this difference is renormalized with the introduction of an electrostatic potential step. Similarly, the code corrects any small integration error in the long-range Hartree potential. In fact, the charge components are evaluated on a finite integration grids and can present numerical errors, in particular with light integration grids.

The smallest unit cells $(1 \times 1 \times 1)$, with one atom per metal layer, are used to obtain the data reported in Figure 9.3. The vacuum has been set to 60 Å for six metal layers and an additional "safe" value of 100 Å has been tested with surfaces made of 12 layers. The two values are found to produce identical results. A total of 6 metal layers are used to build the surfaces used in the first two columns of panels and all of them were allowed to relax. A similar procedure, but with 12 layers, was used for the third column. The k-point grid is set to $(60 \times 60 \times 1)$, except of course for the first column, where the k-points are tested. The cut-off potential is set with $r_{\text{oneset}} = 5$ Å, except in the second row of panels where it is converged up to 8.

We have tested the computational performances of PBE+vdW$^{\text{surf}}$ and PBE+vdW$^{\text{surf}}_{\text{sc}}$ in relation to the cut-off potential, similarly to what has been done for the number of atoms and the number of k-points in Figure 7.4 and 7.5. In Figure D.4, the three coinage metal surfaces Cu, Ag and Au (111) are considered. In the left panel, the example of Cu(111) shows that the time for a calculation is already doubled when the value reaches 5 Å, with respect to the initial value of 3 Å. Also, the scaling of PBE+vdW$^{\text{surf}}$ and PBE+vdW$^{\text{surf}}_{\text{sc}}$ are very similar. The same conclusion is valid also for Ag(111). These two systems show scaling curves with comparable steepness. On the other hand, in the case of Au(111) a shallow scaling is found (the same scale of Ag(111) is used). For instance, the initial CPU time at $r_{\text{oneset}} = 3$ is increased "only" by 50% when $r_{\text{oneset}} = 7$ is considered. This behavior originates from the fact that, in this last example, the light basis set is used. In conclusion, the scaling of PBE with the *a posteriori* scheme has a very similar slope in comparison to PBE+vdW$^{\text{surf}}_{\text{sc}}$. Moreover, the overall performance can be greatly influenced by other factors, as the basis set.

From our experience, well converged values, in good agreement with experiments, are obtained with $(2 \times 2 \times 1)$, $(3 \times 3 \times 1)$ or even larger unit cells, composed by a

Table D.3: Workfunctions of seven pristine metal (111) surfaces computed with the hybrid XC functionals PBE0 and HSE06. For the experimental measurements we refer to Table 9.1. All the values are in [eV].

	Cu	Rh	Pd	Ag	Ir	Pt	Au
PBE0	4.75	5.05	4.49	4.38	5.62	5.99	5.10
HSE06	4.80	5.12	4.51	4.42	4.64	5.98	5.14

minimum of six metal layers and a vacuum larger than 50 Å. Since the lattice constant of each metal/element is different, one needs to find the k-point mesh suitable for these structures with the help of convergence tests. Our suggestion is to consider, for cells smaller than 5 Å, a grid of minimum $(20 \times 20 \times 1)$ k-points. In any case, one should test both small and large unit cells because the relaxation procedure can lead to slightly different geometries and the value of Φ adjusts consequently. When large unit cells are considered, the relaxation can be limited to the first two layers on top of the surface. For what concerns the basis set, we managed to converge all surfaces, up to hundreds of atoms, at the PBE+vdW$_{sc}^{\text{surf}}$ level of theory and tight settings. Unfortunately, when PBE0 is considered, the workload increases substantially. Therefore, in order to converge particularly troublesome systems, the light settings might be necessary. In any case, fairly accurate workfunctions can be obtained with these settings, providing a r_{onset}, which regulates the cut-off potential, not smaller than 5 Å.

The workfunctions for the seven metal (111) surfaces reported in Table 9.1 are computed with PBE with and without SC effects and compared with experiments. In addition to that, we report in Table D.3 the corresponding values computed with PBE0 [61, 62] and HSE06 [66], two hybrid XC functionals, described in Section 3.5.3. In both functionals the correlation is provided by PBE, while the exchange is 75% PBE and 25% EXX (from HF). The HSE06 contains a cut-off that limits the long-range part of the EXX, improving the CPU time, see Equation 3.26. From the table one can see that for the metals of the third and fourth period, *i.e.* copper, rhodium and silver, the values of Φ are reduced with respect to PBE, worsening the agreement with the experimental data. The exception in this group is Pd(111), that belongs to the third period and whose Φ is increased by ~ 0.2 eV with both PBE0 and HSE06. This case has been already discussed in Section 9.1. In our opinion, the peculiar fully-occupied shell structure of Pd is particularly sensitive to the contribution of EXX. In fact, the Φ is improved when 25% of EXX is taken into account. Two of the elements belonging to the fifth period, iridium and gold, display little effects when the hybrid functionals are employed. The functional PBE0 provides tiny modifications of Φ of about 0.06–0.04 eV with respect to the values of PBE. Moreover, these little differences are reduced to 0.04–0.02 eV when HSE06 is used. On the contrary, Pt(111) presents exceptionally large modifications. The PBE0 functional increases the PBE Φ by 0.23 eV, resulting in a workfunction of $\Phi = 5.99$ eV. Similarly, the workfunction of HSE06 is 5.98 eV. These two values are in a better agreement with the experimental Φ. A possible explanation for this exception could be similar to the

one of Pd(111). Both elements belong to the sixth period. The role of EXX might be important to model the two d and s external shells of Pt, which are both almost fully occupied. Nevertheless, an exhaustive explanation can be provided only with a detailed investigation of the role of EXX, along with the relativistic spin-orbit coupling, in the electronic properties of heavy metals. To the best of our knowledge, such a study is still absent in the literature.

We remark here that the workfunctions of the heavy metals (Ir, Pt and Au) presented in Table D.3 were computed with light settings and lighter meshes of k-points with respect to PBE+vdW$^{\mathrm{surf}}$ and PBE+vdW$^{\mathrm{surf}}_{\mathrm{sc}}$ calculations. We kept however, for r_{onset}, the most important parameter, the converged value of 5 Å. Because of the high computational requirements of the hybrid XC functionals, these light settings are often employed in the literature and considered as fairly accurate. It is a common argument that tighter convergence criteria are usually associated with a slight decrease of the workfunctions. Nevertheless, the authors recommend that, for a rigorous study, this empirical argument should be proved case by case. Most importantly, the other results presented in this work were obtained with tight settings and very accurate convergence procedures. For this reasons, we suggest that the comparison of workfunctions obtained with different settings should be taken with extra care.

D.4 Population analysis

In this small section we provide the essential concepts behind the population analysis of the MODOS, used to evaluate the transfer of charge, in HIOS, between the metal substrate and the monolayer. The definition of density of states (DOS) in a normal textbook is

$$g(E) = \frac{1}{V}\frac{dN}{dE}\,, \tag{D.3}$$

where V is the volume that contains the N-particles systems. This means that in an energy interval dE the number of electron levels is $g(E)dE$. However, the practical definition of DOS is

$$g(E) = \sum_i \langle\phi_i|\phi_i\rangle\delta(E-\epsilon_i)\,, \tag{D.4}$$

in which ϵ_i is the eigenvalue associated to the eigenstate $|\phi_i\rangle$. The DOS can be manipulated to obtain the projected density of states, *i.e.* is the DOS projected onto a set of orthonormal orbitals

$$g^p_n(E) = \sum_i \langle\phi_i|n\rangle\langle n|\phi_i\rangle\delta(E-\epsilon_i)\,, \quad \sum_n |n\rangle\langle n| = 1\,. \tag{D.5}$$

For example one can project the DOS onto the orbitals of the isolated atomic species, *i.e.* the angular-momentum resolved partial density of states (pDOS). This procedure is based on the Mulliken analysis, which provide an estimation of partial atomic charges [237]. Of course, the straightforward application of the equations written

above would lead to a series of peaks associated to individual states. Mathematically, this is due to the presence of the Dirac delta function $\delta(E-\epsilon_i)$ in Equation D.4. This issue is solved with the inclusion of a broadening of the eigenvalues. For example, a Gaussian broadening,

$$\delta(E-\epsilon_i) \Longrightarrow \propto \frac{1}{\sigma\sqrt{\pi}} \exp\left[\frac{(E-\epsilon_i)^2}{\sigma^2}\right], \tag{D.6}$$

is usually employed to obtain smooth density of states.

The pDOS is not the only projection available. For example, the space-resolved projection of the DOS is called local density of states (LDOS). In this thesis, we consider a third projection to study the hybrid system, the molecular orbital density of states (MODOS). In this case, the DOS is projected onto the molecular orbitals of the isolated molecule, taken in gas phase. The occupation of a specific molecular orbital i is obtained by integrating the corresponding MODOS, up to the Fermi energy

$$O_i = \int_{-\infty}^{E_F} \text{MODOS}_i(E) dE\,. \tag{D.7}$$

The total charge that fills the molecular orbitals is the sum over all the occupations O_i. Therefore, the transfer of charge induced by the bonding between the molecule and the substrate is just the difference between the occupation of the adsorbed molecule and the occupation of the isolated one

$$Q_{\text{MODOS}} = -e\left(2\sum_i O_i - N_{\text{molecule}}\right), \tag{D.8}$$

in which the factor 2 takes care of the spin degeneracy and N_{molecule} corresponds to the total number of electrons of the isolated molecule. Moreover, the MODOS can be studied similarly to the molecular orbitals. The position of the LUMO with respect to the Fermi energy, for example, indicates whether there is a transfer of charge between molecule and surface or not. Also, because of hybridization process and/or distortion of the geometry during adsorption, the shape of the MODOS can differ from the Lorentzian shape of the corresponding molecular orbital [223].

D.5 Hybrid Systems

A review about the adsorption on molecules on metal surfaces, which include the structures proposed here and many more, is available in Reference [127]. The work focuses on the role of the PBE+vdW$^{\text{surf}}$ in the structure and energy of HIOS. The geometries and the settings used in this thesis correspond to those reported in the review.

The metal surfaces presented in this work are built using a periodic slab approach, the lattice constants are computed at the PBE+vdW$^{\text{surf}}$ level of theory [123]. The structures

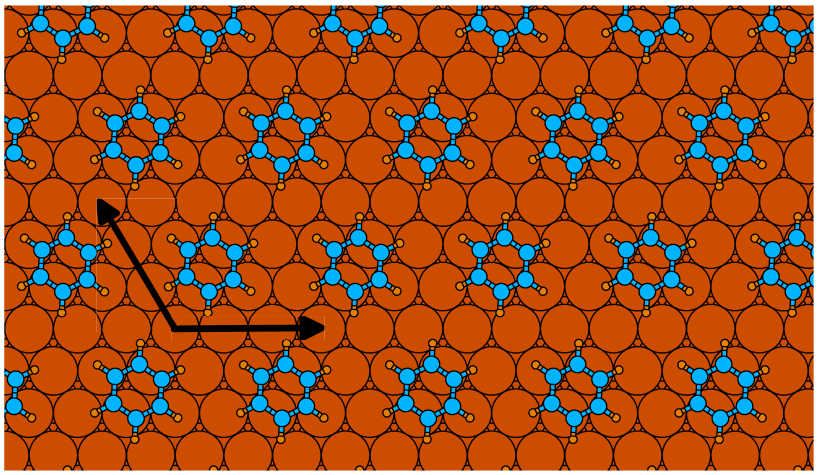

Figure D.5: Benzene on Cu(111), front view. The molecule is taken with the bri30° orientation. The (3×3) unit cell contains a single Bz molecule, the x and y axis are sketched in the figure. The same unit cell and molecular configuration are considered for Bz/Ag(111).

are relaxed using the PBE+vdW$^{\text{surf}}$ scheme and the threshold for the convergence criteria is set to 0.01 eVÅ^{-1} for the maximum final force. All the calculations are performed with the ZORA to include scalar relativistic effects [188]. We set a convergence criteria of 10^{-5} electrons for the electron density and 10^{-6} eV for the total energy of the system. The unit cell and the sampling of the Brillouin zone for each HMOS will be specified in the corresponding section. The binding distances, indicated with d_C, are computed from the relaxed configurations by taking the average position of the carbon atoms of the molecule/monolayer with respect to the unrelaxed topmost metal layer. With this definition we can compare our data with XSW experiments. The stability of a system is obtained with the binding energy formula:

$$E_b = E_{\text{system}} - (E_{\text{surf}} + E_{\text{ads}}) \ , \tag{D.9}$$

where E_{system} indicates the energy of the whole compound, E_{surf} and E_{ads} refer to the clean metal surface and to the adsorbate molecule/monolayer, respectively.

BENZENE

The surfaces employed for the Benzene (Bz) molecule are built with a (3×3) unit cell and six metal layers, a vacuum of 60 Å is used to ensure a negligible interaction between the adsorbed molecules and the periodic images of the metal slab. For slab calculations we implied a Monkhorst-Pack [257] grid with $(6 \times 6 \times 1)$ k-points per unit cell. During the relaxation the adsorbate and the two topmost metal layers are allowed to relax, while the others are kept fixed in their initial positions. The unit cells contain a single Bz molecule adsorbed on a site with an angle of 30° between the C-C and the closed-packed metal rows, referred as bri30° orientation. This structure is represented in Figure D.5. The Bz

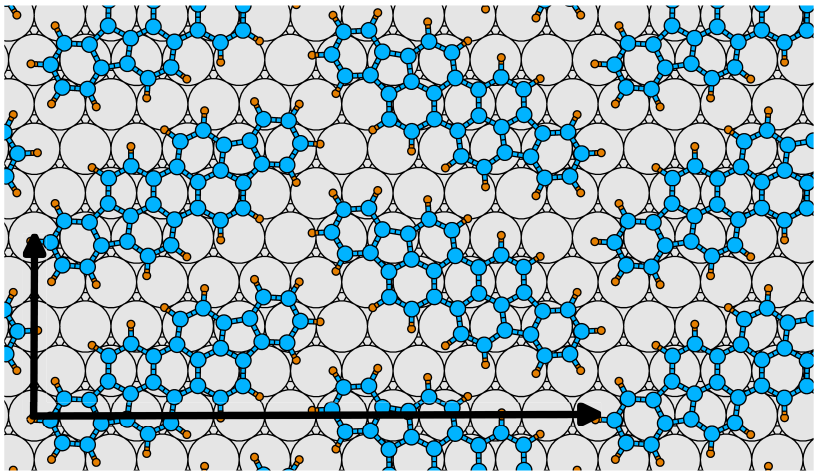

Figure D.6: DIP on Ag(111), front view. The molecules are arranged in a herringbone configuration. The vectors of the unit cell, along the x and y directions, are sketched in the figure. Two molecules are included in the unit cell.

molecule is adsorbed in a flat configuration on both Cu(111) and Ag(111). Energetically, the bri30° is the slightly more stable configuration for chemisorption [134] and is among the most favorable adsorption sites for physisorbed systems (on Cu, Ag and Au) [260].

DIP ON AG(111)

Two unit cells are employed for this HIOS, built with a close-pack monolayer, based on experimental measurements [234], displaced in a brick-wall and herringbone arrangements. Both unit cells contain three metal layers, during the relaxation procedure only the topmost metal layer and the molecules were allowed to relax, while the other two layers remained fixed in their initial positions. The first structure is a $\left(\begin{smallmatrix} 11 & 0 \\ 2 & 4 \end{smallmatrix}\right)$ unit cell with three metal layers and two DIP molecules in a herringbone superstructure. This structure is represented in Figure D.6. The second is made with a $\left(\begin{smallmatrix} 6 & 2 \\ 1 & 4 \end{smallmatrix}\right)$ surface with three metal layers and a single DIP molecule in a brick-wall arrangement. The geometry of the unit cell is depicted in the left panel of Figure 10.4, front and side views. A vacuum of 60 Å has been used for both structures. The Brillouin zone of the herringbone geometry is sampled with a $(1 \times 3 \times 1)$ k-grid points, while a mesh of $(2 \times 4 \times 1)$ is used for the brick-wall.

The induced electron densities produced by PBE and PBE+vdW$_{\text{sc}}^{\text{surf}}$, integrated along the z-direction, are compared in the left panel of Figure D.7. For the definition of $\Delta n(z)$ see Equation 10.1 and 10.2. The system DIP on Ag(111) presents, in addition to the Pauli push-back, a charge transfer. For this reason, the plot in Figure D.7 is more complex than the $\Delta n(z)$ of Bz/Ag(111), see Figure 10.2. First, we can see that, when SC effects are included, the positive peak (accumulation of density) close to the topmost metal layer increases. This accumulation in the vicinity of the substrate is the typical feature of the pillow-effect. Second, self-consistency visibly reduces the

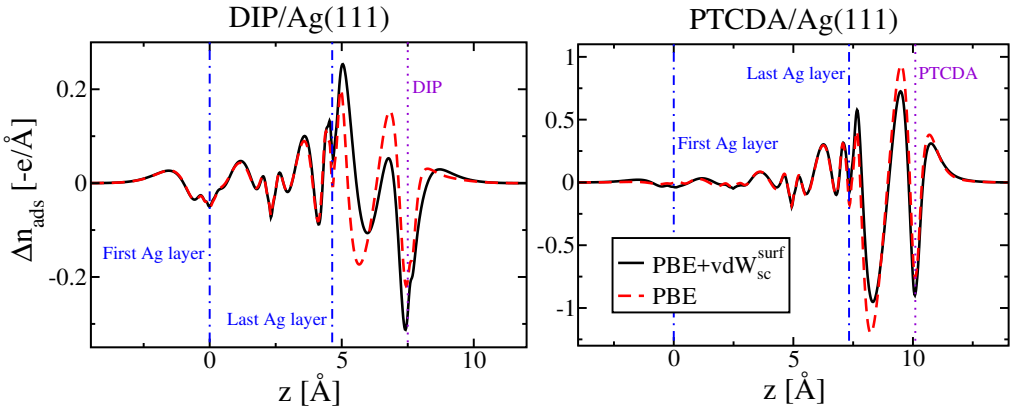

Figure D.7: Integrated electron density induced by molecular adsorption. The curves obtained with PBE and PBE+vdW$_{\rm sc}^{\rm surf}$ for DIP on Ag(111) are plotted in the left panel. The two $\Delta n_{\rm ads}(z)$ for PTCDA on Ag(111) are reported in the right panel. The vertical dotted-dashed lines correspond to the position of the first and the last metal layers, while the vertical dotted line indicates the position of the monolayer.

other positive peak at the interface, located near the DIP monolayer, which is related to the transfer of charge from the substrate to the molecules. It is worth mentioning that the electron density redistribution affects the whole molecule, with a particularly noticeable peak (depletion) at the molecular plane, indicated in Figure D.7 with the vertical dotted line. The modification of the density related to the σ-levels, localized on the rings of the DIP molecule, indicates a net metal-to-molecule charge transfer with the σ-electrons involved in the bonding. As a comparison, we consider the case of Bz/Ag(111) where the rather weak interaction between the substrate and the molecule produces a depletion of electron density above and below the Bz molecules, affecting the π-lobes of the molecule. In this case no charge transfer is established between the two components of the interface and the density at the molecular plane is left practically unaltered, as reported in Figure 10.2.

PTCDA ON AG(111)

PTCDA forms a commensurate monolayer structure on silver surfaces. The lateral ordering of the molecules in the monolayer depends on the orientation of the surface [140]. For PTCDA/Ag(111) we employed a $\begin{pmatrix} 6 & 1 \\ -3 & 5 \end{pmatrix}$ unit cell in accordance with experimental STM and LEED measurements [243, 244]. The unit cell contains a closed-pack monolayer composed by two PTCDA molecules, oriented with a herringbone configuration. The molecules present non-equivalent adsorption geometries and both are adsorbed on bridge position. The structure is shown in Figure D.8 together with the x and y vectors of the unit cell. The vacuum level is set to 60 Å. The silver surface is built with four metal layers and a Monkhorst-Pack grid of $(3 \times 2 \times 1)$ k-points is used to map the reciprocal space.

The integrated induced electron density, $\Delta n_{\rm ads}(z)$, reveals an overall shape very simi-

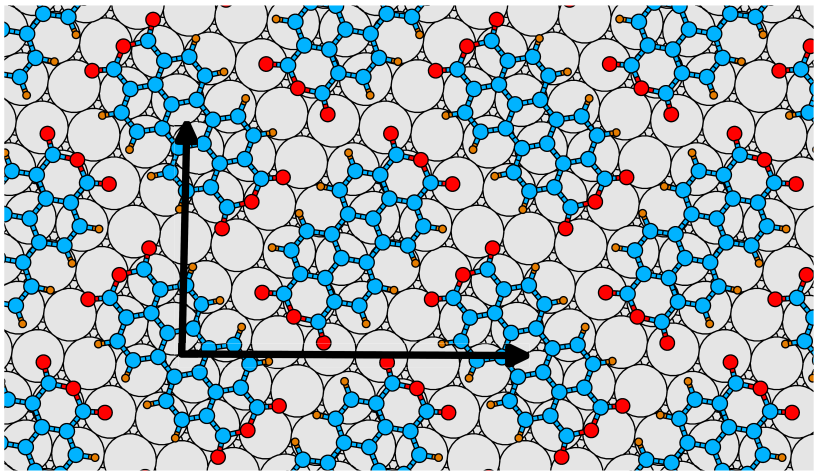

Figure D.8: PTCDA on Ag(111), front view. The monolayer is organized in a herringbone structure with two molecules per unit cell. The x and y vectors of the unit cell are reported in the figure.

lar to DIP/Ag(111). The curves computed with PBE and PBE+vdW$_{\mathrm{sc}}^{\mathrm{surf}}$ are plotted in the right panel of Figure D.7 and display some differences in the interface region. The effect of self-consistency is to increase the accumulation of electron density in the proximity of the topmost metal layer, thus enhancing the Pauli push-back. At the same time, there is a depletion of density close to the PTCDA monolayer, meaning less charge transfer from the metal to the molecules. Notably, the values of the density depletion/accumulation are roughly 2–3 times larger than the ones found for DIP/Ag(111), suggesting a stronger interaction between the substrate and the monolayer. Probably, this is due to the presence of the oxygens. Similarly to DIP/Ag(111), the existence of a transfer of charge is highlighted also by the pronounced depletion of electron density at the monolayer plane, which involves the σ-electrons of the PTCDA molecules.

Publications Related to This Thesis

1. C. Bürker, N. Ferri, A. Tkatchenko, A. Gerlach, J. Niederhausen, T. Hosokai, S. Duhm, J. Zegenhagen, N. Koch and F. Schreiber, *Exploring the bonding of Large Hydrocarbons on Noble Metals: Diindoperylene on Cu(111), Ag(111), and Au(111)*, Phys. Rev. B. **87**, 165443 (2013), DOI: 10.1103/PhysRevB.87.165443.

2. N. Ferri, R. A. DiStasio, Jr., A. Ambrosetti, R. Car and A. Tkatchenko, *Electronic Properties of Molecules and Surfaces with a Self-Consistent Interatomic van der Waals Density Functional*, Phys. Rev. Lett. **114**, 176802 (2015), DOI: 10.1103/PhysRevLett.114.176802.

3. R. J. Maurer, V. G. Ruiz, J. Camarillo-Cisneros, W. Liu, N. Ferri, K. Reuter and A. Tkatchenko, *Adsorption Structures and Energetics of Molecules on Metal Surfaces: Bridging Experiment and Theory*, Prog. Surf. Sci. **91**, 72–100 (2016), DOI: 10.1016/j.progsurf.2016.05.001.

4. N. Ferri, A. Ambrosetti and A. Tkatchenko, *Electronic Charge Rearrangement at Metal/Organic Interfaces Induced by Weak van der Waals Interactions*, in preparation.

BIBLIOGRAPHY

[1] A. M. REILLY and A. TKATCHENKO, *Role of dispersion interactions in the polymorphism and entropic stabilization of the aspirin crystal*, Phys. Rev. Lett., **113**, 055701 (2014), DOI :10.1103/PhysRevLett.113.055701.

[2] J. C. F. RODRIGUEZ-REYES, C. G. F. SILER, W. LIU, A. TKATCHENKO, C. M. FRIEND, and R. J. MADIX, *van der Waals interactions determine selectivity in catalysis by metallic gold*, J. Am. Chem. Soc., **136**, 13333–13340 (2014), DOI :10.1021/ja506447y.

[3] R. A. DISTASIO, JR., O. A. VON LILIENFELD, and A. TKATCHENKO, *Collective many-body van der Waals interactions in molecular systems*, Proc. Natl. Acad. Sci., **109**, 14791–14795 (2012), DOI :10.1073/pnas.1208121109.

[4] B. ROZITIS, E. MACLENNAN, and J. P. EMERY, *Cohesive forces prevent the rotational breakup of rubble-pile asteroid (29075) 1950 DA*, Nature, **512**, 174–176 (2014), DOI :10.1038/nature13632.

[5] A. K. GEIM and I. V. GRIGORIEVA, *Van der Waals heterostructures*, Nature, **499**, 419–425 (2013), DOI :10.1038/nature12385.

[6] N. NERNGCHAMNONG, L. YUAN, D.-C. QI, J. LI, D. THOMPSON, and C. A. NIJHUIS, *The role of van der Waals forces in the performance of molecular diodes*, Nat. Nanotechnol., **8**, 113–118 (2013), DOI :10.1038/nnano.2012.238.

[7] W. LU and C. M. LIEBER, *Nanoelectronics from the bottom up*, Nat. Mater., **6**, 841–850 (2007), DOI :10.1038/nmat2028.

[8] C. WAGNER, N. FOURNIER, V. G. RUIZ, C. LI, K. MÜLLER, M. ROHLFING, A. TKATCHENKO, R. TEMIROV, and S. TAUTZ, *Non-additivity of molecule-surface van der Waals potentials from force measurements*, Nat. Commun., **5**, 5568 (2014), DOI :10.1038/ncomms6568.

[9] A. TKATCHENKO, L. ROMANER, O. T. HOFMANN, E. ZOJER, C. AMBROSCH-DRAXL, and M. SCHEFFLER, *Van der Waals interactions between organic adsorbates and at organic/inorganic interfaces*, MRS Bulletin, **35**, 435–442 (2010), DOI :10.1557/mrs2010.581.

[10] W. LIU, S. N. FILIMONOV, J. CARRASCO, and A. TKATCHENKO, *Molecular switches from benzene derivatives adsorbed on metal surfaces*, Nat. Commun., **4**, 2569 (2013), DOI :10.1038/ncomms3569.

[11] L. KRONIK and N. KOCH, *Electronic properties of organic-based interfaces*, MRS Bulletin, **35**, 417–421 (2010), DOI :10.1557/mrs2010.578.

[12] M. BORN and J. R. OPPENHEIMER, *Zur quantentheorie der molekeln*, Ann. Phys. Leipzig, **84**, 457–484 (1927), DOI :10.1002/andp.19273892002.

[13] M. BARBATTI, M. RUCKENBAUER, J. J. SZYMCZAK, A. J. A. AQUINO, and H. LISCHKA, *Nonadiabatic excited-state dynamics of polar π-systems and related model compounds of biological relevance*, Phys. Chem. Chem. Phys., **10**, 482–494 (2008), DOI :10.1039/B709315M.

[14] S. PISANA, M. LAZZERI, C. CASIRAGHI, K. S. NOVOSELOV, A. K. GEIM, A. C. FERRARI, and F. MAURI, *Breakdown of the adiabatic Born-Oppenheimer approximation in graphene*, Nat. Mater., **6**, 198–201 (2007), DOI :10.1038/nmat1846.

[15] G. GROSSO and G. PASTORI PARRAVICINI, *Solid state physics*, Academic Press (2000).

[16] A. SZABO and N. S. OSTLUND, *Modern quantum chemistry: Introduction to advanced electronic structure theory*, Dover Publications Inc. (1996).

[17] D. R. HARTREE, *The wave mechanics of an atom with a non-Coulomb central field. part i. theory and methods*, Math. Proc. Camb. Phil. Soc., **24**, 89–110 (1928), DOI :10.1017/S0305004100011919.

[18] V. FOCK, *Näherungsmethode zur lösung des quantenmechanischen mehrkörperproblems*, Zeit. für Phys., **61**, 126–148 (1930), DOI :10.1007/BF01340294.

[19] J. C. SLATER, *The theory of complex spectra*, Phys. Rev., **34**, 1293–1322 (1929), DOI :10.1103/PhysRev.34.1293.

[20] P.-O. LÖWDIN, *Quantum theory of many-particle systems. I. physical interpretations by means of density matrices, natural spin-orbitals, and convergence problems in the method of configurational interaction*, Phys. Rev., **97**, 1474–1489 (1955), DOI :10.1103/PhysRev.97.1474.

[21] O. SINANOĞLU, *Many-electron theory of atoms and molecules. I. shells, electron pairs vs many-electron correlations*, J. Chem. Phys., **36**, 706–717 (1962), DOI :10.1063/1.1732596.

[22] F. COESTER and H. KÜMMEL, *Short-range correlations in nuclear wave functions*, Nucl. Phys., **17**, 477–485 (1960), DOI :10.1016/0029-5582(60)90140-1.

[23] J. ČIŽEK, *On the correlation problem in atomic and molecular systems. calculation of wavefunction components in ursell-type expansion using quantum-field theoretical methods*, J. Chem. Phys., **45**, 4256–4266 (1966), DOI :10.1063/1.1727484.

[24] I. SHAVITT and R. J. BARTLETT, *Many-body methods in chemistry and physics*, Cambridge University Press (2009).

[25] K. E. RILEY, M. PITOŇÁK, P. JUREČKA, and P. HOBZA, *Stabilization and structure calculations for noncovalent interactions in extended molecular systems based on wave function and density functional theories*, Chem. Rev., **110**, 5023–5063 (2010), DOI :10.1021/cr1000173.

[26] J. GOLDSTONE, *Derivation of the Brueckner many-body theory*, Proc. R. Soc. A, **239**, 267–279 (1957), DOI :10.1098/rspa.1957.0037.

[27] C. MØLLER and M. S. PLESSET, *Note on an approximation treatment for many-electron systems*, Phys. Rev., **46**, 618–622 (1934), DOI :10.1103/PhysRev.46.618.

[28] X. REN, P. RINKE, C. JOAS, and M. SCHEFFLER, *Random-phase approximation and its applications in computational chemistry and materials science*, J. Mater. Sci., **47**, 7447–7471 (2012), DOI :10.1007/s10853-012-6570-4.

[29] EDITORIAL, *Boosting materials modelling*, Nat. Mater., **15**, 365 (2016), DOI :10.1038/nmat4619.

[30] K. BURKE, *Perspective on density functional theory*, J. Chem. Phys., **136**, 150901 (2012), DOI :10.1063/1.4704546.

[31] A. J. COHEN, P. MORI-SÁNCHEZ, and W. YANG, *Insights into current limitations of density functional theory*, Science, **321**, 792–794 (2008), DOI :10.1126/science.1158722.

[32] A. J. COHEN, P. MORI-SÁNCHEZ, and W. YANG, *Challenges for density functional theory*, Chem. Rev., **112 (1)**, 289–320 (2012), DOI :10.1021/cr200107z.

[33] R. G. PARR and W. YANG, *Density-functional theory of atoms and molecules*, Oxford University Press (1989).

[34] E. ENGEL and R. M. DREIZLER, *Density functional theory: An advanced course*, Springer (2011).

[35] R. M. DREIZLER and E. K. U. GROSS, *Density functional theory*, Springer Verlag (1990).

[36] L. H. THOMAS, *The calculation of atomic fields*, Math. Proc. Cambridge, **23**, 542–548 (1927), DOI :10.1017/S0305004100011683.

[37] E. FERMI, *Un metodo statistico per la determinazione di alcune proprietà dell'atomo*, Rend. Accad. Naz. Lincei, **6**, 602–607 (1927).

[38] P. A. M. DIRAC, *Note on exchange phenomena in the Thomas atom*, Math. Proc. Camb. Phil. Soc., **26**, 376–385 (1930), DOI :10.1017/S0305004100016108.

[39] Z. ROMANOWSKI and S. KRUKOWSKI, *Derivation of von Weizsäcker equation based on Green-Gauss theorem*, Acta Phys. Pol. A, **115**, 653–655 (2009), DOI :10.12693/APhysPolA.115.653.

[40] P. HOHENBERG and W. KOHN, *Inhomogeneous electron gas*, Phys. Rev., **136**, B864–B871 (1964), DOI :10.1103/PhysRev.136.B864.

[41] W. KOHN, *v-representability and density functional theory*, Phys. Rev. Lett., **51**, 1596–1598 (1983), DOI :10.1103/PhysRevLett.51.1596.

[42] W. KOHN and L. J. SHAM, *Self-consistent equations including exchange and correlation effects*, Phys. Rev., **140**, A1133–A1138 (1965), DOI :10.1103/PhysRev.140.A1133.

[43] J. F. JANAK, *Proof that $\frac{\partial e}{\partial n_i} = \epsilon$ in density-functional theory*, Phys. Rev. B, **18**, 7165–7168 (1978), DOI :10.1103/PhysRevB.18.7165.

[44] G. L. OLIVER and J. P. PERDEW, *Spin-density gradient expansion for the kinetic energy*, Phys. Rev. A, **20**, 397–403 (1979), DOI :10.1103/PhysRevA.20.397.

[45] J. HARRIS, *Adiabatic-connection approach to Kohn-Sham theory*, Phys. Rev. A, **29**, 1648–1659 (1984), DOI :10.1103/PhysRevA.29.1648.

[46] L. J. SHAM, *Exchange and correlation in density-functional theory*, Phys. Rev. B, **32**, 3876–3882 (1985), DOI :10.1103/PhysRevB.32.3876.

[47] J. P. PERDEW and A. ZUNGER, *Self-interaction correction to density-functional approximations for many-electron systems*, Phys. Rev. B, **23**, 5048–5079 (1981), DOI :10.1103/PhysRevB.23.5048.

[48] J. P. PERDEW, A. RUZSINSZKY, J. TAO, V. N. STAROVEROV, G. E. SCUSERIA, and G. I. CSONKA, *Prescription for the design and selection of density functional approximations: More constraint satisfaction with fewer fits*, J. Chem. Phys., **123** (2005), DOI :10.1063/1.1904565.

[49] S. H. VOSKO, L. WILK, and M. NUSAIR, *Accurate spin-dependent electron liquid correlation energies for local spin density calculations: a critical analysis*, Can. J. Phys., **58**, 1200–1211 (1980), DOI :10.1139/p80-159.

[50] J. P. PERDEW and A. ZUNGER, *Self-interaction correction to density-functional approximations for many-electron systems*, Phys. Rev. B, **23**, 5048–5079 (1981), DOI :10.1103/PhysRevB.23.5048.

[51] M. ERNZERHOF, J. P. PERDEW, and K. BURKE, *Coupling-constant dependence of atomization energies*, Int. J. Quantum Chem., **64**, 285–295 (1997), DOI :10.1002/(SICI)1097-461X(1997)64:3<285::AID-QUA2>3.0.CO;2-S.

[52] J. P. PERDEW, K. BURKE, and M. ERNZERHOF, *Generalized gradient approximation made simple*, Phys. Rev. Lett., **77**, 3865–3868 (1996), DOI :10.1103/PhysRevLett.77.3865.

[53] J. P. PERDEW, in *electronic structure of solids '91*, p. 11. Edited by P. Ziesche and H. Eschrig, Akademie Verlag, Berlin (1991).

[54] J. PAIER, R. HIRSCHL, M. MARSMAN, and G. KRESSE, *The Perdew-Burke-Ernzerhof exchange-correlation functional applied to the g2-1 test set using a plane-wave basis set*, J. Chem. Phys., **122** (2005), DOI :10.1063/1.1926272.

[55] J. SUN, M. MARSMAN, G. I. CSONKA, A. RUZSINSZKY, P. HAO, Y.-S. KIM, G. KRESSE, and J. P. PERDEW, *Self-consistent meta-generalized gradient approximation within the projector-augmented-wave method*, Phys. Rev. B, **84**, 035117 (2011), DOI :10.1103/PhysRevB.84.035117.

[56] A. D. BECKE, *A new mixing of Hartree-Fock and local density-functional theories*, J. Chem. Phys., **98**, 1372–1377 (1993), DOI :10.1063/1.464304.

[57] A. D. BECKE, *Density-functional exchange-energy approximation with correct asymptotic behavior*, Phys. Rev. A, **38**, 3098–3100 (1988), DOI :10.1103/PhysRevA.38.3098.

[58] C. LEE, W. YANG, and R. G. PARR, *Development of the Colle-Salvetti correlation-energy formula into a functional of the electron density*, Phys. Rev. B, **37**, 785–789 (1988), DOI :10.1103/PhysRevB.37.785.

[59] A. D. BECKE, *Density-functional thermochemistry. III. the role of exact exchange*, J. Chem. Phys., **98**, 5648–5652 (1993), DOI :10.1063/1.464913.

[60] J. PAIER, M. MARSMAN, and G. KRESSE, *Why does the B3LYP hybrid functional fail for metals?*, J. Chem. Phys., **127**, 024103 (2007), DOI :10.1063/1.2747249.

[61] J. P. PERDEW, M. ERNZERHOF, and K. BURKE, *Rationale for mixing exact exchange with density functional approximations*, J. Chem. Phys., **105**, 9982–9985 (1996), DOI :10.1063/1.472933.

[62] C. ADAMO and V. BARONE, *Toward reliable density functional methods without adjustable parameters: The PBE0 model*, J. Chem. Phys., **110**, 6158–6170 (1999), DOI :10.1063/1.478522.

[63] J. PAIER, M. MARSMAN, K. HUMMER, G. KRESSE, I. C. GERBER, and J. G. ÁNGYÁN, *Screened hybrid density functionals applied to solids*, J. Chem. Phys., **124**, 154709 (2006), DOI :10.1063/1.2187006.

[64] J. PAIER, M. MARSMAN, K. HUMMER, G. KRESSE, I. C. GERBER, and J. G. ÁNGYÁN, *Erratum: "Screened hybrid density functionals applied to solids" [J. Chem. Phys. 124, 154709 (2006)]*, J. Chem. Phys., **125**, 249901 (2006), DOI :10.1063/1.2403866.

[65] J. HEYD, G. E. SCUSERIA, and M. ERNZERHOF, *Hybrid functionals based on a screened Coulomb potential*, J. Chem. Phys., **118**, 8207–8215 (2003), DOI :10.1063/1.1564060.

[66] J. HEYD, G. E. SCUSERIA, and M. ERNZERHOF, *Erratum:"Hybrid functionals based on a screened Coulomb potential" [J. Chem. Phys. 118, 8207 (2003)]*, J. Chem. Phys., **124**, 219906 (2006), DOI :10.1063/1.2204597.

[67] L. SCHIMKA, J. HARL, and G. KRESSE, *Improved hybrid functional for solids: The HSEsol functional*, J. Chem. Phys., **134**, 024116 (2011), DOI :10.1063/1.3524336.

[68] A. STROPPA and G. KRESSE, *The shortcomings of semi-local and hybrid functionals: what we can learn from surface science studies*, New J. Phys., **10**, 063020 (2008), DOI :10.1088/1367-2630/10/6/063020.

[69] A. STROPPA, K. TERMENTZIDIS, J. PAIER, G. KRESSE, and J. HAFNER, *Co adsorption on metal surfaces: A hybrid functional study with plane-wave basis set*, Phys. Rev. B, **76**, 195440 (2007), DOI :10.1103/PhysRevB.76.195440.

[70] J. P. PERDEW and L. A. CONSTANTIN, *Laplacian-level density functionals for the kinetic energy density and exchange-correlation energy*, Phys. Rev. B, **75**, 155109 (2007), DOI :10.1103/PhysRevB.75.155109.

[71] J. TAO, J. P. PERDEW, V. N. STAROVEROV, and G. E. SCUSERIA, *Climbing the density functional ladder: Nonempirical meta–generalized gradient approximation designed for molecules and solids*, Phys. Rev. Lett., **91**, 146401 (2003), DOI :10.1103/PhysRevLett.91.146401.

[72] Y. ZHAO and D. G. TRUHLAR, *A new local density functional for main-group thermochemistry, transition metal bonding, thermochemical kinetics, and noncovalent interactions*, J. Chem. Phys., **125**, 194101 (2006), DOI :10.1063/1.2370993.

[73] Y. ZHAO and D. G. TRUHLAR, *Construction of a generalized gradient approximation by restoring the density-gradient expansion and enforcing a tight Lieb-Oxford bound*, J. Chem. Phys., **128**, 184109 (2008), DOI :10.1063/1.2912068.

[74] Y. ZHAO and D. G. TRUHLAR, *The M06 suite of density functionals for main group thermochemistry, thermochemical kinetics, noncovalent interactions, excited states, and transition elements: two new functionals and systematic testing of four M06-class functionals and 12 other functionals*, Theor. Chem. Acc., **120**, 215–241 (2008), DOI :10.1007/s00214-007-0310-x.

[75] Y. ZHAO and D. G. TRUHLAR, *Density functional for spectroscopy: No long-range self-interaction error, good performance for Rydberg and charge-transfer states, and better performance on average than B3LYP for ground states*, J. Phys. Chem. A, **110**, 13126–13130 (2006), DOI :10.1021/jp066479k.

[76] J. SUN, A. RUZSINSZKY, and J. P. PERDEW, *Strongly constrained and appropriately normed semilocal density functional*, Phys. Rev. Lett., **115**, 036402 (2015), DOI :10.1103/PhysRevLett.115.036402.

[77] J. SUN, R. C. REMSING, Y. ZHANG, Z. SUN, A. RUZSINSZKY, H. PENG, Z. YANG, A. PAUL, U. WAGHMARE, X. WU, M. L. KLEIN, and J. P. PERDEW, *Accurate first-principles structures and energies of diversely bonded systems from an efficient density functional*, Nat. Chem., **8**, 831–836 (2016), DOI :10.1038/nchem.2535.

[78] W. KOHN, *Nobel lecture: Electronic structure of matter–wave functions and density functionals*, Rev. Mod. Phys., **71**, 1253–1266 (1999), DOI :10.1103/RevModPhys.71.1253.

[79] D. C. LANGRETH and J. P. PERDEW, *The exchange-correlation energy of a metallic surface*, Solid State Commun., **17**, 1425–1429 (1975), DOI :10.1016/0038-1098(75)90618-3.

[80] O. GUNNARSSON and B. I. LUNDQVIST, *Exchange and correlation in atoms, molecules, and solids by the spin-density-functional formalism*, Phys. Rev. B, **13**, 4274–4298 (1976), DOI :10.1103/PhysRevB.13.4274.

[81] D. C. LANGRETH and J. P. PERDEW, *Exchange-correlation energy of a metallic surface: Wave-vector analysis*, Phys. Rev. B, **15**, 2884–2901 (1977), DOI :10.1103/PhysRevB.15.2884.

[82] D. LU, H.-V. NGUYEN, and G. GALLI, *Power series expansion of the random phase approximation correlation energy: The role of the third- and higher-order contributions*, J. Chem. Phys., **133**, 154110 (2010), DOI :10.1063/1.3494541.

[83] F. FURCHE, *Molecular tests of the random phase approximation to the exchange-correlation energy functional*, Phys. Rev. B, **64**, 195120 (2001), DOI :10.1103/PhysRevB.64.195120.

[84] M. FUCHS and X. GONZE, *Accurate density functionals: Approaches using the adiabatic-connection fluctuation-dissipation theorem*, Phys. Rev. B, **65**, 235109 (2002), DOI :10.1103/PhysRevB.65.235109.

[85] H.-V. NGUYEN and G. GALLI, *A first-principles study of weakly bound molecules using exact exchange and the random phase approximation*, J. Chem. Phys., **132**, 044109 (2010), DOI :10.1063/1.3299247.

[86] J. HARL, L. SCHIMKA, and G. KRESSE, *Assessing the quality of the random phase approximation for lattice constants and atomization energies of solids*, Phys. Rev. B, **81**, 115126 (2010), DOI :10.1103/PhysRevB.81.115126.

[87] S. LEBÈGUE, J. HARL, T. GOULD, J. G. ÁNGYÁN, G. KRESSE, and J. F. DOBSON, *Cohesive properties and asymptotics of the dispersion interaction in graphite by the random phase approximation*, Phys. Rev. Lett., **105**, 196401 (2010), DOI :10.1103/PhysRevLett.105.196401.

[88] P. JUREČKA, J. ŠPONER, J. ČERNÝ, and P. HOBZA, *Benchmark database of accurate (MP2 and CCSD(T) complete basis set limit) interaction energies of small model complexes, dna base pairs, and amino acid pairs*, Phys. Chem. Chem. Phys., **8**, 1985–1993 (2006), DOI :10.1039/B600027D.

[89] X. REN, A. TKATCHENKO, P. RINKE, and M. SCHEFFLER, *Beyond the random-phase approximation for the electron correlation energy: The importance of single excitations*, Phys. Rev. Lett., **106**, 153003 (2011), DOI :10.1103/PhysRevLett.106.153003.

[90] S. KURTH and J. P. PERDEW, *Density-functional correction of random-phase-approximation correlation with results for jellium surface energies*, Phys. Rev. B, **59**, 10461–10468 (1999), DOI :10.1103/PhysRevB.59.10461.

[91] A. GRÜNEIS, M. MARSMAN, J. HARL, L. SCHIMKA, and G. KRESSE, *Making the random phase approximation to electronic correlation accurate*, J. Chem. Phys., **131**, 154115 (2009), DOI :10.1063/1.3250347.

[92] F. FURCHE and T. VAN VOORHIS, *Fluctuation-dissipation theorem density-functional theory*, J. Chem. Phys., **122**, 164106 (2005), DOI :10.1063/1.1884112.

[93] J. PAIER, B. G. JANESKO, T. M. HENDERSON, G. E. SCUSERIA, A. GRÜNEIS, and G. KRESSE, *Hybrid functionals including random phase approximation correlation and second-order screened exchange*, J. Chem. Phys., **132**, 094103 (2010), DOI :10.1063/1.3317437.

[94] A. L. FETTER and J. D. WALECKA, *Quantum theory of many-particle systems*, Dover Publications (2003).

[95] H. LEHMANN, *Über eigenschaften von ausbreitungsfunktionen und renormierungskonstanten quantisierter felder*, Il Nuovo Cimento (1943-1954), **11**, 342–357 (1954), DOI :10.1007/BF02783624.

[96] R. P. FEYNMAN, *Space-time approach to quantum electrodynamics*, Phys. Rev., **76**, 769–789 (1949), DOI :10.1103/PhysRev.76.769.

[97] L. HEDIN, *New method for calculating the one-particle Green's function with application to the electron-gas problem*, Phys. Rev., **139**, A796–A823 (1965), DOI :10.1103/PhysRev.139.A796.

[98] F. CARUSO, P. RINKE, X. REN, M. SCHEFFLER, and A. RUBIO, *Unified description of ground and excited states of finite systems: The self-consistent GW approach*, Phys. Rev. B, **86**, 081102 (2012), DOI :10.1103/PhysRevB.86.081102.

[99] F. CARUSO, *Self-consistent GW approach for the unified description of ground and excited states of finite systems*, Ph.D. thesis, Fritz-Haber-Institut der Max-Planck-Gesellschaf (2013), URL.

[100] B. HOLM and U. VON BARTH, *Fully self-consistent* GW *self-energy of the electron gas*, Phys. Rev. B, **57**, 2108–2117 (1998), DOI :10.1103/PhysRevB.57.2108.

[101] Y. M. NIQUET, M. FUCHS, and X. GONZE, *Exchange-correlation potentials in the adiabatic connection fluctuation-dissipation framework*, Phys. Rev. A, **68**, 032507 (2003), DOI :10.1103/PhysRevA.68.032507.

[102] F. LONDON, *The general theory of molecular forces*, Trans. Faraday Soc., **33**, 8b–26 (1937), DOI :10.1039/TF937330008B.

[103] B. M. AXILROD and E. TELLER, *Interaction of the van der Waals type between three atoms*, J. Chem. Phys., **11**, 299–300 (1943), DOI :10.1063/1.1723844.

[104] H. B. G. CASIMIR and D. POLDER, *The influence of retardation on the London-van der Waals forces*, Phys. Rev., **73**, 360–372 (1948), DOI :10.1103/PhysRev.73.360.

[105] I. G. KAPLAN, *Intermolecular interactions: Physical picture, computational methods and model potentials*, Wiley (2006), DOI :10.1002/047086334X.

[106] A. J. STONE, *The theory of intermolecular forces*, Oxford University Press (2013), DOI :10.1093/acprof:oso/9780199672394.001.0001.

[107] A. V. PARSEGIAN, *Van der Waals forces. a handbook for biologists, chemists, engineers, and physicists*, Cambridge University Press (2005), DOI :10.1017/CBO9780511614606.

[108] A. TKATCHENKO and M. SCHEFFLER, *Accurate molecular van der Waals interactions from ground-state electron density and free-atom reference data*, Phys. Rev. Lett., **102**, 073005 (2009), DOI :10.1103/PhysRevLett.102.073005.

[109] S. GRIMME, *Accurate description of van der Waals complexes by density functional theory including empirical corrections*, J. Comput. Chem., **25**, 1463–1473 (2004), DOI :10.1002/jcc.20078.

[110] S. GRIMME, *Semiempirical GGA-type density functional constructed with a long-range dispersion correction*, J. Comput. Chem., **27**, 1787–1799 (2006), DOI :10.1002/jcc.20495.

[111] Q. WU and W. YANG, *Empirical correction to density functional theory for van der Waals interactions*, J. Chem. Phys., **116**, 515–524 (2002), DOI :10.1063/1.1424928".

[112] S. GRIMME, J. ANTONY, S. EHRLICH, and H. KRIEG, *A consistent and accurate ab initio parametrization of density functional dispersion correction (DFT-D) for the 94 elements H-Pu*, J. Chem. Phys., **132**, 154104 (2010), DOI :10.1063/1.3382344.

[113] A. D. BECKE and E. R. JOHNSON, *Exchange-hole dipole moment and the dispersion interaction*, J. Chem. Phys., **122**, 154104 (2005), DOI :10.1063/1.1884601.

[114] E. R. JOHNSON and A. D. BECKE, *A post-Hartree-Fock model of intermolecular interactions*, J. Chem. Phys., **123**, 024101 (2005), DOI :10.1063/1.1949201.

[115] A. D. BECKE and E. R. JOHNSON, *A density-functional model of the dispersion interaction*, J. Chem. Phys., **123**, 154101 (2005), DOI :10.1063/1.2065267.

[116] F. L. HIRSHFELD, *Bonded-atom fragments for describing molecular charge densities*, Theoret. Chim. Acta, **44**, 129–138 (1977), DOI :10.1007/BF00549096.

[117] K. T. TANG and M. KARPLUS, *Padé-approximant calculation of the nonretarded van der Waals coefficients for two and three helium atoms*, Phys. Rev., **171**, 70–74 (1968), DOI :10.1103/PhysRev.171.70.

[118] X. CHU and A. DALGARNO, *Linear response time-dependent density functional theory for van der Waals coefficients*, J. Chem. Phys., **121**, 4083–4088 (2004), DOI :10.1063/1.1779576.

[119] T. BRINCK, J. S. MURRAY, and P. POLITZER, *Polarizability and volume*, J. Chem. Phys., **98**, 4305–4306 (1993), DOI :10.1063/1.465038.

[120] J. HOJA, A. M. REILLY, and A. TKATCHENKO, *First-principles modeling of molecular crystals: structures and stabilities, temperature and pressure*, WIREs: Comput. Mol. Sci., **7** (2017), DOI :10.1002/wcms.1294.

[121] A. AMBROSETTI, D. ALFÈ, R. A. DISTASIO, JR., and A. TKATCHENKO, *Hard numbers for large molecules: Toward exact energetics for supramolecular systems*, J. Chem. Phys. Lett., **5**, 849–855 (2014), DOI :10.1021/jz402663k.

[122] G.-X. ZHANG, A. TKATCHENKO, J. PAIER, H. APPEL, and M. SCHEFFLER, *van der Waals interactions in ionic and semiconductor solids*, Phys. Rev. Lett., **107**, 245501 (2011), DOI :10.1103/PhysRevLett.107.245501.

[123] V. G. RUIZ, W. LIU, E. ZOJER, M. SCHEFFLER, and A. TKATCHENKO, *Density-functional theory with screened van der Waals interactions for the modeling of hybrid inorganic-organic systems*, Phys. Rev. Lett., **108**, 146103 (2012), DOI :10.1103/PhysRevLett.108.146103.

[124] W. LIU, F. MAASS, M. WILLENBOCKEL, C. BRONNER, M. SCHULZE, S. SOUBATCH, F. S. TAUTZ, P. TEGEDER, and A. TKATCHENKO, *Quantitative prediction of molecular adsorption: Structure and binding of benzene on coinage metals*, Phys. Rev. Lett., **115**, 036104 (2015), DOI :10.1103/PhysRevLett.115.036104.

[125] R. J. MAURER, V. G. RUIZ, and A. TKATCHENKO, *Many-body dispersion effects in the binding of adsorbates on metal surfaces*, J. Chem. Phys., **143**, 102808 (2015), DOI :10.1063/1.4922688.

[126] M. ROHLFING and T. BREDOW, *Binding energy of adsorbates on a noble-metal surface: Exchange and correlation effects*, Phys. Rev. Lett., **101**, 266106 (2008), DOI :10.1103/PhysRevLett.101.266106.

[127] R. J. MAURER, V. G. RUIZ, J. CAMARILLO-CISNEROS, W. LIU, N. FERRI, K. REUTER, and A. TKATCHENKO, *Adsorption structures and energetics of molecules on metal surfaces: Bridging experiment and theory*, Prog. Surf. Sci., **91**, 72–100 (2016), DOI :10.1016/j.progsurf.2016.05.001.

[128] G.-X. ZAHNG, *Understanding the role of van der Waals forces in solids from first principles*, Ph.D. thesis, Fritz-Haber-Institut der Max-Planck-Gesellschaf (2014), URL.

[129] A. LUCAS, *Collective contributions to the long-range dipolar interaction in rare-gas crystals*, Physica, **35**, 353–368 (1967), DOI :10.1016/0031-8914(67)90184-X.

[130] J. J. REHR, E. ZAREMBA, and W. KOHN, *van der Waals forces in the noble metals*, Phys. Rev. B, **12**, 2062–2066 (1975), DOI :10.1103/PhysRevB.12.2062.

[131] A. AMBROSETTI and P. L. SILVESTRELLI, *Cohesive properties of noble metals by van der Waals–corrected density functional theory: Au, Ag, and Cu as case studies*, Phys. Rev. B, **94**, 045124 (2016), DOI :10.1103/PhysRevB.94.045124.

[132] E. M. LIFSHITZ, *The theory of molecular attractive forces between solids*, Sov. Phys. JETP, **2**, 73 (1956) (Available online at `http://www.mit.edu/~kardar/research/seminars/Casimir/LifshitzTheory.pdf`).

[133] E. ZAREMBA and W. KOHN, *Van der Waals interaction between an atom and a solid surface*, Phys. Rev. B, **13**, 2270–2285 (1976), DOI :10.1103/PhysRevB.13.2270.

[134] W. LIU, V. G. RUIZ, G.-X. ZHANG, B. SANTRA, X. REN, M. SCHEFFLER, and A. TKATCHENKO, *Structure and energetics of benzene adsorbed on transition metal surfaces: density-functional theory with van der Waals interactions including collective substrate response*, New J. Phys., **15**, 053046 (2013), DOI :10.1088/1367-2630/15/5/053046.

[135] H. C. HAMAKER, *The london–van der Waals attraction between spherical particles*, Physica, **4**, 1058–1072 (1937), DOI :10.1016/S0031-8914(37)80203-7.

[136] M. W. COLE, H.-Y. KIM, and M. LIEBRECHT, *Van der Waals interactions: Accuracy of pair potential approximations*, J. Chem. Phys., **137**, 194316 (2012), DOI :10.1063/1.4765328.

[137] V. G. L. Ruiz, *Adsorption of Atoms and Molecules on Surfaces: Density-Functional Theory with Screened van der Waals Interactions*, Ph.D. thesis, Fritz-Haber-Institut der Max-Planck-Gesellschaf (2016), URL.

[138] C. Bürker, N. Ferri, A. Tkatchenko, A. Gerlach, J. Niederhausen, T. Hosokai, S. Duhm, J. Zegenhagen, N. Koch, and F. Schreiber, *Exploring the bonding of large hydrocarbons on noble metals: Diindoperylene on Cu(111), Ag(111), and Au(111)*, Phys. Rev. B, **87**, 165443 (2013), DOI :10.1103/PhysRevB.87.165443.

[139] W. Liu, A. Tkatchenko, and M. Scheffler, *Modeling adsorption and reactions of organic molecules at metal surfaces*, Acc. Chem. Res., **47**, 3369–3377 (2014), DOI :10.1021/ar500118y.

[140] V. G. Ruiz, W. Liu, and A. Tkatchenko, *Density-functional theory with screened van der Waals interactions applied to atomic and molecular adsorbates on close-packed and non-close-packed surfaces*, Phys. Rev. B, **93**, 035118 (2016), DOI :10.1103/PhysRevB.93.035118.

[141] M. Dion, H. Rydberg, E. Schröder, D. C. Langreth, and B. I. Lundqvist, *Van der Waals density functional for general geometries*, Phys. Rev. Lett., **92**, 246401 (2004), DOI :10.1103/PhysRevLett.92.246401.

[142] D. C. Langreth, M. Dion, H. Rydberg, E. Schröder, P. Hyldgaard, and B. I. Lundqvist, *Van der Waals density functional theory with applications*, Int. J. Quantum Chem., **101**, 599–610 (2005), DOI :10.1002/qua.20315.

[143] Y. Zhang and W. Yang, *Comment on "Generalized gradient approximation made simple"*, Phys. Rev. Lett., **80**, 890–890 (1998), DOI :10.1103/PhysRevLett.80.890.

[144] K. Lee, É. D. Murray, L. Kong, B. I. Lundqvist, and D. C. Langreth, *Higher-accuracy van der Waals density functional*, Phys. Rev. B, **82**, 081101 (2010), DOI :10.1103/PhysRevB.82.081101.

[145] O. A. Vydrov and T. Van Voorhis, *Dispersion interactions from a local polarizability model*, Phys. Rev. A, **81**, 062708 (2010), DOI :10.1103/PhysRevA.81.062708.

[146] J. F. Dobson, *Prospects for a van der Waals density functional*, Int. J. Quantum Chem., **69**, 615–618 (1998), DOI :10.1002/(SICI)1097-461X(1998)69:4<615::AID-QUA19>3.0.CO;2-Y.

[147] J. Klimeš and A. Michaelides, *Perspective: Advances and challenges in treating van der Waals dispersion forces in density functional theory*, J. Chem. Phys., **137**, 120901 (2012), DOI :10.1063/1.4754130.

[148] J. Hermann, R. A. DiStasio, and A. Tkatchenko, *First-principles models for van der Waals interactions in molecules and materials: Concepts, theory, and applications*, Chem. Rev., **117**, 4714–4758 (2017), DOI :10.1021/acs.chemrev.6b00446.

[149] J. F. Dobson, A. White, and A. Rubio, *Asymptotics of the dispersion interaction: Analytic benchmarks for van der Waals energy functionals*, Phys. Rev. Lett., **96**, 073201 (2006), DOI :10.1103/PhysRevLett.96.073201.

[150] J. F. Dobson and T. Gould, *Calculation of dispersion energies*, J. Phys. Cond. Matt., **24**, 073201 (2012), DOI :10.1088/0953-8984/24/7/073201.

[151] V. BLUM, R. GEHRKE, F. HANKE, P. HAVU, V. HAVU, X. REN, K. REUTER, and M. SCHEFFLER, *Ab initio molecular simulations with numeric atom-centered orbitals*, Comput. Phys. Commun., **180**, 2175–2196 (2009), DOI :10.1016/j.cpc.2009.06.022.

[152] V. LEBEDEV and D. LAIKOV, *A quadrature formula for the sphere of the 131st algebraic order of accuracy*, Doklady Math., **59**, 477–481 (1999).

[153] X. REN, P. RINKE, V. BLUM, J. WIEFERINK, A. TKATCHENKO, A. SANFILIPPO, K. REUTER, and M. SCHEFFLER, *Resolution-of-identity approach to Hartree-Fock, hybrid density functionals, RPA, MP2 and GW with numeric atom-centered orbital basis functions*, New J. Phys., **14**, 053020 (2012), DOI :10.1088/1367-2630/14/5/053020.

[154] V. HAVU, V. BLUM, P. HAVU, and M. SCHEFFLER, *Efficient integration for all-electron electronic structure calculation using numeric basis functions*, J. Comput. Phys., **228**, 8367–8379 (2009), DOI :10.1016/j.jcp.2009.08.008.

[155] T. THONHAUSER, V. R. COOPER, S. LI, A. PUZDER, P. HYLDGAARD, and D. C. LANGRETH, *Van der Waals density functional: Self-consistent potential and the nature of the van der Waals bond*, Phys. Rev. B, **76**, 125112 (2007), DOI :10.1103/PhysRevB.76.125112.

[156] D. C. LANGRETH, L. B. I., S. D. HAKAROVA KÄCK, V. R. COOPER, M. DION, P. HYLDGAARD, A. KELKKANEN, J. KLEIS, L. KONG, S. LI, P. G. MOSES, E. MURRAY, A. PUZDER, H. RYDBERG, E. SCHRÖDER, and T. THONHAUSER, *A density functional for sparse matter*, J. Phys. Cond. Matt., **21**, 084203 (2009), DOI :10.1088/0953-8984/21/8/084203.

[157] O. A. VYDROV, Q. WU, and T. VAN VOORHIS, *Self-consistent implementation of a nonlocal van der Waals density functional with a Gaussian basis set*, J. Chem. Phys., **129**, 014106 (2008), DOI :10.1063/1.2948400.

[158] M. MURA, A. GULANS, T. THONHAUSER, and L. KANTOROVICH, *Role of van der Waals interaction in forming molecule-metal junctions: Flat organic molecules on the Au(111) surface*, Phys. Chem. Chem. Phys., **12**, 4759–4767 (2010), DOI :10.1039/B920121A.

[159] S. N. STEINMANN and C. CORMINBOEUF, *A generalized-gradient approximation exchange hole model for dispersion coefficients*, J. Chem. Phys., **134**, 044117 (2011), DOI :10.1063/1.3545985.

[160] S. N. STEINMANN and C. CORMINBOEUF, *Comprehensive benchmarking of a density-dependent dispersion correction*, J. Chem. Theory Comput., **7**, 3567–3577 (2011), DOI :10.1021/ct200602x.

[161] E. BRÉMOND, N. GOLUBEV, S. N. STEINMANN, and C. CORMINBOEUF, *How important is self-consistency for the dDsC density dependent dispersion correction?*, J. Chem. Phys., **140**, 18A516 (2014), DOI :10.1063/1.4867195.

[162] H. HELLMANN, *Einführung in die Quantenchemie*, Leipzig: Franz Deuticke, page 285 (1937).

[163] R. P. FEYNMAN, *Forces in molecules*, Phys. Rev., **56**, 340–343 (1939), DOI :10.1103/PhysRev.56.340.

[164] P. GIANNOZZI, S. BARONI, N. BONINI, M. CALANDRA, R. CAR, C. CAVAZZONI, D. CERESOLI, G. L. CHIAROTTI, M. COCOCCIONI, I. DABO, A. D. CORSO, S. DE GIRONCOLI, S. FABRIS, G. FRATESI, R. GEBAUER, U. GERSTMANN, C. GOUGOUSSIS, A. KOKALJ,

M. LAZZERI, L. MARTIN-SAMOS, N. MARZARI, F. MAURI, R. MAZZARELLO, S. PAOLINI, A. PASQUARELLO, L. PAULATTO, C. SBRACCIA, S. SCANDOLO, G. SCLAUZERO, A. P. SEITSONEN, A. SMOGUNOV, P. UMARI, and R. M. WENTZCOVITCH, *QUANTUM ESPRESSO: a modular and open-source software project for quantum simulations of materials*, J. Phys.: Condens. Matter, **21**, 395502 (2009), DOI :10.1088/0953-8984/21/39/395502.

[165] R. A. DISTASIO, JR., B. SANTRA, Z. LI, X. WU, and R. CAR, *The individual and collective effects of exact exchange and dispersion interactions on the ab initio structure of liquid water*, J. Chem. Phys., **141**, 084502 (2014), DOI :10.1063/1.4893377.

[166] N. MAROM, A. TKATCHENKO, M. SCHEFFLER, and L. KRONIK, *Describing both dispersion interactions and electronic structure using density functional theory: The case of metal-phthalocyanine dimers*, J. Chem. Theory Comput., **6**, 81–90 (2010), DOI :10.1021/ct900410j.

[167] N. MAROM, A. TKATCHENKO, M. ROSSI, V. V. GOBRE, O. HOD, M. SCHEFFLER, and L. KRONIK, *Dispersion interactions with density-functional theory: Benchmarking semiempirical and interatomic pairwise corrected density functionals*, J. Chem. Theory Comput., **7**, 3944–3951 (2011), DOI :10.1021/ct2005616.

[168] N. FERRI, R. A. DISTASIO, JR., A. AMBROSETTI, R. CAR, and A. TKATCHENKO, *Electronic properties of molecules and surfaces with a self-consistent interatomic van der Waals density functional*, Phys. Rev. Lett., **114**, 176802 (2015), DOI :10.1103/PhysRevLett.114.176802.

[169] J. ŘEZÁČ, K. E. RILEY, and P. HOBZA, *S66: A well-balanced database of benchmark interaction energies relevant to biomolecular structures*, J. Chem. Theory Comput., **7**, 2427–2438 (2011), DOI :10.1021/ct2002946.

[170] Y.-Q. JING, Z.-R. LI, D. WU, Y. LI, B.-Q. WANG, F. L. GU, and Y. AOKI, *Effect of the complexant shape on the large first hyperpolarizability of alkalides* $Li^+(NH_3)_4M^-$, ChemPhysChem, **7**, 1759–1763 (2006), DOI :10.1002/cphc.200600157.

[171] H. W. KROTO, J. R. HEATH, S. C. O'BRIEN, R. F. CURL, and R. E. SMALLEY, *C_{60}: Buckminsterfullerene*, Nature, **318**, 162–163 (1985), DOI :10.1038/318162a0.

[172] A. SYGULA, F. R. FRONCZEK, R. SYGULA, P. W. RABIDEAU, and M. M. OLMSTEAD, *A double concave hydrocarbon buckycatcher*, J. Am. Chem. Soc., **129**, 3842–3843 (2007), DOI :10.1021/ja070616p.

[173] R. B. WOODWARD, G. A. IACOBUCCI, and I. A. HOCHSTEIN, *The synthesis of ellipticine*, J. Am. Chem. Soc., **81**, 4434–4435 (1959), DOI :10.1021/ja01525a085.

[174] M. J. FRISCH, G. W. TRUCKS, H. B. SCHLEGEL, G. E. SCUSERIA, M. A. ROBB, J. R. CHEESEMAN, G. SCALMANI, V. BARONE, B. MENNUCCI, G. A. PETERSSON, H. NAKATSUJI, M. CARICATO, X. LI, H. P. HRATCHIAN, A. F. IZMAYLOV, J. BLOINO, G. ZHENG, J. L. SONNENBERG, M. HADA, M. EHARA, K. TOYOTA, R. FUKUDA, J. HASEGAWA, M. ISHIDA, T. NAKAJIMA, Y. HONDA, O. KITAO, H. NAKAI, T. VREVEN, J. A. MONTGOMERY, JR., J. E. PERALTA, F. OGLIARO, M. BEARPARK, J. J. HEYD, E. BROTHERS, K. N. KUDIN, V. N. STAROVEROV, R. KOBAYASHI, J. NORMAND, K. RAGHAVACHARI, A. RENDELL, J. C. BURANT, S. S. IYENGAR, J. TOMASI, M. COSSI, N. REGA, J. M. MILLAM, M. KLENE, J. E. KNOX, J. B. CROSS, V. BAKKEN, C. ADAMO, J. JARAMILLO, R. GOMPERTS, R. E. STRATMANN,

O. YAZYEV, A. J. AUSTIN, R. CAMMI, C. POMELLI, J. W. OCHTERSKI, R. L. MARTIN, K. MOROKUMA, V. G. ZAKRZEWSKI, G. A. VOTH, P. SALVADOR, J. J. DANNENBERG, S. DAPPRICH, A. D. DANIELS, Ö. FARKAS, J. B. FORESMAN, J. V. ORTIZ, J. CIOSLOWSKI, and D. J. FOX, *Gaussian 09 Revision E.01*, Gaussian Inc. Wallingford CT (2009).

[175] F. CARUSO, P. RINKE, X. REN, A. RUBIO, and M. SCHEFFLER, *Self-consistent GW: All-electron implementation with localized basis functions*, Phys. Rev. B, **88**, 075105 (2013), DOI :10.1103/PhysRevB.88.075105.

[176] M. RAAB, G. HÖNING, W. DEMTRÖDER, and C. R. VIDAL, *High resolution laser spectroscopy of Cs_2. ii. Doppler-free polarization spectroscopy of the $C\,^1\Pi_u \leftarrow X\,^1\Sigma_g^+$ system*, J. Chem. Phys., **76**, 4370–4386 (1982), DOI :10.1063/1.443571.

[177] U. DIEMER, H. WEICKENMEIER, M. WAHL, and W. DEMTRÖDER, *Sub-Doppler spectroscopy of the NaCs molecule*, Chem. Phys. Lett., **104**, 489–495 (1984), DOI :10.1016/0009-2614(84)85628-6.

[178] W. NEUMANN and H. PAULY, *Study of the glory effect for atomic collisions in the hyperthermal energy region*, J. Chem. Phys., **52**, 2548–2555 (1970), DOI :10.1063/1.1673342.

[179] P. J. DAGDIGIAN and L. WHARTON, *Molecular beam electric deflection and resonance spectroscopy of the heteronuclear alkali dimers: $^{39}K^7Li$, Rb^7Li, $^{39}K^{23}Na$, $Rb^{23}Na$, and $^{133}Cs^{23}Na$*, J. Chem. Phys., **57**, 1487–1496 (1972), DOI :10.1063/1.1678429.

[180] W. MÜLLER, J. FLESCH, and W. MEYER, *Treatment of intershell correlation effects in ab initio calculations by use of core polarization potentials. Method and application to alkali and alkaline earth atoms*, J. Chem. Phys., **80**, 3297–3310 (1984), DOI :10.1063/1.447083.

[181] G. IGEL-MANN, U. WEDIG, P. FUENTEALBA, and H. STOLL, *Ground-state properties of alkali dimers XY (X, Y=Li to Cs)*, J. Chem. Phys., **84**, 5007–5012 (1986), DOI :10.1063/1.450649.

[182] M. URBAN and A. J. SADLEJ, *Electronic structure and electric properties of the alkali metal dimers*, J. Chem. Phys., **103**, 9692–9704 (1995), DOI :10.1063/1.469984.

[183] G. MERCURIO, E. R. MCNELLIS, I. MARTIN, S. HAGEN, F. LEYSSNER, S. SOUBATCH, J. MEYER, M. WOLF, P. TEGEDER, F. S. TAUTZ, and K. REUTER, *Structure and energetics of azobenzene on Ag(111): Benchmarking semiempirical dispersion correction approaches*, Phys. Rev. Lett., **104**, 036102 (2010), DOI :10.1103/PhysRevLett.104.036102.

[184] A. KAHN, *Fermi level, work function and vacuum level*, Mater. Horiz., **3**, 7–10 (2016), DOI :10.1039/C5MH00160A.

[185] W. M. HAYNES, D. R. LIDE, and T. J. BRUNO, *Handbook of chemistry and physics 94^{th} edition (2013–2014)*, CRC Press (Available online at `http://www.hbcpnetbase.com`).

[186] G. R. CASTRO, H. BUSSE, S. U., T. JANSSENS, and K. WANDELT, *Geometric and electronic structure of potassium on Rh(111)*, Phys. Scr., **T41**, 208 (1992), DOI :10.1088/0031-8949/1992/T41/036.

[187] J. W. NIEMANTSVERDRIET, *Spectroscopy in catalysis, an introduction*, VCH, Weinheim (1993).

[188] E. VAN LENTHE, E. J. BAERENDS, and J. G. SNIJDERS, *Relativistic total energy using regular approximations*, J. Chem. Phys., **101**, 9783–9792 (1994), DOI :10.1063/1.467943.

[189] N. E. SINGH-MILLER and N. MARZARI, *Surface energies, work functions, and surface relaxations of low-index metallic surfaces from first principles*, Phys. Rev. B, **80**, 235407 (2009), DOI :10.1103/PhysRevB.80.235407.

[190] J. L. DA SILVA, C. STAMPFL, and M. SCHEFFLER, *Converged properties of clean metal surfaces by all-electron first-principles calculations*, Surf. Sci., **600**, 703–715 (2006), DOI :10.1016/j.susc.2005.12.008.

[191] P. ROMANIELLO and P. L. DE BOEIJ, *The role of relativity in the optical response of gold within the time-dependent current-density-functional theory*, J. Chem. Phys., **122**, 164303 (2005), DOI :10.1063/1.1884985.

[192] N. KOCH, *Organic electronic devices and their functional interfaces*, ChemPhysChem, **8**, 1438–1455 (2007), DOI :10.1002/cphc.200700177.

[193] W. LIU, S. N. FILIMONOV, J. CARRASCO, and A. T. TKATCHENKO, *Molecular switches from benzene derivatives adsorbed on metal surfaces*, Nat. Commun., **4**, 2569 (2013), DOI :10.1038/ncomms3569.

[194] Y. L. HUANG, E. WRUSS, D. A. EGGER, S. KERA, N. UENO, W. A. SAIDI, T. BUCKO, A. T. S. WEE, and E. ZOJER, *Understanding the adsorption of CuPc and ZnPc on noble metal surfaces by combining quantum-mechanical modelling and photoelectron spectroscopy*, Molecules, **19**, 2969–2992 (2014), DOI :10.3390/molecules19032969.

[195] M. ROHLFING, R. TEMIROV, and F. S. TAUTZ, *Adsorption structure and scanning tunneling data of a prototype organic-inorganic interface: PTCDA on Ag(111)*, Phys. Rev. B, **76**, 115421 (2007), DOI :10.1103/PhysRevB.76.115421.

[196] P. SONY, P. PUSCHNIG, D. NABOK, and C. AMBROSCH-DRAXL, *Importance of van der Waals interaction for organic molecule-metal junctions: Adsorption of thiophene on Cu(110) as a prototype*, Phys. Rev. Lett., **99**, 176401 (2007), DOI :10.1103/PhysRevLett.99.176401.

[197] M.-T. NGUYEN, C. A. PIGNEDOLI, M. TREIER, R. FASEL, and D. PASSERONE, *The role of van der Waals interactions in surface-supported supramolecular networks*, Phys. Chem. Chem. Phys., **12**, 992–999 (2010), DOI :10.1039/B919102J.

[198] H. RYDBERG, M. DION, N. JACOBSON, E. SCHRÖDER, P. HYLDGAARD, S. I. SIMAK, D. C. LANGRETH, and B. I. LUNDQVIST, *Van der Waals density functional for layered structures*, Phys. Rev. Lett., **91**, 126402 (2003), DOI :10.1103/PhysRevLett.91.126402.

[199] L. ROMANER, D. NABOK, P. PUSCHNIG, E. ZOJER, and C. AMBROSCH-DRAXL, *Theoretical study of PTCDA adsorbed on the coinage metal surfaces, Ag(111), Au(111) and Cu(111)*, New J. Phys., **11**, 053010 (2009), DOI :10.1088/1367-2630/11/5/053010.

[200] G. MERCURIO, R. J. MAURER, W. LIU, S. HAGEN, F. LEYSSNER, P. TEGEDER, J. MEYER, A. TKATCHENKO, S. SOUBATCH, K. REUTER, and F. S. TAUTZ, *Quantification of finite-temperature effects on adsorption geometries of π-conjugated molecules: Azobenzene/Ag(111)*, Phys. Rev. B, **88**, 035421 (2013), DOI :10.1103/PhysRevB.88.035421.

[201] S. D. CHAKAROVA-KÄCK, E. SCHRÖDER, B. I. LUNDQVIST, and D. C. LANGRETH, *Application of van der Waals density functional to an extended system: Adsorption of benzene and naphthalene on graphite*, Phys. Rev. Lett., **96**, 146107 (2006), DOI :10.1103/PhysRevLett.96.146107.

[202] H. ISHII, K. SUGIYAMA, D. YOSHIMURA, E. ITO, Y. OUCHI, and K. SEKI, *Energy-level alignment at model interfaces of organic electroluminescent devices studied by UV photoemission: trend in the deviation from the traditional way of estimating the interfacial electronic structures*, IEEE J. Sel. Top. Quantum Electron., **4**, 24–33 (1998), DOI :10.1109/2944.669459.

[203] H. ISHII, K. SUGIYAMA, E. ITO, and K. SEKI, *Energy level alignment and interfacial electronic structures at organic/metal and organic/organic interfaces*, Adv. Mater., **11**, 605–625 (1999), DOI :10.1002/(SICI)1521-4095(199906)11:8<605::AID-ADMA605>3.0.CO;2-Q.

[204] P. C. RUSU, G. GIOVANNETTI, C. WEIJTENS, R. COEHOORN, and G. BROCKS, *Work function pinning at metal-organic interfaces*, J. Phys. Chem. C, **113**, 9974–9977 (2009), DOI :10.1021/jp902905y.

[205] P. C. RUSU, G. GIOVANNETTI, C. WEIJTENS, R. COEHOORN, and G. BROCKS, *First-principles study of the dipole layer formation at metal-organic interfaces*, Phys. Rev. B, **81**, 125403 (2010), DOI :10.1103/PhysRevB.81.125403.

[206] O. T. HOFMANN, D. A. EGGER, and E. ZOJER, *Work-function modification beyond pinning: When do molecular dipoles count?*, Nano Lett., **10**, 4369–4374 (2010), DOI :10.1021/nl101874k.

[207] Z. MA, F. RISSNER, L. WANG, G. HEIMEL, Q. LI, Z. SHUAI, and E. ZOJER, *Electronic structure of pyridine-based SAMs on flat Au(111) surfaces: extended charge rearrangements and Fermi level pinning*, Phys. Chem. Chem. Phys., **13**, 9747–9760 (2011), DOI :10.1039/C0CP02168G.

[208] C. HÜCKSTÄDT, S. SCHMIDT, S. HÜFNER, F. FORSTER, F. REINERT, and M. SPRINGBORG, *Work function studies of rare-gas/noble metal adsorption systems using a Kelvin probe*, Phys. Rev. B, **73**, 075409 (2006), DOI :10.1103/PhysRevB.73.075409.

[209] O. T. HOFMANN, J.-C. DEINERT, Y. XU, P. RINKE, J. STÄHLER, M. WOLF, and M. SCHEFFLER, *Large work function reduction by adsorption of a molecule with a negative electron affinity: Pyridine on ZnO($10\bar{1}0$)*, J. Chem. Phys., **139**, 174701 (2013), DOI :10.1063/1.4827017.

[210] E. GOIRI, M. MATENA, A. EL-SAYED, J. LOBO-CHECA, P. BORGHETTI, C. ROGERO, B. DETLEFS, J. DUVERNAY, J. E. ORTEGA, and D. G. DE OTEYZA, *Self-assembly of bicomponent molecular monolayers: Adsorption height changes and their consequences*, Phys. Rev. Lett., **112**, 117602 (2014), DOI :10.1103/PhysRevLett.112.117602.

[211] H. H. KIM, J. W. YANG, S. B. JO, B. KANG, S. K. LEE, H. BONG, G. LEE, K. S. KIM, and K. CHO, *Substrate-induced solvent intercalation for stable graphene doping*, ACS Nano, **7**, 1155–1162 (2013), DOI :10.1021/nn306012p.

[212] B. KANG, S. LIM, W. H. LEE, S. B. JO, and K. CHO, *Work-function-tuned reduced graphene oxide via direct surface functionalization as source/drain electrodes in bottom-contact organic transistors*, Adv. Mater., **25**, 5856–5862 (2013), DOI :10.1002/adma.201302358.

[213] W. GAO and A. KAHN, *Controlled p-doping of zinc phthalocyanine by coevaporation with tetrafluorotetracyanoquinodimethane: A direct and inverse photoemission study*, Appl. Phys. Lett., **79**, 4040–4042 (2001), DOI :10.1063/1.1424067.

[214] X. CRISPIN, V. GESKIN, A. CRISPIN, J. CORNIL, R. LAZZARONI, W. R. SALANECK, and J.-L. BRÉDAS, *Characterization of the interface dipole at organic/ metal interfaces*, J. Am. Chem. Soc., **124**, 8131–8141 (2002), DOI :10.1021/ja025673r.

[215] N. KOCH, S. DUHM, J. P. RABE, A. VOLLMER, and R. L. JOHNSON, *Optimized hole injection with strong electron acceptors at organic-metal interfaces*, Phys. Rev. Lett., **95**, 237601 (2005), DOI :10.1103/PhysRevLett.95.237601.

[216] S. BRAUN, M. P. DE JONG, W. OSIKOWICZ, and W. R. SALANECK, *Influence of the electrode work function on the energy level alignment at organic-organic interfaces*, Appl. Phys. Lett., **91**, 202108 (2007), DOI :10.1063/1.2806938.

[217] F. TAUTZ, *Structure and bonding of large aromatic molecules on noble metal surfaces: The example of PTCDA*, Prog. Surf. Sci., **82**, 479–520 (2007), DOI :10.1016/j.progsurf.2007.09.001.

[218] A. CRISPIN, X. CRISPIN, M. FAHLMAN, M. BERGGREN, and W. R. SALANECK, *Transition between energy level alignment regimes at a low band gap polymer-electrode interfaces*, Appl. Phys. Lett., **89**, 213503 (2006), DOI :10.1063/1.2396899.

[219] S. BRAUN, W. R. SALANECK, and M. FAHLMAN, *Energy-level alignment at organic/metal and organic/organic interfaces*, Adv. Mater., **21**, 1450–1472 (2009), DOI :10.1002/adma.200802893.

[220] J. L. F. DA SILVA, C. STAMPFL, and M. SCHEFFLER, *Adsorption of Xe atoms on metal surfaces: New insights from first-principles calculations*, Phys. Rev. Lett., **90**, 066104 (2003), DOI :10.1103/PhysRevLett.90.066104.

[221] G. M. RANGGER, L. ROMANER, G. HEIMEL, and E. ZOJER, *Understanding the properties of interfaces between organic self-assembled monolayers and noble metals—a theoretical perspective*, Surf. Interface Anal., **40**, 371–378 (2008), DOI :10.1002/sia.2645.

[222] G. HEIMEL, L. ROMANER, E. ZOJER, and J.-L. BRÉDAS, *Toward control of the metal-organic interfacial electronic structure in molecular electronics: A first-principles study on self-assembled monolayers of π-conjugated molecules on noble metals*, Nano Lett., **7**, 932–940 (2007), DOI :10.1021/nl0629106.

[223] O. T. HOFMANN, V. ATALLA, N. MOLL, P. RINKE, and M. SCHEFFLER, *Interface dipoles of organic molecules on Ag(111) in hybrid density-functional theory*, New J. Phys., **15**, 123028 (2013), DOI :10.1088/1367-2630/15/12/123028.

[224] C. T. CAMPBELL and J. R. V. SELLERS, *The entropies of adsorbed molecules*, J. Am. Chem. Soc., **134**, 18109–18115 (2012), DOI :10.1021/ja3080117.

[225] G. WITTE, S. LUKAS, P. S. BAGUS, and C. WÖLL, *Vacuum level alignment at organic/metal junctions: "Cushion" effect and the interface dipole*, Appl. Phys. Lett., **87**, 263502 (2005), DOI :10.1063/1.2151253.

[226] X.-L. ZHOU, M. CASTRO, and J. WHITE, *Interactions of UV photons and low energy electrons with chemisorbed benzene on Ag(111)*, Surf. Sci., **238**, 215–225 (1990), DOI :10.1016/0039-6028(90)90079-N.

[227] M. XI, M. X. YANG, S. K. JO, B. E. BENT, and P. STEVENS, *Benzene adsorption on Cu(111): Formation of a stable bilayer*, J. Chem. Phys., **101**, 9122–9131 (1994), DOI :10.1063/1.468041.

[228] P. YANNOULIS, R. DUDDE, K. H. FRANK, and E. E. KOCH, *Orientation of aromatic hydrocarbons on metal surfaces as determined by nexafs*, Surf. Sci., **189**, 519–528 (1987), DOI :10.1016/S0039-6028(87)80476-4.

[229] R. DUDDE, K. H. FRANK, and E. E. KOCH, *The electronic structure of benzene adsorbed on Ag(111) studied by angle resolved photoemission*, Surf. Sci., **225**, 267–272 (1990), DOI :10.1016/0039-6028(90)90447-G.

[230] T. S. CHWEE and M. B. SULLIVAN, *Adsorption studies of C_6H_6 on Cu(111), Ag(111), and Au(111) within dispersion corrected density functional theory*, J. Chem. Phys., **137**, 134703 (2012), DOI :10.1063/1.4755993.

[231] A. K. TRIPATHI and J. PFLAUM, *Correlation between ambipolar transport and structural phase transition in diindenoperylene single crystals*, Appl. Phys. Lett., **89**, 082103 (2006), DOI :10.1063/1.2338587.

[232] A. C. DÜRR, F. SCHREIBER, M. MÜNCH, N. KARL, B. KRAUSE, V. KRUPPA, and H. DOSCH, *High structural order in thin films of the organic semiconductor diindenoperylene*, Appl. Phys. Lett., **81**, 2276–2278 (2002), DOI :10.1063/1.1508436.

[233] D. G. DE OTEYZA, E. BARRENA, H. DOSCH, and Y. WAKAYAMA, *Nanoconfinement effects in the self-assembly of diindenoperylene (DIP) on Cu(111) surfaces*, Phys. Chem. Chem. Phys., **11**, 8741–8744 (2009), DOI :10.1039/B903116B.

[234] H. HUANG, J.-T. SUN, Y. P. FENG, W. CHEN, and A. T. S. WEE, *Epitaxial growth of diindenoperylene ultrathin films on Ag(111) investigated by LT-STM and LEED*, Phys. Chem. Chem. Phys., **13**, 20933–20938 (2011), DOI :10.1039/C1CP22769F.

[235] D. G. DE OTEYZA, E. BARRENA, M. RUIZ-OSÉS, I. SILANES, B. P. DOYLE, J. E. ORTEGA, A. ARNAU, H. DOSCH, and Y. WAKAYAMA, *Crystallographic and electronic structure of self-assembled DIP monolayers on Au(111) substrates*, J. Phys. Chem. C, **112**, 7168–7172 (2008), DOI :10.1021/jp800631p.

[236] O. T. HOFMANN, G. M. RANGGER, and E. ZOJER, *Reducing the metal work function beyond Pauli pushback: A computational investigation of tetrathiafulvalene and viologen on coinage metal surfaces*, J. Phys. Chem. C, **112**, 20357–20365 (2008), DOI :10.1021/jp806834g.

[237] R. S. MULLIKEN, *Criteria for the construction of good self-consistent-field molecular orbital wave functions, and the significance of LCAO-MO population analysis*, J. Chem. Phys., **36**, 3428–3439 (1962), DOI :10.1063/1.1732476.

[238] R. HOFFMANN, *A chemical and theoretical way to look at bonding on surfaces*, Rev. Mod. Phys., **60**, 601–628 (1988), DOI :10.1103/RevModPhys.60.601.

[239] A. HAUSCHILD, R. TEMIROV, S. SOUBATCH, O. BAUER, A. SCHÖLL, B. C. C. COWIE, T.-L. LEE, F. S. TAUTZ, and M. SOKOLOWSKI, *Normal-incidence x-ray standing-wave determination of the adsorption geometry of PTCDA on Ag(111): Comparison of the ordered room-temperature and disordered low-temperature phases*, Phys. Rev. B, **81**, 125432 (2010), DOI :10.1103/PhysRevB.81.125432.

[240] S. DUHM, A. GERLACH, I. SALZMANN, B. BRÖKER, R. JOHNSON, F. SCHREIBER, and N. KOCH, *PTCDA on Au(111), Ag(111) and Cu(111): Correlation of interface charge transfer to bonding distance*, Org. Electron., **9**, 111–118 (2008), DOI :10.1016/j.orgel.2007.10.004.

[241] Y. ZOU, L. KILIAN, A. SCHÖLL, T. SCHMIDT, R. FINK, and E. UMBACH, *Chemical bonding of PTCDA on Ag surfaces and the formation of interface states*, Surf. Sci., **600**, 1240–1251 (2006), DOI :10.1016/j.susc.2005.12.050.

[242] I. KRÖGER, B. STADTMÜLLER, C. STADLER, J. ZIROFF, M. KOCHLER, A. STAHL, F. POLLINGER, T.-L. LEE, J. ZEGENHAGEN, F. REINERT, and C. KUMPF, *Submonolayer growth of copper-phthalocyanine on Ag(111)*, New. J. Phys., **12**, 083038 (2010), DOI :10.1088/1367-2630/12/8/083038.

[243] K. GLÖCKLER, C. SEIDEL, A. SOUKOPP, M. SOKOLOWSKI, E. UMBACH, M. BÖHRINGER, R. BERNDT, and W.-D. SCHNEIDER, *Highly ordered structures and submolecular scanning tunnelling microscopy contrast of PTCDA and DM-PBDCI monolayers on Ag(111) and Ag(110)*, Surf. Sci., **405**, 1–20 (1998), DOI :10.1016/S0039-6028(97)00888-1.

[244] A. KRAFT, R. TEMIROV, S. K. M. HENZE, S. SOUBATCH, M. ROHLFING, and F. S. TAUTZ, *Lateral adsorption geometry and site-specific electronic structure of a large organic chemisorbate on a metal surface*, Phys. Rev. B, **74**, 041402 (2006), DOI :10.1103/PhysRevB.74.041402.

[245] M. EREMTCHENKO, D. BAUER, J. A. SCHAEFER, and F. S. TAUTZ, *Polycyclic aromates on close-packed metal surfaces: functionalization, molecular chemisorption and organic epitaxy*, New J. Phys., **6**, 4 (2004), DOI :10.1088/1367-2630/6/1/004.

[246] I. KRÖGER, B. STADTMÜLLER, C. KLEIMANN, P. RAJPUT, and C. KUMPF, *Normal-incidence x-ray standing-wave study of copper phthalocyanine submonolayers on Cu(111) and Au(111)*, Phys. Rev. B, **83**, 195414 (2011), DOI :10.1103/PhysRevB.83.195414.

[247] G. M. RANGGER, O. T. HOFMANN, L. ROMANER, G. HEIMEL, B. BRÖKER, R.-P. BLUM, R. L. JOHNSON, N. KOCH, and E. ZOJER, *F4TCNQ on Cu, Ag, and Au as prototypical example for a strong organic acceptor on coinage metals*, Phys. Rev. B, **79**, 165306 (2009), DOI :10.1103/PhysRevB.79.165306.

[248] L. ROMANER, G. HEIMEL, J.-L. BRÉDAS, A. GERLACH, F. SCHREIBER, R. L. JOHNSON, J. ZEGENHAGEN, S. DUHM, N. KOCH, and E. ZOJER, *Impact of bidirectional charge transfer and molecular distortions on the electronic structure of a metal-organic interface*, Phys. Rev. Lett., **99**, 256801 (2007), DOI :10.1103/PhysRevLett.99.256801.

[249] J. P. PERDEW, J. A. CHEVARY, S. H. VOSKO, K. A. JACKSON, M. R. PEDERSON, D. J. SINGH, and C. FIOLHAIS, *Atoms, molecules, solids, and surfaces: Applications of the generalized gradient approximation for exchange and correlation*, Phys. Rev. B, **46**, 6671–6687 (1992), DOI :10.1103/PhysRevB.46.6671.

[250] A. TKATCHENKO, R. A. DISTASIO, JR., R. CAR, and M. SCHEFFLER, *Accurate and efficient method for many-body van der Waals interactions*, Phys. Rev. Lett., **108**, 236402 (2012), DOI :10.1103/PhysRevLett.108.236402.

[251] A. TKATCHENKO, A. AMBROSETTI, and R. A. DISTASIO JR., *Interatomic methods for the dispersion energy derived from the adiabatic connection fluctuation-dissipation theorem*, J. Chem. Phys., **138**, 074106 (2013), DOI :10.1063/1.4789814.

[252] H. B. G. CASIMIR and D. POLDER, *Influence of retardation on the London-van der Waals forces*, Nature, **158**, 787–788 (1946), DOI :10.1038/158787a0.

[253] M. LEVY, *Universal variational functionals of electron densities, first-order density matrices, and natural spin-orbitals and solution of the v-representability problem*, Proc. Natl. Acad. Sci., **76**, 6062–6065 (1979), DOI :10.1073/pnas.76.12.6062.

[254] E. H. LIEB, *Density functionals for Coulomb systems*, Int. J. Quantum Chem., **24**, 243–277 (1983), DOI :10.1002/qua.560240302.

[255] J. ŘEZÁČ, P. JUREČKA, K. E. RILEY, J. ČERNÝ, H. VALDES, K. PLUHÁČKOVÁ, K. BERKA, T. ŘEZÁČ, M. PITOŇÁK, J. VONDRÁŠEK, and P. HOBZA, *Quantum chemical benchmark energy and geometry database for molecular clusters and complex molecular systems (www.begdb.com): A users manual and examples*, CCCC, **73**, 1261–1270 (2008), DOI :10.1135/cccc20081261.

[256] J. HARRIS, *Simplified method for calculating the energy of weakly interacting fragments*, Phys. Rev. B, **31**, 1770–1779 (1985), DOI :10.1103/PhysRevB.31.1770.

[257] H. J. MONKHORST and J. D. PACK, *Special points for Brillouin-zone integrations*, Phys. Rev. B, **13**, 5188–5192 (1976), DOI :10.1103/PhysRevB.13.5188.

[258] T. H. DUNNING, *Gaussian basis sets for use in correlated molecular calculations. I. The atoms boron through neon and hydrogen*, J. Chem. Phys., **90**, 1007–1023 (1989), DOI :10.1063/1.456153.

[259] B. DELLEY, *Fast calculation of electrostatics in crystals and large molecules*, J. Phys. Chem., **100**, 6107–6110 (1996), DOI :10.1021/jp952713n.

[260] J. CARRASCO, W. LIU, A. MICHAELIDES, and A. TKATCHENKO, *Insight into the description of van der Waals forces for benzene adsorption on transition metal (111) surfaces*, J. Chem. Phys., **140**, 084704 (2014), DOI :10.1063/1.4866175.